



Università della Calabria

Dipartimento di Ingegneria per l'Ambiente e il Territorio e Ingegneria Chimica
Dottorato in Scienze ed Ingegneria dell'Ambiente, delle Costruzioni e dell'Energia

Ph.D. Dissertation

Mass and momentum transfer in membrane-based
bioartificial liver systems

Ph.D. Candidate: Shervin Khakpour

Supervisors: Dr. Loredana De Bartolo
Prof. Efrem Curcio

Università della Calabria

Dipartimento di Ingegneria per l'Ambiente e il Territorio e Ingegneria Chimica
(DIATIC)

A thesis submitted for the degree of

Doctor of philosophy

in

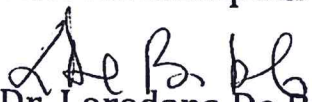
Scienze ed Ingegneria dell'Ambiente, delle Costruzioni e dell' Energia (SIACE)

CHIM/07 Fondamenti Chimici delle Tecnologie

Ciclo XXIX

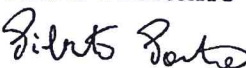
Mass and momentum transfer in membrane-based
bioartificial liver systems


Ph.D. Candidate: Shervin Khakpour


Supervisors: Dr. Loredana De Bartolo


Prof. Efrem Curcio

Coordinator: Prof. Pietro Pantano



Host institution: Istituto per la Tecnologia delle Membrane
Consiglio Nazionale delle Ricerche (ITM – CNR)

This research was funded by:



Marie Skłodowska-Curie Actions

Initial Training Network

Project “BIOART”

*Training network for developing innovative (bio)artificial devices for
treatment of kidney and liver disease*

(Grant no.316690, EU-FP7-PEOPLE-ITN-2012)

To my parents

Contents

LIST OF FIGURES.....	I
LIST OF TABLES	VI
ACKNOWLEDGEMENTS	VII
ABSTRACT	VIII
ABSTRACT	XI
NOMENCLATURE.....	XV

CHAPTER 1

STATE OF THE ART AND AIM OF THE WORK	18
1.1 LIVER ANATOMY AND FUNCTIONS.....	18
1.2 LIVER FAILURE AND TREATMENT MODALITIES	20
1.3 ARTIFICIAL LIVER DEVICES.....	21
1.4 BIOARTIFICIAL LIVER SYSTEMS	22
1.5 MEMBRANE-BASED BIOREACTORS FOR IN VITRO CELL CULTURES	24
1.5.1 FLAT PLATE MEMBRANE BIOREACTORS	24
1.5.2 HOLLOW FIBER MEMBRANE BIOREACTORS	25
1.6 BIOARTIFICIAL LIVER SYSTEMS IN CLINICAL TRIAL	26
1.7 OTHER BIOREACTOR DESIGNS FOR IN VITRO HEPATIC CULTURE STUDIES.....	27
1.8 CHALLENGES IN BIOREACTOR DESIGN.....	29
1.8.1 MEMBRANES	30
1.8.2 TRANSPORT PHENOMENA.....	32
1.9 ABOUT CURRENT RESEARCH STUDY	35
1.9.1 MOTIVATION	35
1.9.2 OBJECTIVE.....	36
1.9.3 APPROACH	38
REFERENCES.....	40

CHAPTER 2

FLUID DYNAMICS AND PERMEABILITY IN THE MEMBRANE BIOREACTOR.....	46
2.1 INTRODUCTION.....	46
2.2 MATERIALS AND METHODS	47
2.2.1 HOLLOW FIBER PERMEABILITY TESTS.....	47
2.2.2 BIOREACTOR FLUID DYNAMICS	49
2.2.3 STATIC SYSTEM	51
2.3 RESULTS.....	53
2.3.1 HOLLOW FIBERS	53
2.3.2 BIOREACTOR	54
2.3.3 STATIC SYSTEM	55
2.4 DISCUSSION	57
2.5 CONCLUSIONS	59
REFERENCES.....	60

CHAPTER 3

<u>OXYGEN TRANSFER MODEL IN STATIC CULTURE SYSTEMS.....</u>	61
3.1 INTRODUCTION.....	61
3.2 METHODS	62
3.2.1 MATHEMATICAL MODEL	62
3.2.2 BOUNDARY CONDITIONS	64
3.3 RESULTS.....	65
3.3.1 SPHEROIDS.....	65
3.3.2 CELLULAR LAYER.....	69
3.4 DISCUSSION.....	71
3.5 CONCLUSIONS	72
REFERENCES.....	73

CHAPTER 4

<u>MASS TRANSFER MODEL FOR HOLLOW FIBER MEMBRANE BIOREACTORS</u>	74
4.1 INTRODUCTION.....	74
4.2 MATHEMATICAL MODEL.....	74
4.3 GEOMETRY AND BOUNDARY CONDITIONS	78
4.3.1 SINGLE-SPHEROID MODEL	78
4.3.2 MINIATURIZED BIOREACTOR.....	80
4.4 IMPLEMENTATION IN COMSOL MULTIPHYSICS	81
4.5 RESULTS.....	82
4.5.1 DEPENDENT VARIABLES.....	82
4.5.2 MESH SENSITIVITY	82
4.5.3 EXTENDED ELEMENT: MODEL VALIDITY	84
4.6 DISCUSSION.....	84
4.7 CONCLUSION	87
REFERENCES.....	88

CHAPTER 5

<u>EFFECT OF DIFFERENT PARAMETERS ON OXYGEN TRANSPORT</u>	90
5.1 INTRODUCTION.....	90
5.2 MATERIALS AND METHODS.....	91
5.3 RESULTS.....	93
5.4 DISCUSSION	98
5.5 CONCLUSION	102
REFERENCES.....	103

CHAPTER 6

<u>ESTABLISHMENT OF IN VIVO-LIKE OXYGEN GRADIENT INSIDE THE SPHEROIDS CULTURED IN THE BIOREACTOR.....</u>	104
6.1 INTRODUCTION.....	104
6.2 MATERIALS AND METHODS.....	105
6.2.1 MATHEMATICAL MODEL	105

6.2.2	EXPERIMENTAL PROCEDURE.....	106
6.3	RESULTS.....	107
6.3.1	MAINTAINING PHYSIOLOGICAL DOC RANGE <i>IN VITRO</i>	107
6.3.2	OXYGEN SUPPLY TO A SHRINKING HEPATOCYTE SPHEROID: CONSTANT NUMBER OF CELLS.....	110
6.3.3	MODEL BASED ON EXPERIMENTAL DATA.....	111
6.4	DISCUSSION.....	114
6.5	CONCLUSION.....	115
	REFERENCES.....	116

CHAPTER 7

MASS TRANSFER IN MINIATURIZED BIOREACTOR.....		118
7.1	INTRODUCTION.....	118
7.2	METHODS.....	119
7.2.1	APPROACH.....	119
7.2.2	MINIATURIZED BIOREACTOR MODEL: SCALING DOWN PROCEDURE.....	119
7.3	RESULTS.....	121
7.3.1	EFFECT OF MINIMIZING THE STAGNANT REGION ON OXYGEN TRANSFER.....	124
7.3.2	EFFECT OF RETENTATE FLOW ON OXYGEN TRANSFER.....	127
7.3.3	EFFECT OF FLOW PATTERN AND FLUID DYNAMICS.....	129
7.3.4	MODEL BASED ON EXPERIMENTAL DATA.....	135
7.4	DISCUSSION.....	137
7.5	CONCLUSIONS.....	139
	REFERENCES.....	139

CHAPTER 8

CONCLUSIONS AND FUTURE DIRECTIONS.....		140
8.1	SUMMARY OF CONTRIBUTIONS.....	140
8.2	RECOMMENDATIONS FOR FUTURE WORK.....	142

APPENDIX 1: FLUIDIZED-BED BIOREACTOR.....

1.	INTRODUCTION.....	147
2.	METHODS.....	148
2.1	ALGINATE BEADS PREPARATION.....	148
2.2	FLUIDIZATION.....	149
2.3	BEADS' SWELLING OVER TIME.....	150
2.4	BEADS' FALLING VELOCITY.....	151
2.5	MASS TRANSPORT INTO THE BEADS.....	151
3.	RESULTS.....	153
4.	DISCUSSION.....	155
5.	CONCLUSIONS.....	158
	REFERENCES.....	159

List of figures

- Figure 1. 1 (Top) Macroanatomy of the liver. (Bottom) Microanatomy of the liver, showing a hepatic lobule. Image source:
https://cms.webstudy.com/WebstudyFileSystem/testovaci/GetFile/293875/Ch%2022/Ch22b/Ch22b_print.html
- Figure 1. 2 Hepatic zonation and distribution of functions along the sinusoid [5].
- Figure 1. 3 Common types of BAL devices and areas in which they are mostly employed [12].
- Figure 1. 4 Examples of bioreactors used for in vitro studies. (a) Oxygen-permeable flat-membrane bioreactor [De Bartolo et al. 2006], (b) Crossed hollow fiber membrane bioreactor [De Bartolo et al. 2009].
- Figure 1. 5 Compartmentalization of the membrane-based BALs. Bidirectional mass transfer occurs between the compartments and through the membranes. The concentration gradient trends shown apply to diffusion-controlled mass transfer and are merely qualitative, since the rate and extent of the gradients differ for each component.
- Figure 1. 6 Crossed-Configuration hollow fiber membrane bioreactor used in this study. (Left) assembled bioreactor for illustration purposes, (Right) schematic illustration of the bioreactor, showing the existing compartments.
- Figure 1. 7 (Top) Assembled circuit and connections used to run the bioreactor. (Bottom) Process flow diagram showing bioreactor's connections during culture.
-
- Figure 2. 1 Hollow fiber module assembled for permeability measurements (25 PEEK-WC hollow fibers, 5x5 arrangement).
- Figure 2. 2 Process flow diagram for testing hydraulic permeability and albumin permeability.
- Figure 2. 3 Experimental setup for residence time distribution analysis for the bioreactor. The reservoirs for water and tracer are not shown in the picture (on the right side).
- Figure 2. 4 Process flow diagram for residence time distribution analysis in the bioreactor.
- Figure 2. 5 OxoDish® and SensorDish® Reader used for the experiment.
- Figure 2. 6 Geometry and boundary conditions for numerical analysis.
- Figure 2. 7 Permeability study on PEEK-WC hollow fibers.
- Figure 2. 8 C_{out}/C_{max} ratio as a function of time, known as the F curve, for albumin permeance experiment.
- Figure 2. 9 E and 1-F curves for ideal mixed flow model [5].
- Figure 2. 10 1-F (top) and E (bottom) curves for experimental results in comparison with the ideal mixed flow (CSTR) model.
- Figure 2. 11 Oxygen concentrations at the bottom of the well (averaged over 4 wells for each condition) recorded over 14.3 hours after changing the oxygen partial pressure in the incubator from 20% to 10%.
- Figure 2. 12 Comparison between the experimental and theoretical values for oxygen concentrations at the bottom of the well after changing the oxygen tension in the incubator from 20% to 10%..

Figure 2. 13 E and 1-F curves for the compartment flow model of mixed flow region + stagnant region [1].

Figure 2. 14 E and 1-F curves for experimental results in comparison with the compartment flow model of mixed flow region + stagnant region.

Figure 3. 1 (Left) Geometry of a single well considered for mass transfer modelling. (Right) arrangement of 99 spheroids at the bottom of the well, and the spheroids for which the oxygen concentration profile will be given in more detail. For reducing the computational time, the geometry was divided in half considering an x-z symmetric plane.

Figure 3. 2 Boundary conditions applied for mass transfer modelling (n is the boundary's normal vector).

Figure 3. 3 Oxygen concentration profile (mol/m^3) in a well containing 1ml of culture medium and 99 spheroids ($200\mu\text{m}$ in diameter with $50\mu\text{m}$ space between them).

Figure 3. 4 Oxygen concentration profile (mol/m^3) inside the spheroids sitting at the bottom of a well containing 1ml of culture medium and 99 spheroids ($200\mu\text{m}$ in diameter, $50\mu\text{m}$ spacing).

Figure 3. 5 Oxygen concentration profile (mol/m^3) inside the spheroids sitting at the bottom of a well containing 1ml of culture medium and 99 spheroids ($200\mu\text{m}$ in diameter, $100\mu\text{m}$ spacing).

Figure 3. 6 Oxygen concentration profile (mol/m^3) inside the spheroids sitting at the bottom of a well containing 1ml of culture medium and 30 spheroids $300\mu\text{m}$ in diameter ($300\mu\text{m}$ spacing) having the same total number of cells as in 100 spheroids $200\mu\text{m}$ in diameter.

Figure 3. 7 Oxygen concentration profile (mol/m^3) inside the spheroids sitting at the bottom of a well containing 1ml of culture medium and 99 spheroids ($300\mu\text{m}$ in diameter, $700\mu\text{m}$ spacing).

Figure 3. 8 Oxygen concentration profile (mol/m^3) inside the spheroids sitting at the bottom of a well containing 2ml of culture medium.

Figure 3. 9 Oxygen concentration profile (mol/m^3) in a well containing 1ml of culture medium and a cellular monolayer with $16\mu\text{m}$ thickness and 2.89mm radius having the same total number of cells as in 99 spheroids $200\mu\text{m}$ in diameter. (Top) Concentration profile through the medium, (Bottom) concentration profile across the cellular layer.

Figure 3. 10 Oxygen concentration profile (mol/m^3) in a well containing 1ml of culture medium and a cellular monolayer fully covering the bottom of the well ($16\mu\text{m}$ thickness). Oxygen concentration in the cellular layer is $0.0432 - 0.0442 \text{ mol}/\text{m}^3$.

Figure 3. 11 Urea concentration profile and its accumulation in 1ml culture medium containing 99 spheroids ($300\mu\text{m}$ in diameter, $700\mu\text{m}$ spacing) at different time points during the culture.

Figure 4. 1 Single-spheroid model: periodic unit element ($750 \times 750 \times 500 \mu\text{m}$) representative of the bioreactor configuration.

Figure 4. 2 Miniaturized bioreactor model considering 9 hollow fibers in each bundle, hosting 20 spheroids in a $4 \times 4 \times 5$ arrangement in the extra-capillary space.

Figure 4. 3 Velocity (top), pressure (center) and concentration (bottom) profiles in the single-spheroid model.

Figure 4. 4 Dissolved oxygen concentration inside the spheroids in single-spheroid model obtained by using different physics-controlled default mesh sizes in COMSOL Multiphysics. (a) Coarser, (b) Coarse, (c) Normal, (d) Fine, (e) Finer, (f) Extra fine.

Figure 4. 5 Extended periodic unit element consisting of 36 spheroids

Figure 5. 1 Minimum and maximum DOC within the spheroid for different saturated DOCs and spheroid porosities.

Figure 5. 2 Minimum and maximum DOC within the spheroid for different perfusion rates and spheroid porosities.

Figure 5. 3 Minimum and maximum DOC within the spheroid for different spheroid diameters and porosities.

Figure 5. 4 Minimum and maximum DOC within the spheroid for different inter-HF spacing and spheroid porosities.

Figure 5. 5 Minimum and maximum DOC within the spheroid for different V_{max} and spheroid porosities.

Figure 5. 6 Minimum and maximum DOC within the spheroid, and oxygen transfer rate into the spheroid for different intra-spheroid porosities.

Figure 5. 7 Minimum and maximum DOC within the spheroid for different membrane and spheroid porosities.

Figure 6. 1 DOC profile ($\mu\text{mol/L}$) in the ECS (left) and inside the spheroid (right) for $D_{sph}=400\mu\text{m}$ and $\epsilon_{cc}=0.20$. ($C_{o,sat}=185\mu\text{mol/L}$, $QBR=1\text{ ml/min}$, $V_{max}=5\text{ nmol/(s.cm}^3)$, $K_m=5.6\text{ mm Hg}$, $\epsilon_m=0.7$, $\delta_{HF}=250\mu\text{m}$.)

Figure 6. 2 Proportion and position of the cells exposed to physiological DOC range within the spheroid with $D_{sph}=400\mu\text{m}$ and $\epsilon_{cc}=0.20$. ($C_{o,sat}=185\mu\text{mol/L}$, $QBR=1\text{ ml/min}$, $V_{max}=5\text{ nmol/(s.cm}^3)$, $K_m=5.6\text{ mm Hg}$, $\epsilon_m=0.7$, $\delta_{HF}=250\mu\text{m}$.)

Figure 6. 3 Shear (left) and normal total (right) stress exerted on the spheroid surface of the spheroid with $D_{sph}=400\mu\text{m}$ and $\epsilon_{cc}=0.20$. ($C_{o,sat}=185\mu\text{mol/L}$, $QBR=1\text{ ml/min}$, $V_{max}=5\text{ nmol/(s.cm}^3)$, $K_m=5.6\text{ mm Hg}$, $\epsilon_m=0.7$, $\delta_{HF}=250\mu\text{m}$.)

Figure 6. 4 DOC profile (mol/m^3) in the ECS (left) and inside the spheroid (right) for $D_{sph}=400\mu\text{m}$ and $\epsilon_{cc}=0.47$. ($C_{o,sat}=115\mu\text{mol/L}$, $QBR=1\text{ ml/min}$, $V_{max}=5\text{ nmol/(s.cm}^3)$, $K_m=5.6\text{ mm Hg}$, $\epsilon_m=0.7$, $\delta_{HF}=250\mu\text{m}$.)

Figure 6. 5 (Left) DOC profile (mol/m^3) in the spheroid before shrinkage. $D_{sph}=400\mu\text{m}$ and $\epsilon_{cc}=0.42$. (Right) DOC profile (mol/m^3) in the spheroid after shrinkage. $D_{sph}=360\mu\text{m}$ and $\epsilon_{cc}=0.20$. Other parameters remain unaltered for both cases: $C_{o,sat}=130\mu\text{mol/L}$, $QBR=0.8\text{ ml/min}$.

Figure 6. 6 Primary hepatocyte spheroids between hollow fibers. (Left) Separate adjacent spheroids, (Right) Spheroids merging together to form larger cellular masses.

Figure 6. 7 DOC profile (mol/m^3) inside the spheroid (left) and in the ECS (right) for $D_{sph}=200\mu\text{m}$ and $\epsilon_{cc}=0.41$. ($C_{o,sat}=224\mu\text{mol/L}$, $QBR=0.6\text{ ml/min}$, $V_{max}=17\text{ nmol/(s.cm}^3)$, $K_m=5.6\text{ mm Hg}$, $\epsilon_m=0.8$, $\delta_{HF}=250\mu\text{m}$.)

Figure 6. 8 DOC profile (mol/m³) inside the spheroid (left) and in the ECS (right) for $D_{sph}=363\mu\text{m}$ and $\epsilon_{cc}=0.41$. ($C_{o,sat}=224\mu\text{mol/L}$, $Q_{BR}=0.6\text{ ml/min}$, $V_{max}=17\text{ nmol/(s.cm}^3)$, $K_m=5.6\text{ mm Hg}$, $\epsilon_m=0.8$, $\delta_{HF}=250\mu\text{m}$).

Figure 7. 1 miniaturized bioreactor considering 9 hollow fibers in a 3x3 arrangement.

Figure 7. 2 Cubic bioreactor considering 9 hollow fibers in a 3x3 arrangement.

Figure 7. 3 Oxygen concentration in the spheroids, supplying-removing flow pattern. $D_{sph}=400\mu\text{m}$, $C_{o,sat}=185\mu\text{mol/L}$, $Q_{BR}=1\text{ ml/min}$, $V_{max}=25\text{ nmol/(s.cm}^3)$, $K_m=5.6\text{ mm Hg}$, $\epsilon_{cc}=0.42$, $\epsilon_m=0.7$.

Figure 7. 4 Oxygen concentration in the extra-capillary space, supplying-removing flow pattern. $D_{sph}=400\mu\text{m}$, $C_{o,sat}=185\mu\text{mol/L}$, $Q_{BR}=1\text{ ml/min}$, $V_{max}=25\text{ nmol/(s.cm}^3)$, $K_m=5.6\text{ mm Hg}$, $\epsilon_{cc}=0.42$, $\epsilon_m=0.7$.

Figure 7. 5 Oxygen concentration in the lumina, supplying-removing flow pattern. $D_{sph}=400\mu\text{m}$, $C_{o,sat}=185\mu\text{mol/L}$, $Q_{BR}=1\text{ ml/min}$, $V_{max}=25\text{ nmol/(s.cm}^3)$, $K_m=5.6\text{ mm Hg}$, $\epsilon_{cc}=0.42$, $\epsilon_m=0.7$.

Figure 7. 6 Urea concentration in the bioreactor, supplying-removing flow pattern. $D_{sph}=400\mu\text{m}$, $Q_{BR}=1\text{ ml/min}$, $\epsilon_{cc}=0.42$, $\epsilon_m=0.7$.

Figure 7. 7 Oxygen concentration in the spheroids for a cubic bioreactor, supplying-removing flow pattern. $D_{sph}=400\mu\text{m}$, $C_{o,sat}=185\mu\text{mol/L}$, $Q_{BR}=1\text{ ml/min}$, $V_{max}=25\text{ nmol/(s.cm}^3)$, $K_m=5.6\text{ mm Hg}$, $\epsilon_{cc}=0.42$, $\epsilon_m=0.7$.

Figure 7. 8 Oxygen concentration and Peclet number in the extra-capillary space for a cubic bioreactor, supplying-removing flow pattern. $D_{sph}=400\mu\text{m}$, $C_{o,sat}=185\mu\text{mol/L}$, $Q_{BR}=1\text{ ml/min}$, $V_{max}=25\text{ nmol/(s.cm}^3)$, $K_m=5.6\text{ mm Hg}$, $\epsilon_{cc}=0.42$, $\epsilon_m=0.7$.

Figure 7. 9 Oxygen concentration and Peclet number in the lumina for a cubic bioreactor, supplying-removing flow pattern. $D_{sph}=400\mu\text{m}$, $C_{o,sat}=185\mu\text{mol/L}$, $Q_{BR}=1\text{ ml/min}$, $V_{max}=25\text{ nmol/(s.cm}^3)$, $K_m=5.6\text{ mm Hg}$, $\epsilon_{cc}=0.42$, $\epsilon_m=0.7$.

Figure 7. 10 Oxygen concentration in the spheroids in the bioreactor with a retentate flow is present, supplying-removing flow pattern. $D_{sph}=400\mu\text{m}$, $C_{o,sat}=185\mu\text{mol/L}$, $Q_{BR}=1\text{ ml/min}$, $V_{max}=25\text{ nmol/(s.cm}^3)$, $K_m=5.6\text{ mm Hg}$, $\epsilon_{cc}=0.42$, $\epsilon_m=0.7$.

Figure 7. 11 Oxygen concentration and Peclet number in the extra-capillary space of the bioreactor with a retentate flow is present, supplying-removing flow pattern. $D_{sph}=400\mu\text{m}$, $C_{o,sat}=185\mu\text{mol/L}$, $Q_{BR}=1\text{ ml/min}$, $V_{max}=25\text{ nmol/(s.cm}^3)$, $K_m=5.6\text{ mm Hg}$, $\epsilon_{cc}=0.42$, $\epsilon_m=0.7$.

Figure 7. 12 Oxygen concentration and Peclet number in the lumina of the bioreactor with a retentate flow is present, supplying-removing flow pattern. $D_{sph}=400\mu\text{m}$, $C_{o,sat}=185\mu\text{mol/L}$, $Q_{BR}=1\text{ ml/min}$, $V_{max}=25\text{ nmol/(s.cm}^3)$, $K_m=5.6\text{ mm Hg}$, $\epsilon_{cc}=0.42$, $\epsilon_m=0.7$.

Figure 7. 13 Oxygen concentration in the spheroids, both bundles supplying the culture medium. $D_{sph}=400\mu\text{m}$, $C_{o,sat}=185\mu\text{mol/L}$, $Q_{BR}=1\text{ ml/min}$, $V_{max}=25\text{ nmol/(s.cm}^3)$, $K_m=5.6\text{ mm Hg}$, $\epsilon_{cc}=0.42$, $\epsilon_m=0.7$.

Figure 7. 14 Oxygen concentration in the extra-capillary space, both bundles supplying the culture medium. $D_{sph}=400\mu\text{m}$, $C_{o,sat}=185\mu\text{mol/L}$, $Q_{BR}=1\text{ ml/min}$, $V_{max}=25\text{ nmol/(s.cm}^3)$, $K_m=5.6\text{ mm Hg}$, $\epsilon_{cc}=0.42$, $\epsilon_m=0.7$.

Figure 7. 15 Oxygen concentration in the lumina, both bundles supplying the culture medium. $D_{sph}=400\mu\text{m}$, $C_{o,sat}=185\mu\text{mol/L}$, $Q_{BR}=1\text{ ml/min}$, $V_{max}=25\text{ nmol/(s.cm}^3)$, $K_m=5.6\text{ mm Hg}$, $\epsilon_{cc}=0.42$, $\epsilon_m=0.7$.

- Figure 7. 16 Urea concentration in the bioreactor, both bundles supplying the culture medium. $D_{\text{sph}}=400 \mu\text{m}$, $Q_{\text{BR}}=1 \text{ ml/min}$, $\epsilon_{\text{cc}}=0.42$, $\epsilon_{\text{m}}=0.7$.
- Figure 7. 17 Oxygen concentration in the spheroids, both bundles removing the culture medium. $D_{\text{sph}}=400 \mu\text{m}$, $C_{\text{o,sat}}=185 \mu\text{mol/L}$, $Q_{\text{BR}}=1 \text{ ml/min}$, $V_{\text{max}}=25 \text{ nmol/(s.cm}^3\text{)}$, $K_{\text{m}}=5.6 \text{ mm Hg}$, $\epsilon_{\text{cc}}=0.42$, $\epsilon_{\text{m}}=0.7$.
- Figure 7. 18 Oxygen concentration in the extra-capillary space, both bundles removing the culture medium. $D_{\text{sph}}=400 \mu\text{m}$, $C_{\text{o,sat}}=185 \mu\text{mol/L}$, $Q_{\text{BR}}=1 \text{ ml/min}$, $V_{\text{max}}=25 \text{ nmol/(s.cm}^3\text{)}$, $K_{\text{m}}=5.6 \text{ mm Hg}$, $\epsilon_{\text{cc}}=0.42$, $\epsilon_{\text{m}}=0.7$.
- Figure 7. 19 Oxygen concentration in the lumina, both bundles removing the culture medium. $D_{\text{sph}}=400 \mu\text{m}$, $C_{\text{o,sat}}=185 \mu\text{mol/L}$, $Q_{\text{BR}}=1 \text{ ml/min}$, $V_{\text{max}}=25 \text{ nmol/(s.cm}^3\text{)}$, $K_{\text{m}}=5.6 \text{ mm Hg}$, $\epsilon_{\text{cc}}=0.42$, $\epsilon_{\text{m}}=0.7$.
- Figure 7. 20 Urea concentration in the bioreactor, both bundles removing the culture medium. $D_{\text{sph}}=400 \mu\text{m}$, $Q_{\text{BR}}=1 \text{ ml/min}$, $\epsilon_{\text{cc}}=0.42$, $\epsilon_{\text{m}}=0.7$.
- Figure 7. 21 F (top) and E (bottom) curves used in residence time distribution analysis, obtained through modelling for three different flow patterns.
- Figure 7. 22 (Left) Oxygen concentration in the spheroids, supplying-removing pattern, 6 spheroids per ECS unit, (Right) oxygen concentration in the ECS. $D_{\text{sph}}=200 \mu\text{m}$, $C_{\text{o,sat}}=224 \mu\text{mol/L}$, $Q_{\text{BR}}=0.6 \text{ ml/min}$, $V_{\text{max}}=17 \text{ nmol/(s.cm}^3\text{)}$, $K_{\text{m}}=5.6 \text{ mm Hg}$, $\epsilon_{\text{cc}}=0.41$, $\epsilon_{\text{m}}=0.8$.
- Figure 7. 23 (Left) Oxygen concentration in the merged 6 spheroids, supplying-removing pattern. (Right) Oxygen concentration in the ECS. Equivalent $D_{\text{sph}}=363 \mu\text{m}$, $C_{\text{o,sat}}=224 \mu\text{mol/L}$, $Q_{\text{BR}}=0.6 \text{ ml/min}$, $V_{\text{max}}=17 \text{ nmol/(s.cm}^3\text{)}$, $K_{\text{m}}=5.6 \text{ mm Hg}$, $\epsilon_{\text{cc}}=0.41$, $\epsilon_{\text{m}}=0.8$.
- Figure 7. 24 (Left) Oxygen concentration in the spheroids based on scaling down seeded cell number, supplying-removing pattern. (Right) Oxygen concentration in the ECS. Equivalent $D_{\text{sph}}=359 \mu\text{m}$, $C_{\text{o,sat}}=224 \mu\text{mol/L}$, $Q_{\text{BR}}=0.6 \text{ ml/min}$, $V_{\text{max}}=17 \text{ nmol/(s.cm}^3\text{)}$, $K_{\text{m}}=5.6 \text{ mm Hg}$, $\epsilon_{\text{cc}}=0.41$, $\epsilon_{\text{m}}=0.8$.

List of tables

Table 5. 1 Parameters, their default value and the range over which they were investigated in the parametric study.

Table 5. 2 Dimensionless parameters used for evaluation of oxygen transfer in the HFMBR.

Table 5. 3 Dimensionless numbers for the default values of the parameters under study reported in Table 5. 1.

Acknowledgements

First and foremost, I would like to sincerely and wholeheartedly thank my main supervisor, Dr. Loredana De Bartolo for her full support and encouragement, and giving me the opportunity to work on a very interesting and challenging research area. I especially appreciate her dedication of time to share her vast expertise in the field and always introduce me to new topics.

I extend my deepest gratitude to Dr. Alberto Di Renzo for his generous guidance and support through the modelling work, provision of the computational means and his meticulous consultations. I was very lucky to benefit from his knowledge as well as his approaches in tackling the complications of the work.

Very special thanks to Prof. Efrem Curcio for his supervision, exchange of ideas during the meetings and insightful notions regarding the direction and drafting of the work. I really appreciate his support, attitude and morale.

Many people helped and supported me from different groups in ITM-CNR and University of Calabria. In particular, I would like to thank Prof. Francesco Paolo Di Maio for his insightful ideas and suggestions on modelling aspects. I am ever so grateful to Dr. Simona Salerno, who always patiently helped me on all the experimental and lab work. I also extend my appreciation to Dr. Franco Tasselli, for preparation and explanation of specific hollow fibers.

I would like to express my sincere gratitude to Dr. Lidietta Giorno, the director of ITM-CNR, for always helping with work-related issues, exceptional management, and all the friendly chats.

I acknowledge Marie Skłodowska-Curie Actions for financial support of this research. I extend my appreciation to all the wonderful people involved in BIOART project. I was fortunate to learn a lot from the supervisors and form memorable friendships with the fellows. I would like to especially thank the coordinator of the project, Prof. Dimitrios Stamatialis, and Prof. Cecile Legallais for arranging my very educational and invaluable secondment in University of Technology of Compiègne. Big thanks to Marie Curie fellows and great friends Haysam Ahmed and Seyed Danial Naghib, with whom I had enjoyable talks and discussions on a daily basis.

I dedicate this to my beloved family, to whom I am eternally grateful. I could not be where I am now without my parents' tremendous support, always encouraging me to move forward.

Abstract

Liver failure, caused by acute or chronic end-stage liver disease (ESLD) imposes a significant disease burden worldwide. Chronic liver disease and cirrhosis is ranked as 12th cause of death in the United States and 4th in middle-aged adults. Researchers in Mayo Clinic report liver-related mortality as 8th by using a more comprehensive definition accounting for other aspects of liver disease as well. Currently, liver transplantation remains the conventional treatment for ESLD as the only medically proven method to promote patient's health. To avoid the problem of inadequate donor organs and yet provide a comprehensive range of liver functions, cell-based therapies have been actively under investigation to potentially provide a substitute for transplantation, or a temporary support for liver failure patients. Studies on the latter aim has led to development of extracorporeal bioartificial liver (BAL) devices.

Hepatic cell cultures are exploited for different applications in liver disease studies, drug toxicity testing, and bioartificial liver (BAL) devices. However, development of such systems is often hindered by the peculiar characteristics and intricate requirements of primary hepatocytes, challenging their prolonged functionality and viability in vitro. Despite the development of various 3D cell culture systems using perfused bioreactors, mass transfer properties still remain a critical and controversial topic, especially oxygen supply as the limiting and modulating factor.

The aim of this work is to enhance and optimize a prototype hollow fiber membrane bioreactor (HFMBR) providing efficient mass transfer for nutrient provision and catabolite removal, promoting prolonged viability and functionality of hepatocytes. In this bioreactor, two bundles of hollow fibers are employed in a crossed configuration: one bundle for supplying the oxygenated medium, and the other for removing the medium from the extra-capillary space. Optimization of the operational culture conditions to enforce an in vivo-like microenvironment is an intrinsic part of the process that requires a clear understanding of the in vitro cellular microenvironment. Oxygen transport in a convection-enhanced, crossed-configuration HFMBR hosting hepatocyte spheroids was investigated through mass transfer modelling using COMSOL Multiphysics[®], a specialized, commercial finite-element software.

The permeability of hollow fibers (hydraulic, albumin solution) was evaluated experimentally, showing significant, irreversible decrease in the permeance of the membranes due to protein absorption during culture period. Bioreactor's hydrodynamics was investigated through residence

time distribution analysis, by which a portion of the bioreactor was diagnosed as stagnant region. Finally, oxygen diffusion through the medium and the effect of different conditionings on the oxygen sensor's readings in multi-well plates were studied.

Mass transfer in static culture systems – both as a monolayer and as spheroids – was evaluated using a diffusion-reaction model numerically solved for oxygen (steady-state study) and urea (time-dependent study). In addition to the size and number of spheroids, sufficiency of oxygen supply to cells also depended on their distribution (the distance between them) and the amount of culture medium in each well.

A convection-diffusion-reaction model was developed to describe momentum and mass transfer in the bioreactor, in which the influential parameters were parametrized through implementation of applicable correlations. The model was numerically solved for two different types of geometries: (i) single-spheroid model using a periodic/symmetric unit cell within the bioreactor to locally represent the system decreasing the computational complexity of the model, (ii) miniaturized bioreactor model.

The single-spheroid model was used to carry out a systematic parametric study to evaluate the effect of different parameters – oxygen tension ($C_{o,sat}$), perfusion rate (Q_{BR}), hollow fiber spacing (δ_{HF}), spheroid diameter (D_{sph}), Michaelis-Menten kinetics for oxygen uptake (V_{max} , K_m) and porosities of the spheroid (ϵ_{cc}) and the membrane (ϵ_m) – on dissolved oxygen concentration (DOC) profile. Dimensionless numbers were defined for in-depth analysis of oxygen transfer and how each parameter can affect that. Among the operational conditions, $C_{o,sat}$ was found much more influential than Q_{BR} . Due to the mild advection added, the extra-spheroid resistances to diffusive mass transfer, i.e. the membrane (governed by ϵ_m) remains an important factor. However, ϵ_{cc} was found as a key intrinsic property strongly affecting intra-spheroid DOC profile.

Maintaining physiological DOC range in large spheroids ($D_{sph}=400\mu m$) with different porosities was investigated in the single-spheroid model. Regulation of DOC profile was more manageable in spheroids with higher ϵ_{cc} , which lead to feasibility of achieving physiological oxygen concentrations. Low-porosity spheroids demonstrated a sharper concentration gradient, challenging sufficient oxygen supply to cells.

Temporal shrinkage of spheroids due to rearrangement of cells changes the microstructure of the spheroid, the effect of which was numerically studied and proved to adversely affect the transport

properties and consequently the DOC profile inside the spheroid. In the end, values from an experimental study were incorporated into the model to analyze the cellular microenvironment during the experiment, and the predictive capacity of the model regarding the outcome.

Miniaturized bioreactor model was developed to reduce the computational cost while providing a more realistic model for the bioreactor. Another major advantage of this approach is capacitating investigation of the fluid dynamics inside the bioreactor. Notable DOC drop along the lumina of the supplying bundle was observed, consistent with the DOC gradient in the extra-capillary space along the supplying bundle. Having retentate flow in the hollow fibers significantly reduced these gradients and improved oxygen supply to the cells. Oxygen transfer was not noticeably affected by different flow patterns realized through using both bundles supplying or both removing the medium. However, minimization of the stagnant region had in fact a negative influence on oxygen supply. The miniaturized bioreactor model was also modified based on the experimental results for comparison with the single-spheroid model and the actual bioreactor, showing better compatibility with the real case.

Abstract

L'insufficienza epatica causata da malattie acute e croniche del fegato rappresenta una delle patologie che hanno un impatto significativo in tutto il mondo. Le malattie epatiche croniche insieme alla cirrosi sono considerate la 12^a causa di morte negli Stati Uniti e la quarta nel caso di adulti di età media. Ricercatori della Mayo Clinic identificano in un quadro più completo la mortalità correlata alle malattie epatiche come ottava causa di morte. Oggigiorno il trapianto di organo rimane l'unico trattamento medico di successo per pazienti affetti da insufficienza epatica. Tuttavia, il numero di organi disponibili per il trapianto sono piuttosto limitati e quindi non sufficienti a rispondere alla richiesta, per cui spesso i pazienti che sono in lista d'attesa non riescono a sopravvivere fino al trapianto d'organo. Un trattamento basato sull'utilizzo di un dispositivo adoperante epatociti può fornire tutte le funzioni epatiche necessarie a supportare temporaneamente pazienti con insufficienza epatica in attesa di trapianto oppure a favorire la rigenerazione epatica in caso di danno parziale. I progressi scientifici raggiunti nel corso degli anni hanno portato allo sviluppo di un dispositivo extracorporeo che funziona da fegato bioartificiale.

Colture epatiche cellulari sono impiegate per diverse applicazioni nello studio di patologie epatiche, nel testare la tossicità di farmaci e in dispositivi che fungono da fegato bioartificiale. Comunque lo sviluppo di questi sistemi è spesso compromesso dalle caratteristiche peculiari e requisiti intrinseci degli epatociti primari che rendono il mantenimento a lungo termine in vitro della loro vitalità e funzionalità una delle sfide più importanti. Diversi sistemi di coltura tridimensionali sono stati sviluppati come bioreattori per favorire il mantenimento in vitro di cellule funzionalmente attive. Rimangono, tuttavia, ancora alcuni aspetti critici da risolvere che sono legati alle proprietà di trasporto di questi sistemi, in particolar modo l'approvvigionamento di ossigeno che rappresenta il fattore limitante principale che modula la funzionalità cellulare.

Lo scopo di questo lavoro è stato quello di migliorare ed ottimizzare un prototipo di bioreattore a fibre cave al fine di garantire un efficiente trasporto di nutrienti alle cellule ed una rimozione di cataboliti, creando in questo modo un microambiente cellulare che supporta la vitalità e funzionalità delle cellule per un tempo prolungato.

In questo bioreattore due fasci di fibre cave sono assemblate in una configurazione incrociata: un fascio di fibre per fornire mezzo di coltura ossigenato alle cellule ed un altro fascio di fibre per rimuovere prodotti cellulari e di scarto dal compartimento cellulare. L'ottimizzazione delle

condizioni di coltura è molto importante al fine di stabilire un microambiente simile a quello in vivo e richiede una comprensione profonda del microambiente cellulare in vitro.

E' stato investigato, quindi, il trasporto di ossigeno diffusivo e convettivo in un bioreattore in configurazione incrociata adoperante aggregati tridimensionali in forma di sferoidi, costituiti da epatociti umani. A tale scopo sono stati effettuati studi di modellazione del trasporto di materia utilizzando un software commerciale di elementi finiti COMSOL Multiphysics®.

La permeabilità delle fibre cave all'acqua ed a soluzioni proteiche di albumina è stata valutata sperimentalmente. La permeanza idraulica delle membrane diminuisce in maniera irreversibile dopo gli esperimenti di permeabilità effettuati con una soluzione di albumina a causa dell'adsorbimento proteico che si verifica sulle membrane. La fluidodinamica del bioreattore è stata investigata attraverso l'analisi della distribuzione dei tempi di permanenza che ha messo in evidenza l'esistenza di una regione stagnante nel dispositivo. Infine è stata studiata la diffusione dell'ossigeno nel mezzo e l'effetto delle diverse condizioni di coltura nelle piastre contenenti alla base il sensore per l'ossigeno.

Il trasporto di materia nei sistemi di coltura statici sia bidimensionali come il monolayer che tridimensionale come gli sferoidi è stato valutato tramite un modello di diffusione-reazione che per l'ossigeno è stato studiato a regime stazionario e per l'urea nel tempo. L'adeguato approvvigionamento di ossigeno dipende non solo dalla dimensione e numero di sferoidi ma anche dalla loro distribuzione, ovvero dalla distanza tra loro, e dalla quantità di mezzo di coltura in ciascun pozzetto.

Un modello di reazione-diffusione-convezione è stato sviluppato allo scopo di descrivere la quantità di moto ed il trasporto di materia nel bioreattore, in cui i parametri che possono avere un'influenza sono stati analizzati attraverso uno studio parametrico. Il modello è stato risolto da un punto di numerico per due diversi tipi di geometria: (i) modello del singolo sferoide adoperando un'unità periodica/simmetrica scelta all'interno del bioreattore rappresentativa del sistema allo scopo di diminuire la complessità computazionale del modello; (ii) modello del bioreattore miniaturizzato.

Il modello del singolo sferoide è stato usato per svolgere uno studio sistematico di tipo parametrico al fine di valutare l'effetto di diversi parametri – pressione parziale di ossigeno ($C_{o,sat}$), portata (Q_{BR}), spazio tra le fibre (δ_{HF}), diametro dello sferoide (D_{sph}), parametri di Michaelis-Menten della

cinetica di consumo di ossigeno (V_{max} , K_m), la porosità dello sferoide (ϵ_{cc}) e della membrana (ϵ_m) – sul profilo di concentrazione di ossigeno presente nel mezzo di coltura (DOC). Per un'analisi approfondita del trasporto di ossigeno sono stati definiti i numeri adimensionali e l'influenza di ciascun parametro sulla concentrazione di ossigeno. Tra le condizioni operative, la concentrazione di ossigeno a saturazione ($C_{o,sat}$) ha un'influenza maggiore della portata (Q_{BR}).

A causa della convezione moderata, le resistenze al trasporto diffusivo nell'ambiente esterno allo sferoide, vale a dire la membrana (dipendente dalla sua porosità ϵ_m) costituisce un fattore importante. Comunque, la porosità del compartimento cellulare ϵ_{cc} è stata identificata come una proprietà intrinseca che influenza fortemente il profilo di concentrazione di ossigeno all'interno dello sferoide stesso.

E' stato investigato il range di concentrazione di ossigeno in sferoidi di grandi dimensioni ($D_{sph}=400\mu m$) a diverse porosità applicando il modello del singolo sferoide. E' stato possibile controllare la regolazione del profilo di concentrazione di ossigeno in sferoidi avente una più alta porosità nel compartimento cellulare ϵ_{cc} , raggiungendo in questo modo concentrazioni di ossigeno fisiologiche. E' stato osservato un gradiente di concentrazione minore in sferoidi aventi una porosità più bassa, ciò ha garantito un approvvigionamento sufficiente di ossigeno alle cellule.

La microstruttura dello sferoide cambia in seguito ad una contrazione che avviene temporalmente dovuta al riarrangiamento delle cellule, pertanto è stato studiato e dimostrato che la contrazione, diminuendo la porosità, influenza sfavorevolmente le proprietà di trasporto e conseguentemente il profilo di concentrazione di ossigeno all'interno dello sferoide stesso. Infine, i risultati ottenuti da uno studio sperimentale sono stati utilizzati nel modello per analizzare il microambiente cellulare durante l'esperimento e la sua capacità predittiva.

Il modello del bioreattore miniaturizzato è stato sviluppato allo scopo di ridurre il costo computazionale e di ottenere un modello più realistico del dispositivo. Un altro vantaggio importante di questo approccio è la capacità di investigare la fluidodinamica all'interno del bioreattore. E' apprezzabile la diminuzione della concentrazione di ossigeno lungo il lumen delle fibre di alimentazione in accordo con il gradiente di concentrazione di ossigeno che è presente nello spazio extracapillare lungo le fibre di alimentazione. Il flusso di retentato delle fibre cave ha ridotto significativamente i gradienti di concentrazione e migliorato il rifornimento di ossigeno alle cellule. Il trasporto di ossigeno non è stato influenzato da andamenti di flusso diversi sia

attraverso le fibre di alimentazione e sia attraverso le fibre di rimozione del mezzo. Comunque la minimizzazione della regione stagnante ha influenzato negativamente l'approvvigionamento di ossigeno. Il modello di bioreattore miniaturizzato è stato modificato sulla base dei risultati sperimentali per confrontare il modello singolo-sferoide con il bioreattore reale mostrando così una migliore compatibilità con il dispositivo reale.

Nomenclature

Symbols	
$c_{j,i}$	Concentration of species j in domain i
$C_{o,sat}$	Saturated oxygen concentration in equilibrium with the oxygen partial pressure in the gas phase
d_{hep}	Mean diameter of hepatocyte cells
$D_{j,i}$	Diffusion coefficient of species j in domain i
$D_{e,j,i}$	Effective diffusion coefficient of species j in porous medium i
d_{mp}	Mean pore diameter of the membrane
D_{BR}	Diameter of the central spherical space of the bioreactor
D_{Bundle}	Diameter of the bundle of hollow fibers
$D_{c,ECS}$	Diameter of the bioreactor connection accessing the extra-capillary space
$D_{c,HF}$	Diameter of the bioreactor connection encompassing the bundle of hollow fibers
D_{sph}	Diameter of the spheroid
D_{water}	Water self-diffusivity
Da	Damköhler number
$E(t)$	Residence time or exit age distribution
$F(t)$	Cumulative residence time distribution
J_{aq}	Permeation flux through the membrane
$K_{br,i}$	Permeability of the porous medium i
K_m	Concentration at which the oxygen uptake rate is half of the maximum rate (Michaelis-Menten kinetics)
l_{mnt}	Length of the element used for modelling
L_p	Membrane hydraulic permeance
M_{water}	Molecular weight of water
p_i	Pressure in domain i
Pe	Péclet number
Q_{BR}	Bioreactor's perfusion rate

$\mathcal{R}_{j,i}$	Reaction rate (production/consumption) of species j in domain i
$\mathcal{R}_{MM}(\mathbf{c}_{o,cc})$	Oxygen uptake rate (Michaelis-Menten kinetics), as a function of oxygen concentration in the cellular compartment
R_g	Universal gas constant
T	Temperature
$\bar{\mathbf{u}}_i$	Fluid velocity (vector field) in domain i
U_{avg}	Mean luminal velocity in a single hollow fiber
V_{max}	Maximum consumption rate (Michaelis-Menten kinetics)
V_{sph}	Volume of the spheroid

Greek letters

β_{Bm}	Biomimicry index
β_{Hpx}	Hypoxia index
β_{Design}	Design ratio used in miniaturization of the bioreactor housing
β_{scale}	Scale ratio used in miniaturization of the bioreactor housing
δ_{HF}	Inter-hollow-fiber spacing
δ_m	Membrane's skin layer thickness
ΔP^{TM}	Trans-membrane pressure
ε_i	Porosity of porous medium i
η	Effectiveness factor
μ_f	Fluid's dynamic viscosity
μ_{e_i}	Effective viscosity in the porous medium i
$\rho_{cell,model}$	Calculated cell density inside the spheroid
$\rho_{cell,ref}$	Reference cell density in a culture
ρ_f	Fluid's density
τ_i	Tortuosity of porous medium i
Φ^2	Thiele modulus

Abbreviations

DOC	Dissolved oxygen concentration
------------	--------------------------------

ECS	Extra-capillary space
HF	Hollow fiber
HFMBR	Hollow fiber membrane bioreactor
PEEK-WC	Modified polyetheretherketone
PES	Polyethersulfone
RTD	Residence time distribution

Subscripts

cc	Cellular compartment (spheroid)
ecs	Extra-capillary space
l	Lumen
m	Membrane
o	Oxygen
miniBR	Miniaturized bioreactor
prototypeBR	Actual bioreactor used in the experiments

Superscripts

sAvg	Surface-averaged value
vAvg	Volume-averaged value

Chapter 1

State of the art and aim of the work

1.1 Liver anatomy and functions

The liver is the second largest organ in the human body, responsible for 20-30% of total oxygen consumption in the body [1]. It has a rather complex architecture, providing a unique cellular microenvironment perfectly in sync with the cells' requirements. Understanding the anatomy of the liver, the type and arrangement of parenchymal and non-parenchymal cells, extracellular matrix molecules, and concentration gradients of oxygen, hormones, nutrients, etc. is a crucial step in in vitro development and optimization of an in vivo-like microenvironment.

At histological scale, the liver is composed of hexagonal, repeating functional units of liver cells known as hepatic lobules, arranged around a central vein with portal venules, arterioles and bile ductules located at the vertices (Figure 1. 1). Blood is supplied to the liver by the hepatic artery and portal vein, and circulated within the liver through sinusoids. Hepatocytes – the parenchymal or functional liver cells – constitute ~70% of the liver and are arranged as unicellular plates along the sinusoids and sandwiched between layers of extra-cellular matrix, experiencing homotypic cell interactions. Interaction of hepatocytes with non-parenchymal cells, namely stellate cells, cholangiocytes, sinusoidal endothelial cells, and Kupffer cells also modulates their functionality [2].

Among all cell types, hepatocytes have one of the highest oxygen consumption rates – over 10 times higher than most other cells – due to their wide variety of functions [1]. The liver performs over 500 functions including metabolic, synthetic, immunologic, homeostatic, detoxification and biotransformation processes. Some of the major liver functions are: metabolism of endogenous (e.g. bilirubin, ammonia) and exogenous (drugs and environmental compounds) substances and liposoluble xenobiotics, lactate elimination, protein synthesis (albumin, fibrinogen), carbohydrate and lipid metabolism, bile acids secretion, and immunomodulation. The liver is also involved in blood flow control and antibacterial immune defense [3-5]. Liver anatomy and functions are well described by Ebrahimkhani et al. [6].

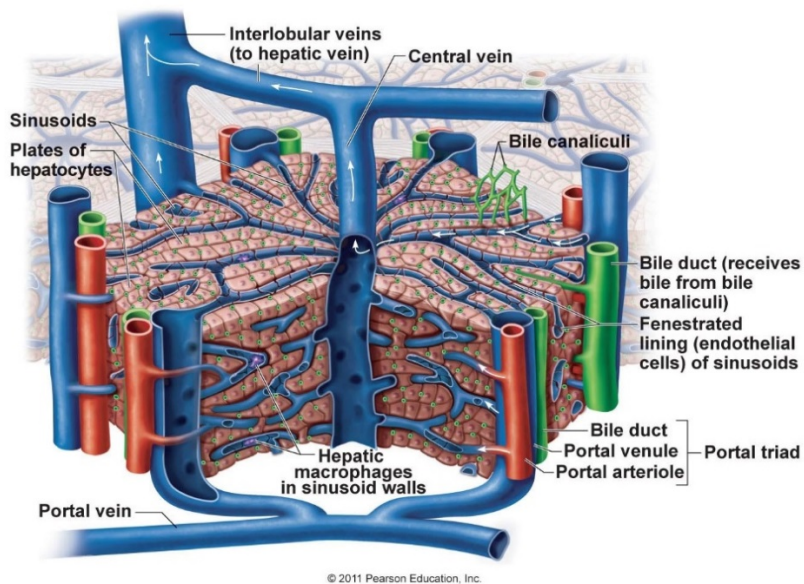
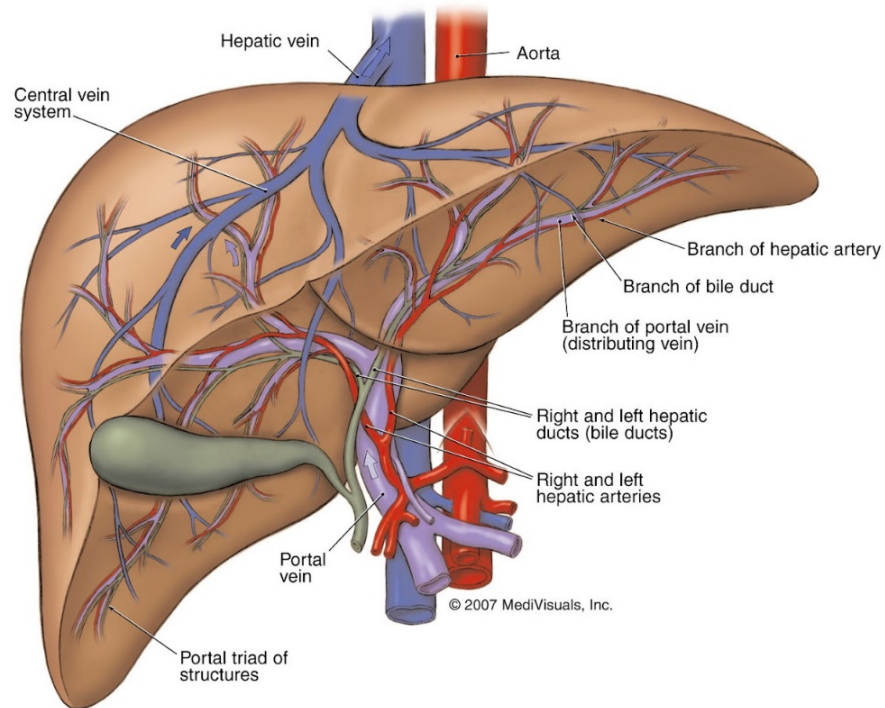


Figure 1.1 (Top) Macroanatomy of the liver. (Bottom) Microanatomy of the liver, showing a hepatic lobule. Image source:

https://cms.webstudy.com/WebstudyFileSystem/testovaci/GetFile/293875/Ch%202022/Ch22b/Ch22b_print.html

High oxygen uptake rate induces a concentration gradient along the sinusoids in the lobules in vivo (Figure 1. 1). The gradients of oxygen, hormones and extra-cellular matrix components (collagen types I-IV, laminin, fibronectin, heparin sulfate proteoglycans) is reportedly the modulator of metabolic zonation of the liver, characterized by distribution of hepatocyte functions along the sinusoid. For example, gluconeogenesis and ureagenesis occur at periportal zone (oxygen concentration 60 to 65 mm Hg, 84-91 $\mu\text{mol/L}$) whereas glycolysis and liponeogenesis are present at perivenous zone (oxygen concentration 30 to 35 mm Hg, 42-49 $\mu\text{mol/L}$) [7-10], as depicted in Figure 1. 2.

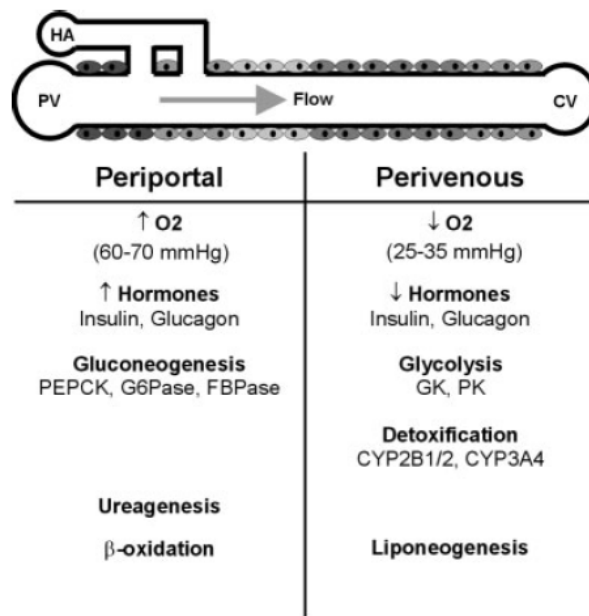


Figure 1. 2 Hepatic zonation and distribution of functions along the sinusoid [5].

1.2 Liver failure and treatment modalities

Liver failure, caused by acute or chronic end-stage liver disease (ESLD) imposes a significant disease burden worldwide. Chronic liver disease and cirrhosis is ranked as 12th cause of death in the US[11], while researchers in Mayo Clinic report liver-related mortality as 8th, using a more comprehensive definition which counts for other aspects of liver disease as well [12].

Currently, liver transplantation remains the conventional treatment for ESLD as the only medically proven method to promote patient's health. However, despite the advances in surgical procedures for partial liver transplant and grafts, transplantation alone is unlikely to meet the increasing

demand due to insufficient donor organs. Such shortcomings, along with high morbidity and mortality rate of ESLD, as well as the costs and complications of transplantation (especially undergoing life-time of immunosuppressive regimens) necessitate novel interventions and treatment strategies.

Artificial systems which process a patient's blood can only perform a limited portion of the functions that are known to be provided by the liver. One should also keep in mind that liver's physiology, anatomy and functions are very complex and not yet fully understood. Therefore, such artificial systems can only act as a transient support instead of providing a permanent solution.

To avoid the problem of inadequate donor organs and yet provide a more comprehensive range of liver functions, incorporation of hepatocytes in an extracorporeal device has been actively under investigation. This approach could potentially provide a temporary support for liver failure patients – e.g. bioartificial liver (BAL) – or more permanent modalities like cell transplantation and implantable tissue engineered liver constructs.

1.3 Artificial liver devices

Over the last three decades, liver support systems have been developed to replace orthotopic liver transplantation, or to complement patient care by promoting liver tissue regeneration, or to provide a bridge to liver transplantation. A successful liver support system should provide sufficient detoxification, synthesis, biotransformation and excretion functionality as performed by the liver. They are commonly divided into two main categories: artificial and bioartificial systems.

Accumulation of endogenous hepatotoxic substances is conjectured to induce loss of liver function, which in turn gives rise to accumulation of toxins, production of cytokines, and further damage of the liver [4]. Artificial liver (AL) devices are typically designed to emulate detoxification functions of the liver through filtration and adsorption mechanisms only, without employing living components. Molecular Adsorbent Recirculating System (MARS[®]; Gambro, Stockholm, Sweden) is a prominent, extensively evaluated AL, based on dialysis, adsorption and filtration processes. It removes both water-soluble and albumin-bound toxins using a high-flux polysulfone hemodialyzer hollow fiber module. Recirculating albumin-enriched dialysate is regenerated through consecutive dialysis, ion exchange and charcoal adsorption units.

Hepa Wash® procedure (Hepa Wash GmbH, Munich, Germany) uses the similar principle as MARS®, except that the albumin dialysate is regenerated through pH and temperature changes. In single-pass albumin dialysis on the other hand, the albumin solution is discarded instead of being regenerated.

In fractionated plasma separation and adsorption (Prometheus®, Fresenius Medical Care, Bad Homburg, Germany), endogenous albumin is purified by passing through an albumin-permeable polysulfone filter, neutral resin, ion exchanger and high-flux hemodialyser.

In selective plasma-exchange therapy (SEPET™, Arbios Systems, Allendale, New Jersey, USA), a size-selective membrane removes smaller molecules (MW<100kDa). The albumin fraction associated with toxins is then replaced by electrolytes, albumin and fresh-frozen plasma.

ALs are merely based on physico-chemical mechanisms and thus lack synthetic and biochemical functions of the liver. Additionally, hepatic detoxification inside the body is not limited to elimination of albumin-bound toxins. Moreover, the probable adverse effects of unselective adsorption and removal of molecules are yet to be evaluated. Moreover, regulatory functions of the liver are broader than acid-base status and electrolyte levels [13].

Considering the range and complexity of functions performed by the liver, artificial systems merely detoxifying the blood are insufficient to support liver failure patients and thus show limited clinical success [14]. To provide a larger complement of important liver functions, including synthetic and metabolic processes, biohybrid support devices incorporating living hepatic cells have been developed [15].

1.4 Bioartificial liver systems

In order to address the shortcomings of the ALs and to provide a more comprehensive range of hepatic functions, extensive research has been dedicated to explore and develop cell-based therapies. Such therapeutic interventions include implantation of tissue-engineered grafts, hepatocyte (primary or stem cell-derived) transplantation by infusion of isolated cells through the portal vein in the liver, and extracorporeal bioartificial liver (BAL) devices incorporating hepatic cell culture in a bioreactor. More recent, cutting-edge technologies include repopulation of decellularized liver, tissue/organ biofabrication through 3D printing techniques, and induced organogenesis [3, 13, 16].

Preserving prolonged and stable functionality of hepatocytes *in vitro* is indeed a major issue. Microenvironmental signals, namely soluble mediators, cell-extracellular matrix (ECM) interactions and cell-cell interactions are reported to regulate hepatic functionality. Consequently, a diverse range of *in vitro* hepatic culture models have been developed to fully understand the regulating mechanisms of hepatocytes, some of which include perfused whole-organs and wedge biopsies, precision-cut liver slices, isolated primary hepatocytes, immortalized liver cell lines and isolated organelles [17].

The BALs provide a promising means towards developing a temporary support for liver failure patients, a platform for drug toxicity testing and for *in vitro* study of hepatic cultures. Thanks to incorporation of functional hepatocytes, BALs can potentially perform a wide range of vital hepatic functions, namely detoxification, metabolism and synthesis.

In vitro cell cultures are expected to actualize a microenvironment in which *in vivo*-like phenotypic functions of cells are maintained. Viability and functionality of isolated hepatocytes *in vitro* highly depend on external cues, introduced in their microenvironment with respect to both time and space [18]. Consequently, hepatic cultures have been investigated in various configurations, in 2D and 3D, with or without perfusion and in different scales.

Numerous BAL designs have been suggested and explored, which fall into four main categories: (i) suspension/encapsulation-based reactors, (ii) perfused packed bed/ scaffold systems, (iii) flat plate systems, (iv) hollow fiber membrane bioreactors (HFMBR). First group of bioreactors consists of cellular masses – isolated or aggregated cells, with or without encapsulation – suspended in the oxygenated culture medium by the impeller in a stirred tank [19, 20] or by the force of the medium flow in a fluidized bed bioreactor [21, 22]. In the second group of bioreactors, a biocompatible, natural or polymeric compound is used to construct a porous scaffold [23, 24] or a packed bed of large particles [25, 26], used as the support material. The isolated cells are then seeded into the scaffold or bed, which is then perfused with oxygenated culture medium. Additionally, microfluidic systems and microfabricated reactor systems have been studied recently [6]. Current study focuses on the membrane-based bioreactors, especially HFMBRs.

1.5 Membrane-based bioreactors for *in vitro* cell cultures

1.5.1 Flat plate membrane bioreactors

The primitive petri dish-based static monolayer (2D) cultures demonstrate several disadvantages, namely: (i) continuous temporal change in cellular microenvironment due to consumption of nutrients and accumulation of cellular metabolic products, (ii) limited oxygen supply due to its low solubility and long diffusion path between oxygen source (i.e. gas-liquid interface) and the cells, (iii) poor cell-cell and cell-extracellular matrix interactions, (iv) smooth, 2D substrate incomparable to *in vivo* situation, (v) unidirectional mass exchange due to impermeable substrate.

Different strategies have been investigated in bioreactors to address the aforementioned shortcomings. The advantages of perfusion – i.e., medium flow over or through the cellular layer – in the bioreactor have been recognized for a long time. Gebhardt and Mecke, for example, reported improved viability and functionality (in terms of urea synthesis) of primary rat hepatocytes over 6 days under perfusion compared to static culture [27].

The added advection in the perfused systems significantly improves mass transfer. However, the shear stress exerted on the cells becomes a new limiting factor and it needs to be maintained within a safe range well-tolerated by the cultured cells.

Incorporation of membranes in flat plate bioreactors introduces many valuable features to the dynamic culture system. Membranes compartmentalize the cells, allowing nutrients and oxygen to pass through to the cellular compartment while protecting the cells from the fluid shear. They may support one or both surfaces of the cellular layer, allowing for mass transfer to/from cells in all directions. Additionally, oxygen-permeable membranes can also be employed so that oxygen gradient is applied separately from the fluid flow. Moreover, porous membranes can offer a more *in vivo*-like three dimensional substrate compared to smooth solid plastic, while facilitating cellular interaction studies [28].

Other enhancements have also been explored for monolayer-based systems, which can be applied to flat membrane bioreactors as well, including co-cultures [29] and sandwich cultures [30] for improving cell-cell and cell-ECM interactions, micro-grooved substrate [31] for protection against shear stress, and substrate micropatterning [32] for cell morphogenesis studies.

1.5.2 Hollow fiber membrane bioreactors

Hollow fiber membrane bioreactors (HFMBR) are commonly used in tissue engineering applications for cell-based therapies [33] including BAL devices [34] and large scale cell cultures [35]. HFMBRs consist of a bundle of semipermeable hollow fibers (HF) placed in an outer housing, similar to ultrafiltration or dialysis applications. Depending on the application and the cell types used, different configurations can serve different functions. The cells are more commonly attached to the outer wall of the HFs with the medium flowing in the lumen of the fibers exchanging nutrient and other components similar to blood capillary network. Alternatively, the cells may be seeded in the lumen of the HF, and the module can be operated under different flow patterns [36]. More complex configurations have also been suggested, such as multi-bore system [37], alginate immobilization [38] and three-compartment multi-coaxial system [39].

HFMBRs can potentially improve mass transfer rates in nutrient provision and waste removal with respect to limitations imposed by the diffusion length. Thanks to this compartmentalization, the cells are separated from direct fluid flow and thus are protected from shear and air-liquid interfacial stresses. Additionally, HFMBRs provide a large surface area to volume ratio, which allows to culture the same amount of cells in 0.58 L, compared to 1 m³ in case of using standard flask culture techniques [40]. This is especially important since hepatocytes are anchorage-dependent, and large number of cells – in the order of 10¹⁰ – is required for cell-based therapies.

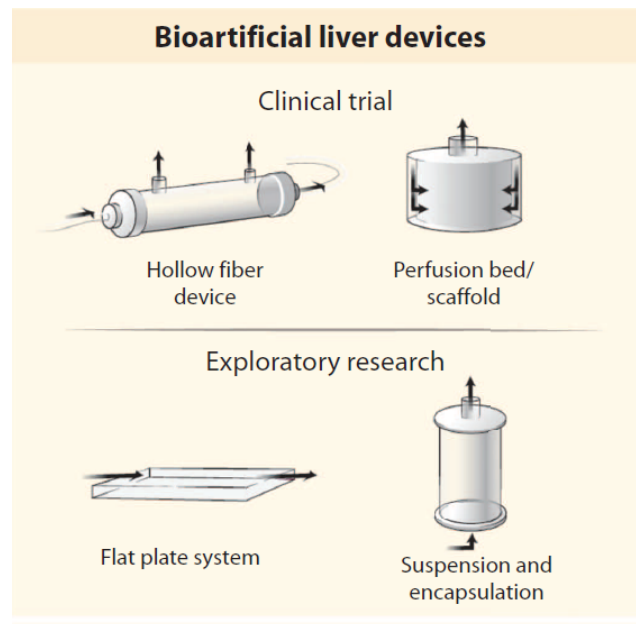


Figure 1. 3 Common types of BAL devices and areas in which they are mostly employed [12].

1.6 Bioartificial liver systems in clinical trial

So far, only few BAL systems have reached clinical trials, while various designs are explored in vitro as dynamic hepatic culture systems. The majority of BALs in clinical trial as well as many in vitro systems are based on hollow fiber bioreactors, further demonstrating their significance in these applications.

One of the most well-known BAL systems that has reached clinical trials is HepatAssist™ Device (Alliqua Inc., Langhorne, PA, USA), developed by Demetriou et al. Porcine hepatocyte cells are maintained in a modified dialysis cartridge based on HF membranes. Patient's plasma is separated, led through an activated charcoal adsorber followed by an oxygenator, and then through the bioreactor [41, 42]. A randomized controlled trial (RCT) of HepatAssist™ in 171 acute liver failure patients showed improved survival at 30 days: 71% for HepatAssist device vs. 62% for standard medical therapy. In fact, survival in fulminant or sub-fulminant liver failure patients was much higher in HepatAssist group. Unfortunately, this is the only RCT carried out on a bioartificial liver support system. The other BAL systems have been assessed in smaller studies [4].

One of the first clinical devices using HF membranes was Extracorporeal Liver Assist Device (ELAD®) (Vital Therapies Inc., San Diego, CA, USA) developed by Sussman et al. It employs C3A human hepatoblastoma cell lines while the flow circuit is conceptually similar to HepatAssist [43, 44].

Chamuleau's group took a different approach in designing the Academisch Medisch Centrum Bioartificial Liver (AMC-BAL). This device consists of non-woven polyester matrix and HFs encased in a housing. HFs distributed within the matrix are used for oxygen supply and CO₂ removal, while the cells are cultured on the matrix in a 3D architecture. Porcine hepatocytes were initially used, but the device has been modified to use immortalized fetal liver cell lines. The unique aspect in AMC-BAL is that after plasmapheresis, patient's plasma is in direct contact with the cells, enhancing cell-plasma mass transfer [45].

Patzer et al. [46] developed the Bioartificial Liver Support System (BLSS) based on a hemofilter containing freshly isolated porcine cells. This system differs from the others in two major aspects: whole blood is perfused rather than plasma, and the cells are in suspension, circulating in the extra-capillary space (ECS) [47].

The Modular Extracorporeal Liver Support (MELS) developed by Gerlach et al. is one of the most complex yet appealing HF bioreactor designs, consisting three separate bundles of HFs interwoven together: two sets of hydrophilic polyethersulfone HFs for plasma perfusion (culture medium flows between the two sets semi-interstitially) and one set of hydrophobic multilayer HFs for local oxygenation. Plasma is perfused into the bioreactor containing primary porcine or primary human liver cells capable of forming tissue-like structures between HFs [48-50].

The aforementioned ALs and BALs, their treatment units and clinical findings have been extensively reviewed by many authors [4, 13, 51].

1.7 Other Bioreactor designs for in vitro hepatic culture studies

Various bioreactor designs have been investigated for dynamic hepatic cultures *in vitro*, as BAL devices or drug testing platforms in pharmaceutical research. Here, few examples with different configurations are exemplified to provide a better understanding of bioreactor design and various design aspects they address.

An oxygen-permeable, flat-membrane bioreactor was developed by De Bartolo *et al.* [52]. Human hepatocytes were cultured between two fluorocarbon flat semipermeable membranes. The cells were directly oxygenated by the bottom membrane to which they adhered, while their upper surface was in contact with the culture medium which in turn was oxygenated through the upper membrane. Hepatic functionality was evaluated by synthesis of urea and albumin, and diclofenac biotransformation, which were maintained for 32 days.

Schmitmeier *et al.* compared conventional well plate cultures with a small-scale bioreactor with gas-permeable membrane at the bottom using a hepatic sandwich culture [53]. Better liver-specific functionality was found for the bioreactor model, without dedifferentiation of cells over 17 days. In another study, formation and cultivation of hepatocyte spheroids in a rotating-wall gas permeable membrane system (RWMS) was investigated and compared with a rotating-wall gas-impermeable polystyrene system (RWPS). Oxygen, glucose and lactate transfer in both systems were also evaluated by mathematical modelling. Improved viability of cells in RWMS was mathematically predicted and experimentally confirmed [54].

Cultivation of cells in the luminal compartment of HFs is also investigated by researchers, but it is less common compared to extra-capillary cultures. Hu *et al.* employed entrapment of a mixture

of spheroids and dispersed hepatocytes in collagen inoculated in the luminal compartment in their HFMBR [55]. High hepatic functionality was maintained in this system. De Bartolo *et al.* developed a multi-bore fiber membrane system. The fibers are made of modified polyethersulfone, each containing seven luminal compartments with suitable mechanical strength and high hydraulic permeance [37]. This system can potentially allow compartmentalization of different types of cells in each fiber to study cell-cell interaction through paracrine signalling. Shiraha *et al.* designed a HFMBR containing hepatocyte spheroids encapsulated into agarose micro-droplets [56]. Circulation of serum from a fulminant hepatic failure patient in the system improved imbalance of the amino acid profile.

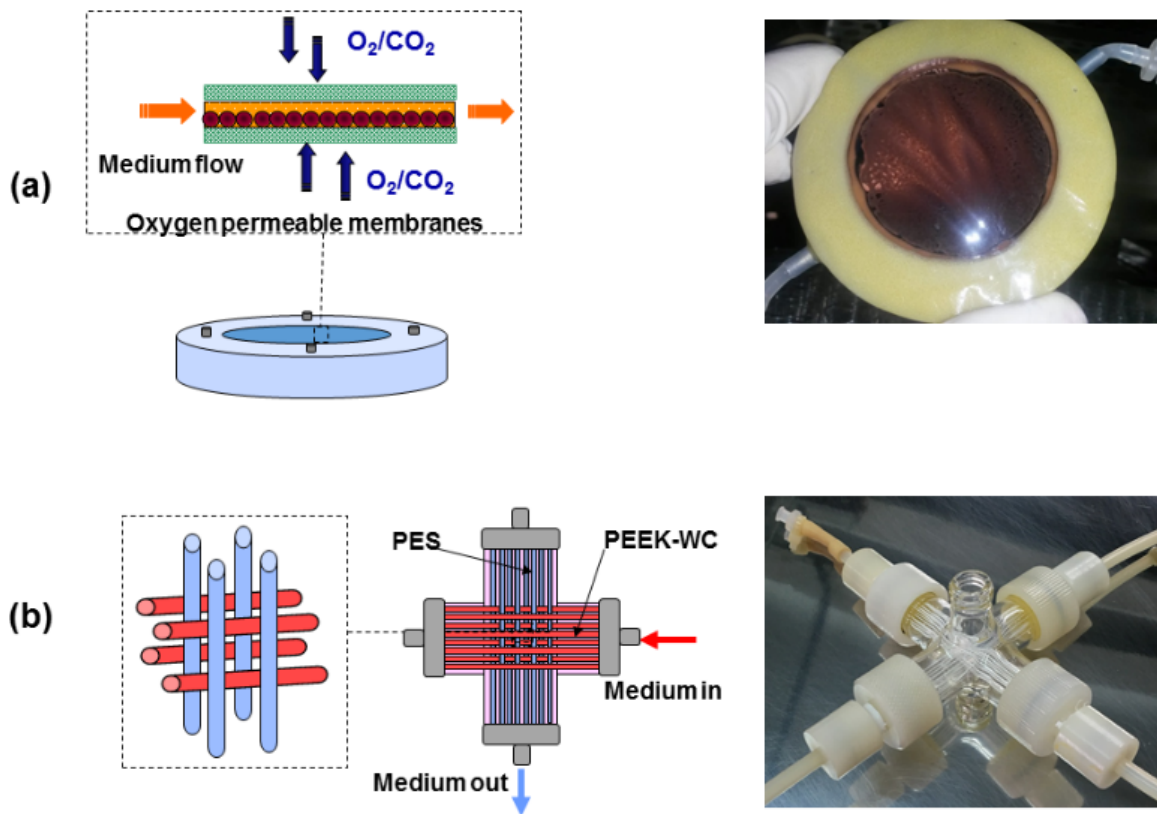


Figure 1. 4 Examples of bioreactors used for in vitro studies. (a) Oxygen-permeable flat-membrane bioreactor [De Bartolo *et al.* 2006], (b) Crossed hollow fiber membrane bioreactor [De Bartolo *et al.* 2009].

A HF module containing porcine hepatocytes entrapped in a basement membrane matrix, Engelbreth-Holm-Swarm (EHS) gel, was developed by Nagaki *et al.* [57]. Animal trials using pigs

with ischemic liver failure showed increased blood bicarbonate levels, improved hemodynamic stability, and decreased ammonia and lactate levels.

The OXY-HFB bioreactor developed by Jasmund *et al.* consists of HF's for oxygenation and for internal heat exchange [58]. Culture medium was circulated in the ECS where primary porcine liver cells were seeded on the HF walls. Hepatic functions of the cells, evaluated in terms of urea, albumin and lactate secretion, glucose consumption, oxygen level and diazepam metabolism, were maintained for three weeks.

Another HFMBR developed by De Bartolo *et al.* consists of two different types of HF's arranged in a crossed configuration, mimicking the blood capillary network. Each type of HF is employed to serve a distinguished function: modified polyetheretherketone (PEEK-WC) for supplying the cells with nutrients and metabolites, and polyethersulfone (PES) for removing the catabolites. Urea, albumin and diazepam transport was mathematically modelled and experimentally evaluated. Primary human hepatocytes maintained their functionality (urea and albumin synthesis, diazepam biotransformation) for 18 days [59].

Application of adhesive substrates in bioreactors to enhance cellular attachment and functionality has also been studied. Lu *et al.* reported enhanced albumin synthesis in rat hepatocytes cultured in a galactosylated polyvinylidene difluoride HF bioreactor [60]. In another study, sustained human hepatocyte functionality was found in a galactosylated polyethersulfone flat membrane bioreactor [61].

A closer look at the bioreactor configurations introduced above, reveals three main challenges in development of BAL devices: (i) membranes as artificial support, (ii) cell sources, (iii) mass transfer considerations.

1.8 Challenges in bioreactor design

In comparison with whole organ transplantation, the results from clinical trials of liver support systems are limited and not as satisfactory. Struecker *et al.* discussed that one key limitation in BAL systems is in fact the membranes [13]. Separation of blood from plasma, and plasma from cells by membranes adversely affects mass transfer rates. Plus, due to flow resistance, the perfusion in BAL systems is by far less than those *in vivo*.

Majority of BAL systems employ HF membrane bioreactors. However, despite their unique advantages mentioned before, there are also disadvantages potentially limiting their application, especially for in vitro studies. Some of such limiting factors include difficult setup, adsorption of proteins and certain species to the membrane and the consequent change in transport properties of the membrane over time, challenging in situ imaging of the cells/tissue, and difficult access to cellular compartment [6].

Despite the extensive efforts devoted to development of a BAL able to perform the same in vivo liver function, to date none of the proposed devices is ready for routinely clinical treatment of patients with hepatic failure. Key challenges that are still encountered include: lack of an ideal cell source, oxygen supply limitations, and realization of an in vivo-like environment for cells. Future research should focus on the production of highly differentiated hepatocytes from progenitor cells or stem cells in order to have a BAL system functionally active. Another important point is to undertake strategies that favour the creation of microvessels and bile canaliculi by using co-culture of hepatocytes with the other liver cell types. Additionally, more efforts should focus on the development of membrane devices able to provide necessary biological, chemical and mechanical demands or stimuli for the maintenance of liver specific functions.

1.8.1 Membranes

The choice of the membrane material is crucially important in bioartificial systems. The material in direct contact with the cells ideally should be non-toxic and biocompatible, promote favourable cellular interactions and functions, support secretion of ECM components required for tissue regeneration, and possess necessary mechanical and physical properties. Depending on the application, e.g. for certain implantable scaffolds, the material should be biodegradable and bioresorbable to avoid inflammation [62].

Development of membranes for tissue engineering applications has evolved significantly over the past three decades, from merely inert biomaterials to bioactive, biodegradable/bioresorbable materials. More recently, biomaterials are designed to stimulate specific cellular response. In other words, resorbable polymers can be modified at molecular level to provoke specific interactions with cell integrins – transmembrane glycoproteins that attach cells to extracellular matrix proteins – bridging cell-cell and cell-ECM interactions.

Advances in the development of polymeric membranes have made a remarkable contribution to the field of tissue engineering and regenerative medicine. Selectivity, stability and biocompatibility of polymeric membranes make them an appealing choice in biohybrid systems for cell culture. Semipermeable membranes provide a suitable support for attachment of anchorage-dependent cells like hepatocytes, allowing selective provision of metabolites and nutrients to cells and selective removal of catabolites and products [63, 64].

Adhesion, proliferation, viability and functionality of cells are strongly regulated by surface properties of the membranes, namely chemical composition, hydrophilicity/hydrophobicity, charge, free energy and roughness. Cell-biomaterial interactions can be promoted through surface modification, e.g. grafting functional groups and immobilization of functional molecules [65]. Synthesized components of ECM, including collagen, laminin, elastin and fibronectin are also used as matrices for tissue engineering applications.

The aforementioned properties are generally expected from biomaterials to be used for *in vitro* culture studies. However, each cell type has its own characteristics, which in turn may call for customized biomaterials that are not always commercially available. Development of cell-specific membranes is in fact a vital and challenging step in realization of bioartificial organs.

Unfortunately, most of the commercial membranes employed for hepatic cultures were initially developed for hemodialysis, thus requiring minimal interactions with proteins and cells in the blood. Consequently, development of membranes promoting adhesion and functionality of hepatocytes is a primary and crucial step in liver tissue engineering in general. Cytocompatibility of membranes can be improved by surface modification strategies such as grafting of functional groups (e.g. COOH, NH₂) or immobilization of biomolecules (e.g. RGD peptide or galactose interacting with cell receptors).

In addition to biocompatibility, a BAL device must also be able to provide and promote: (i) adhesion of cells and secretion of ECM, (ii) immunoprotection of cells, (iii) efficient mass transport between culture medium or blood/plasma compartment and the cellular compartment.

Transport properties of the membranes are determined by pore size and molecular weight cut-off (MWCO), i.e. molecular weight of species retained by 90% within the membrane. Membranes with MWCOs between 70-100 kDa act as an immunoselective barrier, preventing

immunoglobulins from passing while allowing the transport of serum albumin. Mass transfer considerations are discussed in detail in next sections.

Morphological properties (e.g. pore size, pore size distribution, roughness) and physico-chemical properties (e.g. surface charge, wettability, surface free energy) reportedly influence the adhesion and metabolic function of the hepatocytes [66].

1.8.2 Transport phenomena

In vivo, hepatocytes are organized in unicellular plates along the sinusoids, sandwiched between layers of extracellular matrix and equipped with different types of junctions and bile canaliculi, thus provided with a unique microstructure and efficient species transfer enabling their wide range of functions. Ideally, such delicate, well-defined microenvironment should be emulated in culture models *in vitro* and assessed in terms of species transport.

Membrane-based BAL systems generally consist of three compartment: culture medium (in *in vitro* studies) or blood/plasma (in clinical studies), membrane, and cellular compartment. Oxygen, nutrients, metabolites, growth factors, hormones, and other proteins, as well as endogenous catabolites, drugs and toxic compounds (to be metabolized) must be transferred to cells, while catabolites, synthesized proteins and other cellular products need to be efficiently removed from cellular microenvironment.

As one can immediately infer, complex exchange of numerous molecules with a wide range of sizes and physico-chemical properties occurs between the compartments. Each component has a different diffusion rate in the liquid solution. Additionally, the three compartments are all coupled together. Therefore, the transport through the porous media (membranes, cells) as well as the consumption or production rates in the cells affects the overall mass transfer. As previously described, the transport rate through the membrane depends on the MWCO, as well as the morphological and physico-chemical properties of both the membranes and the molecules of interest. Moreover, some molecules can adsorb on the membrane and not pass through. In the cellular compartment, the reaction rate for each component is also different. For example, oxygen (small molecule present in higher concentrations) uptake rate is relatively high, while protein (large molecules present in very low concentrations) secretion rates are very low. The most critical transport phenomena issues which are often recognized as the limiting factors are herewith discussed: oxygen concentration and shear stress.

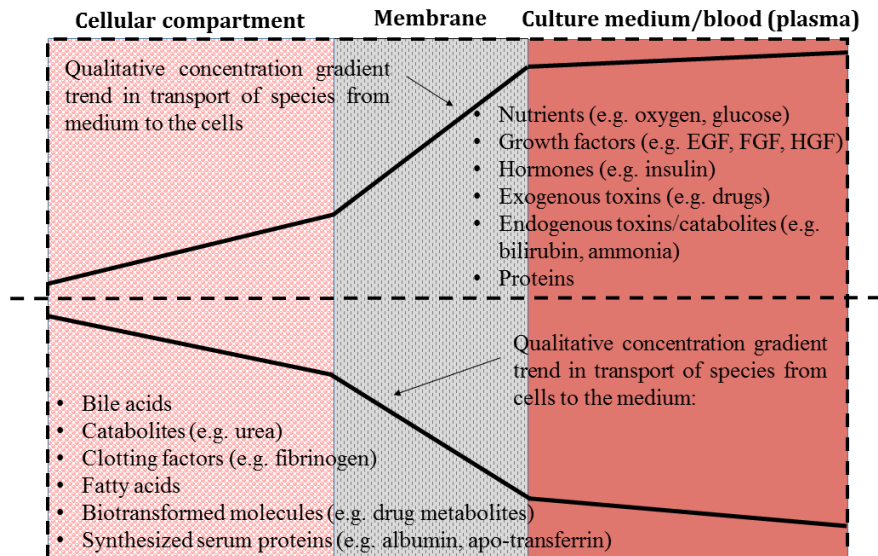


Figure 1. 5 Compartmentalization of the membrane-based BALs. Bidirectional mass transfer occurs between the compartments and through the membranes. The concentration gradient trends shown apply to diffusion-controlled mass transfer and are merely qualitative, since the rate and extent of the gradients differ for each component.

- **Oxygen supply**

Mimicking delicate in vivo oxygen conditions and their realization in vitro is indeed very challenging. In order to avoid hypoxia, sufficient oxygen needs to be supplied to hepatocytes in vitro, which is limited by oxygen's low solubility in culture medium, short diffusive penetration depth in hepatic tissues and – depending on the culture system – possibly long diffusion path between the cells and the oxygen source (e.g. gas-liquid interface, or the oxygenated medium's supply point). Hyperoxic oxygen concentrations on the other hand can cause oxidative effects on cells, potentially compromising hepatocytes' viability and functionality. Additionally, a concentration gradient in accord with the physiological range should also be induced within the hepatic mass inside the bioreactor.

Optimal oxygen concentration range reported in the literature for in vitro applications is also a controversial topic. Wang et al. briefly reviews some of the rather contradictory findings about oxygen concentration as well as the uptake rate reported in the literature, and concludes that the pericellular oxygen concentration of the hepatocytes should mimic the in vivo conditions rather than intracellular values [67].

Amongst the strategies employed to improve oxygen supply and to avoid hypoxia and hyperoxia, the following are most commonly explored: (i) oxygen permeable (HF) membranes to provide sufficient oxygen and to induce an oxygen concentration gradient locally, most notably employed in AMC-BAL and MELS devices introduced before, (ii) enhancing mass transfer by adding advection.

- **Convection-enhanced systems and shear stress effects**

In diffusion-controlled, membrane-based BAL systems, chemical potential is the driving force for mass transfer, dominated by the concentration gradient across the membrane. Mass transport mechanism can be enhanced by advection induced by a pressure gradient applied across the membrane.

Adding convection can significantly improve mass transfer, especially considering that various molecules are present covering a wide size range, from oxygen (32 g/mol) to albumin (67 kDa) and apo-transferrin (80 kDa). However, great care must be taken in inducing culture medium flow over/through the cellular compartment. Needless to say, the flow must not result in detachment and elimination of cells from the bioreactor. Moreover, favorable compounds like autocrine factors should not be washed away from the cellular microenvironment. Besides, formation of extracellular matrix needs to be promoted and not adversely affected by the medium flow [6].

One of the most influential yet controversial outcomes of direct perfusion (i.e., convection in the cellular compartment) is the unavoidable shear stress exerted on the cells. In fact, hepatocytes are very sensitive to shear forces and high flow rates could compromise their viability and functionality [68]. Studies have shown improved functionality as well as higher release of alanine transaminase – a marker of cell damage – in perfused flat plate systems compared to static culture [69, 70]. Acceptable range of shear stress values well-withstood by cells or even beneficial due to favourable stimulation of mechanosensors is still a subject of considerable debate. A review of previous studies actually demonstrates that the effects of shear stress may differ with respect to cell type, culture type (homotypic, heterotypic), culture period, and hepatic functions under evaluation [6, 67].

1.9 About current research study

1.9.1 Motivation

A practical BAL device must provide efficient mass transfer rates – both in nutrient provision and waste removal – and desired, optimal culture conditions. As previously discussed, primary hepatocytes in particular have a unique microenvironment in vivo and they notoriously lose their liver-specific functionality and/or viability in vitro, which strongly hinders the application of biohybrid devices. Additionally, proliferation of mature human hepatocytes in vitro – if present – is very limited. Such hindering characteristics in turn call for improvement and optimization of BAL devices – in terms of bioreactor performance and the type of cell culture – to ensure prolonged viability and functionality of hepatocytes.

Hepatocyte spheroids obtained by self-assembly of cells have the potential to be employed for the fabrication of in vitro liver tissue through fusion process [71]. It is well established that hepatocytes aggregated into 3-D structures such as spheroids display an improved metabolic activity, owing to the high degree of intercellular contacts crucial for communication of signals and integration of gene and metabolic patterns [54]. However, the absence of a vascular network in large spheroids may eventually cause oxygen transfer limitations leading to impairment of cell viability and functions. In order to provide hepatocyte spheroids with sufficient amount of oxygen and other nutrients, and to efficiently remove catabolites and cellular products, dynamic systems like membrane bioreactors have been investigated.

Spheroids are generally studied in static batch systems, rocked suspensions, rotating wall vessels or in encapsulated form in stirred or fluidized bed bioreactors [20, 72-74]. To the best of author's knowledge, HFMBRs hosting spheroids with the aim of forming hepatic microtissues have not been reported in the literature. Moreover, despite the common use of HFMBRs and extensive modelling studies performed, some vital properties and parameters seem to be overlooked or underestimated. Effective diffusion coefficient, permeability and even oxygen uptake rate in the spheroids are quite challenging to measure and are often estimated. However, their dependency on intra-spheroid porosity – the exact value of which is also often unknown and is therefore estimated – is either neglected or minimally reported in the models. Additionally, the porosity of spheroids and membranes are subject to temporal change, due to rearrangement of cells and adsorption of

proteins, respectively. The spheroids are observed to shrink in size and become more compact during the culture time [71], which in turn changes their microstructure and porosity in an uncontrolled manner leading to compromised transport properties. The effect of this phenomenon on oxygen transport into the spheroids is not properly addressed. On the other hand, occlusion of pores in the membrane due to proteins, cell debris and other culture components also changes their porosity and consequently their transport properties.

1.9.2 Objective

The aim of this project is to enhance and optimize a prototype crossed-configuration, convection-enhanced HFMBR previously introduced to ensure prolonged viability and functionality of hepatocytes. The bioreactor investigated in this study consists of two bundles of hollow fibers in a crossed configuration and assembled in an alternative manner, in which one bundle provides oxygenated culture medium to the bioreactor while the other bundle removes the medium from the bioreactor. In the experiments with hepatocyte spheroids, both bundles consisted of commercial polyethersulfone hollow fibers (MicroPES[®], 3M Deutschland GmbH, Germany), which limit the adhesion of hepatocytes that could result in disintegration of the spheroids. Figure 1. 6 shows the bioreactor configuration, and the flow diagram of the perfusion system during culture time is demonstrated in Figure 1. 7.

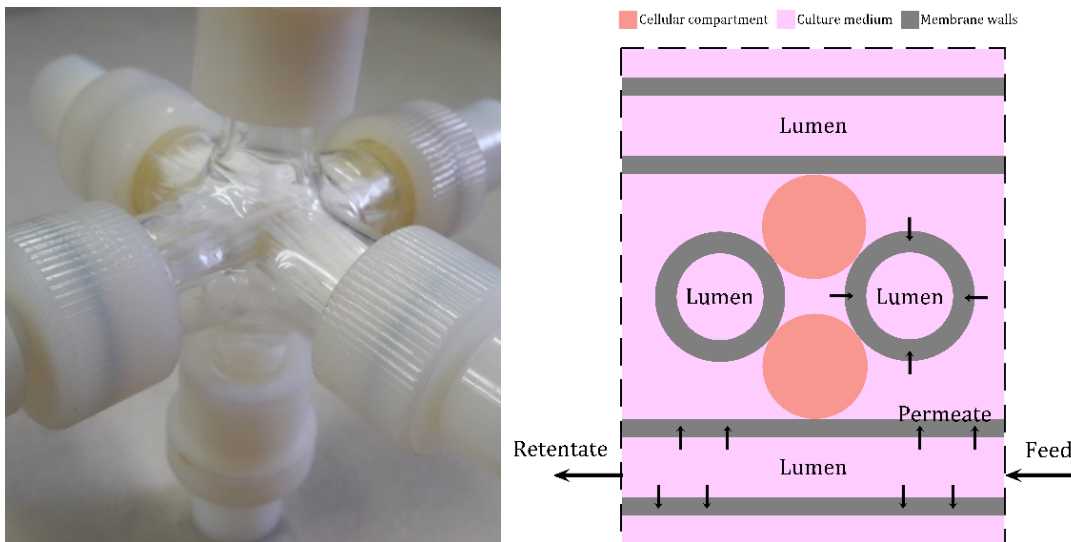


Figure 1. 6 Crossed-Configuration hollow fiber membrane bioreactor used in this study. (Left) assembled bioreactor for illustration purposes, (Right) schematic illustration of the bioreactor, showing the existing compartments.

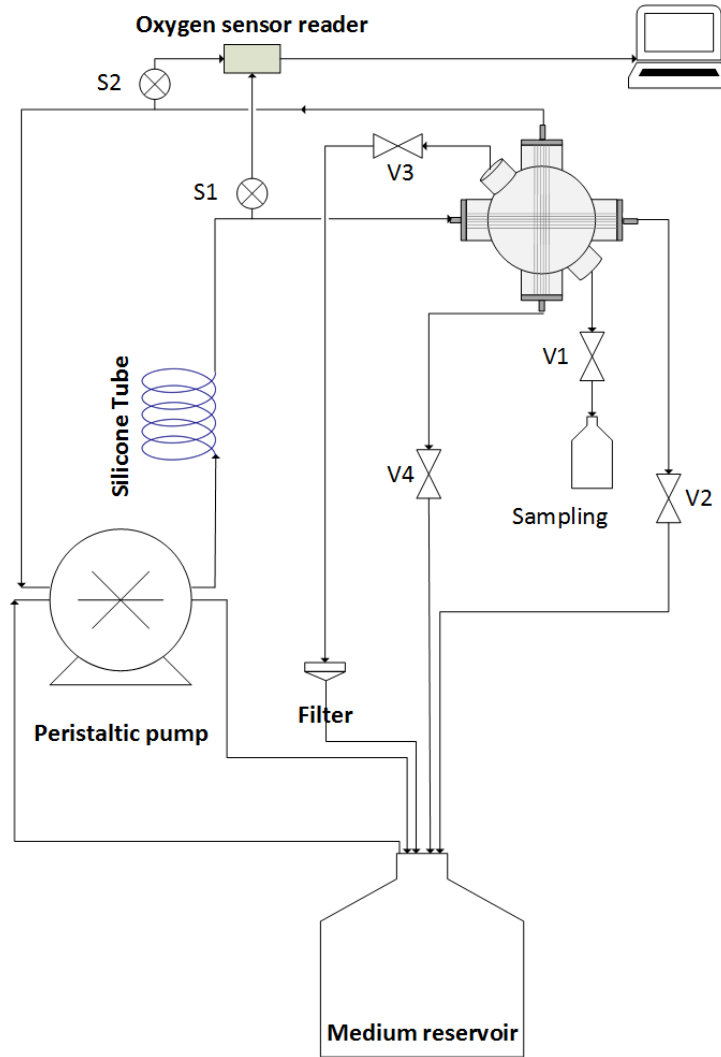
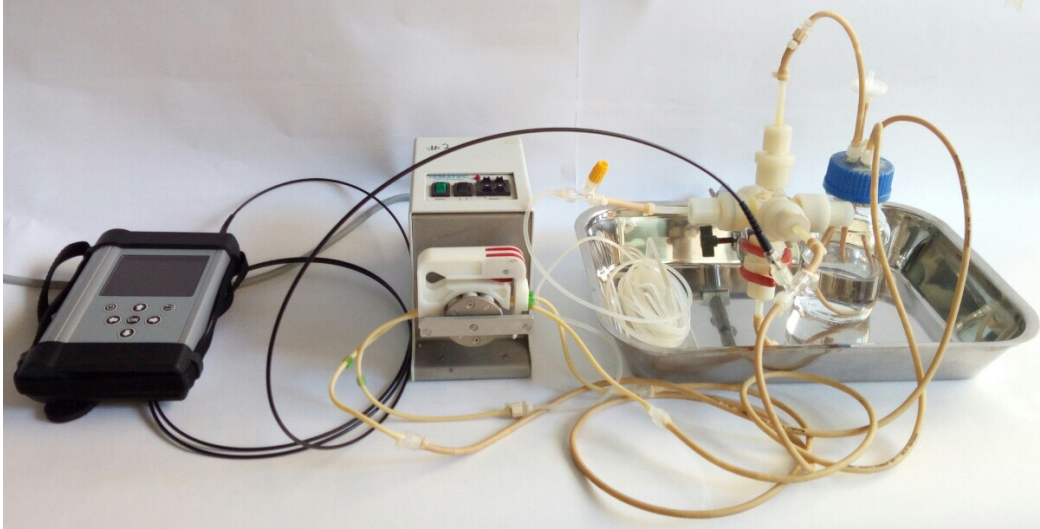


Figure 1. 7 (Top) Assembled circuit and connections used to run the bioreactor. (Bottom) Process flow diagram showing bioreactor's connections during culture.

The culture medium is pumped from the tank into the bioreactor by the peristaltic pump. In order to ensure optimum oxygenation, the medium is passed through the oxygen-permeable silicone tube, implemented before the inlet of the bioreactor. The medium in the extra-capillary space of the bioreactor is pumped out from one end of the other bundle at the same flow rate as the inlet, using the same pump, back into the tank. The other ends of each bundle (i.e., valves V2 and V4 in Figure 1. 7) are closed, and samples are taken from the bottom of the bioreactor (V1). The upper connection of the bioreactor is also connected to the tank to avoid losing medium and further problems due to possible medium over flow (controlled through V3). Oxygen sensors are placed at the inlet and outlet of the bioreactor, respectively.

The mass transfer involves a diverse range of molecules between three phases: free culture medium, the membrane, and the cellular compartment (e.g. spheroids, cellular layers or aggregates, etc) which in turn calls for recognition of the influential parameters and their effect on bioreactor's performance. Additionally, optimization of the operational culture conditions to enforce an *in vivo*-like microenvironment is an intrinsic part of the process which requires a clear understanding of the cellular microenvironment inside the bioreactor. Maintaining oxygen concentrations within physiological levels ($0.042 - 0.091 \text{ mol/m}^3$) is reported to promote and prolong hepatocytes' functionality and thus is of utmost importance [7, 8]. However, despite their significant impact, concentrations of oxygen, nutrients and cellular products are very challenging to measure at micro-scale. Furthermore, the experimental protocols for cell cultures are very costly and time-consuming, inhibiting optimization of the culture conditions through experiments only.

1.9.3 Approach

Computational modelling has increasingly been employed to analyse the transport phenomena inside the bioreactor, to evaluate the cellular microenvironment and to optimize the operational conditions. HFMBRs generally consist of a module packed with straight hollow fibers and the isolated cells are seeded in the extra-capillary space (ECS), either forming a cellular layer on the outer wall of the hollow fiber wall or completely filling the ECS. In majority of the modelling studies HFMBRs are mathematically described by Krogh cylinder approach, originally introduced to describe oxygen supply from blood vessels to tissues [75], as presented and reviewed by different authors [76, 77].

First, the limitations of the system, the potentially influential parameters and critical requirements were studied through simple experimental studies of the membrane permeability and bioreactor's fluid dynamics. Other observations were also made based on previous and ongoing culture experiments in our lab.

A comprehensive, parametrized convection-diffusion-reaction model was developed to describe mass transfer in membrane-based. The model, along with proper boundary conditions was then numerically solved using specialized, finite-element software COMSOL Multiphysics[®]. Two types of geometries were defined to represent the system: (i) single-spheroid study in a periodic element within the bioreactor, used for efficient model setup and for parametric study, (ii) miniaturized version of the whole bioreactor to study the effects of the fluid dynamics inside the bioreactor, which is generally not addressed in Korgh cylinder approach in the literature. The latter approach is compared with the experimental results, and used to better predict the bioreactor's performance in all aspects.

References

- [1] R. E. McClelland, J. M. MacDonald, and R. N. Cogger, "Modeling O₂ transport within engineered hepatic devices," *Biotechnol Bioeng*, vol. 82, pp. 12-27, Apr 5 2003.
- [2] G. H. Underhill, S. R. Khetani, A. A. Chen, and S. N. Bhatia, "Chapter Forty-Eight - Liver A2 - Lanza, Robert," in *Principles of Tissue Engineering (Third Edition)*, R. Langer and J. Vacanti, Eds., ed Burlington: Academic Press, 2007, pp. 707-731.
- [3] S. N. Bhatia, G. H. Underhill, K. S. Zaret, and I. J. Fox, "Cell and tissue engineering for liver disease," *Science Translational Medicine*, vol. 6, pp. 245sr2-245sr2, 2014-07-16 00:00:00 2014.
- [4] B. Carpentier, A. Gautier, and C. Legallais, "Artificial and bioartificial liver devices: present and future," *Gut*, vol. 58, pp. 1690-702, Dec 2009.
- [5] M. van Wenum, R. A. Chamuleau, T. M. van Gulik, A. Siliakus, J. Seppen, and R. Hoekstra, "Bioartificial livers in vitro and in vivo: tailoring biocomponents to the expanding variety of applications," *Expert Opin Biol Ther*, vol. 14, pp. 1745-60, Dec 2014.
- [6] M. R. Ebrahimkhani, J. A. S. Neiman, M. S. B. Raredon, D. J. Hughes, and L. G. Griffith, "Bioreactor technologies to support liver function in vitro," *Advanced Drug Delivery Reviews*, vol. 69-70, pp. 132-157, 4/20/ 2014.
- [7] J. W. Allen and S. N. Bhatia, "Formation of steady-state oxygen gradients in vitro: application to liver zonation," *Biotechnol Bioeng*, vol. 82, pp. 253-62, May 5 2003.
- [8] T. A. Broughan, R. Naukam, C. Tan, C. J. Van De Wiele, H. Refai, and T. K. Teague, "Effects of hepatic zonal oxygen levels on hepatocyte stress responses," *J Surg Res*, vol. 145, pp. 150-60, Mar 2008.
- [9] T. Kietzmann and K. Jungermann, "Modulation by oxygen of zonal gene expression in liver studied in primary rat hepatocyte cultures," *Cell biology and toxicology*, vol. 13, pp. 243-255, 1997.
- [10] K. Jungermann and T. Kietzmann, "Oxygen: modulator of metabolic zonation and disease of the liver," *Hepatology*, vol. 31, pp. 255-60, Feb 2000.
- [11] D. L. Hoyert and J. Xu, "Deaths: preliminary data for 2011," *Natl Vital Stat Rep*, vol. 61, pp. 1-51, 2012.
- [12] (2010, January 12). *Mortality rates from liver diseases underestimated, researchers say*. Available: www.sciencedaily.com/releases/2010/11/101101115616.htm
- [13] B. Struecker, N. Raschzok, and I. M. Sauer, "Liver support strategies: cutting-edge technologies," *Nature Reviews Gastroenterology & Hepatology*, vol. 11, pp. 166-176, 2014.
- [14] S. Rademacher, M. Oppert, and A. Jorres, "Artificial extracorporeal liver support therapy in patients with severe liver failure," *Expert Rev Gastroenterol Hepatol*, vol. 5, pp. 591-9, Oct 2011.
- [15] J. Phua and K. H. Lee, "Liver support devices," *Curr Opin Crit Care*, vol. 14, pp. 208-15, Apr 2008.
- [16] S. Y. Lee, H. J. Kim, and D. Choi, "Cell sources, liver support systems and liver tissue engineering: alternatives to liver transplantation," *International journal of stem cells*, vol. 8, p. 36, 2015.

- [17] G. H. Underhill, S. R. Khetani, A. A. Chen, and S. N. Bhatia, "Chapter Forty-Eight - Liver A2 - Vacanti, Robert Lanza Robert Langer Joseph," in *Principles of Tissue Engineering (Third Edition)*, ed Burlington: Academic Press, 2007, pp. 707-731.
- [18] S. R. Khetani, D. R. Berger, K. R. Ballinger, M. D. Davidson, C. Lin, and B. R. Ware, "Microengineered liver tissues for drug testing," *J Lab Autom*, vol. 20, pp. 216-50, Jun 2015.
- [19] J. P. Miranda, S. B. Leite, U. Muller-Vieira, A. Rodrigues, M. J. Carrondo, and P. M. Alves, "Towards an extended functional hepatocyte in vitro culture," *Tissue Eng Part C Methods*, vol. 15, pp. 157-67, Jun 2009.
- [20] R. M. Tostoes, S. B. Leite, M. Serra, J. Jensen, P. Bjorquist, M. J. Carrondo, *et al.*, "Human liver cell spheroids in extended perfusion bioreactor culture for repeated-dose drug testing," *Hepatology*, vol. 55, pp. 1227-36, Apr 2012.
- [21] S. Figaro, U. Pereira, H. Rada, N. Semenzato, D. Pouchoulin, and C. Legallais, "Development and validation of a bioartificial liver device with fluidized bed bioreactors hosting alginate-encapsulated hepatocyte spheroids," *Conf Proc IEEE Eng Med Biol Soc*, vol. 2015, pp. 1335-8, Aug 2015.
- [22] C. Legallais, E. Dore, and P. Paullier, "Design of a fluidized bed bioartificial liver," *Artif Organs*, vol. 24, pp. 519-25, Jul 2000.
- [23] J. Bao, Y. Shi, H. Sun, X. Yin, R. Yang, L. Li, *et al.*, "Construction of a portal implantable functional tissue-engineered liver using perfusion-decellularized matrix and hepatocytes in rats," *Cell Transplant*, vol. 20, pp. 753-66, 2011.
- [24] B. J. Lawrence, M. Devarapalli, and S. V. Madihally, "Flow dynamics in bioreactors containing tissue engineering scaffolds," *Biotechnol Bioeng*, vol. 102, pp. 935-47, Feb 15 2009.
- [25] A. P. Li, G. Barker, D. Beck, S. Colburn, R. Monsell, and C. Pellegrin, "Culturing of primary hepatocytes as entrapped aggregates in a packed bed bioreactor: a potential bioartificial liver," *In Vitro Cell Dev Biol*, vol. 29a, pp. 249-54, Mar 1993.
- [26] K. Yanagi, H. Miyoshi, and N. Ohshima, "Improvement of metabolic performance of hepatocytes cultured in vitro in a packed-bed reactor for use as a bioartificial liver," *Asaio j*, vol. 44, pp. M436-40, Sep-Oct 1998.
- [27] R. Gebhardt and D. Mecke, "Perfused monolayer cultures of rat hepatocytes as an improved in vitro system for studies on ureogenesis," *Experimental Cell Research*, vol. 124, pp. 349-359, 12// 1979.
- [28] S. D. Sheridan, S. Gil, M. Wilgo, and A. Pitt, "Microporous membrane growth substrates for embryonic stem cell culture and differentiation," *Methods Cell Biol*, vol. 86, pp. 29-57, 2008.
- [29] S. Salerno, C. Campana, S. Morelli, E. Drioli, and L. De Bartolo, "Human hepatocytes and endothelial cells in organotypic membrane systems," *Biomaterials*, vol. 32, pp. 8848-59, Dec 2011.
- [30] J. C. Dunn, R. G. Tompkins, and M. L. Yarmush, "Hepatocytes in collagen sandwich: evidence for transcriptional and translational regulation," *J Cell Biol*, vol. 116, pp. 1043-53, Feb 1992.

- [31] J. Park, F. Berthiaume, M. Toner, M. L. Yarmush, and A. W. Tilles, "Microfabricated grooved substrates as platforms for bioartificial liver reactors," *Biotechnol Bioeng*, vol. 90, pp. 632-44, Jun 5 2005.
- [32] M. Thery, "Micropatterning as a tool to decipher cell morphogenesis and functions," *J Cell Sci*, vol. 123, pp. 4201-13, Dec 15 2010.
- [33] N. Diban and D. Stamatialis, "Polymeric hollow fiber membranes for bioartificial organs and tissue engineering applications," *Journal of Chemical Technology & Biotechnology*, vol. 89, pp. 633-643, 2014.
- [34] Y. Yu, J. E. Fisher, J. B. Lillegard, B. Rodysill, B. Amiot, and S. L. Nyberg, "Cell Therapies for Liver Diseases," *Liver transplantation : official publication of the American Association for the Study of Liver Diseases and the International Liver Transplantation Society*, vol. 18, pp. 9-21, 2012.
- [35] R. A. Knazek, P. M. Gullino, P. O. Kohler, and R. L. Dedrick, "Cell culture on artificial capillaries: an approach to tissue growth in vitro," *Science*, vol. 178, pp. 65-6, Oct 6 1972.
- [36] N. Wung, S. M. Acott, D. Tosh, and M. J. Ellis, "Hollow fibre membrane bioreactors for tissue engineering applications," *Biotechnol Lett*, vol. 36, pp. 2357-66, Dec 2014.
- [37] L. De Bartolo, S. Morelli, M. Rende, C. Campana, S. Salerno, N. Quintiero, *et al.*, "Human hepatocyte morphology and functions in a multibore fiber bioreactor," *Macromol Biosci*, vol. 7, pp. 671-80, May 10 2007.
- [38] C. A. Hoesli, M. Luu, and J. M. Piret, "A novel alginate hollow fiber bioreactor process for cellular therapy applications," *Biotechnol Prog*, vol. 25, pp. 1740-51, Nov-Dec 2009.
- [39] A. Hilal-Alnaqbi, A. H. Mourad, B. F. Yousef, and J. D. Gaylor, "Experimental evaluation and theoretical modeling of oxygen transfer rate for the newly developed hollow fiber bioreactor with three compartments," *Biomed Mater Eng*, vol. 23, pp. 387-403, 2013.
- [40] R. J. Shipley, A. J. Davidson, K. Chan, J. B. Chaudhuri, S. L. Waters, and M. J. Ellis, "A strategy to determine operating parameters in tissue engineering hollow fiber bioreactors," *Biotechnol Bioeng*, vol. 108, pp. 1450-61, Jun 2011.
- [41] A. A. Demetriou, R. S. Brown, Jr., R. W. Busuttil, J. Fair, B. M. McGuire, P. Rosenthal, *et al.*, "Prospective, randomized, multicenter, controlled trial of a bioartificial liver in treating acute liver failure," *Ann Surg*, vol. 239, pp. 660-7; discussion 667-70, May 2004.
- [42] A. A. Demetriou, J. Whiting, S. M. Levenson, N. R. Chowdhury, R. Schechner, S. Michalski, *et al.*, "New method of hepatocyte transplantation and extracorporeal liver support," *Ann Surg*, vol. 204, pp. 259-71, Sep 1986.
- [43] A. J. Ellis, R. D. Hughes, J. A. Wendon, J. Dunne, P. G. Langley, J. H. Kelly, *et al.*, "Pilot-controlled trial of the extracorporeal liver assist device in acute liver failure," *Hepatology*, vol. 24, pp. 1446-51, Dec 1996.
- [44] N. L. Sussman, G. T. Gislason, C. A. Conlin, and J. H. Kelly, "The Hepatix extracorporeal liver assist device: initial clinical experience," *Artif Organs*, vol. 18, pp. 390-6, May 1994.
- [45] L. M. Flendrig, J. W. la Soe, G. G. Jorning, A. Steenbeek, O. T. Karlsen, W. M. Bovee, *et al.*, "In vitro evaluation of a novel bioreactor based on an integral oxygenator and a spirally wound nonwoven polyester matrix for hepatocyte culture as small aggregates," *J Hepatol*, vol. 26, pp. 1379-92, Jun 1997.

- [46] J. F. Patzer, 2nd, G. V. Mazariegos, R. Lopez, E. Molmenti, D. Gerber, F. Riddervold, *et al.*, "Novel bioartificial liver support system: preclinical evaluation," *Ann N Y Acad Sci*, vol. 875, pp. 340-52, Jun 18 1999.
- [47] G. V. Mazariegos, J. F. Patzer, 2nd, R. C. Lopez, M. Giraldo, M. E. Devera, T. A. Grogan, *et al.*, "First clinical use of a novel bioartificial liver support system (BLSS)," *Am J Transplant*, vol. 2, pp. 260-6, Mar 2002.
- [48] I. M. Sauer, D. Kardassis, K. Zeillinger, A. Pascher, A. Gruenwald, G. Pless, *et al.*, "Clinical extracorporeal hybrid liver support--phase I study with primary porcine liver cells," *Xenotransplantation*, vol. 10, pp. 460-9, Sep 2003.
- [49] I. M. Sauer, K. Zeilinger, G. Pless, D. Kardassis, T. Theruvath, A. Pascher, *et al.*, "Extracorporeal liver support based on primary human liver cells and albumin dialysis--treatment of a patient with primary graft non-function," *J Hepatol*, vol. 39, pp. 649-53, Oct 2003.
- [50] I. M. Sauer, N. Obermeyer, D. Kardassis, T. Theruvath, and J. C. Gerlach, "Development of a hybrid liver support system," *Ann N Y Acad Sci*, vol. 944, pp. 308-19, Nov 2001.
- [51] A. S. Podoll, A. DeGolovine, and K. W. Finkel, "Liver support systems—a review," *Asaio Journal*, vol. 58, pp. 443-449, 2012.
- [52] L. De Bartolo, S. Salerno, S. Morelli, L. Giorno, M. Rende, B. Memoli, *et al.*, "Long-term maintenance of human hepatocytes in oxygen-permeable membrane bioreactor," *Biomaterials*, vol. 27, pp. 4794-803, Sep 2006.
- [53] S. Schmitmeier, A. Langsch, I. Jasmund, and A. Bader, "Development and characterization of a small-scale bioreactor based on a bioartificial hepatic culture model for predictive pharmacological in vitro screenings," *Biotechnol Bioeng*, vol. 95, pp. 1198-206, Dec 20 2006.
- [54] E. Curcio, S. Salerno, G. Barbieri, L. De Bartolo, E. Drioli, and A. Bader, "Mass transfer and metabolic reactions in hepatocyte spheroids cultured in rotating wall gas-permeable membrane system," *Biomaterials*, vol. 28, pp. 5487-97, Dec 2007.
- [55] W. S. Hu, J. R. Friend, F. J. Wu, T. Sielaff, M. V. Peshwa, A. Lazar, *et al.*, "Development of a bioartificial liver employing xenogeneic hepatocytes," *Cytotechnology*, vol. 23, pp. 29-38, Jan 1997.
- [56] H. Shiraha, N. Koide, H. Hada, K. Ujike, M. Nakamura, T. Shinji, *et al.*, "Improvement of serum amino acid profile in hepatic failure with the bioartificial liver using multicellular hepatocyte spheroids," *Biotechnology and bioengineering*, vol. 50, pp. 416-421, 1996.
- [57] M. Nagaki, K. Miki, Y. I. Kim, H. Ishiyama, I. Hirahara, H. Takahashi, *et al.*, "Development and characterization of a hybrid bioartificial liver using primary hepatocytes entrapped in a basement membrane matrix," *Dig Dis Sci*, vol. 46, pp. 1046-56, May 2001.
- [58] I. Jasmund, A. Langsch, R. Simmoteit, and A. Bader, "Cultivation of primary porcine hepatocytes in an OXY-HFB for use as a bioartificial liver device," *Biotechnol Prog*, vol. 18, pp. 839-46, Jul-Aug 2002.
- [59] L. De Bartolo, S. Salerno, E. Curcio, A. Piscioneri, M. Rende, S. Morelli, *et al.*, "Human hepatocyte functions in a crossed hollow fiber membrane bioreactor," *Biomaterials*, vol. 30, pp. 2531-43, May 2009.

- [60] H. F. Lu, W. S. Lim, P. C. Zhang, S. M. Chia, H. Yu, H. Q. Mao, *et al.*, "Galactosylated poly(vinylidene difluoride) hollow fiber bioreactor for hepatocyte culture," *Tissue Eng*, vol. 11, pp. 1667-77, Nov-Dec 2005.
- [61] B. Memoli, L. De Bartolo, P. Favia, S. Morelli, L. C. Lopez, A. Procino, *et al.*, "Fetuin-A gene expression, synthesis and release in primary human hepatocytes cultured in a galactosylated membrane bioreactor," *Biomaterials*, vol. 28, pp. 4836-44, Nov 2007.
- [62] B. S. Kim, C. E. Baez, and A. Atala, "Biomaterials for tissue engineering," *World J Urol*, vol. 18, pp. 2-9, Feb 2000.
- [63] L. De Bartolo, G. Jarosch-Von Schweder, A. Haverich, and A. Bader, "A novel full-scale flat membrane bioreactor utilizing porcine hepatocytes: cell viability and tissue-specific functions," *Biotechnol Prog*, vol. 16, pp. 102-8, Jan-Feb 2000.
- [64] R. E. Unger, Q. Huang, K. Peters, D. Protzer, D. Paul, and C. J. Kirkpatrick, "Growth of human cells on polyethersulfone (PES) hollow fiber membranes," *Biomaterials*, vol. 26, pp. 1877-84, May 2005.
- [65] S. Morelli, S. Salerno, A. Piscioneri, M. Rende, C. Campana, and L. De Bartolo, "3.10 - Membrane Approaches for Liver and Neuronal Tissue Engineering A2 - Drioli, Enrico," in *Comprehensive Membrane Science and Engineering*, L. Giorno, Ed., ed Oxford: Elsevier, 2010, pp. 229-252.
- [66] L. De Bartolo, S. Morelli, A. Bader, and E. Drioli, "Evaluation of cell behaviour related to physico-chemical properties of polymeric membranes to be used in bioartificial organs," *Biomaterials*, vol. 23, pp. 2485-97, Jun 2002.
- [67] Y. Wang, T. Susando, X. Lei, C. Anene-Nzelu, H. Zhou, L. H. Liang, *et al.*, "Current development of bioreactors for extracorporeal bioartificial liver (Review)," *Biointerphases*, vol. 5, pp. Fa116-31, Sep 2010.
- [68] D. Mazzei, M. A. Guzzardi, S. Giusti, and A. Ahluwalia, "A low shear stress modular bioreactor for connected cell culture under high flow rates," *Biotechnol Bioeng*, vol. 106, pp. 127-37, May 1 2010.
- [69] P. Kan, H. Miyoshi, K. Yanagi, and N. Ohshima, "Effects of shear stress on metabolic function of the co-culture system of hepatocyte/nonparenchymal cells for a bioartificial liver," *Asaio j*, vol. 44, pp. M441-4, Sep-Oct 1998.
- [70] P. Kan, H. Miyoshi, and N. Ohshima, "Perfusion of medium with supplemented growth factors changes metabolic activities and cell morphology of hepatocyte-nonparenchymal cell coculture," *Tissue Eng*, vol. 10, pp. 1297-307, Sep-Oct 2004.
- [71] A. Messina, S. Morelli, G. Forgacs, G. Barbieri, E. Drioli, and L. De Bartolo, "Self-assembly of tissue spheroids on polymeric membranes," *J Tissue Eng Regen Med*, Nov 09 2015.
- [72] S. Figaro, U. Pereira, H. Rada, N. Semenzato, D. Pouchoulin, and C. Legallais, "Development and validation of a bioartificial liver device with fluidized bed bioreactors hosting alginate-encapsulated hepatocyte spheroids," in *2015 37th Annual International Conference of the IEEE Engineering in Medicine and Biology Society (EMBC)*, 2015, pp. 1335-1338.
- [73] J. M. Glorioso, S. A. Mao, B. Rodysill, T. Mounajjed, W. K. Kremers, F. Elgilani, *et al.*, "Pivotal preclinical trial of the spheroid reservoir bioartificial liver," *Journal of hepatology*, vol. 63, pp. 388-398, 2015.

- [74] B. Yoffe, G. J. Darlington, H. E. Soriano, B. Krishnan, D. Risin, N. R. Pellis, *et al.*, "Cultures of human liver cells in simulated microgravity environment," *Adv Space Res*, vol. 24, pp. 829-36, 1999.
- [75] A. Krogh, "The number and distribution of capillaries in muscles with calculations of the oxygen pressure head necessary for supplying the tissue," *The Journal of physiology*, vol. 52, pp. 409-415, 1919.
- [76] R. J. Shipley and S. L. Waters, "Fluid and mass transport modelling to drive the design of cell-packed hollow fibre bioreactors for tissue engineering applications," *Math Med Biol*, vol. 29, pp. 329-59, Dec 2012.
- [77] J. D. Brotherton and P. C. Chau, "Modeling of Axial-Flow Hollow Fiber Cell Culture Bioreactors," *Biotechnology progress*, vol. 12, pp. 575-590, 1996.

Chapter 2

Fluid dynamics and permeability in the membrane bioreactor

2.1 Introduction

As discussed in Chapter 1, hollow fiber membrane bioreactors consist of three phases: the liquid phase (culture medium containing numerous types of molecules) in the lumina and possibly in the extra-capillary space, the membranes and the cellular mass, with the latter two being generally considered as porous media. Thus, a complex multi-species transport with different mechanisms occurs. Transport of larger molecules – proteins in particular – could change the pores and the microstructure of the membranes, affecting the transport rate through them. Moreover, having a convection-enhanced system calls for evaluation of the fluid dynamics and mixing properties inside the bioreactor.

Multi-well plates on the other hand are the simplest cell culture platform for *in vitro* studies. Generally, the bottom surfaces of the sterilized wells are coated with a biocompatible material – usually components from the extra-cellular matrix – promoting cell viability, functionality and growth. Known volume of culture medium is added to the wells and finally the cells are seeded. The plates are placed in the incubator to have sterile and controlled conditions in terms of gas composition (oxygen, nitrogen and carbon dioxide) and humidity. The upper surface of the culture medium, the gas-liquid interface is available for gas exchange (oxygen for the cellular uptake and carbon dioxide for buffering), making each well a semi-batch system. Since oxygen is the limiting and most vital factor in these systems, its diffusion in the culture medium used, and the effect of the “conditioning” on oxygen transport in multi-well plates equipped with oxygen sensor spots (used for online monitoring of the oxygen concentration) should be evaluated.

In this chapter, the results on the permeability of modified polyetheretherketone (PEEK-WC) hollow fibers using water and albumin solution is presented. Bioreactor’s hydrodynamics is investigated through residence time distribution analysis, used to characterize fluid distribution and mixing inside the bioreactor [1-3] For this study, PEEK-WC HF bundle was used to supply the medium and polysulfone (PES) HF bundle was used to remove the medium. In the end, the

effect of different conditionings on the oxygen sensor's readings was studied, and its diffusion coefficient in the medium was assessed.

2.2 Materials and methods

2.2.1 Hollow fiber permeability tests

The complex geometry and assembly process of the crossed-configuration hollow fiber membrane bioreactor made it unsuitable to carry out and analyze permeability measurements for characterization of the hollow fibers. Alternatively, simple straight modules were assembled in-house for this purpose.

A metal wire mesh (wire thickness $50\mu\text{m}$, mesh size $700\times 700\mu\text{m}$) was carefully fixed at each end of the glass housing, through which twenty five PEEK-WC hollow fibers were passed in a 5×5 arrangement with a nominal spacing of $250\mu\text{m}$ in between. The module was potted at each end using polyurethane potting compound (BASF Polyurethanes GmbH, Germany). Upon finishing the assembly, the module was left for 24 hours at room temperature for curing the potting compound. Then, the excess potting was cut by a sharp blade, assuring that the hollow fibers are open and not occluded. A completed module is shown in Figure 2. 1.



Figure 2. 1 Hollow fiber module assembled for permeability measurements (25 PEEK-WC hollow fibers, 5×5 arrangement).

The permeability studies were carried out in 4 parts, the flow diagram for which is shown in Figure 2. 2. First, hydraulic permeability of the hollow fibers was measured. Newly assembled module

was first flushed by distilled water for 4 hours at a flow rate of 3.4 ml/min using a peristaltic pump (ISMATEC, Switzerland), during which the V2 valve was closed and the permeate was disposed of. Then, V2 valve was very slightly opened; pressure values from P1 and P2 gauges were recorded once stabilized, the permeate volume collected in 1 minute was measured (repeated 3 times). The whole procedure was repeated for different pressures.

This part of the experiment was carried out to measure membrane hydraulic permeance, L_p , the key factor in convective solute transport through the membrane. L_p is evaluated from permeation flux through the membrane (J_{aq}) at different trans-membrane pressure (ΔP^{TM}) [4]:

$$L_p = \left(\frac{J_{aq}}{\Delta P^{TM}} \right)_{\Delta C=0} \quad (2.1)$$

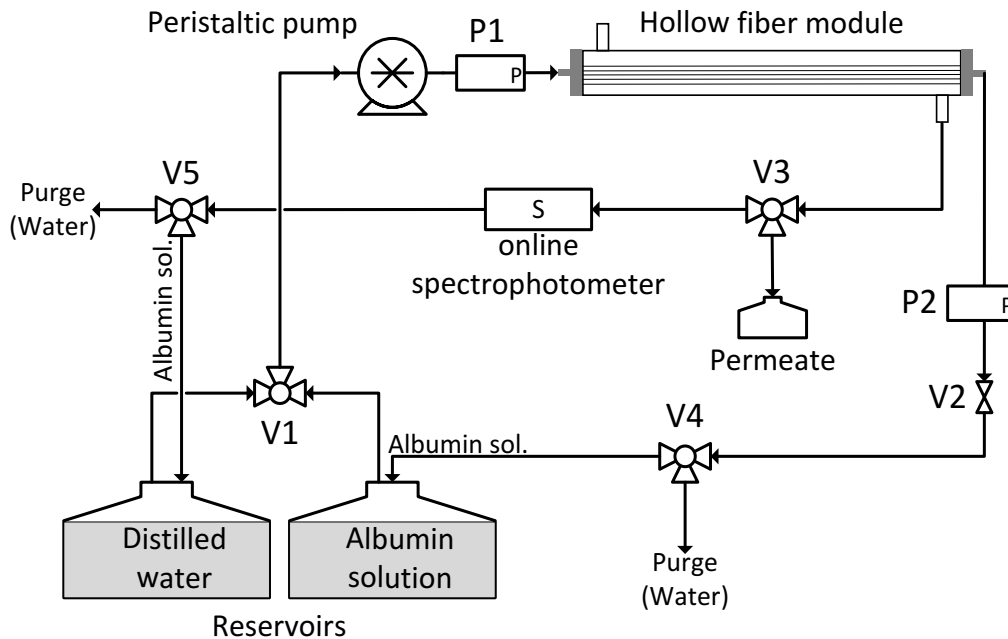


Figure 2. 2 Process flow diagram for testing hydraulic permeability and albumin permeability.

In the next step, albumin permeance through the PEEK-WC hollow fibers was evaluated. V2 valve was closed and V3 valve was switched to the online spectrophotometer. At $t=0$, V1 was switched to albumin solution ($C_{max}=0.25$ mg/ml human serum albumin dissolved in 10% PBS, 200ml total) which was pumped into the module at a flow rate of 2 ml/min. The outlet (permeate) tracer

concentration C_{out} was recorded over time in terms of absorbance, until reaching the plateau. Absorbance of the albumin solution was directly measured beforehand, without passing through the hollow fibers. Albumin solution from spectrophotometer's outlet was recycled into its reservoir.

In the third part of the experiment, the permeability of the hollow fibers using albumin solution was measured. V3 valve was switched back for permeate collection, and the same procedure as measuring hydraulic permeability was repeated, except for using albumin solution instead of distilled water.

In the last part of the experiment, V1 was switched to distilled water and the module was flushed for 1 hour at high flow rate (around 7ml/min). Then, the hydraulic permeability was measured again following the aforementioned procedure.

2.2.2 Bioreactor fluid dynamics

Fluid dynamics and mixing inside the bioreactor was investigated by residence time distribution (RTD) analysis. First, the bioreactor described (section 1.9.2) was assembled in-house. Similar to assembly of the module, metallic wire meshes were fixed at four inlet of the glass housing, 10 PEEK-WC hollow fibers were passed through two meshes in one direction forming one layer of fibers, then 10 PES hollow fibers (MicroPES® capillary membranes, 3M Deutschland GmbH, Germany) were passed as one layer in the crossing direction. The hollow fibers were consecutively inserted until a 10×10 arrangement was reached in each bundle. The four ends were then potted as explained before.

Figure 2. 3 shows the experimental setup for RTD measurement, the flow diagram for which is shown in Figure 2. 4. The newly assembled bioreactor was first flushed with distilled water for 4 hours. Then, at $t=0$, V1 valve was switched to the tracer solution (2.2 g/L sodium bicarbonate dissolved in William's medium E). The tracer solution was pumped at 1.5 ml/min as a step input into the bioreactor through PEEK-WC bundle while the opposite end of the bundle was closed. One end of the PES bundle was closed while the other was connected to the same peristaltic pump, removing the liquid from inside the bioreactor at the same rate and feeding it into the online spectrophotometer. The absorbance of the PES outlet (C_{out}) was recorded over time until reaching the plateau, while absorbance of the tracer solution (C_{in}) was directly measured beforehand, without passing through the bioreactor.

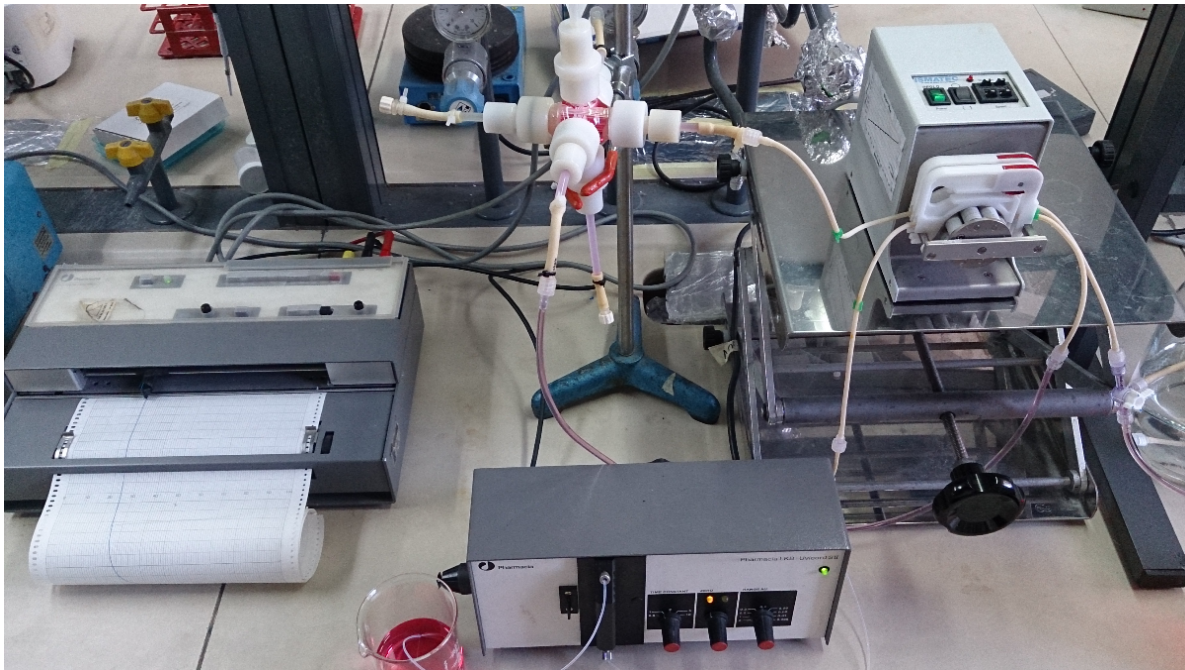


Figure 2. 3 Experimental setup for residence time distribution analysis for the bioreactor. The reservoirs for water and tracer are not shown in the picture (on the right side).

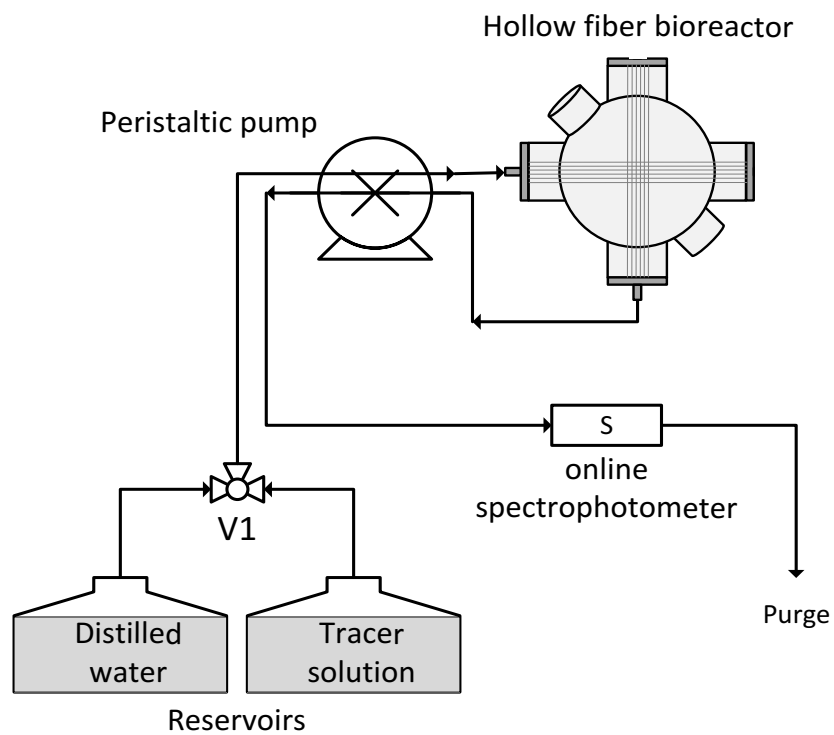


Figure 2. 4 Process flow diagram for residence time distribution analysis in the bioreactor.

Cumulative residence time distribution is used to characterize bioreactor's fluid dynamics:

$$F(t) = \frac{C_{out}}{C_{in}} \quad (2.2)$$

The theoretical mean retention time (τ) is calculated as the ratio of the perfusion flow rate to the volume of the bioreactor.

2.2.3 Static system

- **Experimental setup**

The 24-well plate equipped with oxygen sensor spots (OxoDish® OD24, PreSens, Germany) was allocated to the following conditions (each row of 4 wells for one condition):

- (i) Culture medium: 1ml of medium was added to each well.
- (ii) Medium + serum: %10 serum was added to the culture medium and 1ml of the mixed solution was added to each well.
- (iii) Collagen coating + medium: 35 μ L of collagen was used to coat the bottom surface of each well and after two hours, 1ml of culture medium was added to each well.
- (iv) PES + medium: A flat circular PES membrane with the same diameter as the well was placed carefully at the bottom of each well and a rubber ring with the same diameter as the well was used to hold it down in place. 1ml of medium was added to each well.
- (v) Teflon + medium: Condition (iv) was repeated using Teflon membranes.

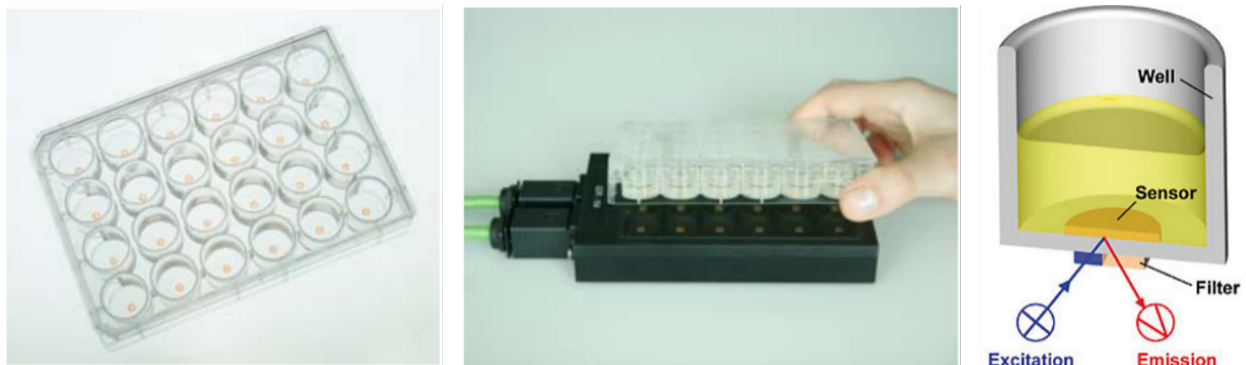


Figure 2.5 OxoDish® and SensorDish® Reader used for the experiment.

The prepared plate was connected to the SDR SensorDish® Reader (presens, Germany) and placed in the incubator. The reader was connected to a computer to record the data. The oxygen partial pressure was initially set at %20 and once equilibrium was reached in all the wells, oxygen tension was changed to %10 ($t=0$) and the oxygen concentrations were recorded for over 14 hours, with measurements made every 30 seconds.

- **Mathematical model**

The obtained data for condition (i) was used to calculate oxygen diffusion coefficient in the culture medium ($D_{o,l}$). Mass transfer for oxygen in the liquid medium is described by a simple diffusion model following Fick's law:

$$\frac{\partial c_{o,l}}{\partial t} = D_{o,l} \nabla^2 c_{o,l} \quad (2.1)$$

in which $c_{o,l}$ is the concentration of oxygen in culture medium (l), and $D_{o,l}$ is the diffusion coefficient of oxygen in the medium. The geometry is a cylinder 1ml in volume and 7.8mm in radius representing the medium in the well. In order to reduce the computational time, symmetry condition was applied. The geometry and applied boundary conditions are demonstrated in Figure 2. 6. The time-dependent equation is numerically solved for different $D_{o,l}$ values and the oxygen concentration read at the center of the bottom surface was plotted against the experimental data for comparison.

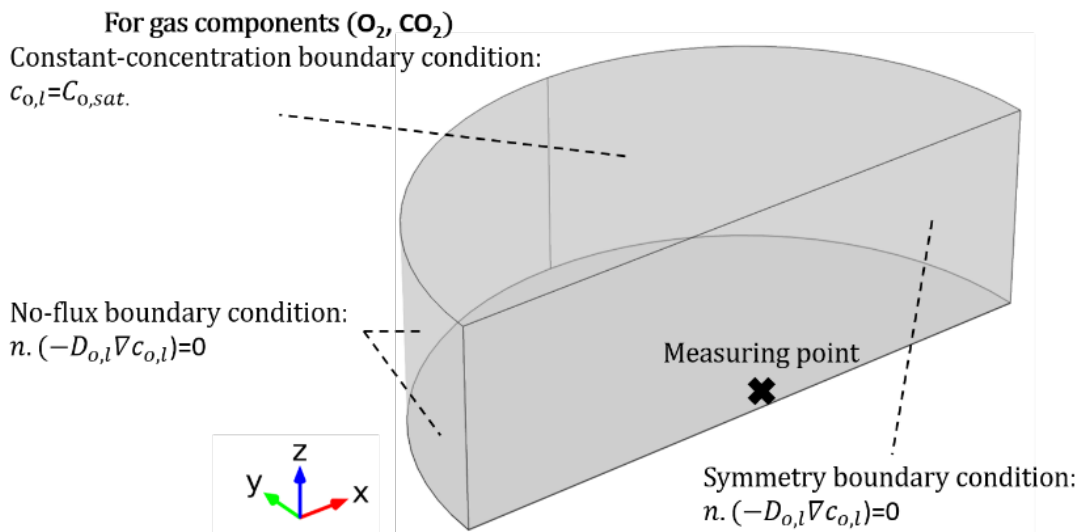


Figure 2. 6 Geometry and boundary conditions for numerical analysis.

2.3 Results

2.3.1 Hollow fibers

The steady-state hydraulic permeance of the membranes was calculated according to Eq. 2.2. as the slope of the straight line in Figure 2. 7 (permeation flux (J) versus ΔP^{TM}), and was found to be 0.799 L/(h.m².mbar). Using albumin solution decreased the permeance of the membranes to 0.313 L/(h.m².mbar), owing to membrane's ability to transfer albumin molecules, considering its molecular weight (66.5 kDa) compared to membranes molecular weight cutoff (190kDa). In order to evaluate the change o membrane permeability properties after the albumin solution, the hydraulic permeability after flushing the used hollow fibers with water was measured again, showing a lower value of 0.419 L/(h.m².mbar), as shown in Figure 2. 7. This decrease in hydraulic permeability indicates irreversible adsorption of protein to the membrane surface.

During the albumin permeance study, albumin concentrations at module's outlet, i.e. the permeate (C_{out}) was continuously recorded over time while the maximum albumin concentration at module's inlet (C_{in}) was known (both in terms of the absorbance). The ratio C_{out}/C_{in} was plotted as a function of elapsed time (Figure 2. 8), known as the F curve (Eq. 2.2). The ratio reaches the plateau at 0.97 after around 10 minutes.

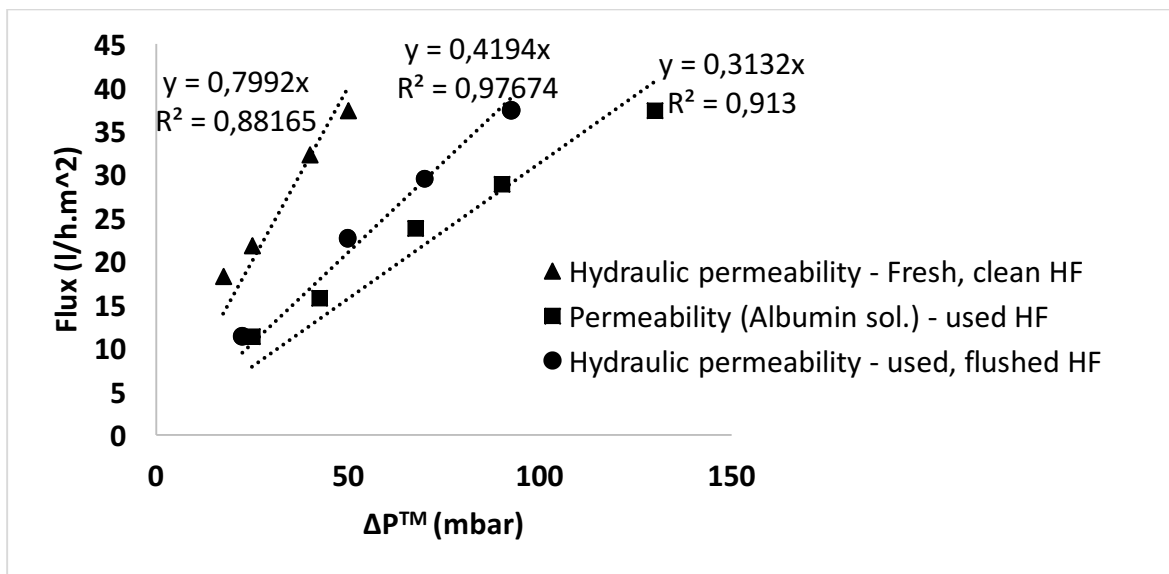


Figure 2. 7 Permeability study on PEEK-WC hollow fibers.

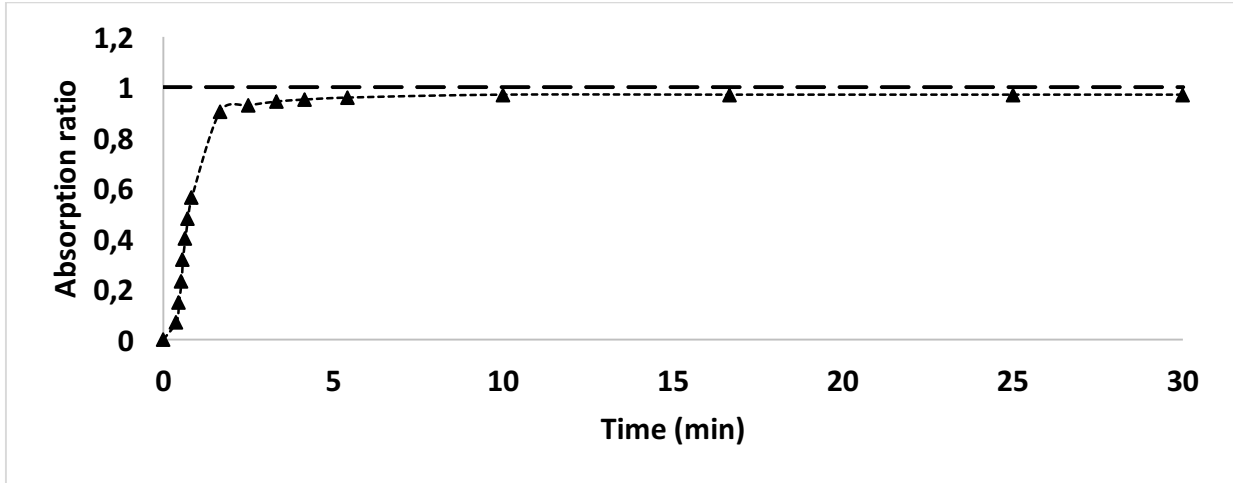


Figure 2. 8 C_{out}/C_{max} ratio as a function of time, known as the F curve, for albumin permeance experiment.

2.3.2 Bioreactor

The transport path inside the bioreactor differs among fluid elements. Consequently, the elements have different “residence times” or durations of time for them to pass through the bioreactor, the distribution of which at the bioreactor outlet is called the exit age distribution (E) or the residence time distribution of the fluid. At time t , E is related to F by:

$$E = \frac{dF}{dt} \quad (1)$$

The F curve can be obtained by introducing an inert, nonreactive tracer as a step input, as previously explained. The E and F curves for the hollow fiber membrane bioreactor are demonstrated in Figure 2. 10, in comparison with the curves for the ideal mixed flow (Figure 2. 9) as described by Levenspiel [5].

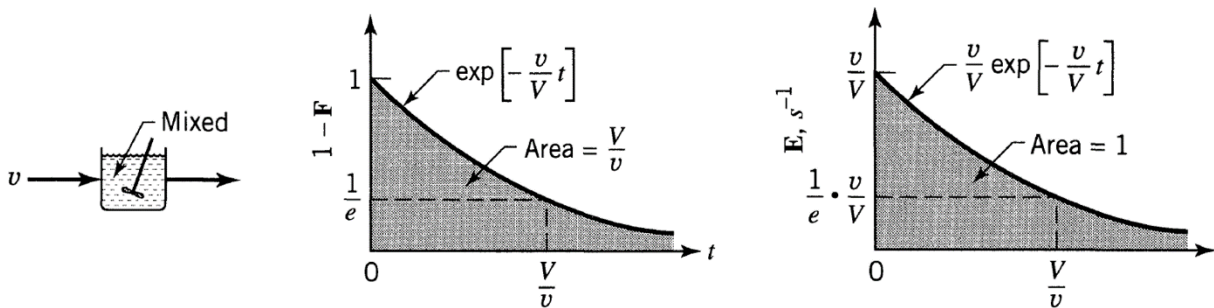


Figure 2. 9 E and $1-F$ curves for ideal mixed flow model [5].

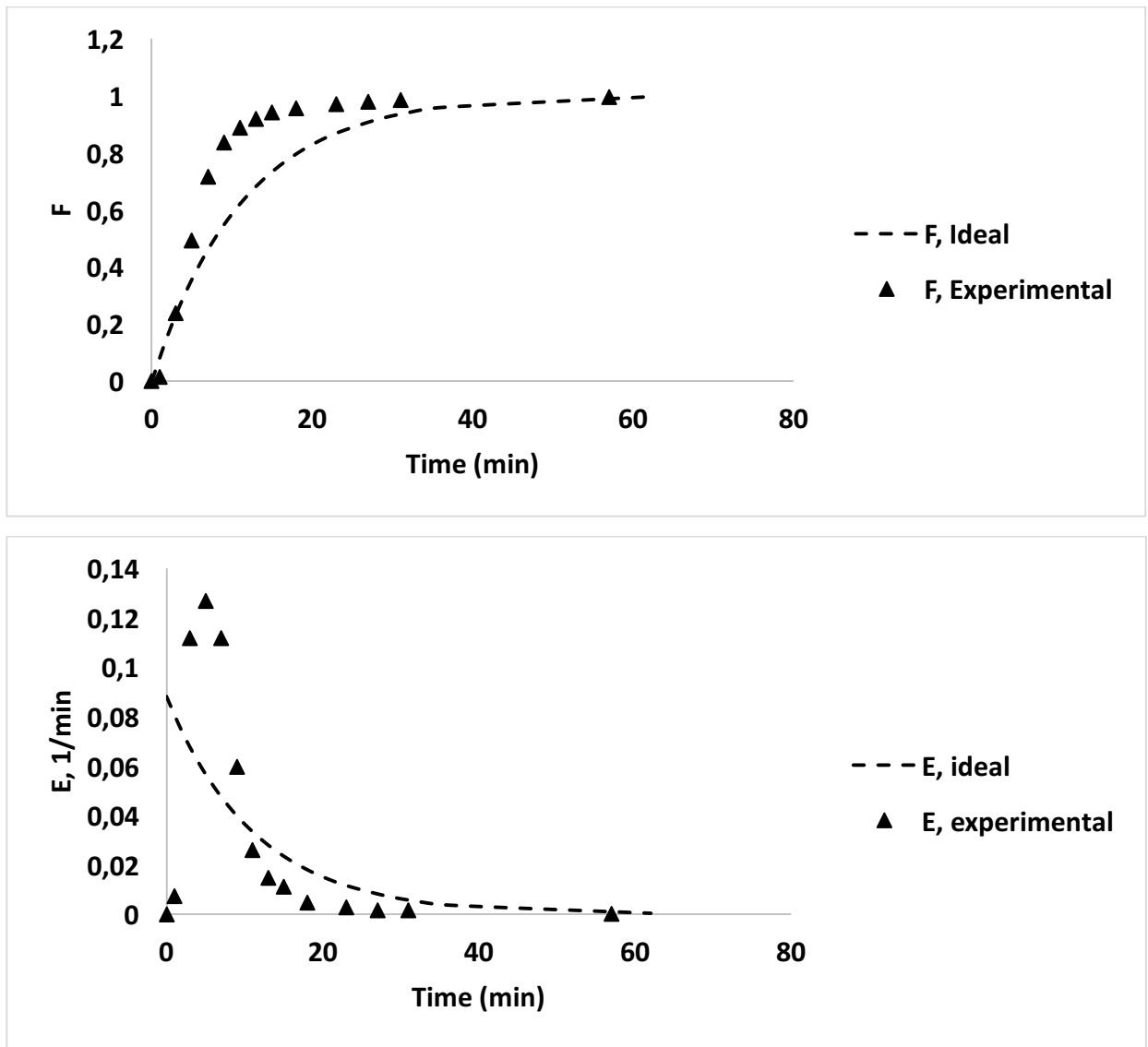


Figure 2. 10 $1-F$ (top) and E (bottom) curves for experimental results in comparison with the ideal mixed flow (CSTR) model.

2.3.3 Static system

Figure 2. 11 shows how the oxygen concentration at the bottom of a column of culture medium (1 ml volume, 5.25 mm height) changes over time when the oxygen partial pressure in the gas phase is changed (20% to 10%). Due to reduction of oxygen partial pressure in the incubator, dissolved oxygen diffuses from the liquid towards the gas-liquid interface and finally into the air. The concentration reduction at the bottom of the well is affected by the conditioning used: the response is slowed down in case of collagen coating and significantly fast in PES membrane, while teflon

membrane has a moderate effect on the reading. For the case of having only the culture medium in the well, the concentration profile is compared to the numerical solutions of Eq. 2.1 for three different $D_{o,l}$ values (3×10^{-9} , 3.5×10^{-9} and $4 \times 10^{-9} \text{ m}^2/\text{s}$), plotted for the same elapsed times in Figure 2. 12.

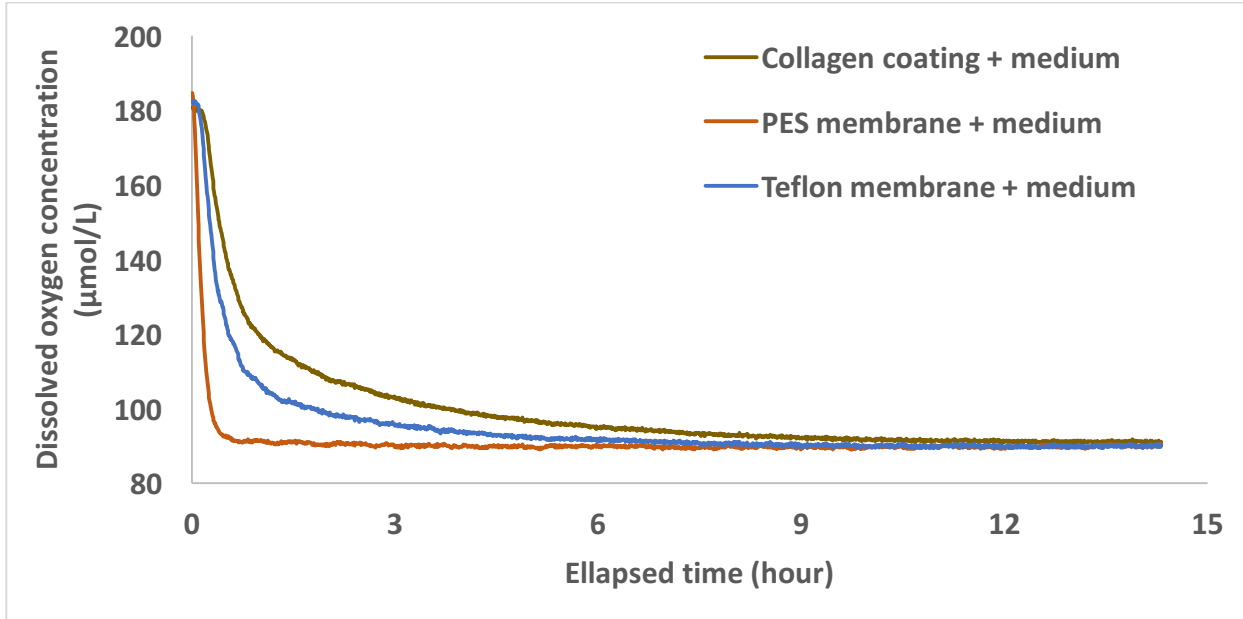


Figure 2. 11 Oxygen concentrations at the bottom of the well (averaged over 4 wells for each condition) recorded over 14.3 hours after changing the oxygen partial pressure in the incubator from 20% to 10%.

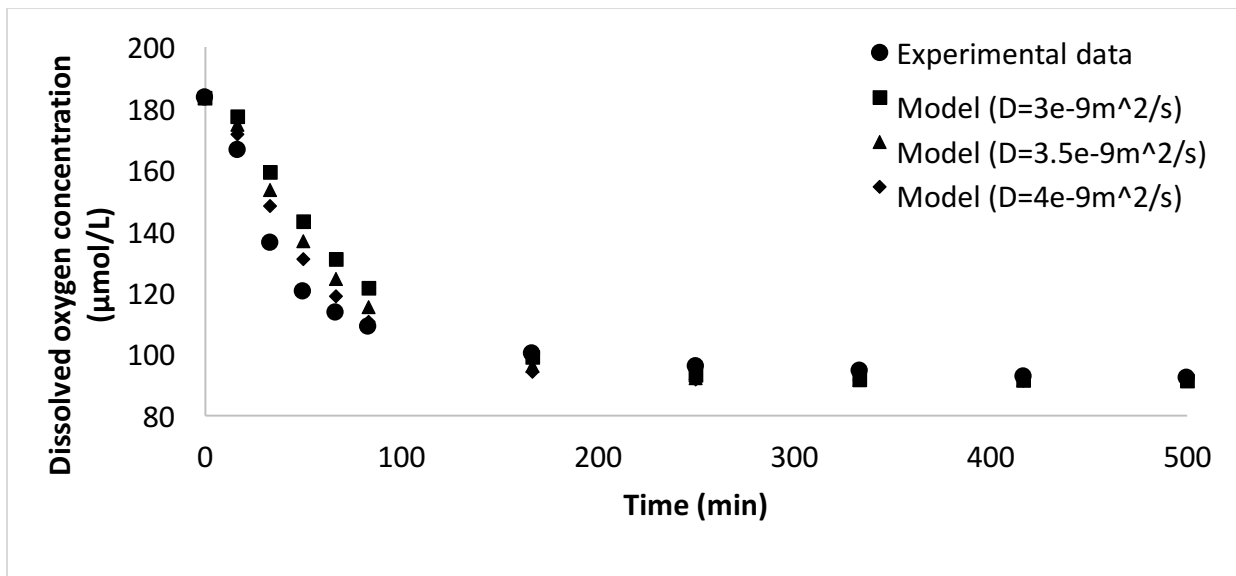


Figure 2. 12 Comparison between the experimental and theoretical values for oxygen concentrations at the bottom of the well after changing the oxygen tension in the incubator from 20% to 10%..

2.4 Discussion

As expected, the molecules of human serum albumin (molecular weight 66.5 kDa) can pass through the PEEK-WC hollow fiber membrane (molecular weight cutoff 190 kDa). The remaining difference in the concentrations (final ratio of 0.97) most likely indicates reduced albumin concentration due to its absorption within the pores of the membrane. Another observation that proves this phenomenon is the reduced permeability of the membrane. During current part of the test, the pressure gauges were also monitored. Under the same flow rate of 2ml/min and when using distilled water in fresh, clean hollow fibers, ΔP^{TM} – the driving force for convection – was 25mbar. During the permeance study, ΔP^{TM} was observed to increase to 70, 75, and 80 mbar at 21.7, 25.8 and 30 minutes after switching to albumin solution, respectively. Using albumin solution reduces membrane's permeability by 60%, and flushing the membrane at high throughputs only slightly increases the permeability and cannot reverse it back to the initial value as a result of the membrane fouling. Albumin absorbs on the membrane surfaces and eventually blocks the pores, as already demonstrated by the reduced hydraulic permeability after the albumin solution experiment.

The RTD analysis shows that the behavior of the bioreactor significantly diverges from the ideal mixed flow. One cause for which is readily diagnosable from the F curve: the observed early curve – i.e. narrow distribution with a rather steep slope – implies a presence of stagnant region.

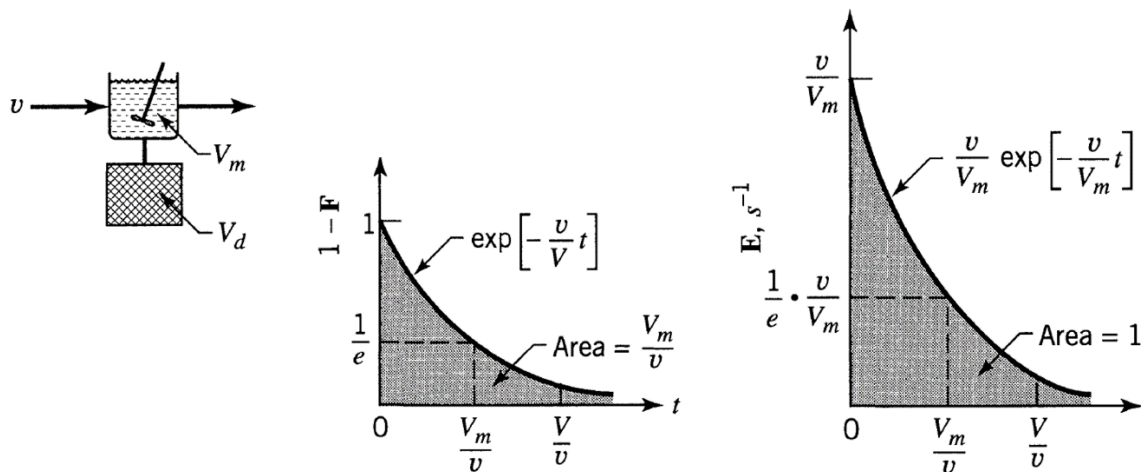


Figure 2.13 E and $1-F$ curves for the compartment flow model of mixed flow region + stagnant region [1].

A compartment model has been presented for this diagnosis by Levenspiel (Figure 2. 13), for which the extra-capillary space of the bioreactor was considered as a combination of a mixed flow region and a dead or stagnant region. The model was adopted to fit the data for this bioreactor. Accordingly, the total volume of the bioreactor ($V_t=25\text{ml}$) is assumed to be the mixed volume (V_m) plus the dead volume (V_d) (Figure 2. 14). The 1-F curve for this compartment model perfectly fits the data from tracer experiment, with $V_d=17\text{ml}$.

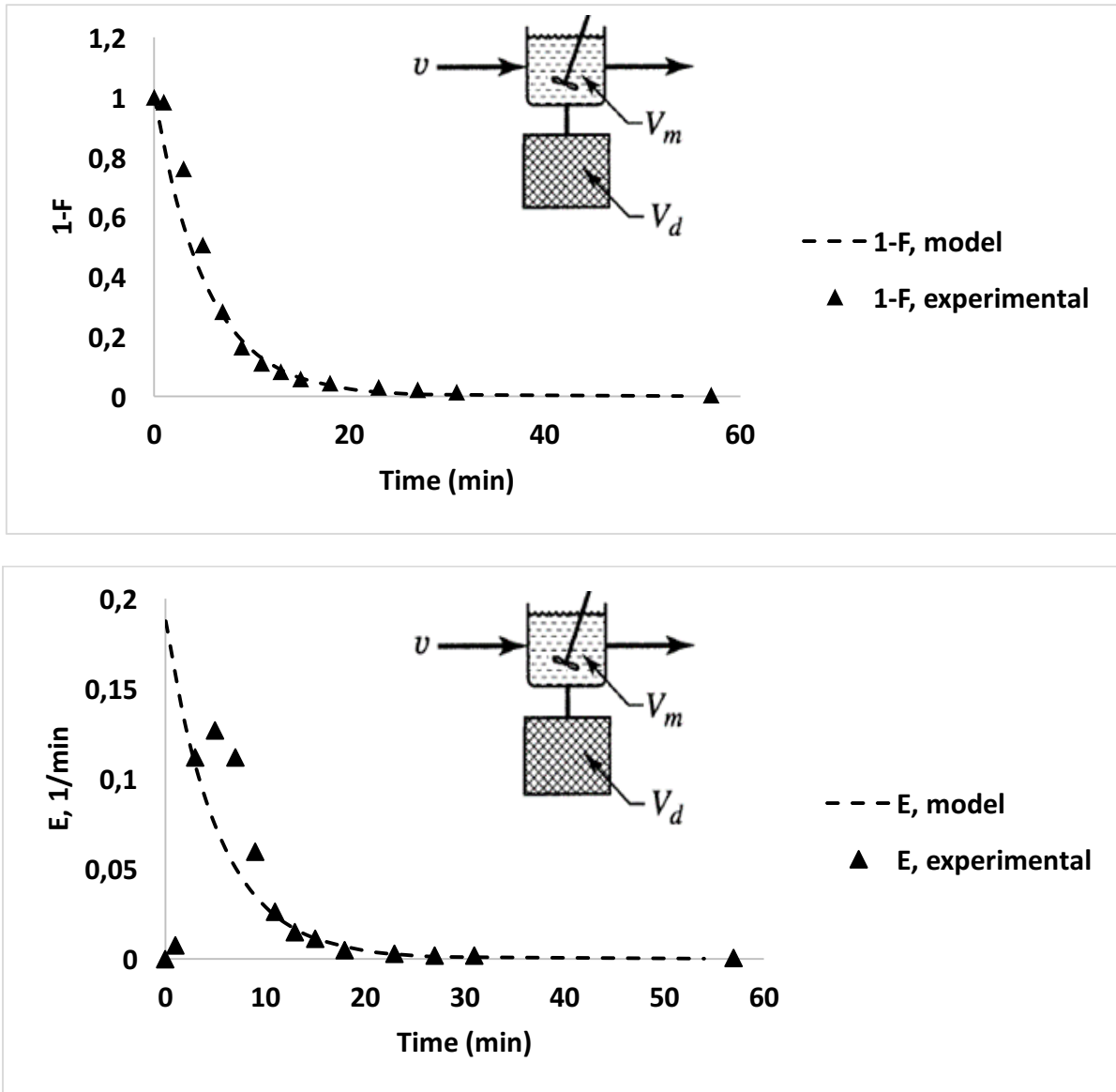


Figure 2. 14 E and 1-F curves for experimental results in comparison with the compartment flow model of mixed flow region + stagnant region.

For oxygen measurements in batch systems, optic oxygen sensors were implemented for accurate, real-time *in situ* measurement of oxygen concentration in culture medium. This approach has recently gained special interest in comparison with other methods such as Clark-type electrodes or in-situ near infrared spectroscopy. Advantages of using this system include non-invasive and non-destructive online measurement of dissolved oxygen with high accuracy, no consumption of oxygen, and signal independent of flow velocity when advection is present. Measurements can be taken at preferred time intervals (fastest possible is 1s), with limit of detection of 0.03 % oxygen, 15 ppb dissolved. In this system, the sensor spots are excited by an LED to emit fluorescence. The degree of quenching in the fluorescence signal – measured from outside of the bioreactor - due to oxygen molecules is correlated to the dissolved oxygen concentration in the medium.

In batch systems, the conditionings used at the bottom surface of the wells in fact add a barrier to oxygen transport between the cells and the sensor spots. Adding serum to the culture medium does not have a significant influence on oxygen transport rate, thus its diffusion coefficient. For different conditionings, however, changing oxygen concentration in the gas phase resulted in different responses of the sensors in comparison with the medium-only case. As expected, the sensor spots covered with collagen showed a slower response due to slower oxygen transport. The surprising outcome was for the membranes, especially PES, in which the sensors responded faster to oxygen change and their readings reached the equilibrium value more rapidly.

2.5 Conclusions

In this chapter, basic yet crucial aspects of transport phenomena in static (batch) and dynamic (bioreactor) systems were studied. In albumin permeance test, significant drop in permeability of the hollow fibers was observed. Adsorption of proteins in the membrane can eventually block the smaller pores, thus altering membrane's microstructure and mass transfer properties. The findings from this test were notable for several reasons: (i) only one protein was studied here while a culture medium consists of numerous components, (ii) the culture medium changes over time due to cellular consumption and production of different molecules, which could further complicate this phenomenon, (iii) the process seems irreversible, potentially making it problematic considering the long culture periods.

Investigation of the fluid dynamics inside the bioreactor using RTD analysis revealed that the central part of the bioreactor in which cells are cultured was diagnosed as well mixed while a stagnant region was found in the edge of the device. The effect of this dead volume on mass transfer to/from cells needs to be further studied. Moreover, the non-ideal mixing must be taken into account for making decisions about positioning the sensors inside the bioreactor or choosing sampling points, especially in large-scale systems.

The effect of different conditionings used in multi-well plates was also investigated. While each added material alters the oxygen transfer between the cells and the sensor, the readings were not substantially compromised. Surprisingly, adding a membrane layer seemed to improve the reading of the sensor, especially when using PES.

References

- [1] E. Curcio, "Mass Transfer and Computational Fluid-dynamics in Bioreactors," in *Biomaterials for Stem Cell Therapy*, ed: CRC Press, 2013, pp. 448-474.
- [2] B. J. Lawrence, M. Devarapalli, and S. V. Madhally, "Flow dynamics in bioreactors containing tissue engineering scaffolds," *Biotechnol Bioeng*, vol. 102, pp. 935-47, Feb 15 2009.
- [3] L. De Bartolo, S. Salerno, E. Curcio, A. Piscioneri, M. Rende, S. Morelli, *et al.*, "Human hepatocyte functions in a crossed hollow fiber membrane bioreactor," *Biomaterials*, vol. 30, pp. 2531-43, May 2009.
- [4] E. Curcio, L. De Bartolo, G. Barbieri, M. Rende, L. Giorno, S. Morelli, *et al.*, "Diffusive and convective transport through hollow fiber membranes for liver cell culture," *Journal of biotechnology*, vol. 117, pp. 309-321, 2005.
- [5] O. Levenspiel, "Chemical reaction engineering," *Industrial & engineering chemistry research*, vol. 38, pp. 4140-4143, 1999.

Chapter 3

Oxygen transfer model in static culture systems

3.1 Introduction

Multi-well plates are the simplest cell culture platform for *in vitro* studies and depending on the cell type, they can be employed for different applications such as establishment of culture conditions and protocols, cell functionality evaluation, cell expansion and differentiation, drug biotransformation, etc.

Depending on the cell type and the application, the multi-well plates can be prepared in different ways. Generally, the bottom surfaces of the sterilized wells are coated with a biocompatible material – usually components from the extra-cellular matrix – promoting cell viability, functionality and growth. Known volume of culture medium is added to the wells and finally the cells are seeded. The plates are placed in the incubator to have sterile and controlled conditions in terms of gas composition (oxygen, nitrogen and carbon dioxide) and humidity. The upper surface of the culture medium, the gas-liquid interface is available for gas exchange (oxygen for the cellular uptake and carbon dioxide for buffering), making each well a semi-batch system. The static systems are subject to depletion of nutrients – most importantly glucose – or possibly other components such as hormones and growth factors. Additionally, the catabolites and cellular products accumulate in the medium over time. Consequently, the culture medium is carefully removed after certain period of time and replaced with fresh medium. However, the exposure of cells to temporal changes of nutrients and catabolites is not normally observed *in vivo*, which may potentially affect their functionality *in vitro*.

Arguably, the most critical issue in static culture systems is sufficiency of oxygen supply to the cells. It is based merely on the gas-liquid thermodynamic equilibrium at the interface, and diffusion through the medium to the cells. In this chapter, the sufficiency of oxygen supply to hepatocytes both as a monolayer and as spheroids in batch culture systems is evaluated in terms of the dissolved oxygen concentration (DOC) values. The accumulation of urea as a catabolite is also demonstrated.

3.2 Methods

The geometry of the semi-batch system (single well) is depicted in Figure 3. 1. The cylinder represents the culture medium (1ml in volume, 15.6mm in diameter with a height of 5.25mm). Two different types of cellular masses are considered: 99 spheroids or cellular monolayer (16 μ m in thickness, equivalent to the size of hepatocytes). The arrangement of the cells are also shown in Figure 3. 1.

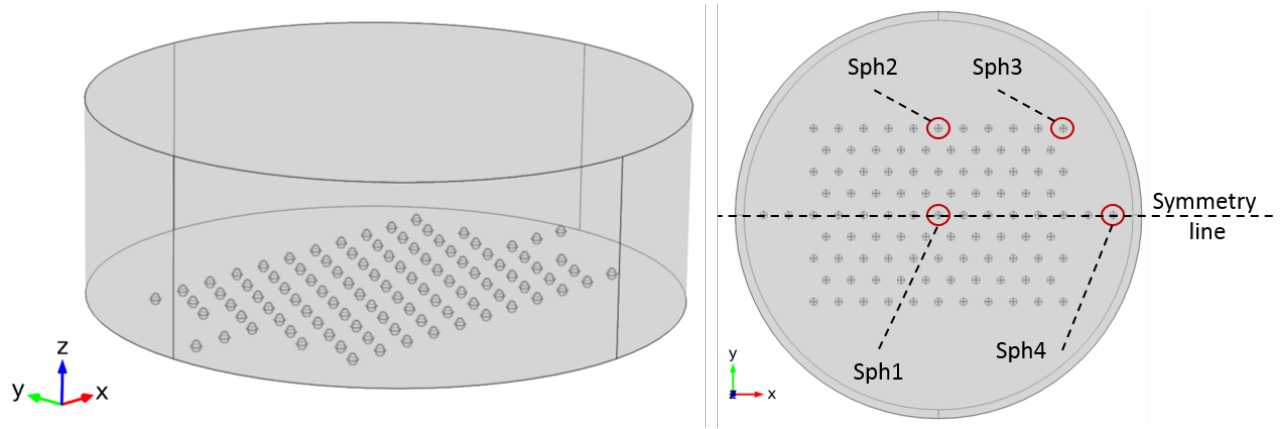


Figure 3. 1 (Left) Geometry of a single well considered for mass transfer modelling. (Right) arrangement of 99 spheroids at the bottom of the well, and the spheroids for which the oxygen concentration profile will be given in more detail. For reducing the computational time, the geometry was divided in half considering an x-z symmetric plane.

By choosing a symmetrical arrangement of the cells, the geometry was divided in half to use symmetry condition, thus reducing the computational cost and facilitating the use of finer mesh sizes. Having the origin of the coordinates at the center of the bottom surface of the well, the symmetry plane used here is the x-z plane passing through the center of the cylinder.

3.2.1 Mathematical model

Mass transfer in static systems is described by a simple diffusion-reaction model [1]. Using Fick's law, mass balance for component j in the medium (marked by subscript l) yields:

$$\frac{\partial c_{j,l}}{\partial t} = \nabla \cdot (D_{j,l} \nabla c_{j,l}) \quad (3.1)$$

in which $c_{j,l}$ is the concentration of species j in medium phase I, and $D_{j,l}$ is the diffusion coefficient of species j in medium phase I. Considering the cellular compartment (marked by subscript cc) as uniform, isotropic porous media, mass balance yields:

$$\frac{\partial c_{j,cc}}{\partial t} = \nabla \cdot (D_{e,j,cc} \nabla c_{j,cc}) + \mathcal{R}_{j,cc} \quad (3.2)$$

in which D_e is the effective diffusion coefficient and \mathcal{R} is the metabolic rate of consumption or production of the molecule of interest in the cellular compartment. Oxygen uptake rate is generally described by Michaelis-Menten kinetics:

$$\mathcal{R}_{o,cc} = \frac{V_{max} c_{o,cc}}{c_{o,cc} + K_m} \quad (3.3)$$

K_m value of 5.6 mm Hg and V_{max} value of 5nmol/(cm³.s) reported based on the cell density used in ELAD[®] device [2, 3] was used here. Accordingly, oxygen uptake rate is corrected with respect to the applicable theoretical cell density ($\rho_{cell,model}$) compared to that of reference cell density ($\rho_{cell,ref}$):

$$\mathcal{R}_{o,cc} = (\mathcal{R}_{o,cc})_{ref} \frac{\rho_{cell,model}}{\rho_{cell,ref}} \quad (3.4)$$

where the theoretical cell density within the spheroid is in turn expressed as a function of the porosity of the spheroid (ϵ_{cc}) and the volume of a single hepatocyte (V_{cell}):

$$\rho_{cell,model} = \frac{1 - \epsilon_{cc}}{V_{cell}} \quad (3.5)$$

To the best of author's knowledge, formulated kinetic rates of protein or catabolite synthesis for primary hepatocytes are not available in the literature. Therefore, the metabolic production rates experimentally-obtained by colleagues in our group were used as a constant source (zeroth-order kinetics). For urea, a production rate of 133nmol/(h.10⁶cells) was calculated. Effective diffusion coefficient of component j within the cellular compartment is generally related to the diffusion coefficient in the liquid phase:

$$D_{e_{j,cc}} = \frac{\varepsilon_{cc}}{\tau_{cc}} D_{j,l} \quad (3.6)$$

Several correlations have been reported to relate the tortuosity (τ) to the porosity of the medium. Here, Bruggeman equation was used for the tortuosity of the cellular compartment with $\varepsilon_{cc} > 0.2$ [4]:

$$\tau_{cc} = \frac{1}{\varepsilon_{cc}^{0.5}} \quad (3.7)$$

3.2.2 Boundary conditions

The boundary conditions describing the system are shown in Figure 3. 2. The walls of the well are impermeable, thus no-flux boundary condition all around and below the geometry was applied. The symmetry condition is applied to both the medium and the cellular compartment at the symmetry plane described earlier. The interfacial boundary is considered to be in equilibrium with the gas phase according to Henry's law, which results in the (constant) saturation concentration at the interface.

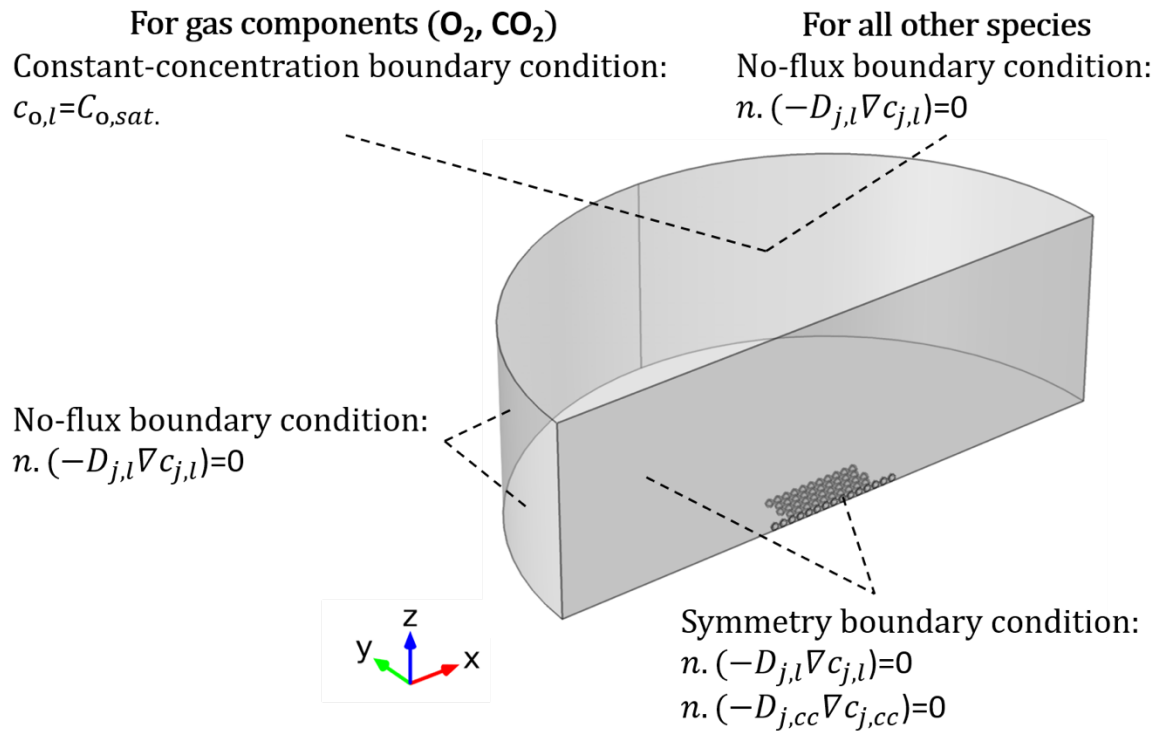


Figure 3. 2 Boundary conditions applied for mass transfer modelling (n is the boundary's normal vector).

As discussed earlier, the system under investigation is semi-batch due to oxygen exchange with the gas phase. Consequently, Eq. 1 was numerically analyzed in steady-state condition for oxygen and in time-dependent mode for urea, using COMSOL Multiphysics® (COMSOL Inc., Stockholm, Sweden). Oxygen concentration profiles for different spheroid sizes and gap sizes between them, and for the cellular monolayer are presented and discussed in the following sections. Although oxygen transfer is the focus of this study, accumulation of urea during culture time is also illustrated.

3.3 Results

3.3.1 Spheroids

- **Effect of intra-spheroid spacing**

First, a well containing 1ml of culture medium and 99 spheroids with diameters of 200 μm positioned 50 μm away from each other (center-to-center distance between two adjacent spheroids: 250 μm) was considered. An oxygen concentration gradient was observed along the well, with DOC dropping from 0.185 mol/m³ at the gas-liquid interface to a minimum of 0.033 mol/m³ near the spheroids (Figure 3. 3). A radial oxygen gradient was also present in the well, at the bottom of which the DOC drops from 0.176 mol/m³ near the wall to 0.033 mol/m³.

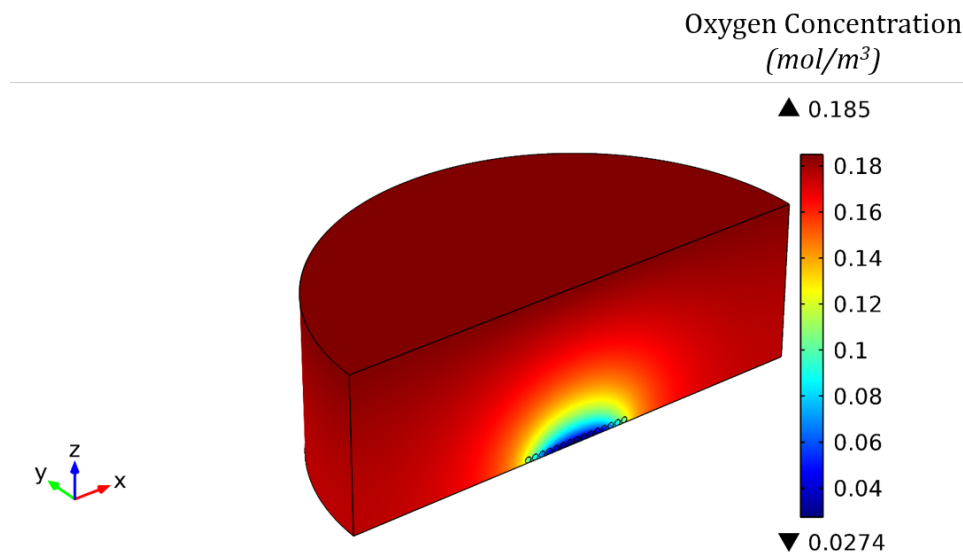


Figure 3. 3 Oxygen concentration profile (mol/m³) in a well containing 1ml of culture medium and 99 spheroids (200 μm in diameter with 50 μm space between them).

As anticipated, and predicted by the DOC gradients in the culture medium, spheroids experience different DOC values based on their location. Considering the physiological oxygen concentrations (0.042 – 0.091 mol/m³), the central spheroids are partially exposed to hypoxic conditions, as demonstrated by the oxygen concentration dropping as low as 0.027 mol/m³ in the core of the spheroid at the center (Figure 3. 4). DOC values in spheroids positioned at the edge were found within or higher than the physiological range. However, hypoxia was not observed with an intra-spheroid spacing of 100µm for the same conditions (Figure 3. 5). Indeed, the minimum oxygen concentration in the core of the central spheroids reaches 0.048 mol/m³, which is still within the physiological range.

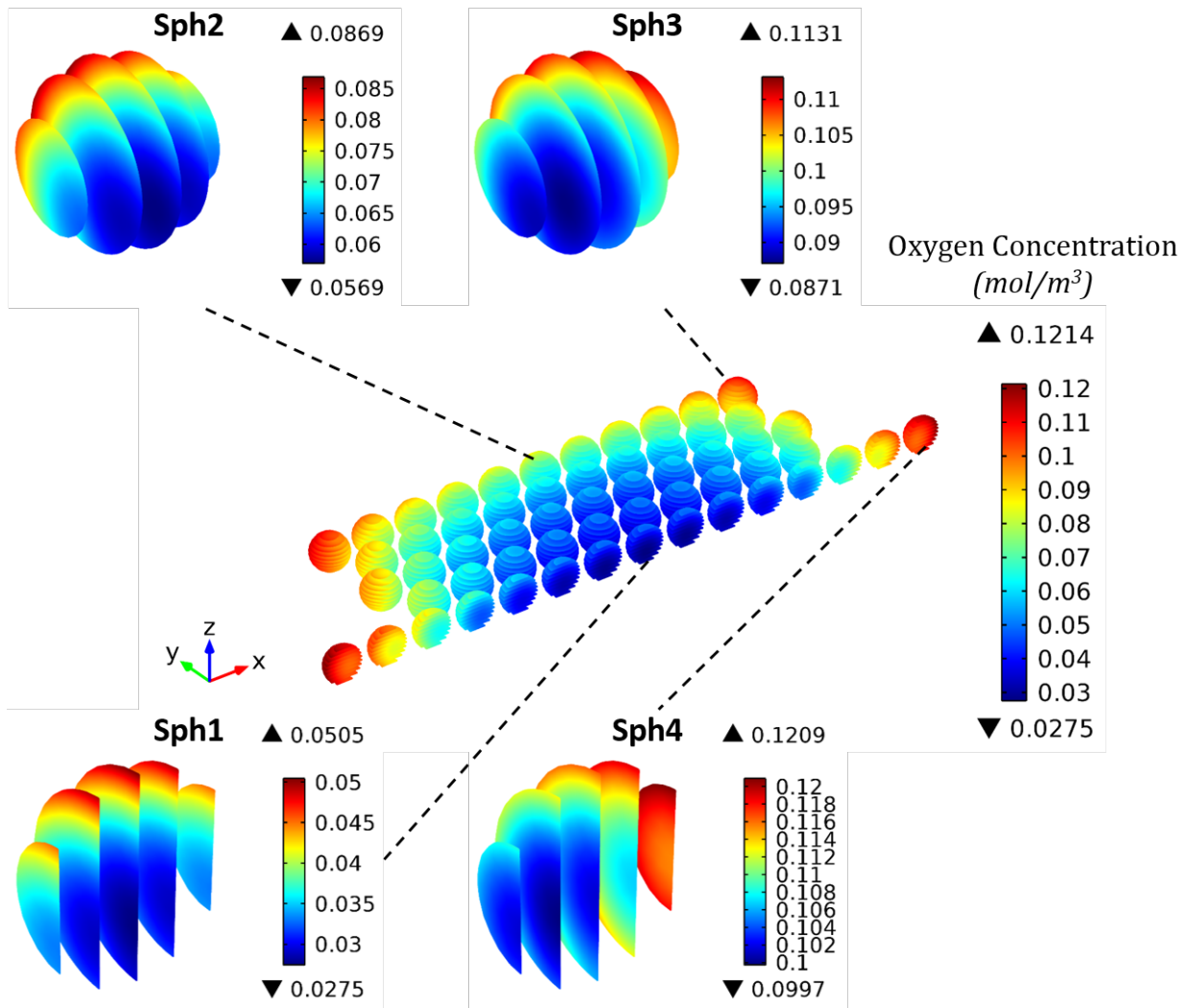


Figure 3. 4 Oxygen concentration profile (mol/m³) inside the spheroids sitting at the bottom of a well containing 1ml of culture medium and 99 spheroids (200µm in diameter, 50µm spacing).

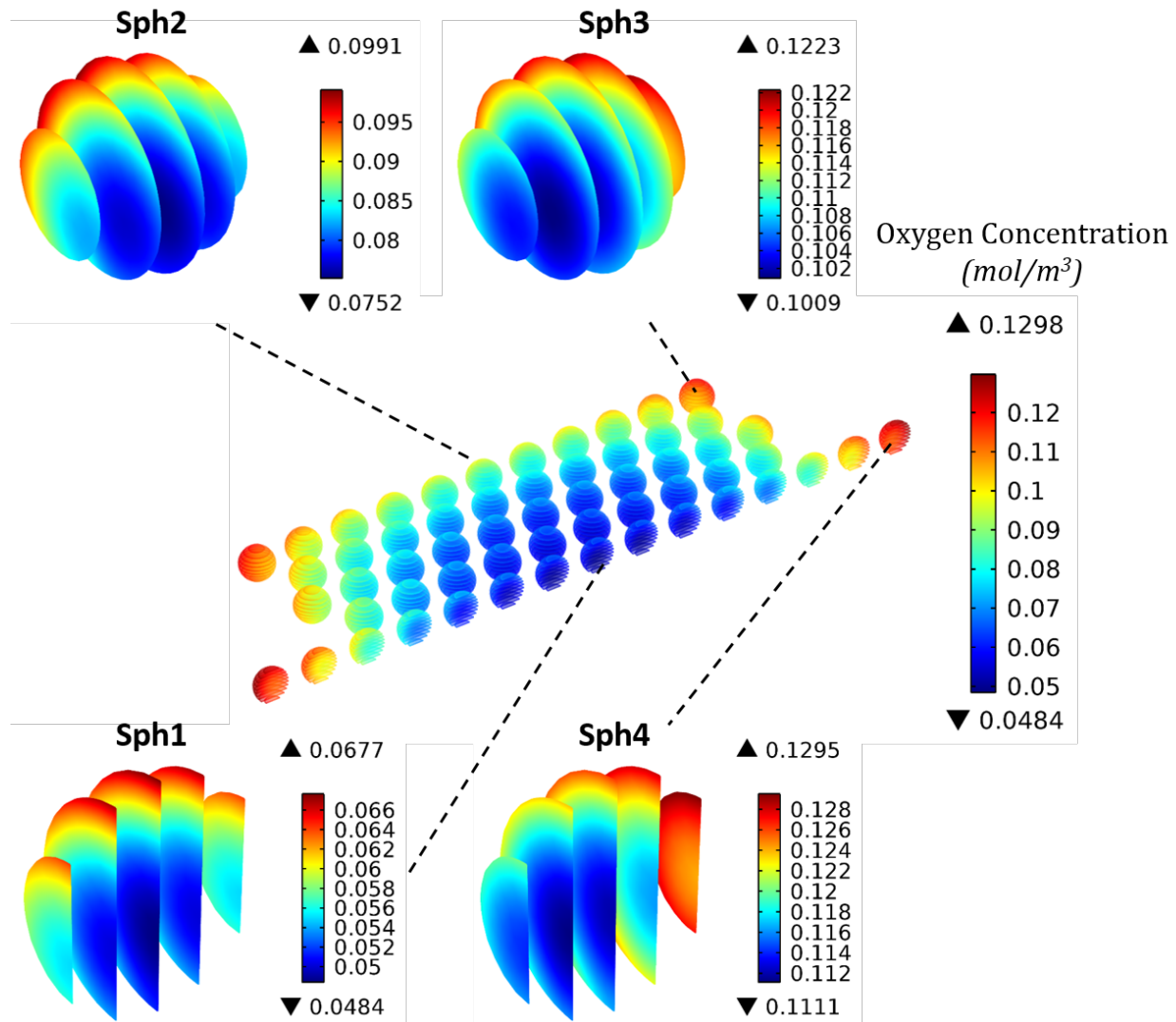


Figure 3. 5 Oxygen concentration profile (mol/m^3) inside the spheroids sitting at the bottom of a well containing 1ml of culture medium and 99 spheroids ($200\mu\text{m}$ in diameter, $100\mu\text{m}$ spacing).

- **Effect of spheroid size**

The effect of spheroid size was evaluated by using larger spheroids ($300\mu\text{m}$ in diameter) and (almost) the same total number of cells as in 99 spheroids $200\mu\text{m}$ in diameter, resulting in 30 spheroids. The spheroids in this case can also be sufficiently supplied with oxygen, as long as there is a minimum of $300\mu\text{m}$ gap between them (Figure 3. 6). Culturing 99 spheroids with diameters of $300\mu\text{m}$ and the arrangement used before is still feasible, despite the triple number of cells. However, it requires a spacing of at least $700\mu\text{m}$ (Figure 3. 7).

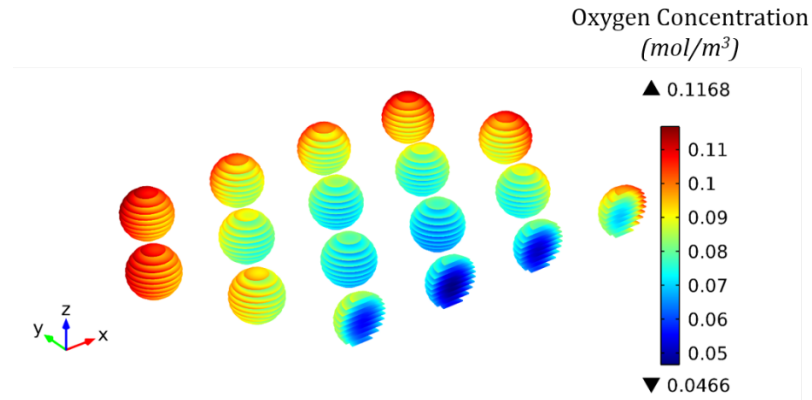


Figure 3. 6 Oxygen concentration profile (mol/m^3) inside the spheroids sitting at the bottom of a well containing 1ml of culture medium and 30 spheroids $300\mu\text{m}$ in diameter ($300\mu\text{m}$ spacing) having the same total number of cells as in 100 spheroids $200\mu\text{m}$ in diameter.

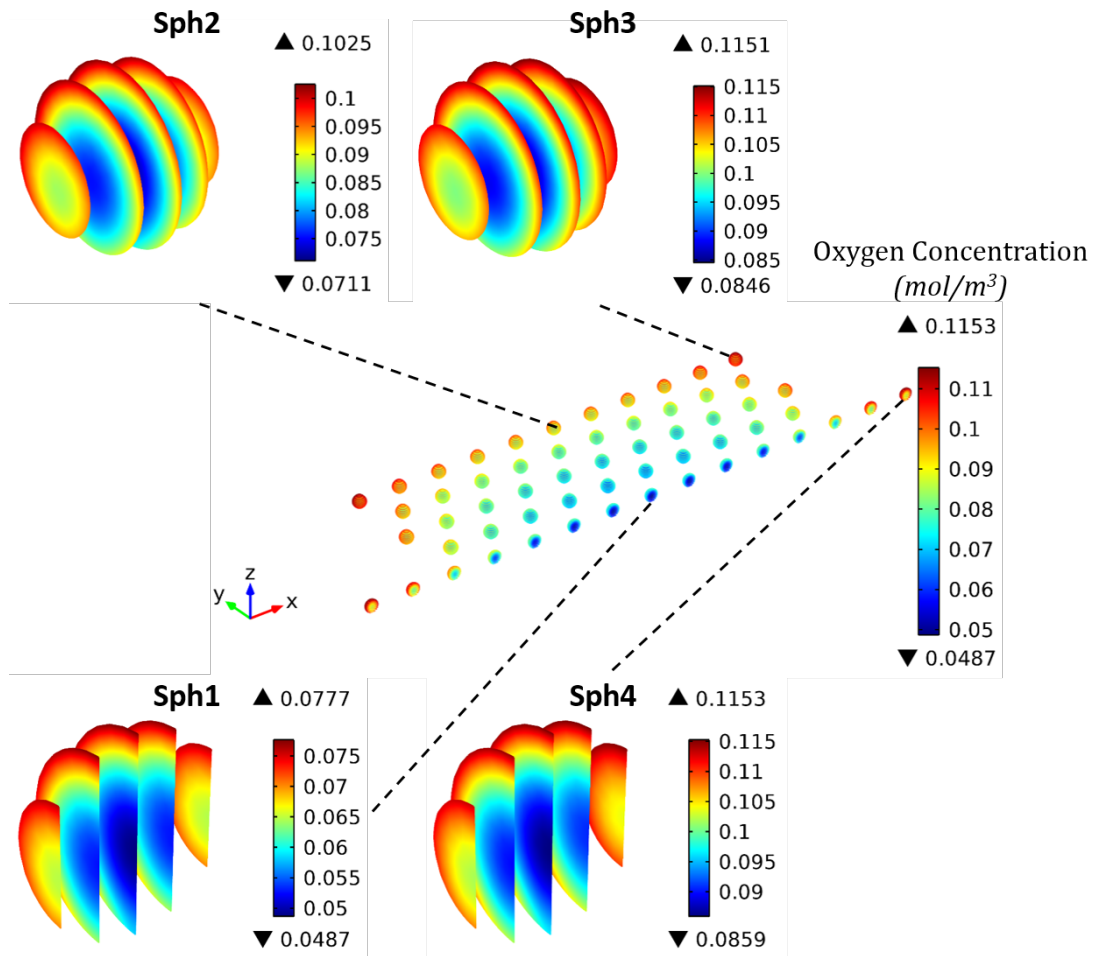


Figure 3. 7 Oxygen concentration profile (mol/m^3) inside the spheroids sitting at the bottom of a well containing 1ml of culture medium and 99 spheroids ($300\mu\text{m}$ in diameter, $700\mu\text{m}$ spacing).

- **Effect of culture medium's height**

Using higher volume of culture medium results in higher height thus longer diffusion path from the interface to the cells. Figure 3. 8 shows the oxygen concentration profile in two different spheroid sizes with 2ml of medium. In comparison with Figure 3. 5 and Figure 3. 7, one can readily infer that doubling the medium volume adversely affects the oxygen supply to cells, increasing hypoxia within the spheroids.

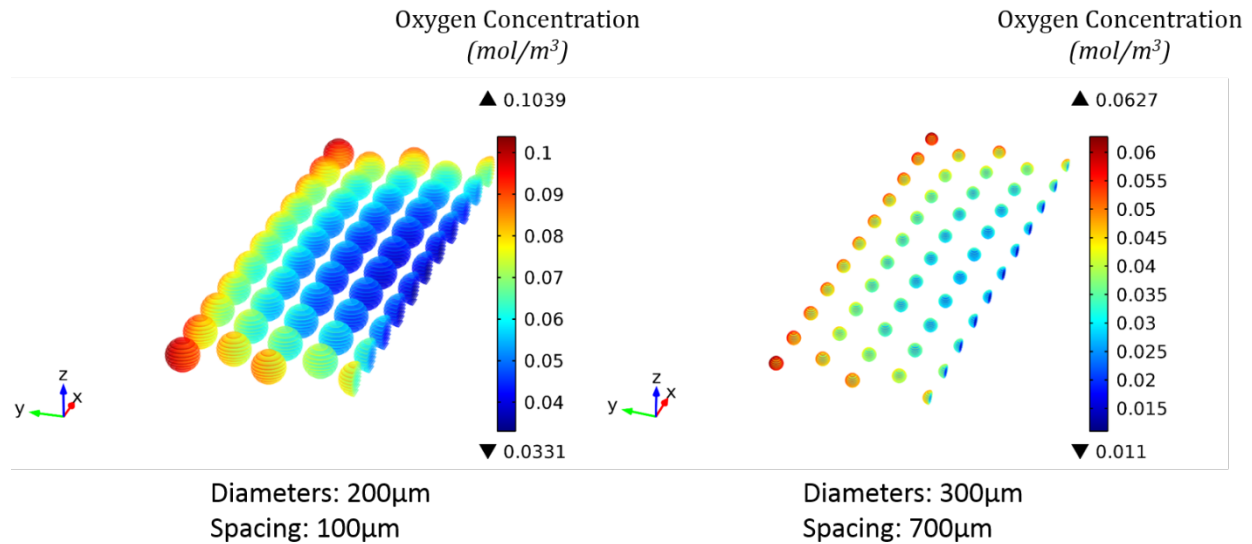


Figure 3. 8 Oxygen concentration profile (mol/m³) inside the spheroids sitting at the bottom of a well containing 2ml of culture medium.

3.3.2 Cellular layer

Seeding isolated cells into the wells instead of the previously-formed spheroids results in a layer of cells. A monolayer of cells was herewith considered for two different cases: (i) having the same total number of cells as in 99 spheroids 200µm in diameter, (ii) covering the bottom surface of the well completely. Keeping in mind the physiological oxygen concentration range, in the first case, all the cells are highly exposed to hyperoxic conditions (Figure 3. 9), while a concentration gradient is still observed along the radius of the layer.

In the case where the cells completely cover the bottom of the well, constituting higher number of cells (8.27×10^5 vs. 1.13×10^5), the oxygen concentration is just above the minimum amount in vivo while no significant gradient is observed along the layer as oxygen concentration throughout the cellular layer is between 0.0432 – 0.0442 mol/m³ (Figure 3. 10).

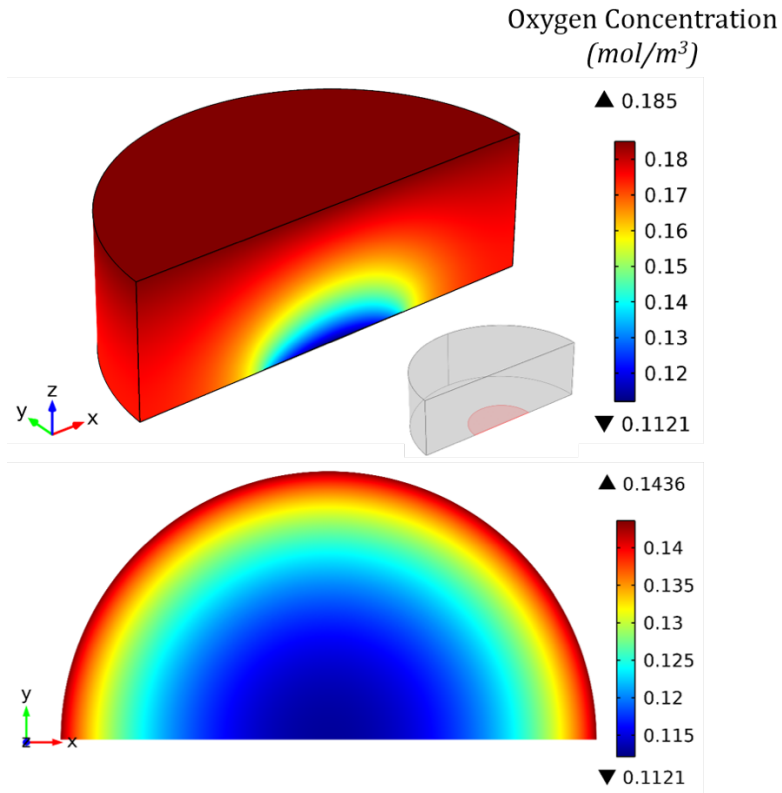


Figure 3. 9 Oxygen concentration profile (mol/m^3) in a well containing 1ml of culture medium and a cellular monolayer with $16\mu\text{m}$ thickness and 2.89mm radius having the same total number of cells as in 99 spheroids $200\mu\text{m}$ in diameter. (Top) Concentration profile through the medium, (Bottom) concentration profile across the cellular layer.

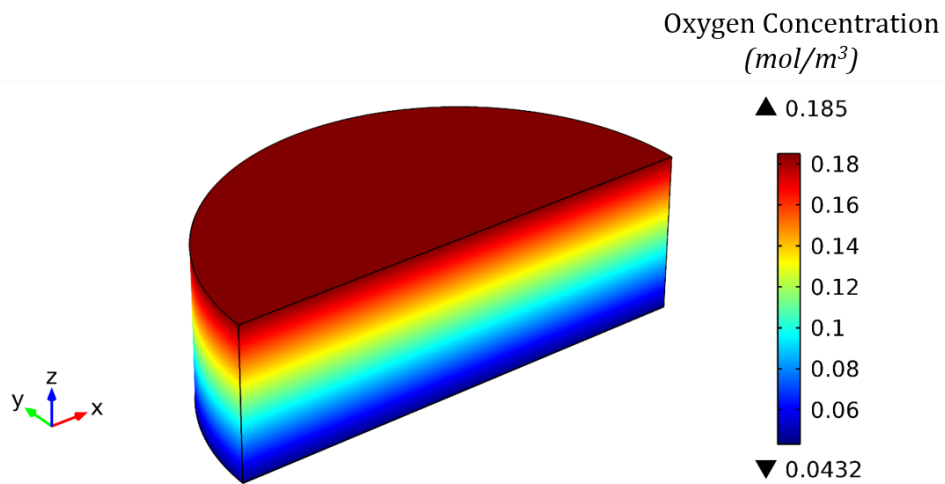


Figure 3. 10 Oxygen concentration profile (mol/m^3) in a well containing 1ml of culture medium and a cellular monolayer fully covering the bottom of the well ($16\mu\text{m}$ thickness). Oxygen concentration in the cellular layer is $0.0432 - 0.0442 \text{ mol/m}^3$.

Finally, the urea concentration profile in a well containing 1ml of culture medium and 99 spheroids (300 μm in diameter, 700 μm spacing) was obtained at 6, 12, 18, and 24 hours after starting the culture (Figure 3. 11). In this case, the highest concentration of urea was inside the spheroid, and a concentration gradient was observed through the medium.

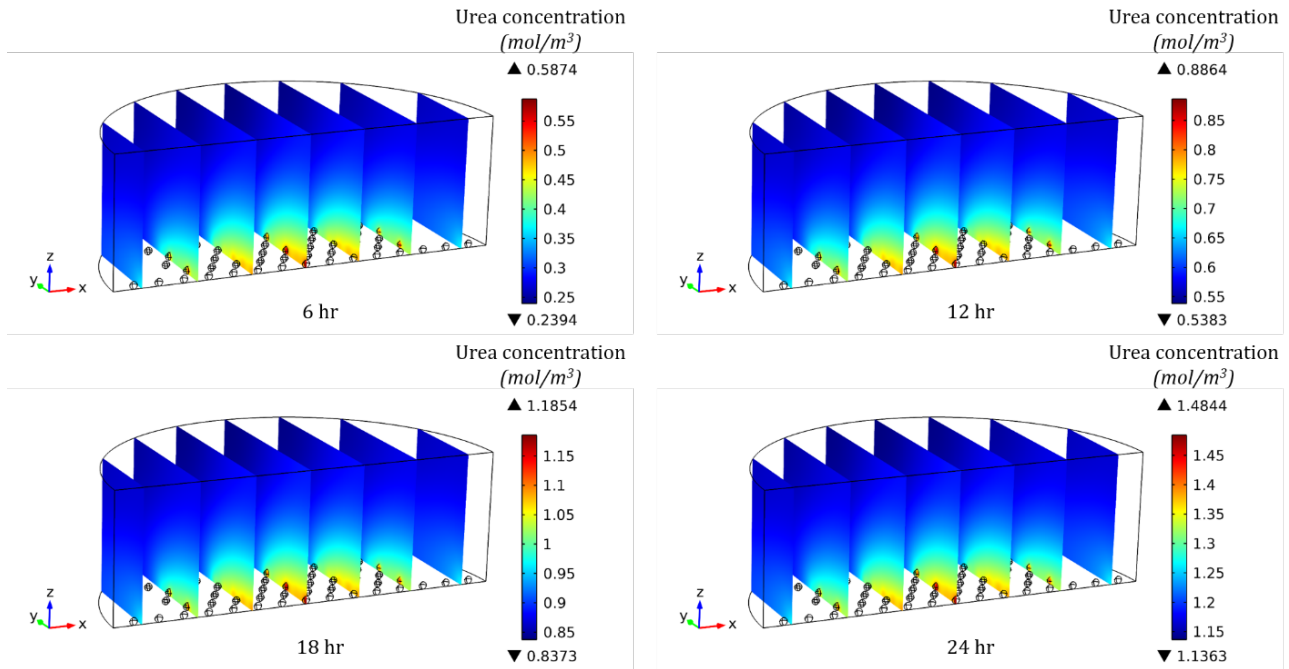


Figure 3. 11 Urea concentration profile and its accumulation in 1ml culture medium containing 99 spheroids (300 μm in diameter, 700 μm spacing) at different time points during the culture.

3.4 Discussion

In order to make a better comparison between the expected DOC profiles obtained from mass transfer modelling and the physiological DOC range in vivo, two parameters are herewith defined. Biomimicry index (β_{Bm}) was adapted from the approach taken by Dulong et al. in which they defined a necrosed region and a viable region based on the oxygen concentration in islets of Langerhans in a bioartificial pancreas [5]. β_{Bm} here is the fraction of the cellular compartment exposed to physiological DOC range (42-91 $\mu\text{mol/L}$), thus ideally it should be equal to 1. Exposure to DOC values higher or lower than in vivo range does not necessary mean total loss of functionality or viability. β_{Bm} discriminates between cells under ideal conditions and cells “at risk”. Hypoxia is a vital issue to be addressed in in vitro cultures, the extent of which was expressed by the hypoxia index (β_{Hpx}) defined as the fraction of the spheroid with $\text{DOC} < 42 \mu\text{mol/L}$.

Oxygen penetration depth in hepatic tissue is very short, reportedly 100-150 μm [6]. Consequently, the same range was considered for the spheroid radius. The significance of spheroid size in sufficiency of oxygen supply and minimizing cell necrosis was already well-known. However, the modelling results presented here suggest that the distribution of spheroids is also a key factor.

When the spheroids with diameters of 200 μm are 50 μm away from each other, β_{Bm} was 0.736 and β_{Hpx} was 0.176, meaning that 8.8% of the total number of cells are exposed to hyperoxia. Increasing the intra-spheroid spacing to 100 μm caused β_{Hpx} to drop to zero, while also slightly increasing β_{Bm} to 0.772 and higher number of cells were hyperoxic.

Having almost the same total number of cells in the form of 300 μm spheroids with a spacing of 300 μm , all the cells were above the minimum DOC values in vivo ($\beta_{\text{Hpx}}=0$), while β_{Bm} was 0.765. In case of having 99 spheroids 300 μm in diameter, the minimum spacing required was 700 μm , resulting in higher β_{Bm} of 0.808 with zero hypoxia.

Having a cellular monolayer is a completely different scenario. When having the same total number of cells as in 99 spheroids 200 μm in diameter, both β_{Bm} and β_{Hpx} are zero, thus all the cells are exposed to hyperoxic conditions. But with higher number of cells fully covering the bottom of the well, all the cells are just above the minimum DOC value in vivo ($\beta_{\text{Bm}}=1$), although a very small portion of the physiological DOC range is covered (43.2-44.2 $\mu\text{mol/L}$).

Doubling the culture medium to 2ml was found to reduce DOC values within the spheroids, increasing hypoxia and reducing hyperoxia. For 200 μm spheroids (100 μm spacing), β_{Bm} increased to 0.856 and β_{Hpx} increased to 0.088, while for 300 μm spheroids (700 μm spacing) β_{Bm} drops to 0.177 and β_{Hpx} increases to 0.812.

In batch systems, accumulation of catabolites during the culture period can potentially affect the cells. Using the model enables us to evaluate the catabolite concentrations at the cellular periphery. Knowing the safe concentrations of catabolites that do not adversely affect the cells, as well as the glucose uptake rate is crucial to decide when the medium needs to be changed.

3.5 Conclusions

In this chapter, oxygen transfer to cells in semi-batch systems was studied in spheroids (3D culture) and cellular monolayers (2D culture). Aside from the size of the spheroid, their arrangement and

the height of culture medium – i.e. the diffusive length between the gas-liquid interfacial boundary and the cells – were also found highly influential. The trend and extent of the observed oxygen concentration profile in a monolayer was found to be quite different compared to the spheroids.

It is noteworthy to mention that a relatively low oxygen uptake rate was considered here, as reported for HepG2 cell line. Using primary hepatocytes with higher oxygen uptake rate will further exacerbate the shortcomings in static systems.

The simple model herewith presented enabled us to evaluate oxygen and urea concentrations at the cellular periphery. It also illustrates the necessity of having well-designed perfused systems. For simplicity, the spheroids were assumed to remain in an organized arrangement with fixed, equal spacing between them. Needless to say, such organization cannot be established experimentally. Plus, if the spacing is removed, the adjacent spheroids can merge to form larger spheroids leading eventually to hypoxia and cell necrosis. Consequently, an efficient, dynamic system should be employed in order to supply sufficient oxygen to temporally varying 3-D culture systems and establish full physiological DOC range.

References

- [1] E. Curcio, A. Piscioneri, S. Morelli, S. Salerno, P. Macchiarini, and L. De Bartolo, "Kinetics of oxygen uptake by cells potentially used in a tissue engineered trachea," *Biomaterials*, vol. 35, pp. 6829-37, Aug 2014.
- [2] P. Hay, A. Veitch, M. Smith, R. Cousins, and J. Gaylor, "Oxygen Transfer in a Diffusion-Limited Hollow Fiber Bioartificial Liver," *Artificial organs*, vol. 24, pp. 278-288, 2000.
- [3] J. F. Patzer, 2nd, "Oxygen consumption in a hollow fiber bioartificial liver--revisited," *Artif Organs*, vol. 28, pp. 83-98, Jan 2004.
- [4] K. Vafai, *Handbook of porous media*: Crc Press, 2015.
- [5] J. L. Dulong and C. Legallais, "A theoretical study of oxygen transfer including cell necrosis for the design of a bioartificial pancreas," *Biotechnol Bioeng*, vol. 96, pp. 990-8, Apr 1 2007.
- [6] A. Dash, W. Inman, K. Hoffmaster, S. Sevidal, J. Kelly, R. S. Obach, *et al.*, "Liver tissue engineering in the evaluation of drug safety," *Expert opinion on drug metabolism & toxicology*, vol. 5, pp. 1159-1174, 2009.

Chapter 4

Mass transfer model for hollow fiber membrane bioreactors

4.1 Introduction

Computational modelling has increasingly been employed to analyze the transport phenomena inside the bioreactor, to evaluate the cellular microenvironment and to optimize the operational conditions [1]. HFMBRs generally consist of a module packed with straight hollow fibers and the isolated cells are seeded in the extra-capillary space (ECS), either forming a cellular layer on the outer wall of the hollow fiber wall or completely filling the ECS.

Mathematical models for fluid motion between a capillary and the surrounding tissue has long been studied [2]. In majority of the modelling studies, the membranes and the cellular compartment are considered as a porous medium, and HFMBRs are described by Krogh cylinder approach, which was originally introduced to describe oxygen supply from blood vessels to tissues [3]. This approach has been employed for decades now [4] to model hollow fibers used for different applications and under different operating modes, a good review of which is given by Brotherton et al. [5].

Several modelling studies have been reported for HFMBRs for different applications and conditions, including diffusion-controlled [6-8] and convection-enhanced [9-13] systems, considering multi-component interactions [14] or study of hydrodynamics in different operating modes [15]. Very well-explained development of the model, including non-dimensionalization and analytical solution for simplified cases is given by Shipley et al. [16, 17].

4.2 Mathematical model

Partial differential equations (PDE) of continuity and momentum balance customized for each domain (compartment) are coupled between domains through interfacial boundary conditions. Conservation of mass for incompressible fluids reveals:

$$\nabla \cdot \bar{u}_i = 0 \tag{4.1}$$

The subscript i refers to the bioreactor compartment as the computational domain: lumen (l), membrane (m), cellular compartment (cc), and extra-capillary space (ecs). The equation of motion in the free flow regions – i.e., the lumina and parts of the ECS – is described by the Navier-Stokes equation:

$$\rho_f \frac{\partial \bar{u}_i}{\partial t} = -\rho_f (\bar{u}_i \cdot \nabla) \bar{u}_i + \mu_f \nabla^2 \bar{u}_i - \nabla p_i \quad (4.2)$$

HF membranes and the spheroids are considered as uniform, isotropic porous media. The fluid transport in the porous media – i.e., membranes and cellular compartment – is described by Brinkman equation,

$$\rho_f \frac{\partial \bar{u}_i}{\partial t} = -\rho_f (\bar{u}_i \cdot \nabla) \bar{u}_i + \mu_e \nabla^2 \bar{u}_i - \nabla p_i - \frac{\mu_f}{K_{br_i}} \bar{u}_i \quad (4.3)$$

μ_e , effective viscosity in the porous medium, is generally considered either equal to μ_f or, as implemented in COMSOL, defined as a function of μ_f and porosity. Species material balance for each component in the free fluid regions yields:

$$\frac{\partial c_{j,i}}{\partial t} = -\nabla \cdot (c_{j,i} \bar{u}_i) + \nabla \cdot (D_{j,i} \nabla c_{j,i}) \quad (4.4)$$

The subscript j refers to the molecule of interest. Mass balance in the porous media is described by Eq. 4.5:

$$\frac{\partial c_{j,i}}{\partial t} = -\nabla \cdot (c_{j,i} \bar{u}_i) + \nabla \cdot (D_{e_{j,i}} \nabla c_{j,i}) + \mathcal{R}_{j,i} \quad (4.5)$$

No reaction term is generally considered to occur in the membrane, thus $\mathcal{R}_{j,m} = 0$. In the cellular compartment, \mathcal{R} is the metabolic rate of consumption or production of the molecule, which depends on the molecule of interest and the cell type. Oxygen uptake rate is generally modeled by Michaelis-Menten kinetics (Eq. 4.6). To the best of author's knowledge, a kinetic rate describing urea synthesis in hepatocytes has not been reported. In this model, the experimental value obtained in our lab was used.

$$\mathcal{R}_{oxygen} = \frac{V_{max} c_{o,cc}}{c_{o,cc} + K_m} \quad (4.6)$$

$$\mathcal{R}_{urea,cc} = 133 \frac{nmol}{h \cdot 10^6 cells} \quad (4.7)$$

$$\mathcal{R}_{j,m} = 0 \quad (4.8)$$

Michaelis-Menten parameters for oxygen uptake in hepatocytes depend on the cell density. In order to make a better comparison with the results reported in the literature for ELAD[®] device [7, 8], oxygen uptake rate can be corrected with respect to the applicable theoretical cell density ($\rho_{cell,model}$) compared to that of reference cell density ($\rho_{cell,ref}$):

$$\mathcal{R}_{o,cc} = (\mathcal{R}_{oxygen})_{ref} \frac{\rho_{cell,model}}{\rho_{cell,ref}} \quad (4.9)$$

where the theoretical cell density within the spheroid is in turn expressed as a function of the porosity of the spheroid (ε_{cc}) and the volume of a single hepatocyte (V_{cell}):

$$\rho_{cell,model} = \frac{1 - \varepsilon_{cc}}{V_{cell}} \quad (4.10)$$

Otherwise, a more general approach can be taken to directly modify V_{max} for hepatocyte spheroids, incorporating the porosity:

$$\mathcal{R}_{o,cc} = (\mathcal{R}_{oxygen})(1 - \varepsilon_{cc}) \quad (4.11)$$

Effective diffusion coefficient of component j within the porous medium i is generally related to the diffusion coefficient in the liquid phase,

$$D_{e,j,i} = \frac{\varepsilon_i}{\tau_i} D_{j,aq} \quad (4.12)$$

Several correlations have been reported which relate tortuosity to the porosity of the medium. Here, Bruggeman equation (Eq. 13) was used for the tortuosity of the cellular compartment for $\varepsilon_{cc} > 0.2$ [18], and Wakao-Smith equation (Eq. 14) for tortuosity of the polymeric hollow fiber membrane [19] :

$$\tau_{cc} = \frac{1}{\varepsilon_{cc}^{0.5}} \quad (4.13)$$

$$\tau_m = \frac{1}{\varepsilon_m} \quad (4.14)$$

Permeability of the cellular compartment was approximated through Carman-Kozeny model considering a mass of hepatocytes as a bed of spheres with a diameter of $d_{hep}=16\mu\text{m}$ [17],

$$K_{br\,cc} = \frac{\varepsilon_{cc}^3 d_{hep}^2}{180 (1 - \varepsilon_{cc})^2} \quad (4.15)$$

The pure-water permeability model in polymeric membranes suggested by Merdaw was adopted [19]. This semi-empirical model is in fact a combination of the solution diffusion (first term in Eq. 11) and pore flow (second term in Eq. 11) models.

$$K_{br\,m} = \frac{D_{water} M_{water}}{\rho_f R_g T \delta_m} \varepsilon_m^2 + \frac{d_{mp}^2}{11.25 \mu_f \delta_m} \frac{\varepsilon_m^3}{(1 - \varepsilon_m)^2} \quad (4.16)$$

According to the process flow of the bioreactor, the system can be considered to reach steady-state in terms of velocity field and oxygen concentration profile, assuming (i) efficient oxygenation, so that the oxygen concentration at bioreactor's inlet is the saturation concentration, (ii) negligible temporal changes in the properties of the fluid and porous media. Consequently:

$$\frac{\partial \bar{u}_i}{\partial t} = 0 \quad (4.17)$$

$$\frac{\partial c_{O,i}}{\partial t} = 0$$

However, the system resembles a batch system in terms of the other nutrients and cellular products, due to their continuous depletion and accumulation respectively. Therefore, the urea concentration profile is indeed a time-dependent study.

4.3 Geometry and boundary conditions

Generally speaking, equation of motion in each domain, along with the equation of continuity (Eq. 4.1), are then coupled through continuity of the normal components of stress and velocity applied at interfacial boundaries. Concentration of the same species in different domains are also coupled through continuity of concentration and flux at interfacial boundaries. Other boundary conditions are applied in accord with the geometry and the assumptions used.

To decrease the computational complexity of the model, two different approaches were taken:

- (i) **Single-spheroid model:** a periodic/symmetric unit cell was chosen within the bioreactor to locally represent the system.
- (ii) **Miniaturized bioreactor:** a method is developed to scale down the bioreactor in an attempt to predict bioreactor's performance. Here only the geometry and boundary conditions are discussed; the scaling down method is explained in Chapter 7.

The basis of calculations is the bioreactor assembly in our lab, consisting of 100 hollow fibers per bundle in a 10×10 arrangement and an active length of 34mm. The flowrate values herewith reported are in fact at the inlet of the bioreactor, from which the inlet into and out of the element are calculated and used in the model.

In this bioreactor, one bundle provides oxygenated culture medium to the bioreactor (HFs along x-direction in Figure 4. 1) while the other bundle removes the medium from the bioreactor (HFs along y-direction in Figure 4. 1). In the experiments with hepatocyte spheroids, both bundles consisted of commercial polyethersulfone hollow fibers (MicroPES®, 3M Deutschland GmbH, Germany), which limit the adhesion of hepatocytes that could result in disintegration of the spheroids.

4.3.1 Single-spheroid model

The geometry for this model is demonstrated in Figure 4. 1. Considering the hollow fiber length inside the bioreactor (~34mm) and the size of this element (750×750×500 μm), the hollow fibers in each bundle are divided into 45 elements.

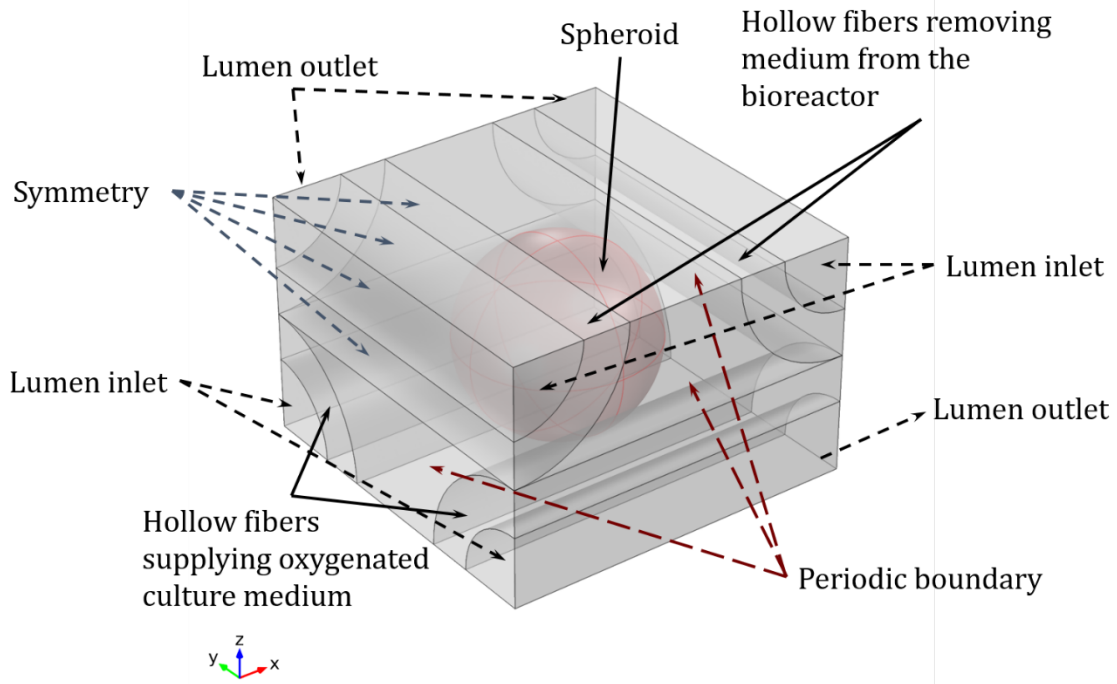


Figure 4. 1 Single-spheroid model: periodic unit element ($750 \times 750 \times 500 \mu\text{m}$) representative of the bioreactor configuration.

In order to properly address the axial and radial fluid flow in the lumina, and correctly apply the permeation flux through the hollow fibers, the permeation rate of the culture medium into and out of the HFs is assumed to be uniform along the HFs. This was experimentally verified by observing zero or negligible pressure drop in the HF lumen thanks to low permeation rate and short HF length in the bioreactor. Consequently, luminal flow rate along the bioreactor is assumed to decrease uniformly from the inlet condition to zero at the closed end. In the model, the luminal inlets and outlets are carefully inserted according to the location of the element in the bioreactor, assuring uniform radial flux through the membrane wall along the hollow fiber length. For the luminal inlets and outlets, laminar inflow and outflow (average velocity) boundary conditions were applied, as following:

$$U_{in,supply} = \left(1 - (n_{spl} - 1) \frac{l_{mnt}}{L_{BR}}\right) U_{avg} \quad (4.18)$$

$$U_{out,supply} = \left(1 - n_{spl} \frac{l_{mnt}}{L_{BR}}\right) U_{avg} \quad (4.19)$$

$$U_{in,removal} = (n_{rmv} - 1) \frac{l_{lmnt}}{L_{BR}} U_{avg} \quad (4.20)$$

$$U_{out,removal} = n_{rmv} \frac{l_{lmnt}}{L_{BR}} U_{avg} \quad (4.21)$$

in which $U_{in,supply}$ and $U_{out,supply}$ are the average inlet and outlet luminal velocity for each element along the hollow fibers in the supplying bundle, respectively. Similarly, $U_{in,removal}$ and $U_{out,removal}$ are the average inlet and outlet luminal velocity for each element along the hollow fibers in the removing bundle. n_{spl} and n_{rmv} are the number (location) of the element along the hollow fiber in the supplying and removing bundles, respectively. l_{lmnt} is the HF length in the element (750 μ m), L_{BR} is the HF length in the bioreactor (~34mm), and U_{avg} is the average inlet velocity into each HF of the bioreactor (perfusion rate divided by total number of HF in the bundle, divided by luminal cross-section area).

Using only average velocities as the boundary conditions without introducing pressure conditions causes the solution fail to converge. Additionally, in the experiments the ECS pressure is kept atmospheric. This condition is realized in the model by introducing pressure point constraints with atmospheric pressure in ECS or on the spheroid surface.

Using the element approach introduces virtual boundaries in ECS, for which periodic conditions are used in COMSOL to define periodicity. Periodic condition is also applied to the cross-sections of the membrane at the inlets and outlets. Finally, symmetry boundary condition is applied to the cross-section of the lumina and membranes along the axis. The periodic and symmetric boundaries are shown in Figure 4. 1.

4.3.2 Miniaturized bioreactor

The geometry for this model is presented in Figure 4. 2. The boundary conditions in this case depend on the operational mode. When one bundle (along x-direction) is supplying and one bundle (along y-direction) is removing the culture medium, the connection at the bottom of the bioreactor and the inlet of the removing bundle are closed (no-flux). Laminar inflow and outflow boundary conditions (average velocity) are applied to the luminal inlets and outlets. They are calculated in such a way that the (radial) permeation flux through the hollow fiber is the same as in the experiments performed by other colleagues in our lab.

Average velocities at the inlet of the supply bundle and the outlet of the removing bundle is the perfusion rate multiplied by the scale ratio (diameter of the scaled-down bioreactor to that of the real bioreactor) divided by total number of HF in the bundle, divided by luminal cross-section area. If a retentate flow is considered for the supplying bundle, the inlet and outlet velocities are calculated accordingly.

Additionally, if both bundles supply or both remove the medium to/from the bioreactor, the boundary condition for the bottom connection of the bioreactor is considered as laminar outflow/inflow, and the velocities are applied accordingly.

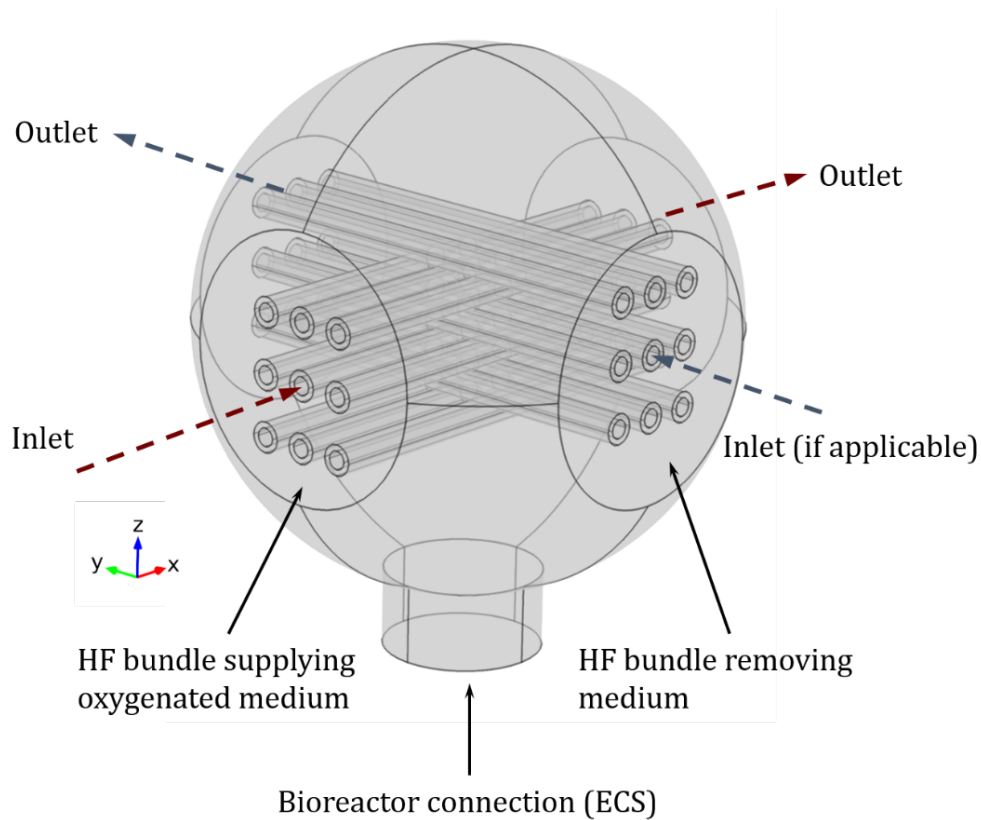


Figure 4. 2 Miniaturized bioreactor model considering 9 hollow fibers in each bundle, hosting 20 spheroids in a 4×4×5 arrangement in the extra-capillary space.

4.4 Implementation in COMSOL Multiphysics

The COMSOL model consists of two types of physics: “Free and Porous Media Flow” for the fluid dynamics and “Transport of Diluted Species” for mass transfer. The physics are applied to all domains of the geometries and are solved simultaneously. “Free and Porous Media Flow”, is

under the fluid flow branch of the Chemical Reaction Engineering Module in COMSOL Multiphysics. As the name suggests, it is developed for fluid flow in geometries containing both porous and free liquid domains. “Transport of Diluted Species” is under chemical species transport branch of the same module. Stationary (steady-state) study type is used for oxygen models, while urea transport is investigated using time-dependent study, both fully coupled. Direct PARDISO solver type was used throughout this study. This configuration of solver is more robust, but it also needs more memory. Using segregated and iterative solver uses less memory thus more affordable, but it is not as robust and convergence problems were often observed.

4.5 Results

The purpose of this chapter is to explain the developed model and the some aspects of the numerical analysis. The detailed results for different cases are thoroughly discussed in the following chapters. Therefore, only some of the relevant and illustrative data from the numerical analysis are herewith explained.

4.5.1 Dependent variables

The dependent variables solved for in the latter physics are velocity (u) and pressure (p), and for the latter is concentration (c). These variables, as well as other derived variables such as dimensionless numbers can then be plotted and studied in the whole geometry or in each individual domain (compartment). As an example, the profiles of the three dependent variables are illustrated in Figure 4. 3.

4.5.2 Mesh sensitivity

Selection of the optimum mesh size is a critical part of the modelling study. Reducing the mesh size increases the accuracy of the solution. On the other hand, it means higher degrees of freedom (DoF) solved for, increasing the computational cost of the process, i.e. the need for stronger processors, higher memory and of longer solution time. Too fine mesh sizes can also compromise the convergence of the solution. Generally, a mesh convergence approach is recommended in which the mesh size is gradually reduced until no significant difference in the obtained results is observed. This obviously depends on the hardware specifications available for the computational work as well.

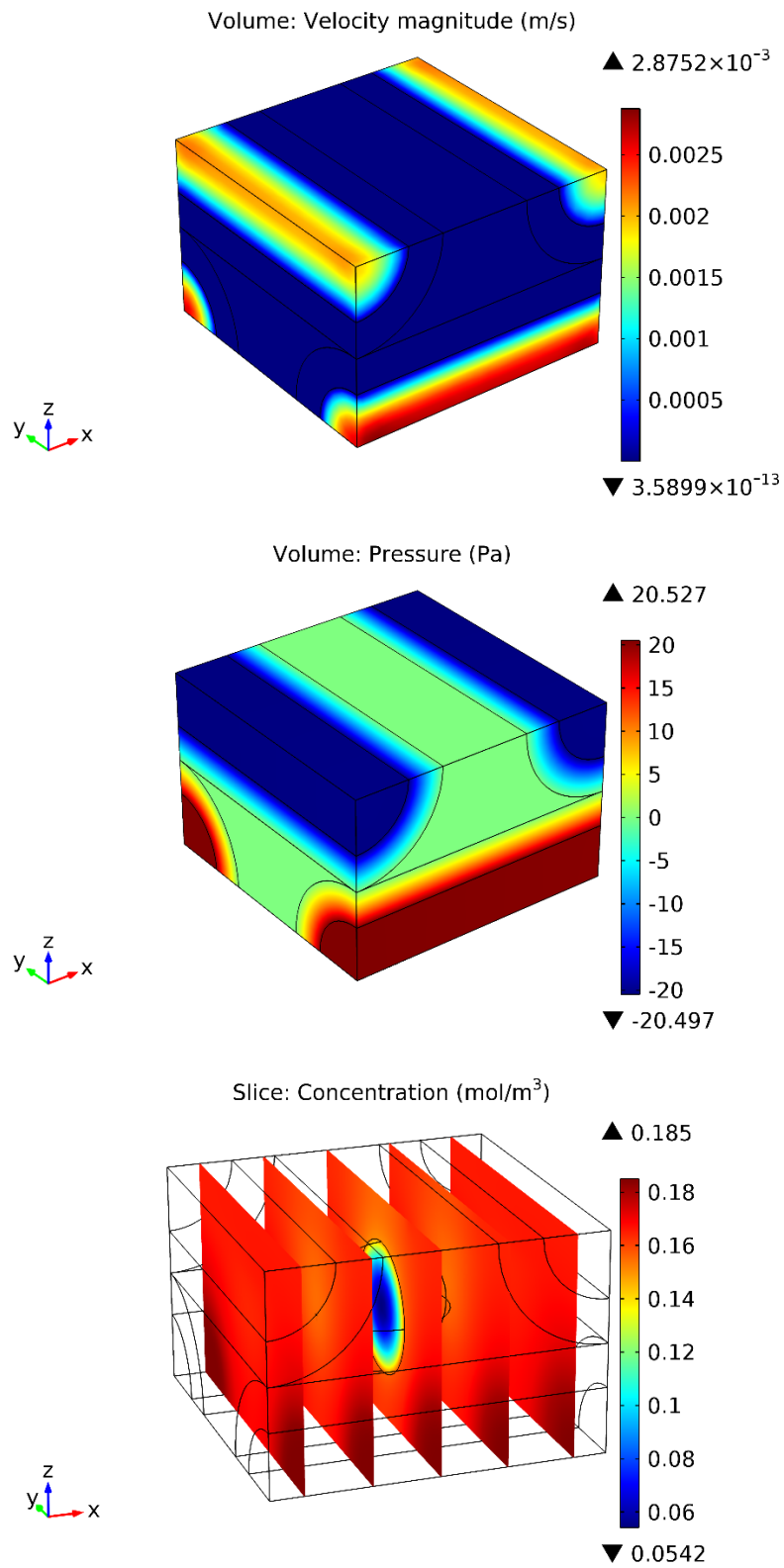


Figure 4. 3 Velocity (top), pressure (center) and concentration (bottom) profiles in the single-spheroid model.

Here, different mesh sizes as physics-controlled defaults provided by COMSOL Multiphysics software were selected and the concentration profile inside the spheroid was monitored. The grid sizes for the single-spheroid model are herewith presented in the format Name (minimum-maximum grid size, DoF), and include: Coarser (24.5-79.6 μm , 16000), Coarse (18.4-61.2 μm , 29000), Normal (12.2-41 μm , 82000), Fine (6.1-32.5 μm , 188000), Finer (2.45-22.7 μm , 630000), Extra fine (0.9-14.1 μm , 2352000).

As illustrated in Figure 4. 4, the results strongly depend on the mesh size. Considering these results and the computational limitations, “Fine” (Figure 4. 4-d) or “Finer” (Figure 4. 4-e) mesh sizes were mostly used for the single-spheroid model. Changing the grid to “extra fine” (Figure 4. 4-f) changed the results by only %3 at most, while increasing the computational time more than 10 times and in some cases even failing to converge. Computational work for the miniaturized bioreactor model is a lot heavier, therefore they could only be carried out for “Normal” or “Fine” grid sizes.

4.5.3 Extended element: model validity

The periodic unit cell previously described was extended to include 36 spheroids ($3\times 3\times 4$) in order to evaluate the validity of the model and to see whether a single element can act as a building block for larger scales. The dissolved oxygen concentration profile inside the spheroids is illustrated in Figure 4. 5, which is similar to that of a single element in Figure 4. 4-e.

4.6 Discussion

The partial differential equations describing momentum and mass transfer (Eqs. 4.1-4.5) are well-known and already established. The challenging part is application of these equations by using a well-defined geometry and boundary conditions, and accurate measurement or estimation of the properties. The latter was accomplished during the course of study through parametrization and implementation of correlations most suitable and in accord with the experimental findings. The finalized model runs smoothly and can be applied to any membrane-based bioreactor.

One common problem often faced during the numerical computations was getting negative concentration values, mostly when there is a reaction term. No real definitive answer has been given to tackle this issue other than general recommendations, especially since it depends on the

Oxygen Concentration (mol/m^3)

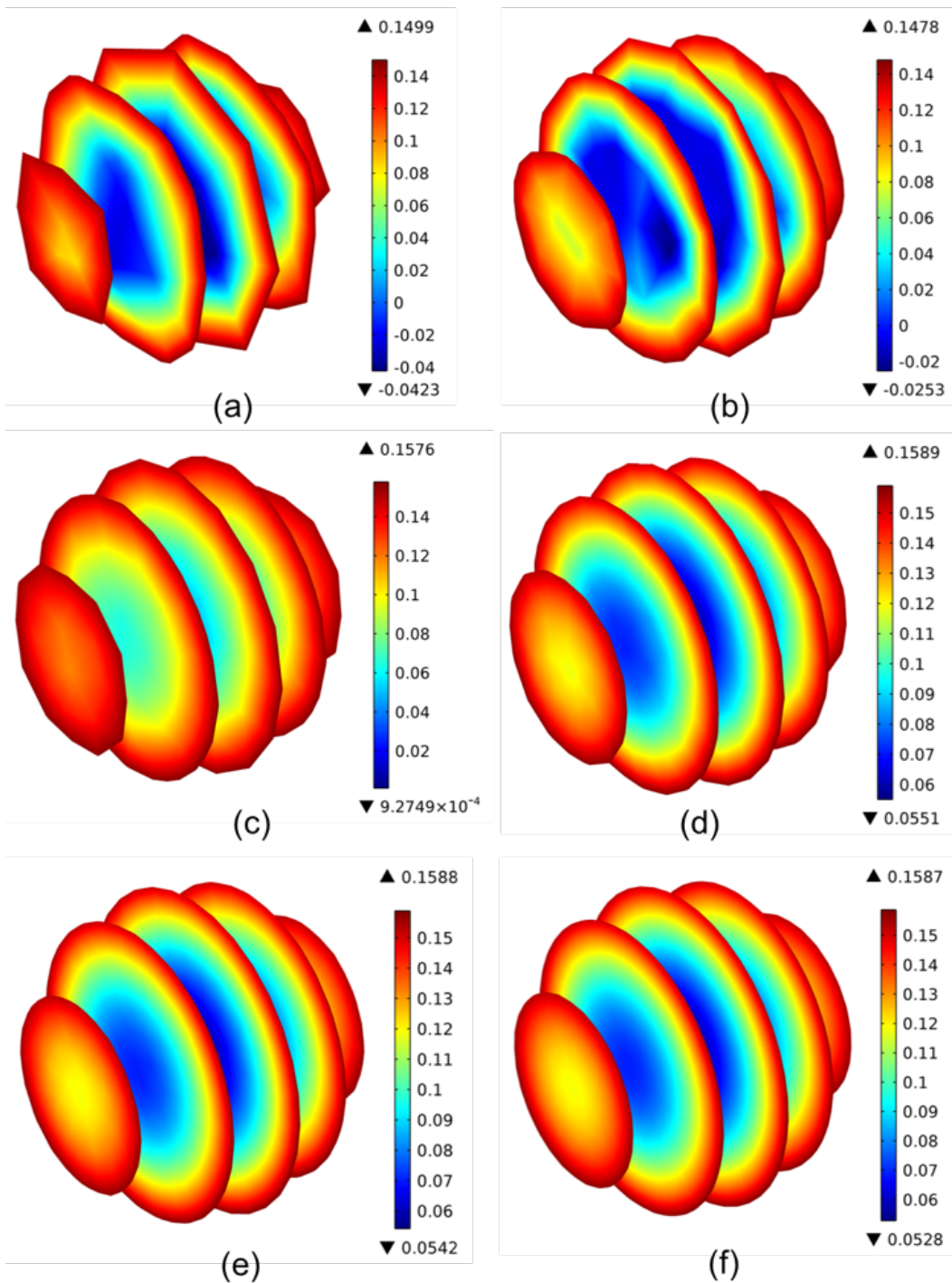


Figure 4. 4 Dissolved oxygen concentration inside the spheroids in single-spheroid model obtained by using different physics-controlled default mesh sizes in COMSOL Multiphysics. (a) Coarser, (b) Coarse, (c) Normal, (d) Fine, (e) Finer, (f) Extra fine.

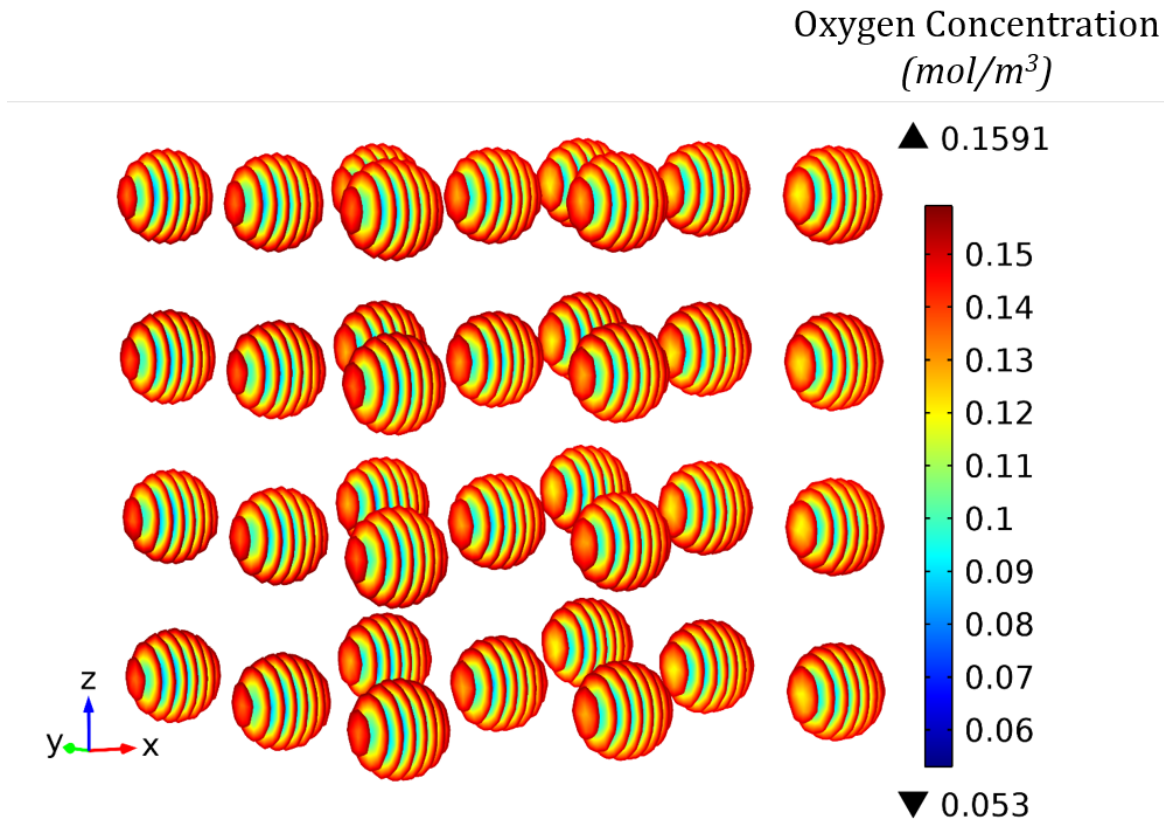


Figure 4. 5 Extended periodic unit element consisting of 36 spheroids

system under investigation. One option suggested by COMSOL is using logarithmic transform to avoid the possibility of negative concentrations. This solution was not tried as it can potentially cause instabilities for our system.

Different tactics were tried out to resolve the negative concentration issue, which can be summarized into the following rules of thumb:

- If the negative concentrations are observed in a minor part of the domain with inappreciable magnitudes ($\sim 10^{-5} - 10^{-6} \text{ mol/m}^3$), the problem is most likely accuracy-related and it may be solved by using a smaller relative tolerance for the error.
- If the magnitude of the negative concentrations is significant ($\sim 10^{-3} - 10^{-4} \text{ mol/m}^3$) then a finer grid must be applied, as can be seen in Figure 4. 4.
- If the concentration values are very significantly negative ($\sim 10^{-2} - 10^{-3} \text{ mol/m}^3$) in a considerable part of the domain and using a finer mesh has no effect or even worsens the

situation, then the problem lies within the prepared model. It is important to check all the boundary conditions and properties (values and units). Most effective solution in this case was carefully choosing the initial values so that the numerical solution is carried out in the right direction. Setting the initial concentration in the domain with reaction term (i.e. the spheroid) equal to zero, while in all other domains it is equal to the saturation concentration (used at the inlet) particularly was found to be the optimum option.

The initial values in general should never be overlooked in such computations as accurate initial values contribute to reachable and faster convergence to the right solution. The aforementioned initial value setting for concentration in some cases reduced the computational time by 6 times in miniaturized bioreactor model, compared to using saturated concentration as initial value in all the domains.

4.7 Conclusion

In this chapter, the developed mathematical model and the properties were described, the geometries and boundary conditions applicable to our cross-configuration hollow fiber membrane bioreactor were introduced, and guidelines for model setup in COMSOL Multiphysics were illustrated. The completed model was running smoothly most of the models, although some aspects were modified for some of the cases. The approach herewith explained forms the basis of current study and is used in the following chapters. With minor adjustments, it can also be applied to other membrane-based bioreactors.

References

- [1] E. Curcio, "Mass Transfer and Computational Fluid-dynamics in Bioreactors," in *Biomaterials for Stem Cell Therapy*, ed: CRC Press, 2013, pp. 448-474.
- [2] E. P. Salathe and K.-N. An, "A mathematical analysis of fluid movement across capillary walls," *Microvascular research*, vol. 11, pp. 1-23, 1976.
- [3] A. Krogh, "The number and distribution of capillaries in muscles with calculations of the oxygen pressure head necessary for supplying the tissue," *The Journal of physiology*, vol. 52, pp. 409-415, 1919.
- [4] A. Apelblat, A. Katzir-Katchalsky, and A. Silberberg, "A mathematical analysis of capillary-tissue fluid exchange," *Biorheology*, vol. 11, pp. 1-49, 1974.
- [5] J. D. Brotherton and P. C. Chau, "Modeling of Axial-Flow Hollow Fiber Cell Culture Bioreactors," *Biotechnology progress*, vol. 12, pp. 575-590, 1996.
- [6] H. Ye, D. B. Das, J. T. Triffitt, and Z. Cui, "Modelling nutrient transport in hollow fibre membrane bioreactors for growing three-dimensional bone tissue," *Journal of Membrane Science*, vol. 272, pp. 169-178, 2006.
- [7] P. Hay, A. Veitch, M. Smith, R. Cousins, and J. Gaylor, "Oxygen Transfer in a Diffusion-Limited Hollow Fiber Bioartificial Liver," *Artificial organs*, vol. 24, pp. 278-288, 2000.
- [8] J. F. Patzer, 2nd, "Oxygen consumption in a hollow fiber bioartificial liver--revisited," *Artif Organs*, vol. 28, pp. 83-98, Jan 2004.
- [9] P. Hay, A. Veitch, and J. Gaylor, "Oxygen Transfer in a Convection-Enhanced Hollow Fiber Bioartificial Liver," *Artificial organs*, vol. 25, pp. 119-130, 2001.
- [10] I. E. De Napoli, E. M. Zanetti, G. Fragomeni, E. Giuzio, A. L. Audenino, and G. Catapano, "Transport modeling of convection-enhanced hollow fiber membrane bioreactors for therapeutic applications," *Journal of Membrane Science*, vol. 471, pp. 347-361, 2014.
- [11] E. Curcio, L. De Bartolo, G. Barbieri, M. Rende, L. Giorno, S. Morelli, *et al.*, "Diffusive and convective transport through hollow fiber membranes for liver cell culture," *Journal of biotechnology*, vol. 117, pp. 309-321, 2005.
- [12] Y. Moussy, "Convective flow through a hollow fiber bioartificial liver," *Artif Organs*, vol. 27, pp. 1041-9, Nov 2003.
- [13] L. J. Kelsey, M. R. Pillarella, and A. L. Zydney, "Theoretical analysis of convective flow profiles in a hollow-fiber membrane bioreactor," *Chemical Engineering Science*, vol. 45, pp. 3211-3220, 1990.
- [14] N. Abdullah and D. Das, "Modelling nutrient transport in hollow fibre membrane bioreactor for growing bone tissue with consideration of multi-component interactions," *Chemical Engineering Science*, vol. 62, pp. 5821-5839, 2007.
- [15] W. Bruining, "A general description of flows and pressures in hollow fiber membrane modules," *Chemical Engineering Science*, vol. 44, pp. 1441-1447, 1989.
- [16] R. J. Shipley, A. J. Davidson, K. Chan, J. B. Chaudhuri, S. L. Waters, and M. J. Ellis, "A strategy to determine operating parameters in tissue engineering hollow fiber bioreactors," *Biotechnol Bioeng*, vol. 108, pp. 1450-61, Jun 2011.

- [17] R. J. Shipley and S. L. Waters, "Fluid and mass transport modelling to drive the design of cell-packed hollow fibre bioreactors for tissue engineering applications," *Math Med Biol*, vol. 29, pp. 329-59, Dec 2012.
- [18] K. Vafai, *Handbook of Porous Media*: CRC Press, 2005.
- [19] A. A. Merdaw, A. O. Sharif, and G. A. W. Derwish, "Water permeability in polymeric membranes, Part I," *Desalination*, vol. 260, pp. 180-192, 9/30/ 2010.

Chapter 5

Effect of different parameters on oxygen transport

5.1 Introduction

Despite the common use of HFMBRs and extensive modelling studies performed, some vital properties and parameters seem to be overlooked or underestimated. Effective diffusion coefficient, permeability and even oxygen uptake rate in the spheroids are quite challenging to measure and are often estimated. However, their dependency on intra-spheroid porosity – the exact value of which is also often unknown and is therefore estimated – is either neglected or minimally reported in the models. Additionally, the porosity of spheroids and membranes are subject to temporal change, due to rearrangement of cells and adsorption of proteins, respectively. The spheroids are observed to shrink in size and become more compact during the culture time [1], which in turn changes their microstructure and porosity in an uncontrolled manner leading to compromised transport properties. The effect of this phenomenon on oxygen transport into the spheroids is not properly addressed. On the other hand, occlusion of pores in the membrane due to proteins, cell debris and other culture components also changes their porosity and consequently their transport properties.

In this chapter, the effect of different parameters on oxygen transfer to hepatocyte spheroids cultured in a previously developed crossed-configuration HFMBR is investigated. Due to the geometry of the bioreactor, the conventional Krogh cylinder approach is not applicable. The decisive parameters influencing oxygen transfer in porous media (i.e. spheroids and membranes) are expressed as a function of porosity. The mathematical model along with the boundary conditions are applied to an element representative of the spheroid's microenvironment. First, a systematic parametric study is carried out to evaluate the effect of different parameters on oxygen transfer: operational parameters (oxygen tension, perfusion rate), design parameters (hollow fiber spacing, spheroid size), kinetic parameters (Michaelis-Menten kinetics for oxygen uptake) and microstructural properties (porosities of the spheroid and the membrane).

5.2 Materials and methods

The parametric study was performed for the crossed HFMBR introduced in Chapter 1, using the single-spheroid model defined in Chapter 4. The described model was numerically solved using COMSOL Multiphysics® (COMSOL Inc., Stockholm, Sweden). First, the effect of different design and operational parameters on bioreactor’s performance was investigated. Each parameter, namely perfusion rate, saturated DOC, intra-spheroid porosity, membrane porosity, V_{\max} and K_m in Michaelis-Menten kinetics, spheroid diameter and inter-HF spacing was changed (or “swept”) individually over an applicable range while the other parameters were maintained at their default values (Table 5. 1). The basis of calculations is the bioreactor assembly in our lab, consisting of 100 hollow fibers per bundle in a 10x10 arrangement and an active length of 34mm. The flowrate values herewith reported are in fact at the inlet of the bioreactor, from which the inlet into and out of the element are calculated and used in the model.

Intra-spheroid DOC range reported by the minimum and maximum DOC values inside the spheroid was used to present the results as a more explicit measure. Further analysis of the data was carried out by using other criteria, including the dimensionless numbers (Table 5. 2) and oxygen transfer rate into the spheroid.

Table 5. 1 Parameters, their default value and the range over which they were investigated in the parametric study.

Parameter	Unit	Default value	Sweep range
Saturated oxygen concentration, $C_{o,sat}$	$\mu\text{mol/L}$	185	100 – 250
Perfusion rate, Q_{BR}	ml/min	1	0.1 – 2.70
Spheroid diameter, D_{sph}	μm	300	100 – 400
Inter-hollow-fiber spacing, δ_{HF}	μm	250	150 – 300
Maximum consumption rate (Michaelis-Menten), V_{\max}	$\text{nmol}/(\text{s}\cdot\text{cm}^3)$	5	5 – 20
Concentration associated with $V_{\max}/2$ (Michaelis-Menten), K_m	mm Hg	5.6	0.5 and 5.6
Intra-spheroid porosity, ϵ_{cc}	-	0.2	0.15 – 0.80
Membrane porosity, ϵ_m	-	0.7	0.15 – 0.90

The microstructural properties in porous media (ϵ_{cc} , ϵ_m) govern the transport phenomena in the respective medium, evidenced by the dependence of effective diffusion coefficient (Eq. 4.12) and

permeability (Eqs. 4.15-4.16) on the porosities. However, there is limited information about the porosity of an in vitro hepatic mass. Evaluation of ε_{cc} in a cell culture is quite challenging. Additionally, ε_{cc} is subject to temporal changes as the cells rearrange during the culture time, which in turn alters D_{sph} and ε_{cc} .

Getting a clear idea about practical values for ε_{cc} helps us to better follow the porosity study presented here. We calculated a porosity of 0.42 at the final stage of the spheroid preparation in our lab, which is close to 0.47 reported for ELAD[®] [2]. Several models have been reported for packed beds of monodisperse rigid spheres, covering a range of porosities (void fractions): 0.4764 for thinnest regular packing, 0.44 in very loose random packing, 0.40-0.41 in loose random packing, 0.375-0.391 in poured random packing, 0.359-0.375 in close random packing, and 0.2595 in densest regular packing (hexagonal close pack) [3]. Considering that the cells are not in fact rigid spheres and can fit tight together, porosities lower than 0.26 can be expected. Consequently, current parametric study was performed under three different ε_{cc} values (0.20, 0.35, 0.50) to have a better view over a wider range of culture systems, considering porosity of 0.2 as default value.

Table 5.2 Dimensionless parameters used for evaluation of oxygen transfer in the HFMBR.

Parameter	Definition	Description
Péclet number (ECS domain)	$Pe_{ecs} = \frac{U_{avg} l_{tmnt}}{D_{o,ecs}}$	$\frac{\text{Convective transport rate}}{\text{Diffusive transport rate}}$
Péclet number (intra-spheroid)	$Pe_{cc} = \frac{U_{avg} D_{sph}}{D_{e,o,cc}}$	$\frac{\text{Convective transport rate}}{\text{Diffusive transport rate}}$
Damköhler number	$Da = \frac{V_{max} l_{tmnt}^2}{D_{o,ecs} C_{o,sat}}$	$\frac{\text{Oxygen consumption rate}}{\text{External diffusion rate}}$
Thiele modulus	$\Phi^2 = \frac{\mathcal{R}_{MM}(c_{o,cc}^{SAvg}) R_{sph}^2}{D_{e,sph} c_{o,cc}^{SAvg}}$	$\frac{\text{Characteristic reaction rate at spheroid surface}}{\text{Characteristic diffusion rate}}$
Effectiveness factor	$\eta = \frac{(\mathcal{R}_{MM}(c_{o,cc}))^{vAvg}}{\mathcal{R}_{MM}(c_{o,cc}^{SAvg})}$	$\frac{\text{Averaged actual reaction rate (modelled)}}{\text{Reaction rate at spheroid surface}}$
Biomimicry index	β_{Bm}	$\frac{\text{Spheroid volume with } c_o \text{ within in vivo range}}{\text{Total spheroid volume}}$
Hypoxicity index	β_{Hpx}	$\frac{\text{Spheroid volume with } c_o < \text{in vivo values}}{\text{Total spheroid volume}}$

5.3 Results

The effect of the most important parameters on bioreactor's performance was investigated. Operational parameters ($C_{o,sat}$, Q_{BR}) can readily be altered to optimize the cellular microenvironment. The design parameters (D_{sph} , δ_{HF}) can also be modified in order to improve bioreactor's performance, although controlling D_{sph} is very challenging once they are seeded in the bioreactor due to their shrinking, merging or possibly their disintegration. Kinetic parameters (V_{max} , K_m) on the other hand are intrinsic to the cell type and their phenotypical characteristics, thus not modifiable in a controlled way. Understanding the impact of structural and kinetic parameters provides advantageous predictive measures on the outcome.

Saturated DOC

Oxygen tension inside the incubator is a vital operational condition in cell culture systems, which was studied here in terms of saturated DOC at the inlet of the bioreactor. Intra-spheroid DOC strongly depends on the oxygen tension (Figure 5. 1). In higher porosities, increasing $C_{o,sat}$ by 10 $\mu\text{mol/L}$ (i.e., increasing oxygen tension in the incubator by 1.08%) increases the minimum and maximum DOC values inside the spheroid by almost the same (slightly less) amount. However, such linearity in the rate of change in minimum DOC values at the center of the spheroid seem to be compromised in low spheroid porosities.

Perfusion rate

Perfusion rate – the net permeation rate through the membrane – was studied as the other key operational condition and the modulator of convective transport in ECS. As expected, enhancing convection results in higher oxygen concentrations in ECS and consequently in the spheroid (Figure 5. 2). In fact, the concentrations increase with increasing perfusion rate and the overall concentration difference in each domain remains more or less the same. However, under the studied range of the perfusion rate, the observed changes in concentrations do not exceed %15.

Spheroid diameter

Culturing smaller spheroids minimizes the exposure of cells to hypoxic conditions, considering the short diffusive penetration depth of oxygen in hepatic tissues. Figure 5. 3 shows the expected DOC profile in spheroids of different sizes, further emphasizing the challenge in sufficient oxygen supply to large masses of hepatocytes, especially at low porosities.

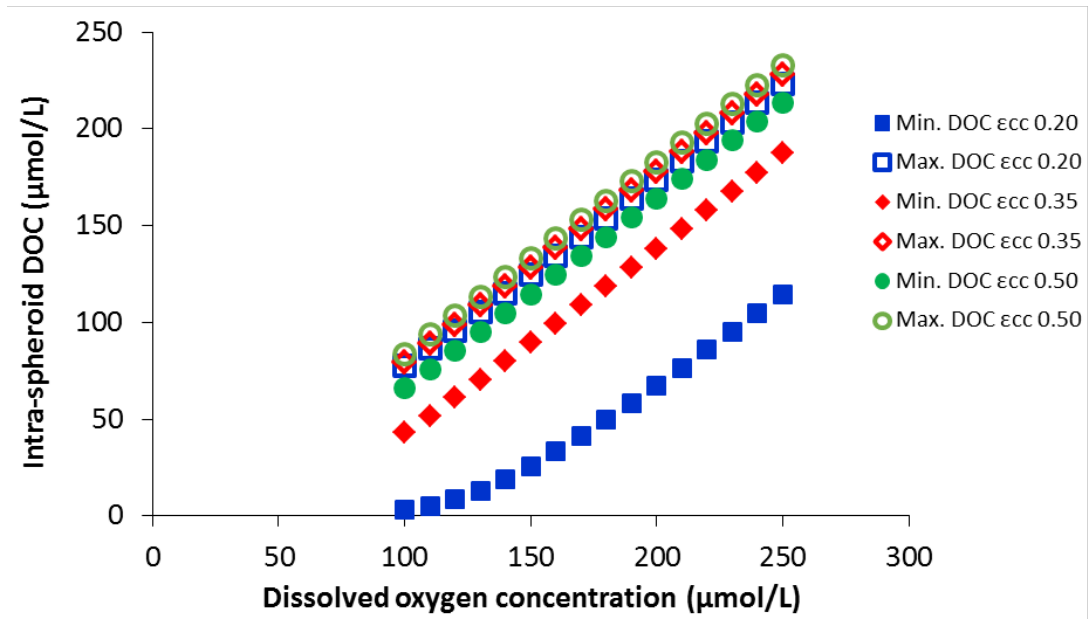


Figure 5.1 Minimum and maximum DOC within the spheroid for different saturated DOCs and spheroid porosities.

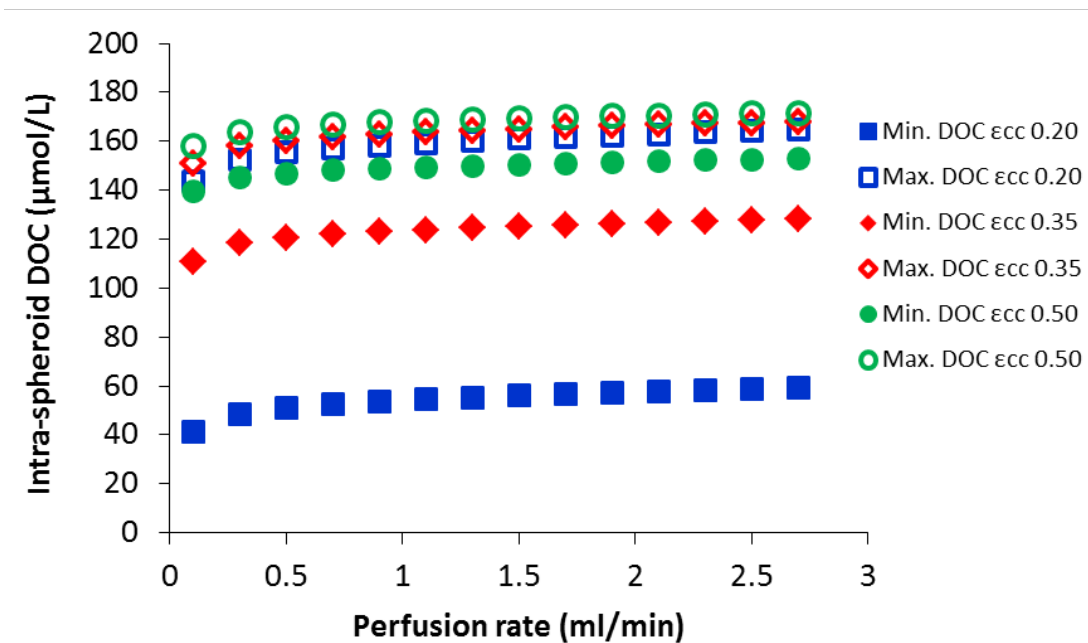


Figure 5.2 Minimum and maximum DOC within the spheroid for different perfusion rates and spheroid porosities.

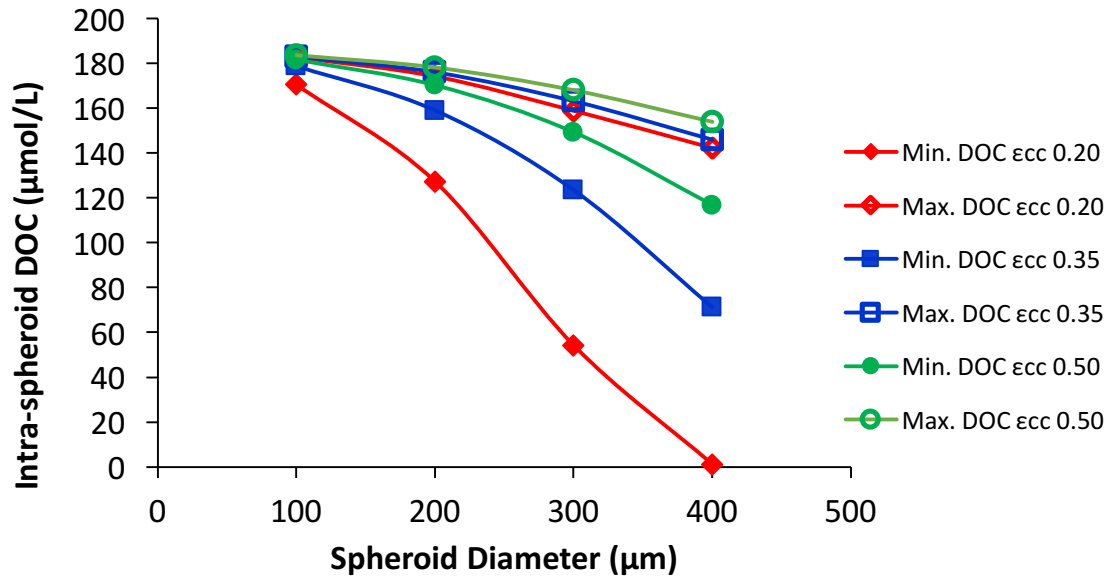


Figure 5. 3 Minimum and maximum DOC within the spheroid for different spheroid diameters and porosities.

HF spacing

The gap between the hollow fibers was studied as a parameter in designing the bioreactor. As illustrated in Figure 5. 4, the DOC profile is not expected to vary when the inter-HF spacing is changed, at least not within the 150-300 μm ranges studied here.

V_m , K_m (Michaelis – Menten kinetics)

Due to the complexity and lack of data on K_m , only the two available values of K_m was studied here (0.5 and 5.6 mm Hg), in accord with Hay [4]. DOC profile inside the spheroid weakly depends on K_m , with dependency decreasing at higher spheroid porosities. Varying K_m from 0.5 to 5.6 mm Hg increases minimum and maximum DOC values in the spheroid by 25% and 1.1% respectively at a porosity of 0.2, while these changes are less than 1% at a porosity of 0.5. The uptake rate and consequently the DOC profile are strongly affected by V_{max} , as illustrated in Figure 5. 5.

Spheroid porosity

Minimum and maximum values of DOC within the spheroid as well as the normal total oxygen transfer rate into the spheroid is studied over a range of spheroid porosities (Figure 5. 6). Higher porosity means less number of cells in a constant volume of spheroid (Eq. 4.10) and therefore less oxygen demand, resulting in reduced oxygen transfer into the spheroid. Additionally, effective

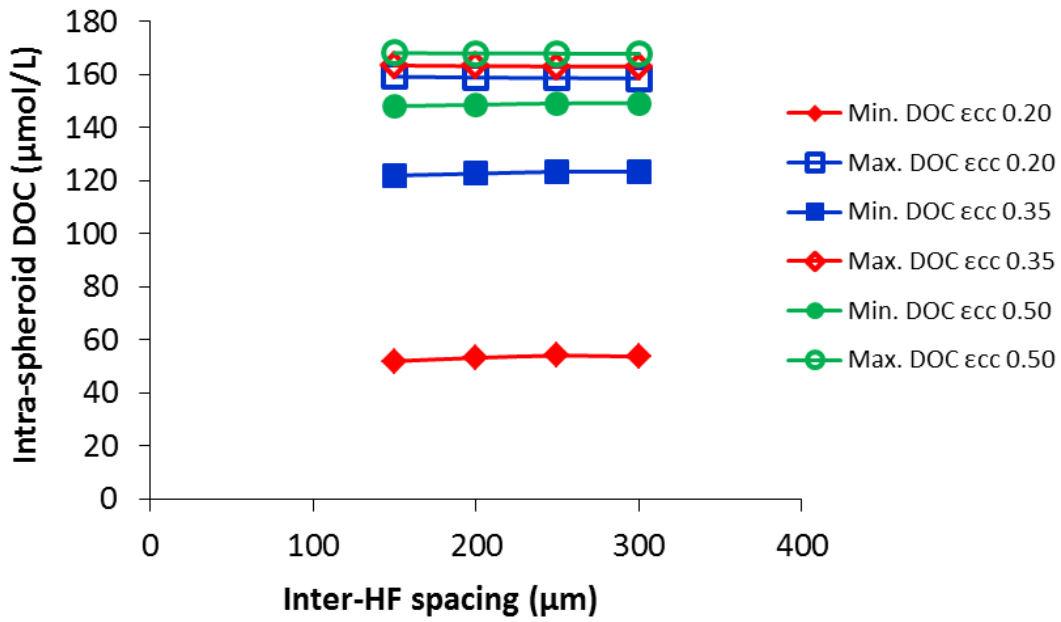


Figure 5. 4 Minimum and maximum DOC within the spheroid for different inter-HF spacing and spheroid porosities.

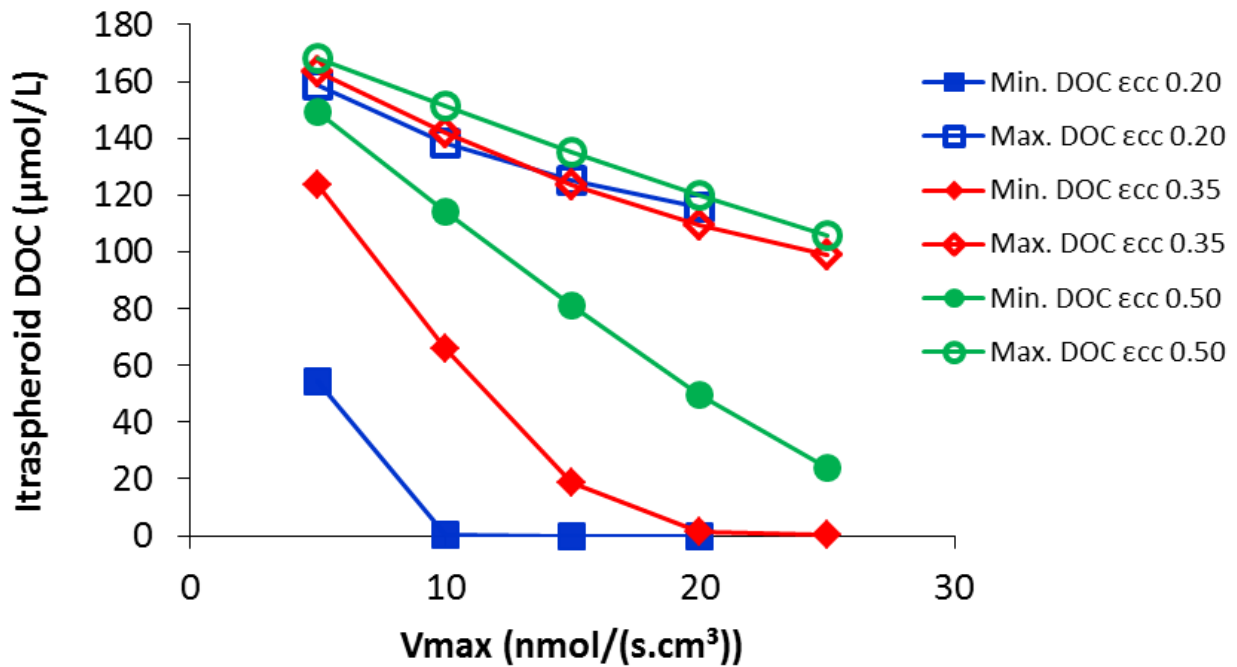


Figure 5. 5 Minimum and maximum DOC within the spheroid for different Vmax and spheroid porosities.

diffusion coefficient increases with increasing porosity (Eqs. 4.12-4.14). With smaller mass transfer resistance and less oxygen consumption, concentration gradient within the spheroid is reduced. Minimum DOC values at the center of the spheroid increase drastically with increasing porosity, while the changes in the maximum values are more moderate.

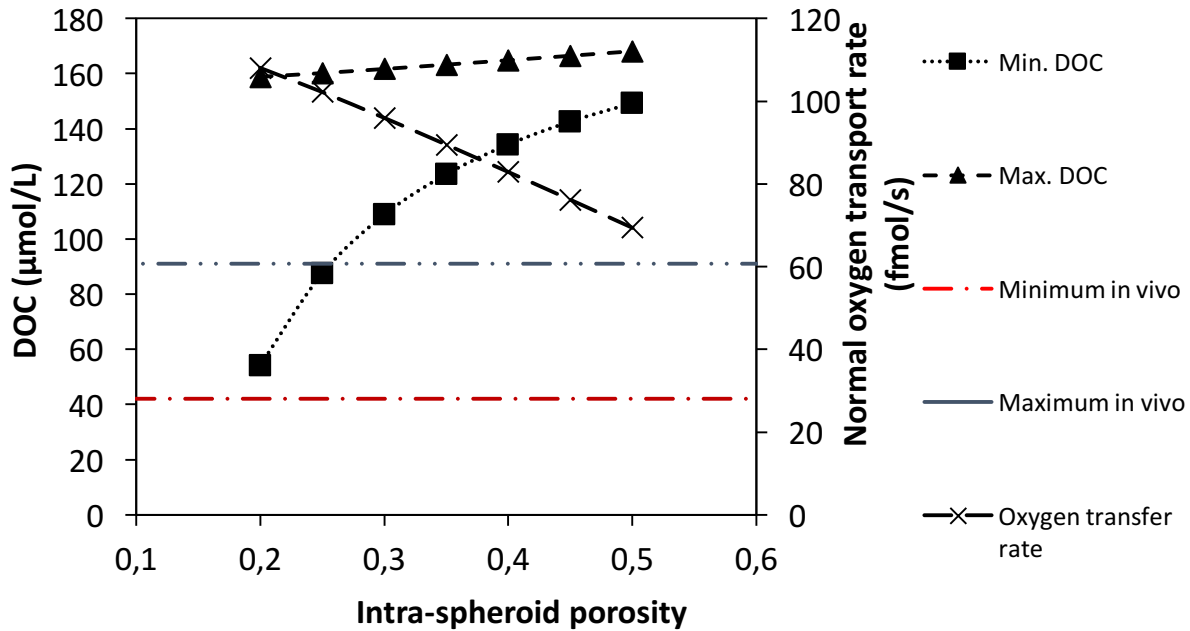


Figure 5. 6 Minimum and maximum DOC within the spheroid, and oxygen transfer rate into the spheroid for different intra-spheroid porosities.

Membrane porosity

As explained above, higher porosity corresponds to lower mass transfer resistance, thus increasing membrane porosity improves oxygen supply to the spheroids, shown by the higher DOC values observed in Figure 5. 7. Additionally, changing ϵ_m affects both minimum and maximum DOC values in quite the same manner. It is important to keep in mind that in this model, changing ϵ_m only influences diffusive transport rate and not the convective rate. Peristaltic pumps are generally used for perfused bioreactors, and they provide a constant volumetric flow rate. Consequently, when using these pumps while blocking one end of the hollow fibers, permeation rate through the membrane remains the same for different membrane porosities. However, the cross-membrane pressure difference – the driving force for fluid flow – and therefore the luminal pressure reduces with increasing ϵ_m , as theoretically expected (Eq. 4.3 and Eq. 4.16). In fact, the cross membrane

pressure difference changes from 16.6 kPa to 1 Pa when changing ϵ_m from 0.15 to 0.9. The default ϵ_m value of 0.7 results in a low pressure difference of 20 Pa.

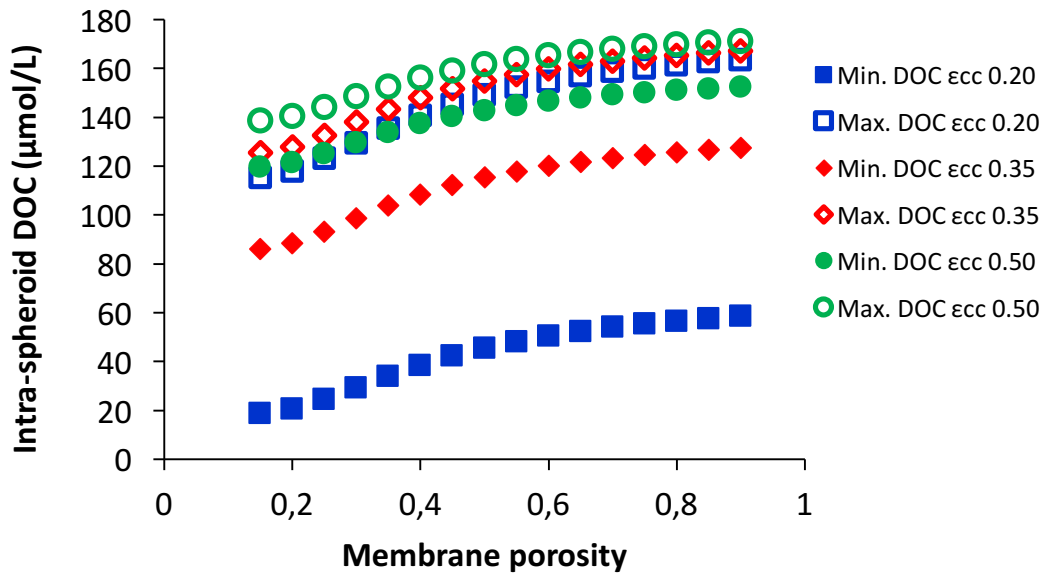


Figure 5. 7 Minimum and maximum DOC within the spheroid for different membrane and spheroid porosities.

5.4 Discussion

Understanding the effect of each influential parameter independent of the others helps us to optimize operational and design conditions of the bioreactor to ensure prolonged functionality of cells. Sufficient oxygen supply depends on numerous factors, including seeded cell density and bioreactor's design aspects, operational conditions, physicochemical properties of the components, and intrinsic biological characteristics. Mass transfer modelling was employed to study the effect of these influential parameters on cellular microenvironment. The concentration profile, especially inside the spheroid, directly elucidates bioreactor's performance under given conditions. Several dimensionless parameters were also derived to better understand which transport mechanism is dominant, which one is limiting, and to what extent they are affected by the parameters under study.

Péclet number compares the rates of transport mechanisms (i.e. convection and diffusion) for oxygen supply to the cells. Pe_{sph} is defined locally for inside the spheroid and it varies under

different conditions, its order of magnitude nonetheless remains between $O(10^{-3})$ to $O(10^{-5})$ throughout this study. Such low values of Pe_{sph} indicates that inside the spheroid, diffusion is the dominant mechanism for oxygen transport. Pe_{ecs} on the other hand is mostly within $O(1)$, which means that convection and diffusion rates are more or less in the same range.

Oxygen uptake rate (consumption) and diffusion rate (supply) are analyzed through Damköhler number and Thiele modulus. The former provides a comparison between oxygen diffusion rate in ECS (from hollow fibers to the spheroid) to the maximum reaction rate V_{max} . Thiele modulus is the ratio between oxygen consumption rate at (mean) DOC value on the surface of the spheroid to the intra-spheroid diffusion rate. Effectiveness factor is another informative parameter generally used in chemical reaction engineering to further illustrate the diffusion-reaction in porous media. η is the mean actual reaction rate (considering the concentration profile due to diffusion) divided by the reaction rate at (mean) DOC value on the surface of the spheroid (i.e., in the absence of any diffusional limitations and thus no concentration profile).

We defined two other parameters as additional criteria in analyzing the suitability of the cellular microenvironment. Biomimicry index was adapted from the approach taken by Dulong et al. in which they defined a necrosed region and a viable region based on the oxygen concentration in islets of Langerhans in a bioartificial pancreas [5]. β_{Bm} here is the fraction of the spheroid exposed to physiological DOC range (42-91 $\mu\text{mol/L}$), thus ideally it should be equal to 1. Exposure to DOC values higher or lower than *in vivo* range does not necessary mean total loss of functionality or viability. β_{Bm} simply discriminates between cells under ideal conditions and cells “at risk”. Hypoxicity is a vital issue to be addressed in *in vitro* cultures, the extent of which was expressed by the hypoxicity index defined as the fraction of the spheroid with $\text{DOC} < 42 \mu\text{mol/L}$. Table 3 shows the dimensionless numbers obtained for the default conditions.

Table 5. 3 Dimensionless numbers for the default values of the parameters under study reported in Table 5. 1.

Pe_{sph}	Pe_{ECS}	Da	Φ^2	η	β_{Bm}	β_{Hpx}	$\frac{\mathcal{R}_{MM}(C_{o,cc}^{vAvg})}{V_{max}}$
4×10^{-5}	0.62	4.47	4.22	0.98	0.22	0	0.93

One of the most controversial parameters in in vitro cell culture systems is the oxygen tension inside the incubator. Even though the majority of studies consider atmospheric conditions (in terms of oxygen partial pressure), higher and lower values have also been reported. Here, the effect of oxygen partial pressure was investigated within the range of 10.8% and 27% and atmospheric oxygen tension was considered as the default value. Exposure of cells to hyperoxicity increases at higher oxygen tensions, better quantified by β_{Bm} which drops from 0.51 at $\epsilon_{cc}=0.2$ and 0.99 at $\epsilon_{cc}=0.35$ and 0.5 to zero. Higher oxygen supply arising from elevated intra- and extra-spheroid DOC values yields in lower Da and Φ^2 . At $\epsilon_{cc}=0.2$, Da reduces from 8.3 to 3.3 and Φ^2 drops from 8.4 to 3 when changing $C_{o,sat}$ from 100 to 250 $\mu\text{mol/L}$. At higher porosities, Φ^2 changes at a lower rate. For example here, at $\epsilon_{cc}=0.5$, Φ^2 drops from 1.2 to 0.46.

Optimum perfusion rate should enable sufficient oxygen supply to the cells without inducing any impairment to the spheroids, such as excessive shear stress or separating them from the hollow fibers. The chosen value was in accord with our previous experiments in which the spheroids were seeded in the bioreactor and the oxygen concentration was monitored at the inlet and the outlet of the bioreactor. A simple estimation of the forces exerted on the 400 μm -diameter spheroid reveals that the drag force is 6 to 8 orders of magnitude smaller than the gravitational force, thus unable to move the spheroid when there is no bonding or interaction with the HF.

The dominance between diffusive and convective transport in the ECS (outside the spheroid) can only be manipulated through the perfusion rate. Enhancing convection reduces the concentration gradient in ECS and consequently induces higher DOC at spheroid surface. As a matter of fact, increasing Q_{BR} (0.1 to 2.7 ml/min) increases both the Pe_{ecs} (0.06 to 1.7) and Pe_{sph} (by two orders of magnitude).

Another key topic in culture systems is the size of the cellular mass – here spheroid diameter – which can be sufficiently supplied with oxygen and nutrients. While the size of the individual spheroids seeded to the bioreactor can be controlled to some extent, maintaining and even monitoring this parameter throughout the experiment is very challenging. Even though the spheroid size cannot increase due to lack of proliferative capacity in vitro, they can however merge and form larger masses. Moreover, spatial rearrangement of cells results in the shrinkage of spheroids over time. Consequently, spheroid size during culture time is much more complex to be treated merely as a design parameter.

Focusing on the porosity of 0.2, higher spheroid diameter (100 to 400 μm) yielded in increasing Φ^2 (0.4 to 8.8), β_{Bm} (0 to 0.37), β_{Hpx} (0 to 0.28) and decreasing η (\sim 1 to 0.89). In small spheroids, oxygen consumption rate is much lower than the diffusion rate as expressed by the Thiele modulus. This in turn results in small DOC difference across the spheroid thus the higher effectiveness factor. Depending on the $C_{\text{o,sat}}$, this also results in hyperoxic conditions in very small spheroids.

Spacing between the hollow fibers as a design parameter in current setup should be optimized in terms of efficiently trapping maximum amount of spheroids. Increasing the gap between 150-300 μm was found to be inconsequential in terms of oxygen transfer as it only slightly increased Da from 3.4 to 5.1.

Oxygen consumption rate and consequently the parameters in Michaelis-Menten kinetics depend on the cell type and the phenotypic characteristics. V_{max} and K_{m} cannot be controlled, nor can they change for a certain cell culture system. However, should these parameters differ among various systems or among different studies, investigation of the oxygen transport under different uptake rates helps to understand its effect and what can be expected under different circumstances. The spheroid is basically a reaction-diffusion system and increasing V_{max} from 5 to 25 $\text{nmol}/(\text{s}\cdot\text{cm}^3)$ results in increased Thiele modulus, which in turn slows down at higher porosities. At $\epsilon_{\text{cc}}=0.2$, Φ^2 increases from 4.2 to 32, while it ranges from 0.6 to 5 at $\epsilon_{\text{cc}}=0.5$. Da also increases from 4.5 to 22.4 in the ECS. Higher oxygen uptake rate with respect to the diffusion rate results in sharper DOC decrease along the diffusion path in the spheroid and consequently in lower effectiveness factor. η drops from 0.98 to 0.58 at $\epsilon_{\text{cc}}=0.2$, while the change at a higher porosity of 0.5 is much less (\sim 1 to 0.96). At higher uptake rates, the cells are at higher risk of hypoxia. At $\epsilon_{\text{cc}}=0.2$, β_{Hpx} increases from 0 to 0.68, while it only ranges between 0-0.13 at $\epsilon_{\text{cc}}=0.5$.

Defining transport properties such as permeability and effective diffusion coefficients in porous media in terms of common parameters enabled a proper, systematic investigation of their effect on oxygen transfer to the cells. Looking back at the mathematical model, one can readily infer the significance of spheroid porosity as it affects both the oxygen demand and diffusional limitations. Unfortunately, there is limited data about ϵ_{cc} since the micro-structural properties of the cellular mass are very challenging to measure and in many modelling studies on bioreactors, ϵ_{cc} is rather taken for granted as it is often not the key component under investigation. Additionally, reported values available in the literature are subject to change for different systems and cell types.

The following changes were observed through increasing ε_{cc} from 0.2 to 0.5: increased Pe_{sph} (from 4×10^{-5} to 4×10^{-4}) and η (from 0.98 to ~ 1), decreased Φ^2 (from 4.2 to 0.63) and β_{Bm} (from 0.22 to 0). Higher mass transfer rate at higher porosity is characterized by higher effective diffusion coefficient and manifested by the increase in Pe_{sph} and the decrease in Φ^2 .

Transport properties of the membranes also change during the culture time. Adsorption of proteins and possibly impurities such as cell debris diminishes membrane's transport capacity. Occlusion of pores in this case can be presented by decreased ε_m , resulting in decreased diffusivity and permeability. Consequently, higher luminal pressure for the same permeation rate will be observed, which in turn can deform the membrane's structure. In this study, the membrane was considered as a homogenous, isotropic porous medium, but different membranes may have very different structures. High diversion from the assumptions made here may call for further customization of the model to properly project the species transport for a particular membrane.

ε_m sweep explicates the relationship between membrane's diffusive mass transfer resistance to the concentration profile inside the spheroid. Although ε_m is fairly expected to have negligible effect on convective transport in ECS at the cost of altered luminal pressure, its influence on oxygen transport and consequently on DOC profile is nonetheless considerable. Therefore, the extra-spheroid diffusive transport cannot be neglected in convection-enhanced bioreactors when Péclet number is in the order of $O(0)$ or less, such as here ($Pe_{ecs}=0.6$). The effect of diffusive transport through the membrane as a function of ε_m is best realized through the DOC profiles as previously shown. Lower extra-spheroid transport resistance slightly influences intra-spheroid rates, manifested by the small decrease in Thiele modulus (5.8 to 4.1 at $\varepsilon_{cc}=0.2$) and increase in effectiveness factor (0.95 to 0.98 at $\varepsilon_{cc}=0.2$).

5.5 Conclusion

Oxygen transport in a crossed-configuration hollow fiber membrane bioreactor used for culturing hepatocyte spheroids was investigated. First, the influence of different parameters was evaluated individually, namely operational parameters (oxygen tension, perfusion rate), design parameters (hollow fiber spacing, spheroid size), kinetic parameters (Michaelis-Menten kinetics for oxygen uptake) and microstructural properties (porosities of the spheroid and the membrane). Aside from hollow fiber spacing which was found to have negligible effect on oxygen transport within the

studied scale, oxygen tension and perfusion rate are in fact the only parameters that can be monitored and manipulated in order to optimize oxygen transport, while the rest are intrinsic to the system. Among the operational conditions, $C_{o,sat}$ was much more influential than Q_{BR} significantly affecting intra-spheroid DOC. Thus, it should be highly considered in optimization of the bioreactor. The system under investigation was convection-enhanced but convection was not the dominating transport mechanism. Therefore, the extra-spheroid resistances to diffusive mass transfer – namely the membrane – still plays an important role. However, ϵ_{cc} was found as a key intrinsic property strongly affecting intra-spheroid DOC profile.

References

- [1] A. Messina, S. Morelli, G. Forgacs, G. Barbieri, E. Drioli, and L. De Bartolo, "Self-assembly of tissue spheroids on polymeric membranes," *J Tissue Eng Regen Med*, Nov 09 2015.
- [2] Y. Moussy, "Convective flow through a hollow fiber bioartificial liver," *Artif Organs*, vol. 27, pp. 1041-9, Nov 2003.
- [3] F. Dullien, "Porous Media-Fluid Transport and Pore Structure. 1992," *Access Online via Elsevier*.
- [4] P. D. Hay, A. R. Veitch, M. D. Smith, R. B. Cousins, and J. D. Gaylor, "Oxygen transfer in a diffusion-limited hollow fiber bioartificial liver," *Artif Organs*, vol. 24, pp. 278-88, Apr 2000.
- [5] J. L. Dulong and C. Legallais, "A theoretical study of oxygen transfer including cell necrosis for the design of a bioartificial pancreas," *Biotechnol Bioeng*, vol. 96, pp. 990-8, Apr 1 2007.

Chapter 6

Establishment of *in vivo*-like oxygen gradient inside the spheroids cultured in the bioreactor

6.1 Introduction

In biological systems, oxygen gradient between capillaries and surrounding tissues provide the key driving force for efficient oxygen transport, which is crucial for the maintenance of homeostasis and induction of cellular response. Tissue oxygenation is a critical issue in the development of *in vitro* cell-based systems, especially in the case of three-dimensional constructs such as multicellular spheroids [1, 2]. This is further exacerbated in hepatic cell cultures due to hepatocytes' high oxygen consumption rate. *In vivo*, hepatocytes have a unique, vascularized microstructure efficiently in sync with their high oxygen demand to perform a wide range of specific functions in detoxification, protein synthesis, biotransformation, metabolism, and excretion of hormones and bile. However, isolated hepatocytes notoriously lose their proliferative capacity and their specific functions *in vitro* [3], which strongly hinders the application of such devices.

Low solubility of oxygen in culture medium, its high uptake rate and short diffusive penetration depth in hepatic tissue ($\sim 100\mu\text{m}$) [4] are not the only challenges in oxygen supply to *in vitro* hepatic cultures. *In vivo*, the oxygen gradient along the sinusoid in the lobule, along with the gradients of hormones and extra-cellular matrix is reportedly the modulator of metabolic zonation of the liver, characterized by distribution of hepatocyte functions along the sinusoid. For example, gluconeogenesis and ureagenesis occur at periportal zone (oxygen concentration 60 to 65 mm Hg, 84-91 $\mu\text{mol/L}$) whereas glycolysis and liponeogenesis are present at perivenous zone (oxygen concentration 30 to 35 mm Hg, 42-49 $\mu\text{mol/L}$) [5, 6]. While it is important to have similar oxygen gradient *in vitro* [7], different oxygen tensions used during the culture affects the behavior of hepatocytes. Even though the *in vivo* environment of the hepatocytes is slightly hypoxic, low oxygen tensions *in vitro* are reported to adversely affect hepatocytes' viability and metabolism [8, 9]. Lillegard et al. investigated the effect of different oxygen tensions to hepatocyte spheroids in serum-based culture, finding normoxic conditions favorable for hepatocyte viability and

functionality, while higher oxygen tensions increase the formation of reactive oxygen species. Broughan et al. reported different stress responses for hepatocytes under perivenous and periportal oxygen tensions [10]. While such studies accentuate the intricacy of oxygen supply, they are carried out on different systems. Thus, DOC profiles need to be evaluated for any system under investigation.

Hepatocyte spheroids obtained by self-assembly of cells have the potential to be employed for the fabrication of in vitro liver tissue through fusion process [1]. It is well established that hepatocytes aggregated into 3-D structures such as spheroids display an improved metabolic activity, owing to the high degree of intercellular contacts crucial for communication of signals and integration of gene and metabolic patterns [2]. However, the absence of a vascular network in large spheroids may eventually cause oxygen transfer limitations leading to impairment of cell viability and functions. In order to provide hepatocyte spheroids with sufficient amount of oxygen and other nutrients, and to efficiently remove catabolites and cellular products, dynamic systems like membrane bioreactors have been investigated.

The spheroids are observed to shrink in size and become more compact during the culture time [1], which in turn changes their microstructure and porosity in an uncontrolled manner leading to compromised transport properties. The effect of this phenomenon on oxygen transport into the spheroids is not properly addressed

The feasibility of achieving physiological oxygen concentrations in large spheroids is investigated for two different intra-spheroid porosities. Finally, the changes in oxygen gradient due to shrinkage of spheroids are addressed, all of which evaluate the oxygen concentration at cellular microenvironment. Finally, experimental data regarding oxygen concentrations and operational conditions are implemented in the model to gain insight over a realistic case.

6.2 Materials and methods

6.2.1 Mathematical model

The same geometry, mathematical model and boundary conditions as described in Chapter 4 are employed here. Three separate cases were considered for this part of the study. First, the culture conditions for a 400 μ m-spheroid (constant volume) under two different ϵ_{cc} values of 0.47 and 0.2 were optimized. In the second case, spheroid shrinkage due to rearrangement of cells was

investigated (constant number of cells per spheroid). Finally, the data from the experimental work of colleagues in our group was used in the model to provide a realistic case and to make a comparison between modelling and experimental data.

6.2.2 Experimental procedure

Preparation and seeding of spheroids was performed by colleagues as it was not part of this study. For clarification and better appreciation of this section, the procedure is herewith explained.

For the formation of human hepatocytes spheroids an agarose mold was fabricated by using 3D Petri Dish[®] micro-mold (Sigma) consisting of 256 circular recesses (16×16 array) with diameter of 400µm and depth of 800µm. Molten agarose at %2 (500 µl) was cast on each of the micro-molds and left for 10 minutes to set then the agarose molds were removed and placed in 12-well plates.

The primary human hepatocytes isolated from human tissue were seeded in 256-well agarose molds at a density of 3×10^5 cells/mold. To promote cell aggregation into spheroids, thawing medium was supplemented with %10 FBS; cells were cultured in this medium for 5 days.

Spheroids were then seeded into the HFMBR on the outer surface of PES HF membranes previously sterilized and conditioned with medium containing %10 FBS. Afterwards, the FBS content in the medium was decreased gradually reaching a serum-free medium. The bioreactors were incubated at 37° C in %5 CO₂ with %95 relative humidity for the duration of the experiments.

Dissolved oxygen concentration was measured in HF membrane bioreactor by using a flow-through oxygen cells (Presens, Regensburg, Germany). The flow-through chemical optical oxygen sensors, based on the quenching of luminescence by oxygen, were incorporated into the culturing perfusion loop at the inlet and outlet of the bioreactor. The sensors do not consume oxygen, are independent of the flow rate and maintain long-term stability. A fiber optic cable transmitted the optical signal between the sensor and the Fibox 4 portable oxygen meter (PreSens GmbH, Germany); the latter was connected to a PC at the end of the experiment to export the stored data in excel files which were then elaborated. The oxygen probes detected oxygen concentration with resolution of $\pm 0.4\%$ O₂ at 20.9% O₂ and a response time <30s.

6.3 Results

6.3.1 Maintaining physiological DOC range *in vitro*

Once the significance and effect of each parameter is understood, the feasibility of reaching physiological DOC range within a spheroid inside the bioreactor was evaluated. Despite its utmost significance, the most indeterminate parameter in Table 1 is the intra-spheroid porosity for two reasons: lack of control over ϵ_{cc} and challenging evaluation of its value, and the temporal changes of ϵ_{cc} over culture time. Two separate cases were considered for this part of the study. First, the culture conditions for a 400 μm -spheroid under two different ϵ_{cc} values were optimized. In the second case, spheroid shrinkage due to rearrangement of cells was investigated. Here, reaching physiological DOC range within a spheroid with a diameter of 400 μm was studied. Two values of ϵ_{cc} were considered: 0.2 and 0.47 calculated from available data on ELAD[®] bioreactor [11].

Figure 6. 1 shows the DOC profile in spheroid with porosity to 0.2. In this case, the saturated DOC must be increased to atmospheric conditions to minimize both hypoxic and hyperoxic conditions within the 400 μm -diameter spheroid. DOC varies from 113 $\mu\text{mol/L}$ to 159 $\mu\text{mol/L}$ in ECS, while inside the spheroid it covers a much wider range in comparison with the previous case (1-142 $\mu\text{mol/L}$ vs. 44-84 $\mu\text{mol/L}$). Calculation of β_{BM} and β_{HPX} reveals that only %37 of the spheroid benefits from physiological DOC range as shown by the colored shell in Figure 6. 2, while 29% of the spheroid (i.e. the central part) is exposed to hypoxia.

The shear stress range tolerated by cells or required as favourable stimulation of mechanosensors is an intricate issue, the effects of which may differ with respect to cell type, culture type (homotypic, heterotypic), culture period, and evaluated hepatic functions [12] [13]. Figure 6. 3 shows the shear and normal total stress on spheroid surface ($D_{\text{sph}}=400\mu\text{m}$, $\epsilon_{cc}=0.2$). Under the examined conditions, the shear stress is well-below the reported 0.03Pa threshold [8]. Highest shear and normal stress is distinguishable at the spheroid-hollow fiber tangential points.

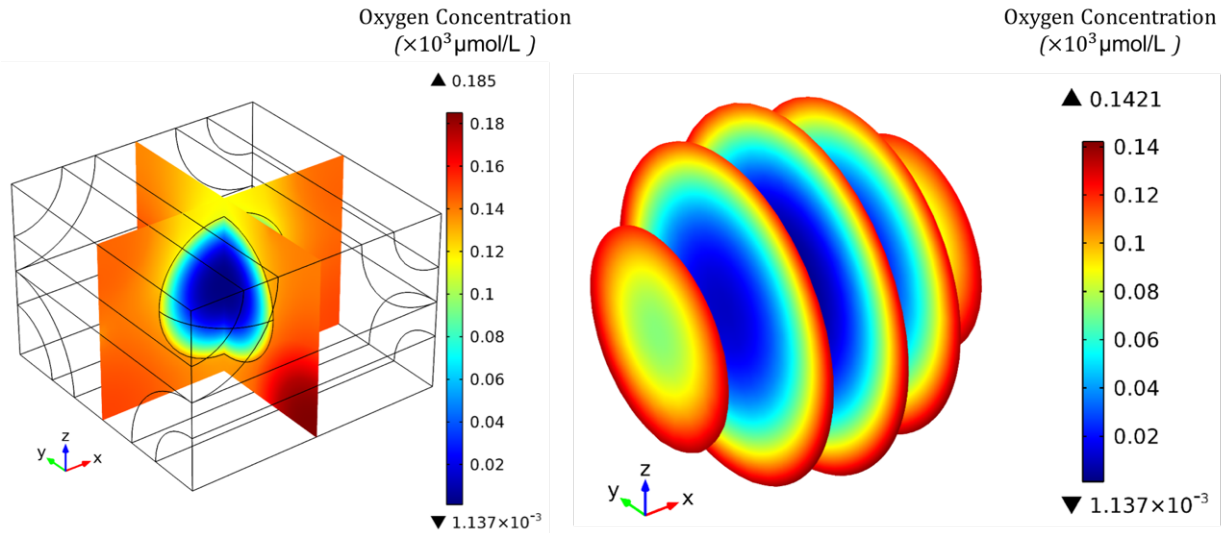


Figure 6. 1 DOC profile ($\mu\text{mol/L}$) in the ECS (left) and inside the spheroid (right) for $D_{\text{sph}}=400\mu\text{m}$ and $\text{ecc}=0.20$. ($C_{o,\text{sat}}=185 \mu\text{mol/L}$, $Q_{\text{BR}}=1 \text{ ml/min}$, $V_{\text{max}}=5 \text{ nmol}/(\text{s}\cdot\text{cm}^3)$, $K_{\text{m}}=5.6 \text{ mm Hg}$, $\epsilon_{\text{m}}=0.7$, $\delta_{\text{HF}}=250\mu\text{m}$.)

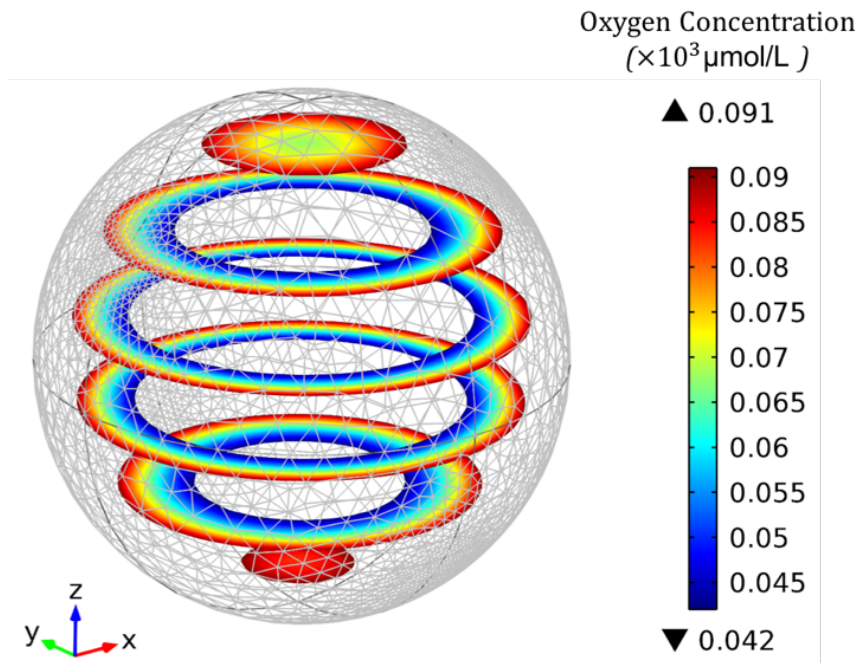


Figure 6. 2 Proportion and position of the cells exposed to physiological DOC range within the spheroid with $D_{\text{sph}}=400\mu\text{m}$ and $\text{ecc}=0.20$. ($C_{o,\text{sat}}=185 \mu\text{mol/L}$, $Q_{\text{BR}}=1 \text{ ml/min}$, $V_{\text{max}}=5 \text{ nmol}/(\text{s}\cdot\text{cm}^3)$, $K_{\text{m}}=5.6 \text{ mm Hg}$, $\epsilon_{\text{m}}=0.7$, $\delta_{\text{HF}}=250\mu\text{m}$.)

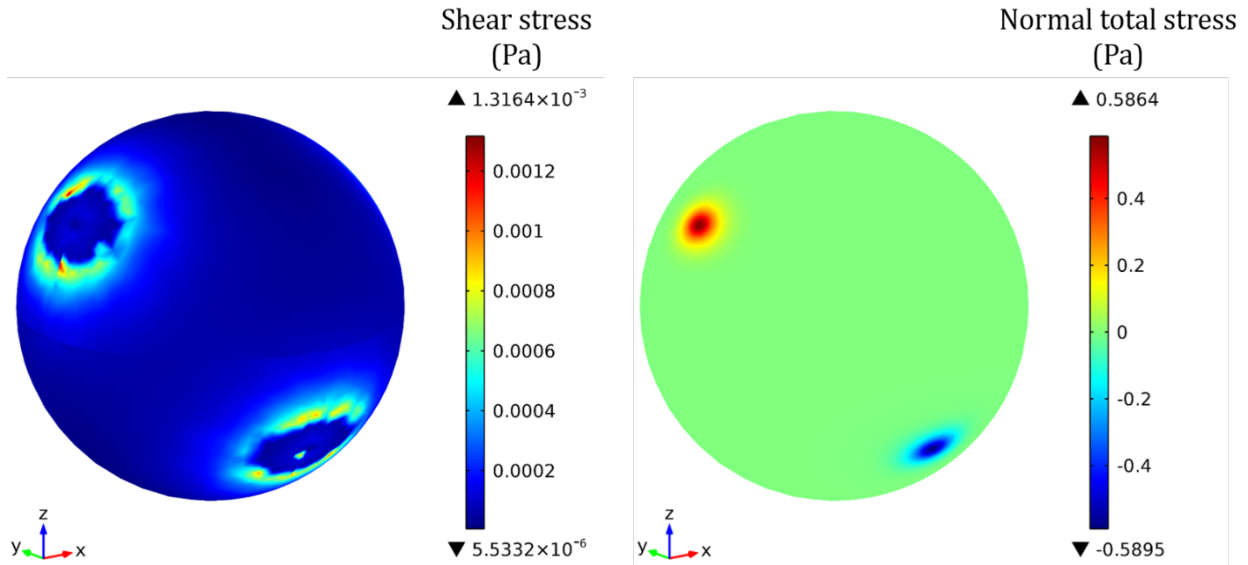


Figure 6.3 Shear (left) and normal total (right) stress exerted on the spheroid surface of the spheroid the spheroid with $D_{sph}=400\mu\text{m}$ and $\text{ecc}=0.20$. ($C_{o,sat}=185\ \mu\text{mol/L}$, $QBR=1\ \text{ml/min}$, $V_{max}=5\ \text{nmol}/(\text{s.cm}^3)$, $Km=5.6\ \text{mm Hg}$, $\epsilon m=0.7$, $\delta HF=250\mu\text{m}$.)

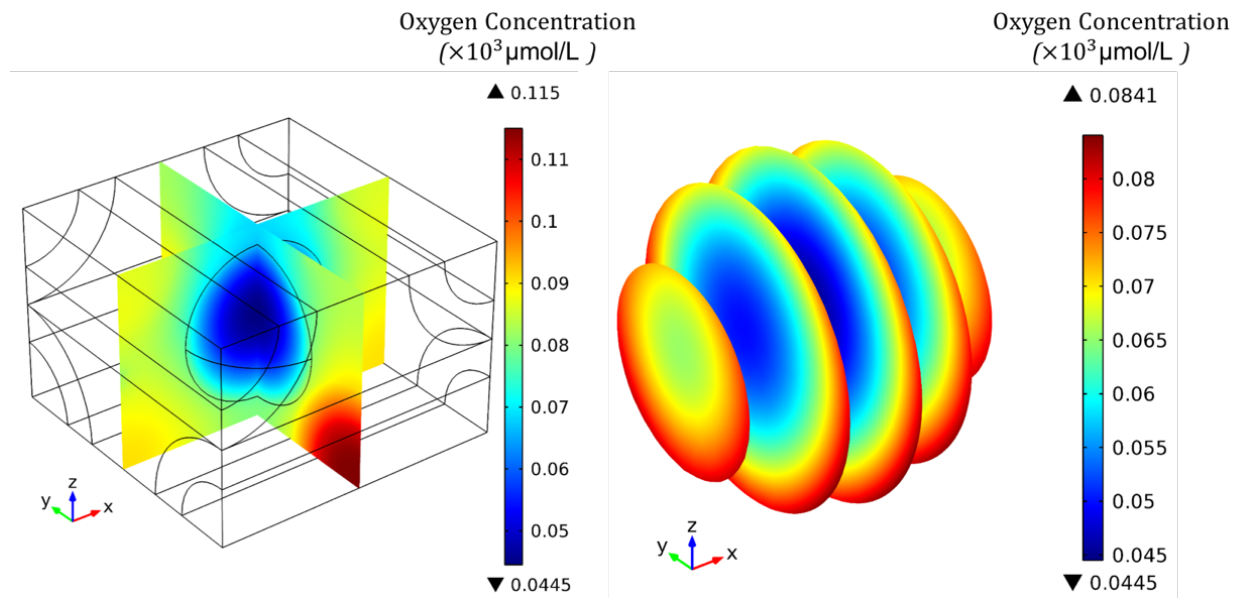


Figure 6.4 DOC profile (mol/m^3) in the ECS (left) and inside the spheroid (right) for $D_{sph}=400\mu\text{m}$ and $\text{ecc}=0.47$. ($C_{o,sat}=115\ \mu\text{mol/L}$, $QBR=1\ \text{ml/min}$, $V_{max}=5\ \text{nmol}/(\text{s.cm}^3)$, $Km=5.6\ \text{mm Hg}$, $\epsilon m=0.7$, $\delta HF=250\mu\text{m}$.)

Increasing the spheroid porosity to 0.47, the DOC profile in the spheroid and in the ECS changes significantly (Figure 6. 4). In order to have physiological DOC range and avoid hyperoxic conditions, the saturated DOC at the inlet was reduced to 115 $\mu\text{mol/L}$, which is equivalent to an oxygen tension of 12.4% in the incubator. In this case, the DOC within the spheroid is completely within the physiological range ($\beta_{\text{BM}}=1$), while in ECS the DOC drops from 97 $\mu\text{mol/L}$ in the vicinity of HFs supplying oxygenated culture medium to a minimum of 67 $\mu\text{mol/L}$ furthest away from the HFs. DOC profile within the spheroid is rather asymmetrical, with varying surface concentrations in accord with their distance from supplying HFs.

6.3.2 Oxygen supply to a shrinking hepatocyte spheroid: constant number of cells

During another study in our group, the spheroids were formed in a mould in vitro and they seeded into the bioreactor after 5 days. During the preparation, the spheroids were observed to shrink in time, and subsequent sampling from the bioreactor suggested further shrinkage of the spheroids after seeding. Moreover, the adjacent spheroids merged to form larger spheroids. Before being seeded to the bioreactor, the spheroids were 200 μm in diameter. Based on the average number of cells in each spheroid (total number of cells divided by number of wells in the mould) and assuming a hepatocyte diameter of 16 μm , a porosity of 0.42 was calculated.

Due to limited data available on the level of merging and shrinkage of the spheroids inside the bioreactor, a spheroid with $D_{\text{sph}}=400\mu\text{m}$ and $\epsilon_{\text{cc}}=0.42$ was considered and assumed to shrink by %10 to a diameter of 360 μm . Assuming constant number of hepatocytes inside the spheroid, ϵ_{cc} after shrinkage would be 0.2. Figure 6. 5 shows the DOC profile inside the spheroid before and after the shrinkage. At initial diameter of 400 μm and porosity of 0.42, setting the flow rate at 0.8ml/min and $C_{\text{o,sat}}$ at 130 $\mu\text{mol/L}$ (14% oxygen in the incubator), almost the entire spheroid will be maintained within physiological DOC range ($\beta_{\text{BM}}=0.98$), also completely covering the in vivo oxygen gradient. Spheroid shrinkage adversely affects the DOC profile despite the fact that the number of cells and the operational conditions remain unaltered. The β_{BM} drops to 0.52, with 45% of cells exposed to hypoxic conditions. Increasing the oxygen tension to atmospheric conditions (%20 oxygen in the incubator, resulting in $C_{\text{o,sat}}=185 \mu\text{mol/L}$) ameliorates the condition by reducing hypoxity index to 0.15, although the outer cells will be hyperoxic ($\beta_{\text{BM}}=0.38$).

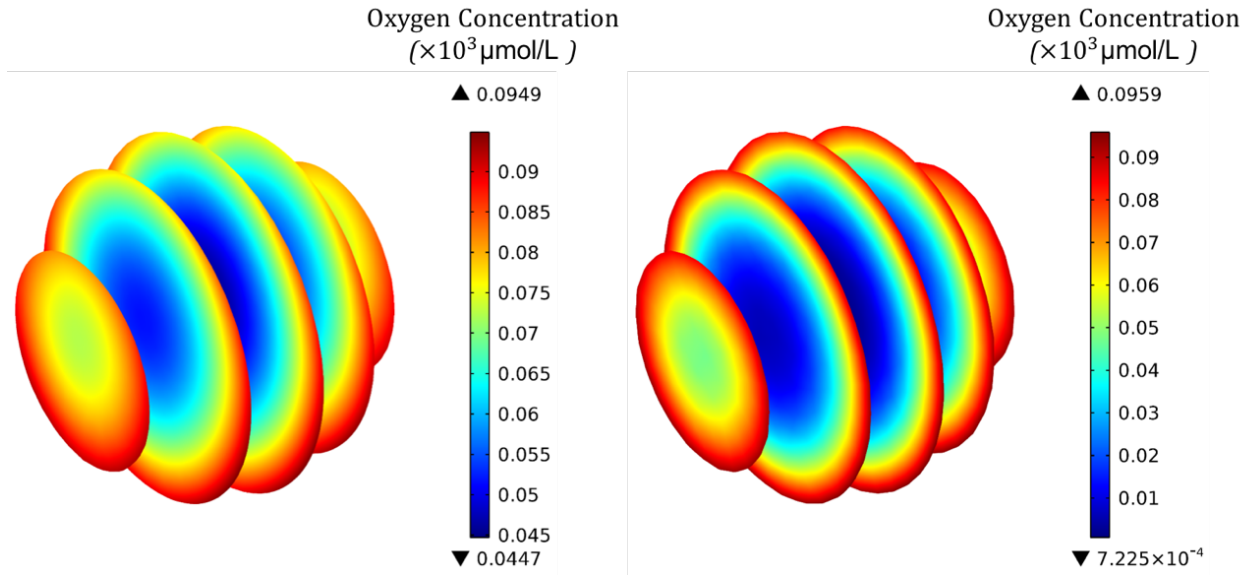


Figure 6. 5 (Left) DOC profile (mol/m³) in the spheroid before shrinkage. $D_{sph}=400\mu\text{m}$ and $\text{ecc}=0.42$. (Right) DOC profile (mol/m³) in the spheroid after shrinkage. $D_{sph}=360\mu\text{m}$ and $\text{ecc}=0.20$. Other parameters remain unaltered for both cases: $C_{o,sat}=130\mu\text{mol/L}$, $QBR=0.8m$.

6.3.3 Model based on experimental data

Considering the arrangement of the hollow fibers in the assembled bioreactor, and assuming uniform distribution of the seeded spheroids within the crossed section of the bioreactor, 5-6 spheroids occupy the extra-capillary space in the unit element. Thus, oxygen transport into two configurations of cellular masses are studied: 6 spheroids (200 μm in diameter) arranged within the extra-capillary space in the element, and one large spheroid (400 μm in diameter) resulting from merging smaller spheroids. The latter phenomenon is illustrated in Figure 6. 6. The spheroids were cultured between the hollow fibers in static culture systems to mimicking the bioreactor environment, excluding the perfusion. Naturally, several spheroids may coexist in the space between crossing hollow fibers. The adjacent spheroids can then merge together. The merging process is rather complex, involving microstructural changes. However, here the merging spheroids were assumed to form a larger spheroid with the same porosity. Thus, the volume of the new spheroid is equal to the sum of small spheroids' volumes.

Based on the diameter of the prepared spheroids (before being seeded into the bioreactor) and average number of cells per spheroid, an intra-spheroid porosity of 0.41 was calculated. V_{max} in Michaelis-Menten kinetics for oxygen uptake rate was estimated by adaptation of the model to

experimentally-obtained average oxygen consumption rate per spheroid, resulting in $V_{\max}=17$ nmol/(cm³.s). Due to the limited data on K_m and relatively high cell density in the spheroids ($\sim 10^8$ cells/cm³), K_m value of 5.6 mmHg reported for hepatocytes [14] was used. Operational conditions (perfusion rate 0.6 ml/min, dissolved oxygen concentration at the inlet 224 μ mol/L) were also taken from experimental measurements. Based on the experimental results, the average oxygen consumption rate per spheroid is around 37 fmol/s, which was used in development of the model.

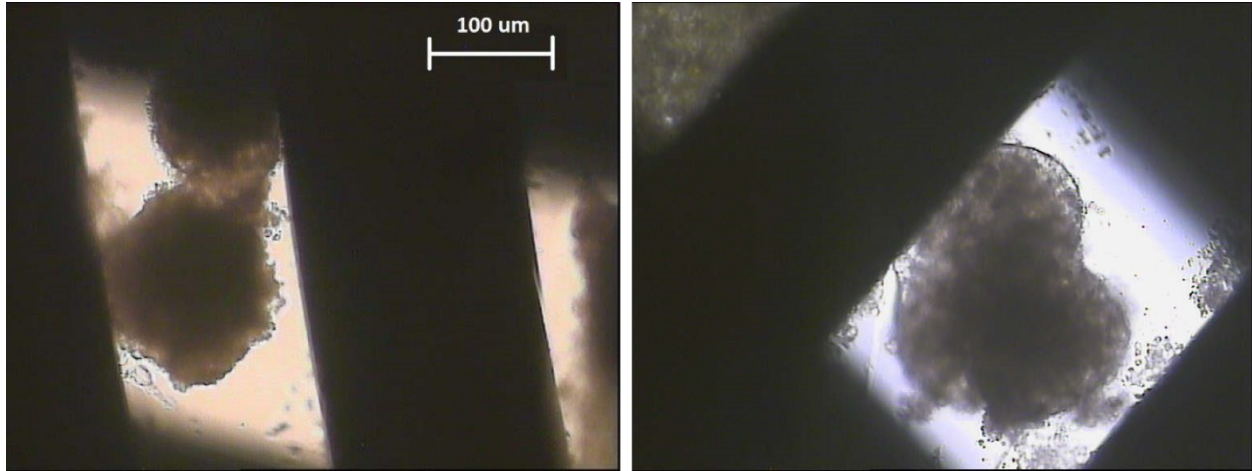


Figure 6. 6 Primary hepatocyte spheroids between hollow fibers. (Left) Separate adjacent spheroids, (Right) Spheroids merging together to form larger cellular masses.

Figure 6. 7 shows the concentration profile inside the 6 spheroids cultured at the ECS in each unit element (the origin of the Cartesian coordinate is at the center of the block, with spheroids arranged around it). DOC in all the adjacent spheroids range between 144-188 μ mol/L, i.e. much higher than the periportal values. The minimum DOC value in each spheroid is not exactly at the core of it, but shifted towards the coordinate origin, and the maximum values are observed on the walls away from the origin. The minimum DOC in ECS is within the space in the middle of spheroids around the origin (149 μ mol/L).

Next, the possibility of having the six spheroids merged together was considered, assuming that the resulting cellular mass is a larger spheroid with the same porosity. The volume of the resulting spheroid is 6 times larger than 200 μ m spheroids, resulting in an equivalent diameter of 363 μ m. Figure 6. 8 shows the concentration profile inside the formed spheroid and in the ECS. In this case, DOC in the spheroid is still higher than the periportal zone; however, a higher gradient is observed within the spheroid and the minimum DOC is significantly lower (117 μ mol/L) than the 6

spheroids (144 $\mu\text{mol/L}$). Moreover, relatively higher DOC values are observed in ECS (162-201 $\mu\text{mol/L}$).

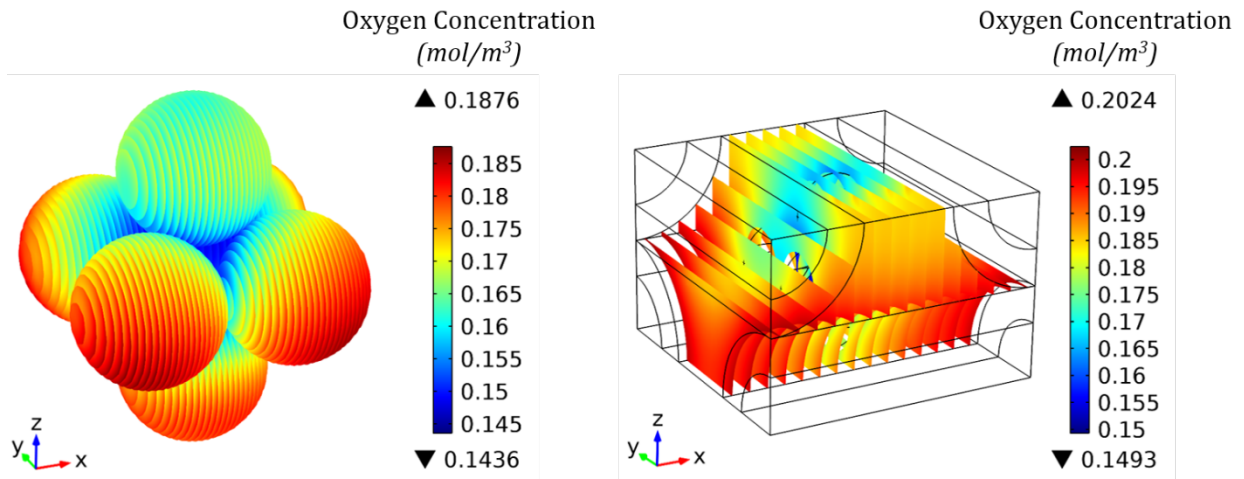


Figure 6. 7 DOC profile (mol/m^3) inside the spheroid (left) and in the ECS (right) for $D_{sph}=200\mu\text{m}$ and $\text{ecc}=0.41$. ($C_{o,sat}=224 \mu\text{mol/L}$, $QBR=0.6 \text{ ml/min}$, $V_{max}=17 \text{ nmol/(s.cm}^3)$, $K_m=5.6 \text{ mm Hg}$, $\epsilon_m=0.8$, $\delta HF=250\mu\text{m}$).

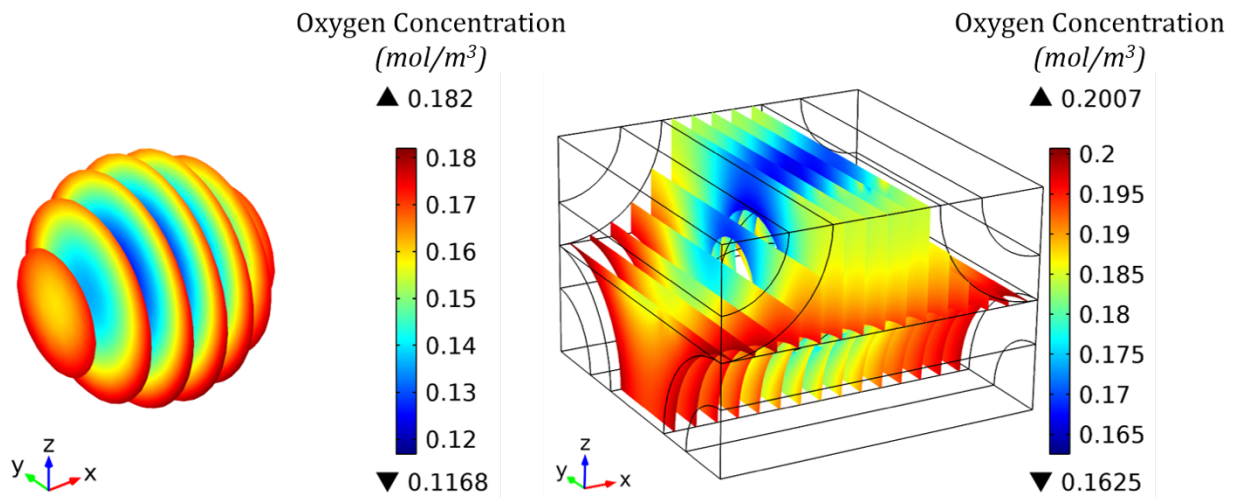


Figure 6. 8 DOC profile (mol/m^3) inside the spheroid (left) and in the ECS (right) for $D_{sph}=363\mu\text{m}$ and $\text{ecc}=0.41$. ($C_{o,sat}=224 \mu\text{mol/L}$, $QBR=0.6 \text{ ml/min}$, $V_{max}=17 \text{ nmol/(s.cm}^3)$, $K_m=5.6 \text{ mm Hg}$, $\epsilon_m=0.8$, $\delta HF=250\mu\text{m}$).

6.4 Discussion

The feasibility of achieving physiological DOC gradient within a 400 μ m-diameter spheroid was evaluated for porosities of 0.47 and 0.2. Notable differences were observed between the two cases. In higher porosity of 0.47, there was more control over DOC profile through manipulation of QBR or $C_{o,sat}$, thus possible to closely mimic the oxygen concentration gradient in vivo ($\beta B_m=1$) with low $C_{o,sat}$ value of 115 μ mol/L. A porosity of 0.2 on the other hand significantly affected the diffuse penetration depth, resulting in a large DOC range across the spheroid, with values approaching zero at the center. In the latter case, βB_m dropped to 0.37 with 29% of the cells under hypoxic conditions despite the fact that $C_{o,sat}$ was increased to atmospheric conditions (185 μ mol/L). As discussed earlier, lower porosity means higher cell density as imparted by the increase in the correction factor in Eq. 4.10 from 1.24 to 1.86. Effectiveness factor was observed to decrease from 0.98 at $\epsilon_{cc}=0.47$ to 0.89 at $\epsilon_{cc}=0.2$, indicating higher mass transfer resistance. Even though diffusion remains the dominant transport mechanism inside the spheroid, convective term gains more influence at the higher porosity. This was assumed by the higher asymmetry in Figure 6. 1 compared to Figure 6. 4, expected from Eq. 4.15, and proved by Pe_{cc} being higher by an order of magnitude. The combined effect of higher oxygen consumption and lower oxygen diffusion at lower porosity is reflected by the increase in Thiele modulus from 2.6 to 8.8.

Shrinkage of the spheroids during the culture time is a complex yet interesting phenomenon. When the 400 μ m-spheroid shrinks by %10, the modelling shows a decrease in Pe_{sph} (from 1×10^{-2} to 1×10^{-4}), an increase in Φ^2 (3.1 to 10.2), a decrease in η (0.98 to 0.85), a decrease in βB_m (0.98 to 0.52) and an increase in βH_{px} (0 to 0.45). In this case, the arrangement of the same number of cells results in reduced porosity and consequently lower mass transfer rate, the effects of which on Pe_{sph} , Φ^2 and η is already discussed. This microstructural change is so severe that the same bioreactor with optimized operational conditions is now incapable of providing sufficient oxygen to the same number of cells, resulting in much lower biomimicry index and much higher hypoxity inside the spheroid. This is also indicated by the lower oxygen consumption rate (177 fmol/s compared to 203 fmol/s).

In the case based on the experimental data, all the cells were in hyperoxic conditions as the minimum concentration observed was significantly higher than the perivenous zone in vivo. However, after the 6 spheroids merged together, the DOC in the “cellular compartment” and in the

ECS dropped by 19% and 9%, respectively. The average DOC at the outlet of the HFs removing the medium in the element did not change significantly (187.96 $\mu\text{mol/L}$ before merging vs. 187.75 $\mu\text{mol/L}$ after merging), which is lower than the measured DOC at the outlet of the bioreactor (198 $\mu\text{mol/L}$). Although it is noteworthy to mention that slightly higher number of cells were considered in the model compared to the experiment.

6.5 Conclusion

Regulation of DOC profile was more manageable in spheroids with higher ε_{cc} which lead to feasibility of achieving and in vivo-like microenvironment in terms of DOC. At low porosities, e.g. 0.2 considered here, the spheroid core suffers from hypoxia while the outer shell is exposed to hyperoxia. Shrinkage of spheroids during the culture period, due to which the number of cells per spheroid remains intact but the diameter and consequently the porosity changes, is often overlooked in optimization of their culture conditions. A %10 decrease in the diameter of the spheroid was mathematically investigated. The results showed drastic changes in DOC profile with nearly anoxic conditions at the center, despite keeping the number of cells per spheroid intact.

More studies on the changes in size and structure of the spheroids over the culture time helps to develop more realistic models providing accurate predictions. Moreover, mass transfer modelling provided a microscopic view over the cellular microenvironment, including DOC value and even shear stress at the cellular periphery and not at a macroscopic level, which is decisive in optimization of the operational conditions.

The model was also adjusted based on experimental data to investigate a real case. In the following chapter, the miniaturized bioreactor will be investigated. Using the same approach based on the experimental data will better elucidate the suitability of each model.

References

- [1] A. Messina, S. Morelli, G. Forgacs, G. Barbieri, E. Drioli, and L. De Bartolo, "Self-assembly of tissue spheroids on polymeric membranes," *J Tissue Eng Regen Med*, Nov 09 2015.
- [2] E. Curcio, S. Salerno, G. Barbieri, L. De Bartolo, E. Drioli, and A. Bader, "Mass transfer and metabolic reactions in hepatocyte spheroids cultured in rotating wall gas-permeable membrane system," *Biomaterials*, vol. 28, pp. 5487-97, Dec 2007.
- [3] L. De Bartolo, S. Salerno, S. Morelli, L. Giorno, M. Rende, B. Memoli, *et al.*, "Long-term maintenance of human hepatocytes in oxygen-permeable membrane bioreactor," *Biomaterials*, vol. 27, pp. 4794-803, Sep 2006.
- [4] A. Dash, W. Inman, K. Hoffmaster, S. Sevidal, J. Kelly, R. S. Obach, *et al.*, "Liver tissue engineering in the evaluation of drug safety," *Expert opinion on drug metabolism & toxicology*, vol. 5, pp. 1159-1174, 2009.
- [5] T. Kietzmann and K. Jungermann, "Modulation by oxygen of zonal gene expression in liver studied in primary rat hepatocyte cultures," *Cell biology and toxicology*, vol. 13, pp. 243-255, 1997.
- [6] K. Jungermann and T. Kietzmann, "Oxygen: modulator of metabolic zonation and disease of the liver," *Hepatology*, vol. 31, pp. 255-260, 2000.
- [7] J. W. Allen and S. N. Bhatia, "Formation of steady-state oxygen gradients in vitro: Application to liver zonation," *Biotechnology and Bioengineering*, vol. 82, pp. 253-262, 2003.
- [8] A. W. Tilles, H. Baskaran, P. Roy, M. L. Yarmush, and M. Toner, "Effects of oxygenation and flow on the viability and function of rat hepatocytes cocultured in a microchannel flat-plate bioreactor," *Biotechnology and bioengineering*, vol. 73, pp. 379-389, 2001.
- [9] K. Yanagi and N. Ohshima, "Improvement of metabolic performance of cultured hepatocytes by high oxygen tension in the atmosphere," *Artificial organs*, vol. 25, pp. 1-6, 2001.
- [10] T. A. Broughan, R. Naukam, C. Tan, C. J. Van De Wiele, H. Refai, and T. K. Teague, "Effects of hepatic zonal oxygen levels on hepatocyte stress responses," *Journal of Surgical Research*, vol. 145, pp. 150-160, 2008.

- [11] Y. Moussy, "Convective flow through a hollow fiber bioartificial liver," *Artif Organs*, vol. 27, pp. 1041-9, Nov 2003.
- [12] Y. Wang, T. Susando, X. Lei, C. Anene-Nzelu, H. Zhou, L. H. Liang, *et al.*, "Current development of bioreactors for extracorporeal bioartificial liver (Review)," *Biointerphases*, vol. 5, pp. FA116-FA131, 2010.
- [13] M. R. Ebrahimkhani, J. A. S. Neiman, M. S. B. Raredon, D. J. Hughes, and L. G. Griffith, "Bioreactor technologies to support liver function in vitro," *Advanced Drug Delivery Reviews*, vol. 69–70, pp. 132-157, 4/20/ 2014.
- [14] P. Hay, A. Veitch, M. Smith, R. Cousins, and J. Gaylor, "Oxygen Transfer in a Diffusion-Limited Hollow Fiber Bioartificial Liver," *Artificial organs*, vol. 24, pp. 278-288, 2000.

Chapter 7

Mass transfer in Miniaturized bioreactor

7.1 Introduction

Various simplifications have been employed in modelling hollow fiber membrane bioreactors (HFMBR) to reduce the computational cost, most popularly the Krogh cylinder approach [1, 2] and element-based representation [3]. While these techniques significantly reduce the time and memory required to perform the numerical computations, they are accompanied by certain limitations. For example, virtual boundaries appear in the element based model that need to be properly addressed, or different conditions in the extra-capillary space (ECS) may affect the boundary condition applied to the outer cell-layer wall in Krogh cylinder approach. Additionally, these simplifications may not accurately reflect on the fluid-dynamics characteristics that arise from the design of the bioreactor as a whole.

In an attempt to provide a more realistic model, to address the hydrodynamics effects in ECS and to study the effect of bioreactor's dead volume (previously discussed in chapter 2) on mass transfer, a model was developed in which the bioreactor is scaled down or "miniaturized". Taking this approach enables us to investigate the dead volume effect more accurately while keeping the computational cost reasonable.

First, the miniaturized bioreactor model was used to investigate different flow patterns and their effect on the oxygen and urea concentration profiles. Then, another hypothetical geometry was studied in which the housing was limited to the crossed-section of the bioreactor, eliminating the stagnant region of the bioreactor. The miniaturized bioreactor with a retentate flow in the supplying bundle was also investigated. Finally, the model was adjusted to conditions in a previously performed experiment, similar to the approach described in Chapter 6.

7.2 Methods

7.2.1 Approach

The mathematical model described in Chapter 4 was applied to the miniaturized bioreactor geometry defined as follows and numerically solved for oxygen transfer in steady-state condition using COMSOL Multiphysics[®]. Oxygen transport in the new geometry was studied under steady-state conditions and different flow patterns: (i) one bundle supplying the culture medium into the bioreactor and one bundle removing the medium from it, (ii) both bundles supplying the medium into the bioreactor, which is then removed from the bottom connection of the bioreactor housing, (iii) both bundles removing the medium supplied via the bottom connection. Transport of urea as the cellular catabolite was modelled under time-dependent conditions and the concentration profile in the ECS and the spheroids was analyzed.

Employment of the miniaturized bioreactor enabled the investigation of two other important conditions: minimization stagnant region by considering a cubic space around the crossed section, and minimization of the dissolved oxygen concentration (DOC) drop along the lumen by using higher inlet flow rate and having retentate flow at the outlet of the supplying bundle. These two conditions were studied in the supplying-removing pattern.

The properties and operational conditions heretofore were based on experimental findings and measurements (e.g. $C_{o,sat}=185 \mu\text{mol/L}$, $Q_{BR}=1 \text{ ml/min}$, $\delta_{HF}=250\mu\text{m}$), approximations and assumptions ($\epsilon_{cc}=0.42$, $\epsilon_m=0.7$, $D_{sph}=400 \mu\text{m}$) or taken from the literature ($V_{max}=25 \text{ nmol/(s.cm}^3\text{)}$, $K_m=5.6 \text{ mmHg}$ [4]), as previously explained in Chapters 5-6. In this chapter, the miniaturized bioreactor model was adjusted based on values from a recent experiment – as discussed in Chapter 6 – for better comparison.

7.2.2 Miniaturized bioreactor model: scaling down procedure

The prototype bioreactor introduced in the previous chapters is the basis of calculation for the miniaturization process. The glass housing accommodate ~100 hollow fibers per bundle and has 6 connections: four for the bundles (diameter $D_{c,HF}$) and two for accessing the extra-capillary space (ECS) used for seeding, sampling, etc. (diameter $D_{c,ECS}$). Due to assembly complexities, the bundle did not completely fill the connection, leaving some extra space. The minimum theoretical diameter which encompasses the bundle, named D_{Bundle} , was calculated from the number of fibers

and the spacing between them. For miniaturization of the HFMBR, first the D_{Bundle} and $D_{c,\text{HF}}$ of the prototype bioreactor, as well as diameter of the central space (D_{BR}) were measured. Then, based on the considered number of hollow fibers in the miniaturized bioreactor (here 9, in a 3×3 arrangement), D_{Bundle} was calculated. The $D_{c,\text{HF}}$ of the miniaturized model, marked with the subscript miniBR, is calculated as:

$$(D_{c,\text{HF}})_{\text{miniBR}} = (D_{\text{Bundle}})_{\text{miniBR}} \frac{(D_{c,\text{HF}})_{\text{prototypeBR}}}{(D_{\text{Bundle}})_{\text{prototypeBR}}} \quad (7.1)$$

Design ratio was defined as:

$$\beta_{\text{Design}} = \frac{(D_{\text{BR}})_{\text{prototypeBR}}}{(D_{c,\text{HF}})_{\text{prototypeBR}}} \quad (7.2)$$

And keeping it constant in all the minimized models allows us to calculate $(D_{\text{BR}})_{\text{miniBR}}$. Then, a scale ratio was defined to quantify the extent of minimization:

$$\beta_{\text{scale}} = \frac{(D_{\text{BR}})_{\text{miniBR}}}{(D_{\text{BR}})_{\text{prototypeBR}}} \quad (7.3)$$

This ratio is then used to calculate $(D_{c,\text{ECS}})_{\text{miniBR}}$:

$$(D_{c,\text{ECS}})_{\text{miniBR}} = \beta_{\text{scale}} \cdot (D_{c,\text{ECS}})_{\text{prototypeBR}} \quad (7.4)$$

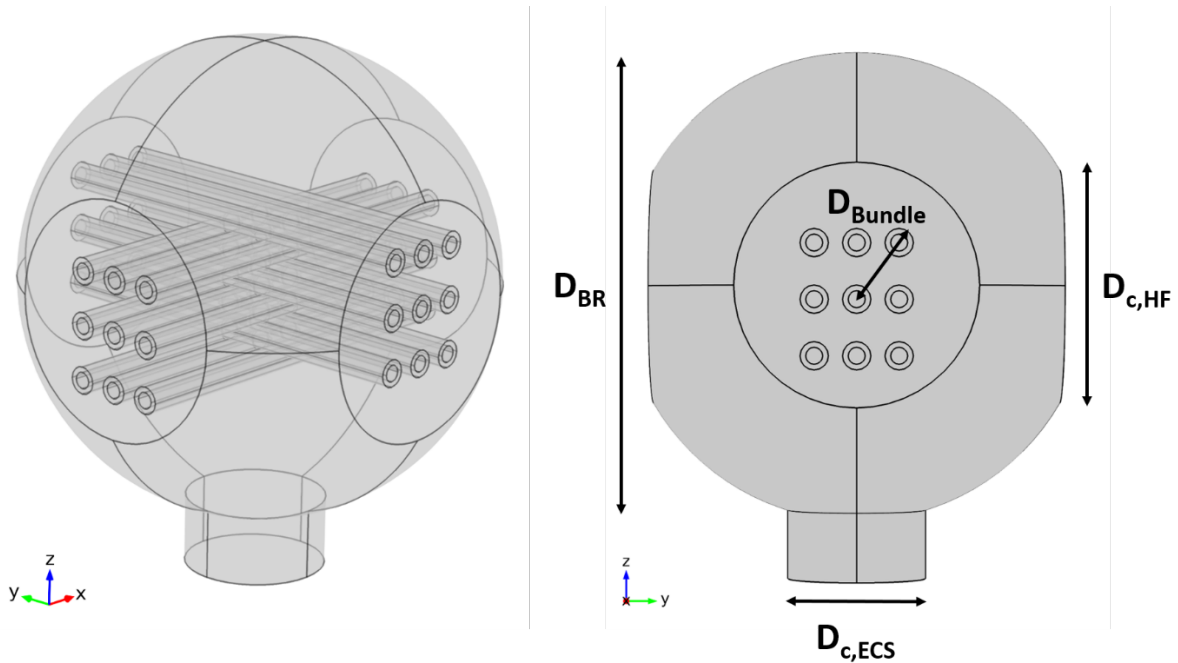


Figure 7. 1 miniaturized bioreactor considering 9 hollow fibers in a 3×3 arrangement.

Using the following steps enabled us to obtain all the necessary dimensions for the miniature HFMBR. For the 3×3 hollow fiber arrangement considered: $\beta_{Design} = 2, \beta_{scale} = 0.255, (D_{BR})_{miniBR} = 8.7mm$.

Minimized stagnant-region model

The geometry in this study includes a significant unused, stagnant region. In order to study the effect of this region, another geometry was studied in which the crossed-section part of the previous geometry was encompassed by a cube. Comparison of the results for this “cubic” bioreactor and the miniaturized bioreactor model can be useful in optimizing the bioreactor design.

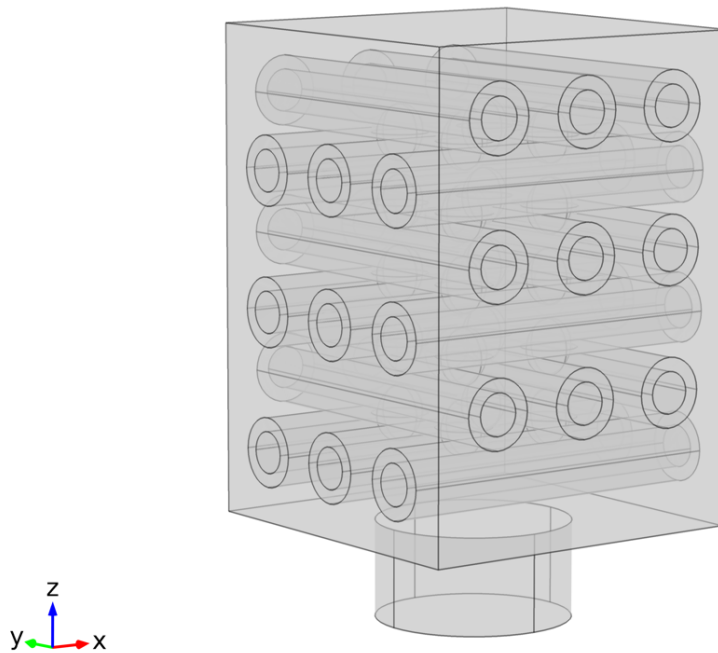


Figure 7.2 Cubic bioreactor considering 9 hollow fibers in a 3×3 arrangement.

7.3 Results

Due to sensitivity of the oxygen supply, the profiles are demonstrated separately for spheroids, ECS and lumina to better distinguish between the domains. Urea concentration profile is only illustrated for ECS, and the values inside the spheroids are reported. Concentration and velocity profiles in the lumina and the ECS are investigated as the ratio of obtained concentrations over saturation concentration and as Péclet number (Pe), respectively.

DOC profile inside the spheroids for supplying-removing flow pattern is presented in Figure 7. 3, according to which DOC values much higher than the periportal zone and lower than the perivenous zone was observed [5]. Figure 7. 4 shows the oxygen ratio and Péclet number in the ECS. The most conspicuous phenomenon observed is the significant reduction in DOC values within the ECS in x-direction (i.e. along the supplying bundle). DOC ratio in the ECS drops from 1 around the supplying bundle's inlet to ~0.86 around the supplying bundle's closed end, with the minimum values (as low as 0.62) within the crossed section near the spheroids. As expected, the velocity drops from the maximum values observed between the hollow fibers (with Pe as high as 20) to 0 on the housing wall.

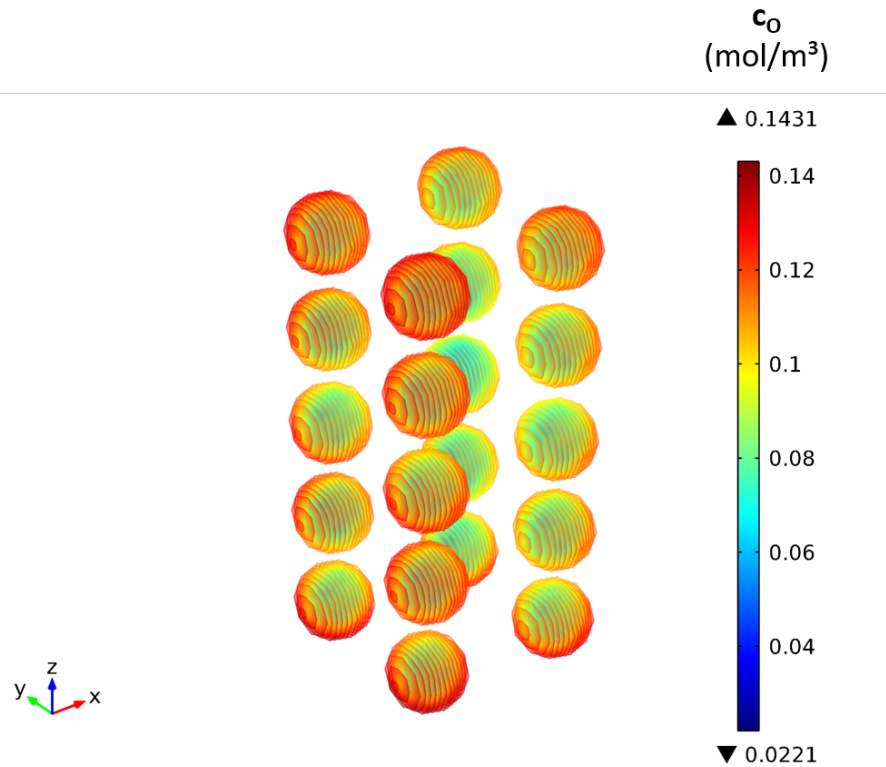


Figure 7. 3 Oxygen concentration in the spheroids, supplying-removing flow pattern. $D_{sph}=400 \mu m$, $C_{o,sat}=185 \mu mol/L$, $Q_{BR}=1 ml/min$, $V_{max}=25 nmol/(s.cm^3)$, $K_m=5.6 mm Hg$, $\epsilon_{cc}=0.42$, $\epsilon_m=0.7$.

Similar DOC drop of ~14% is observed in the x-direction along the supplying lumina (Figure 7. 5). The concentrations at the outlet of removing bundles are not similar as they decrease in hollow fibers further in the x-direction, in accord with the DOC profile in ECS. The minimum DOC values are found half way along the removing bundle, i.e. at the center of the crossed section. Needless

to say, the luminal velocity is much higher than that of the ECS, with Pe varying between ~ 1800 and 0 in each bundle.

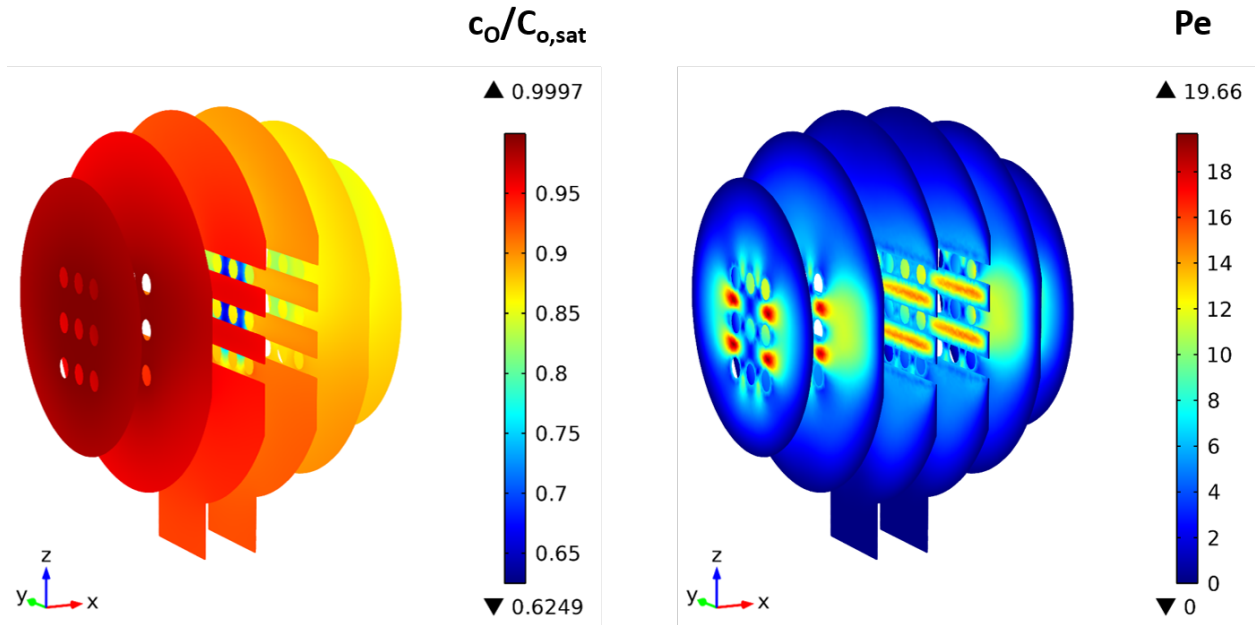


Figure 7.4 Oxygen concentration in the extra-capillary space, supplying-removing flow pattern. $D_{sph}=400 \mu\text{m}$, $C_{O,sat}=185 \mu\text{mol/L}$, $Q_{BR}=1 \text{ ml/min}$, $V_{max}=25 \text{ nmol/(s.cm}^3\text{)}$, $K_m=5.6 \text{ mm Hg}$, $\epsilon_{cc}=0.42$, $\epsilon_m=0.7$.

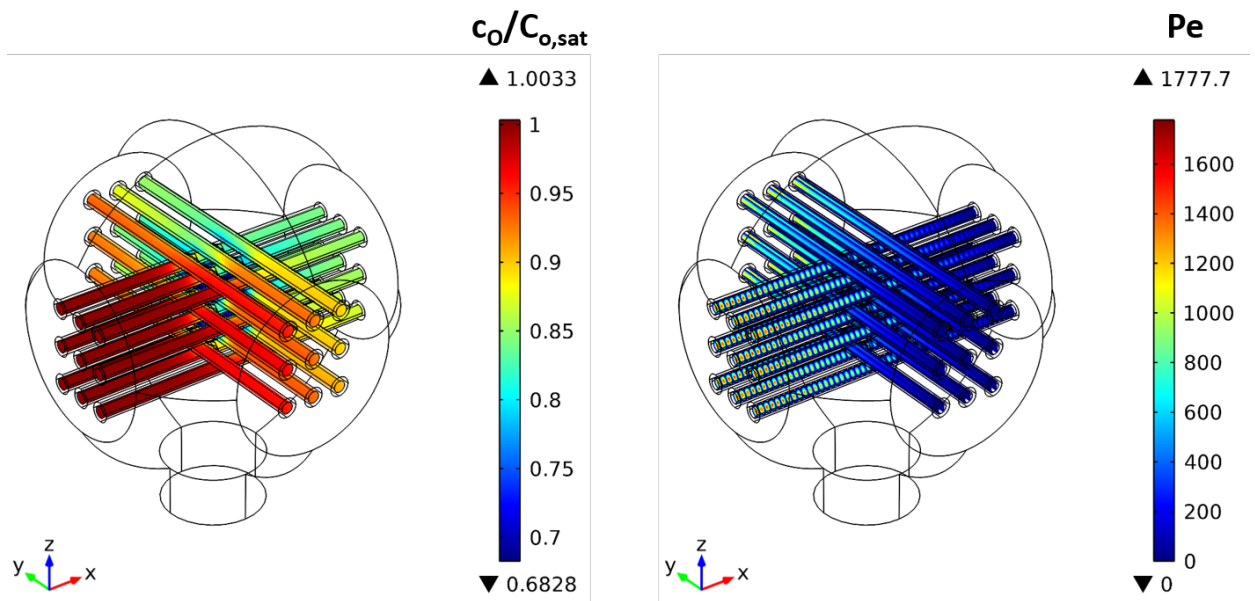


Figure 7.5 Oxygen concentration in the lumina, supplying-removing flow pattern. $D_{sph}=400 \mu\text{m}$, $C_{O,sat}=185 \mu\text{mol/L}$, $Q_{BR}=1 \text{ ml/min}$, $V_{max}=25 \text{ nmol/(s.cm}^3\text{)}$, $K_m=5.6 \text{ mm Hg}$, $\epsilon_{cc}=0.42$, $\epsilon_m=0.7$.

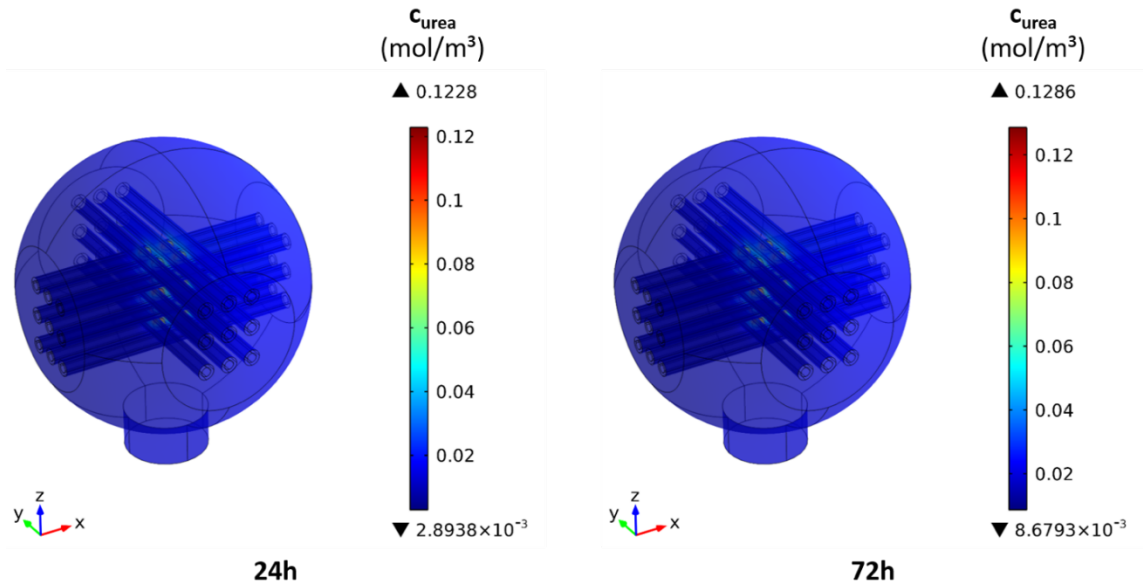


Figure 7. 6 Urea concentration in the bioreactor, supplying-removing flow pattern. $D_{sph}=400 \mu\text{m}$, $Q_{BR}=1 \text{ ml/min}$, $\epsilon_{cc}=0.42$, $\epsilon_m=0.7$.

Figure 7. 6 shows the urea concentrations in the ECS. As expected, the highest urea concentrations are found inside the spheroids (52-220 $\mu\text{mol/L}$ after 24 hours). Urea concentration in the ECS also changes in the x direction, this time increasing in the ECS along the supplying bundle (from 3 to $\sim 19 \mu\text{mol/L}$ after 24h).

7.3.1 Effect of minimizing the stagnant region on oxygen transfer

The same approach was applied to the cubic bioreactor to obtain the oxygen profiles under steady-state conditions and supplying-removing flow pattern. The calculations here were again based on the actual bioreactor with 100 HF/bundle and the inlet flow rate was calculated in such a way that the radial permeation flux through the hollow fiber is equal to that of both miniaturized and actual bioreactor.

The trends observed here are similar to the miniaturized bioreactor. However, the DOC values are significantly lower in all domains. Inside the spheroids (

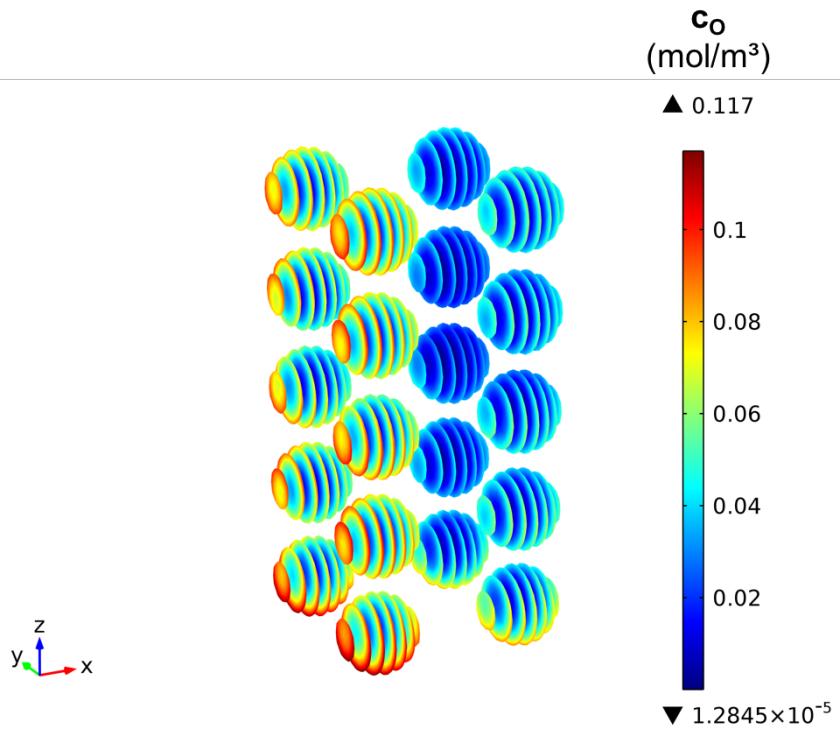


Figure 7. 7), the DOC drops from 117 $\mu\text{mol/L}$ to almost zero, suggesting more severe hypoxia. DOC drop within ECS along the supplying bundle also decreases by around 50%, from 161 to 81 $\mu\text{mol/L}$, average values (Figure 7. 8), consistent with the luminal concentrations (Figure 7. 9).

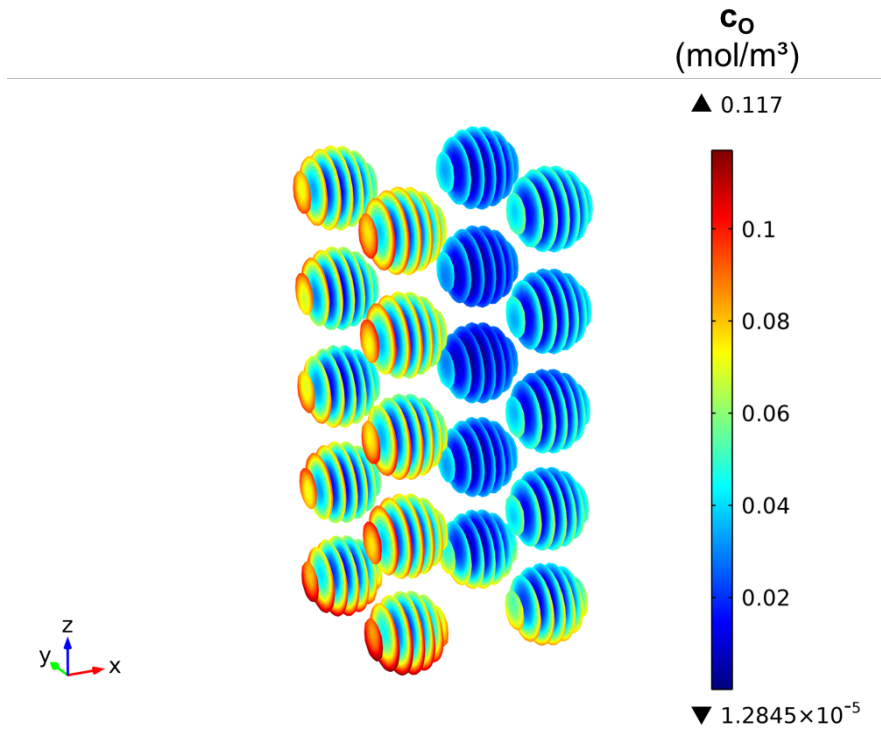


Figure 7.7 Oxygen concentration in the spheroids for a cubic bioreactor, supplying-removing flow pattern.

$D_{sph}=400 \mu\text{m}$, $C_{o,sat}=185 \mu\text{mol/L}$, $Q_{BR}=1 \text{ ml/min}$, $V_{max}=25 \text{ nmol}/(\text{s.cm}^3)$, $K_m=5.6 \text{ mm Hg}$, $\epsilon_{cc}=0.42$, $\epsilon_m=0.7$.

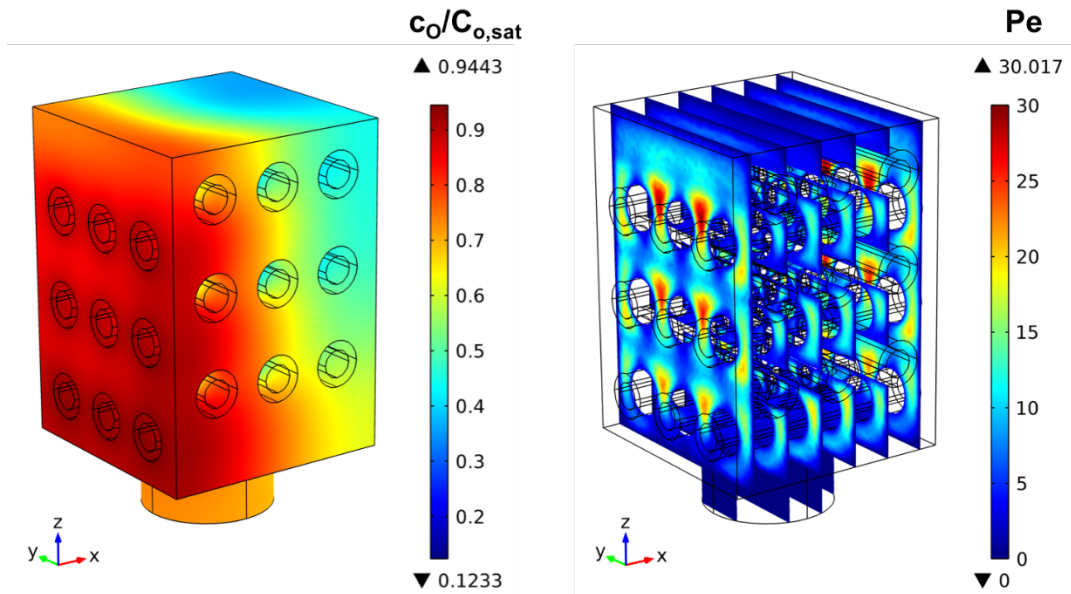


Figure 7.8 Oxygen concentration and Peclet number in the extra-capillary space for a cubic bioreactor, supplying-removing flow pattern.

$D_{sph}=400 \mu\text{m}$, $C_{o,sat}=185 \mu\text{mol/L}$, $Q_{BR}=1 \text{ ml/min}$, $V_{max}=25 \text{ nmol}/(\text{s.cm}^3)$, $K_m=5.6 \text{ mm Hg}$, $\epsilon_{cc}=0.42$, $\epsilon_m=0.7$.

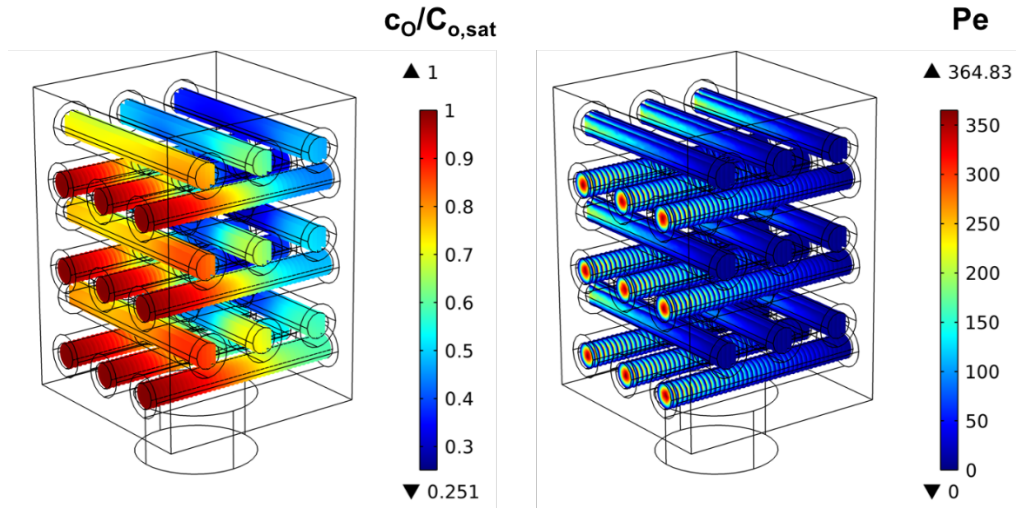


Figure 7. 9 Oxygen concentration and Peclet number in the lumina for a cubic bioreactor, supplying-removing flow pattern. $D_{sph}=400 \mu\text{m}$, $C_{o,sat}=185 \mu\text{mol/L}$, $Q_{BR}=1 \text{ ml/min}$, $V_{max}=25 \text{ nmol}/(\text{s.cm}^3)$, $K_m=5.6 \text{ mm Hg}$, $\epsilon_{cc}=0.42$, $\epsilon_m=0.7$.

7.3.2 Effect of retentate flow on oxygen transfer

Effect of adding a retentate flow on the oxygen concentration within the lumen and consequently the ECS was investigated in the supplying-removing flow pattern.

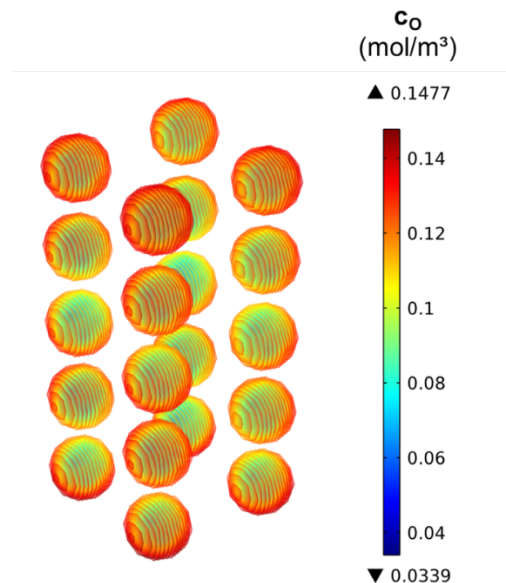


Figure 7. 10 Oxygen concentration in the spheroids in the bioreactor with a retentate flow is present, supplying-removing flow pattern. $D_{sph}=400 \mu\text{m}$, $C_{o,sat}=185 \mu\text{mol/L}$, $Q_{BR}=1 \text{ ml/min}$, $V_{max}=25 \text{ nmol}/(\text{s.cm}^3)$, $K_m=5.6 \text{ mm Hg}$, $\epsilon_{cc}=0.42$, $\epsilon_m=0.7$.

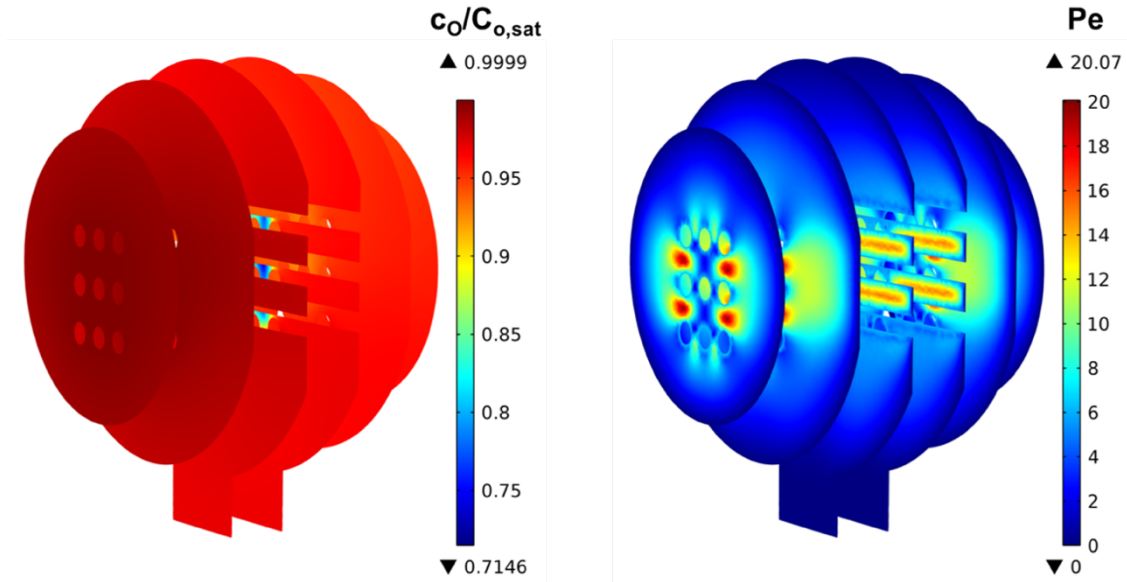


Figure 7. 11 Oxygen concentration and Peclet number in the extra-capillary space of the bioreactor with a retentate flow is present, supplying-removing flow pattern. $D_{sph}=400 \mu m$, $C_{o,sat}=185 \mu mol/L$, $Q_{BR}=1 ml/min$, $V_{max}=25 nmol/(s.cm^3)$, $K_m=5.6 mm Hg$, $\epsilon_{cc}=0.42$, $\epsilon_m=0.7$.

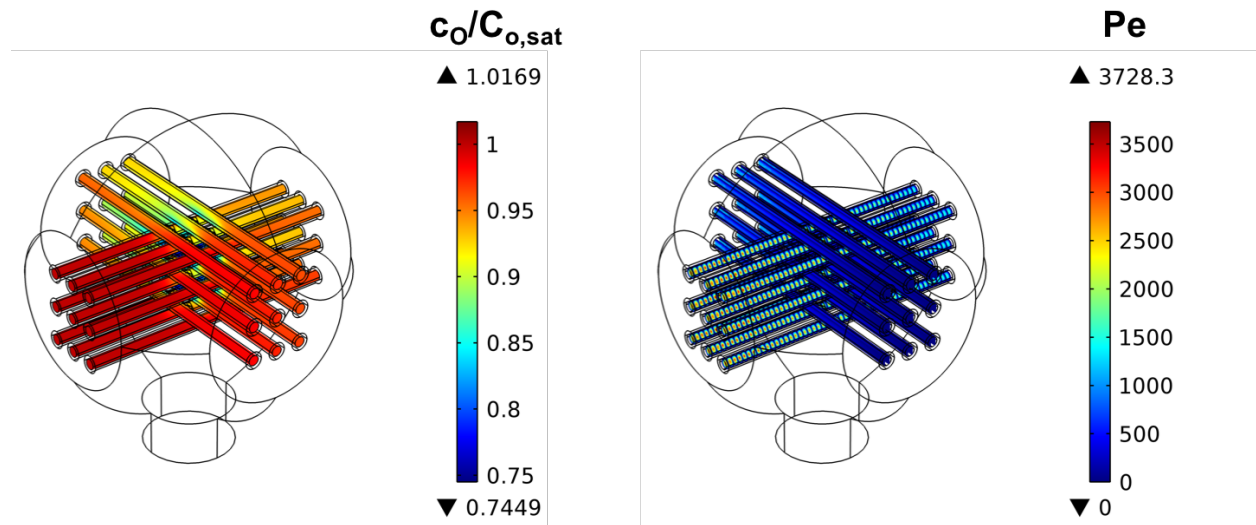


Figure 7. 12 Oxygen concentration and Peclet number in the lumina of the bioreactor with a retentate flow is present, supplying-removing flow pattern. $D_{sph}=400 \mu m$, $C_{o,sat}=185 \mu mol/L$, $Q_{BR}=1 ml/min$, $V_{max}=25 nmol/(s.cm^3)$, $K_m=5.6 mm Hg$, $\epsilon_{cc}=0.42$, $\epsilon_m=0.7$.

As shown in Figure 7. 10, adding retentate flow to the supplying lumina increased DOC values inside the spheroids (34-148 $\mu mol/L$) in comparison with the closed-end case previously described (22-143 $\mu mol/L$), reducing exposure to hypoxic conditions. Adding retentate also reduces DOC

drop in the ECS by ~5% in the x-direction, with the minimum value of 98 $\mu\text{mol/L}$ (Figure 7. 11). A 5% drop in luminal DOC was also observed in the supplying bundle (Figure 7. 12).

7.3.3 Effect of flow pattern and fluid dynamics

In case both bundles are used to either supply or remove the culture medium to/from the bioreactor, fluid dynamics inside the ECS is affected which can potentially influence oxygen transfer to cells. Miniaturized bioreactor was used to evaluate such effects and the results are herewith presented.

- **Both bundles supplying the culture medium:**

In this case, the supplying bundle actually consists of 18 hollow fibers instead of 9. Therefore, the inlet flow rate and consequently the radial permeation flux through each hollow fiber are half of those of the supplying-removing model, but the total permeation rate into the bioreactor is the same. Figure 7. 13 shows the DOC profile inside the spheroids. Lower values observed in comparison with the supplying-removing model (Figure 7. 3) suggest aggravated performance of the bioreactor. DOC values in ECS decrease in both x and y directions by around 18%, in agreement with luminal DOC drop in both bundles.

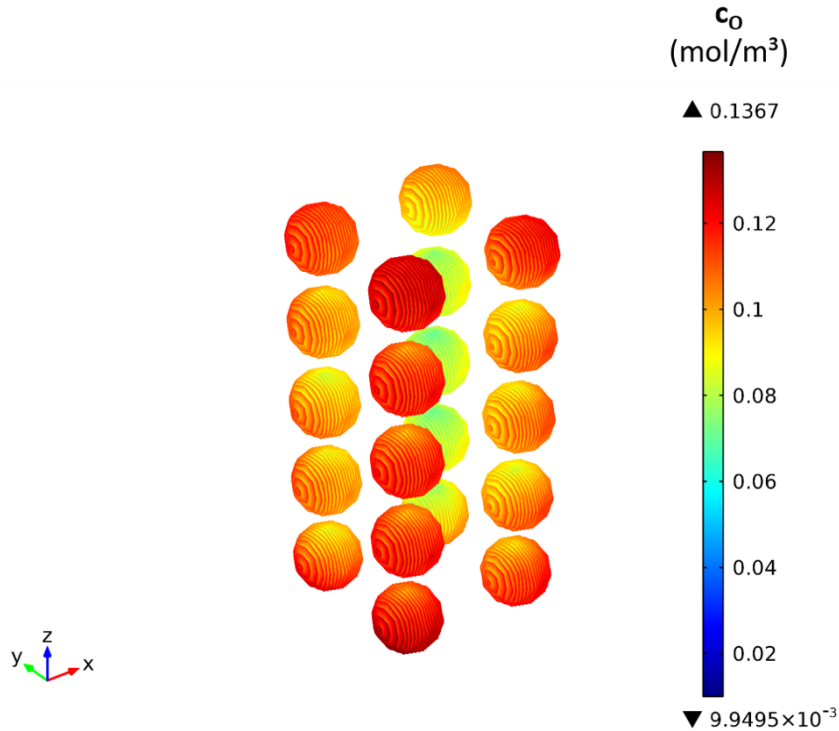


Figure 7. 13 Oxygen concentration in the spheroids, both bundles supplying the culture medium. $D_{sph}=400 \mu\text{m}$, $C_{o,sat}=185 \mu\text{mol/L}$, $Q_{BR}=1 \text{ ml/min}$, $V_{max}=25 \text{ nmol/(s.cm}^3)$, $K_m=5.6 \text{ mm Hg}$, $\epsilon_{cc}=0.42$, $\epsilon_m=0.7$.

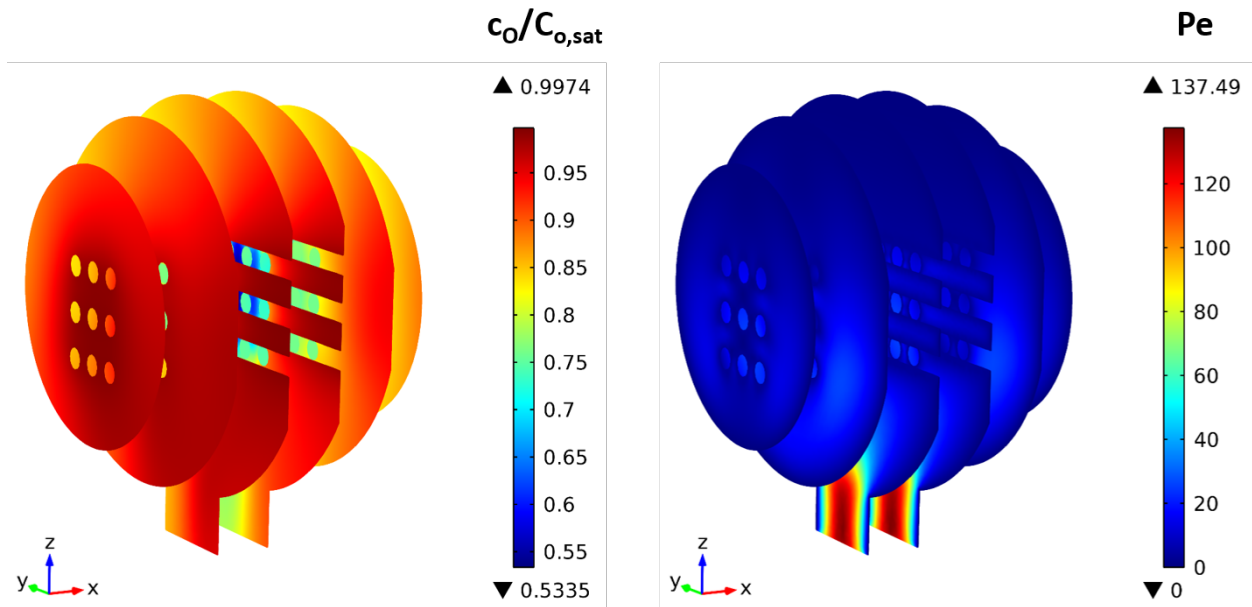


Figure 7. 14 Oxygen concentration in the extra-capillary space, both bundles supplying the culture medium. $D_{sph}=400 \mu\text{m}$, $C_{o,sat}=185 \mu\text{mol/L}$, $Q_{BR}=1 \text{ ml/min}$, $V_{max}=25 \text{ nmol}/(\text{s.cm}^3)$, $K_m=5.6 \text{ mm Hg}$, $\epsilon_{cc}=0.42$, $\epsilon_m=0.7$.

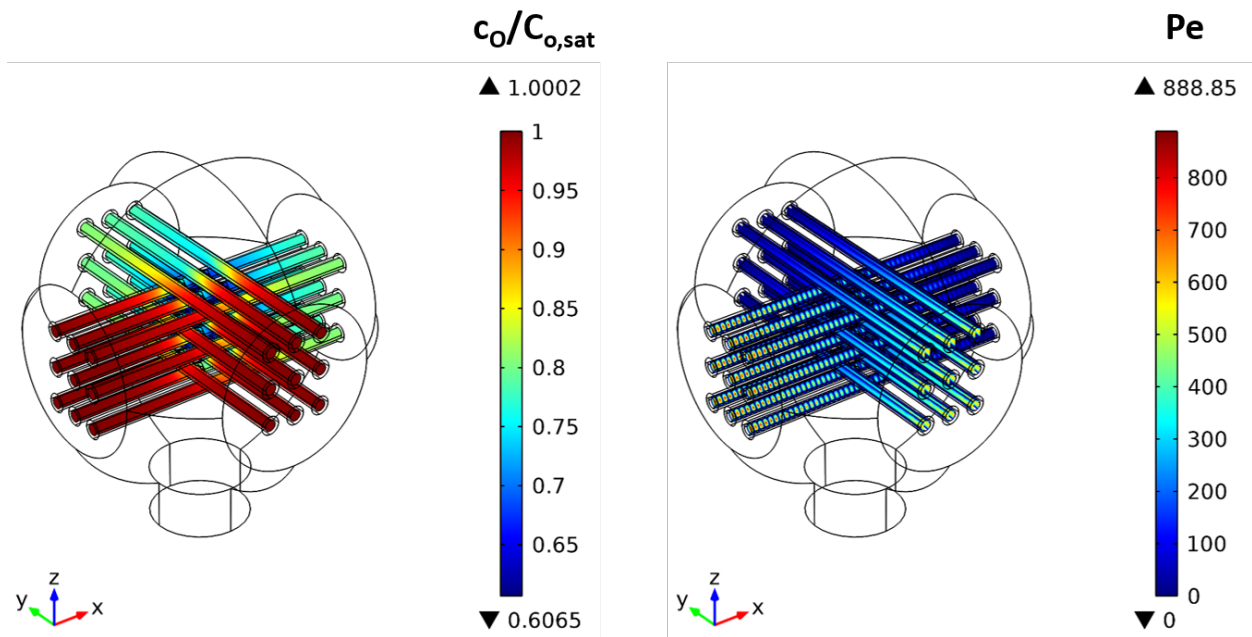


Figure 7. 15 Oxygen concentration in the lumina, both bundles supplying the culture medium. $D_{sph}=400 \mu\text{m}$, $C_{o,sat}=185 \mu\text{mol/L}$, $Q_{BR}=1 \text{ ml/min}$, $V_{max}=25 \text{ nmol}/(\text{s.cm}^3)$, $K_m=5.6 \text{ mm Hg}$, $\epsilon_{cc}=0.42$, $\epsilon_m=0.7$.

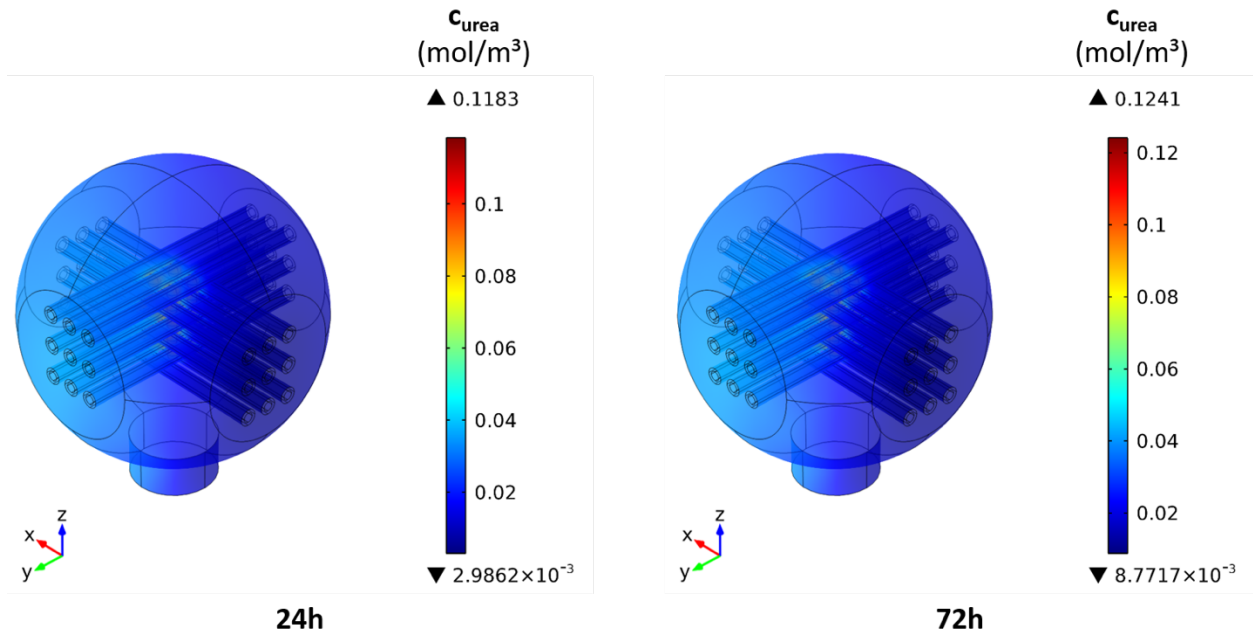


Figure 7. 16 Urea concentration in the bioreactor, both bundles supplying the culture medium. $D_{sph}=400 \mu m$, $Q_{BR}=1 \text{ ml/min}$, $\epsilon_{cc}=0.42$, $\epsilon_m=0.7$.

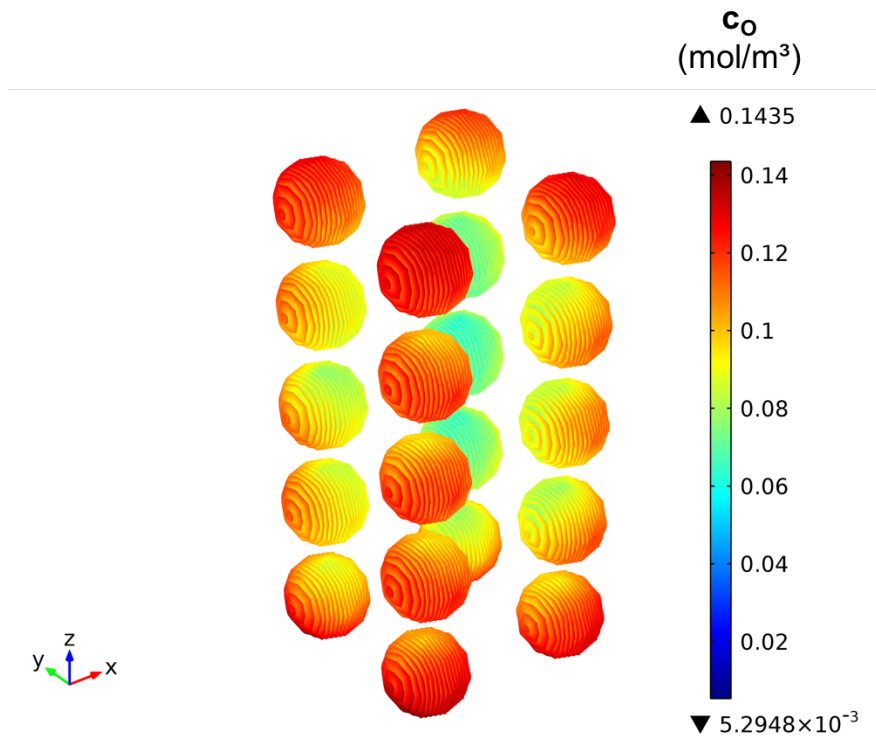


Figure 7. 17 Oxygen concentration in the spheroids, both bundles removing the culture medium. $D_{sph}=400 \mu m$, $C_{o,sat}=185 \mu mol/L$, $Q_{BR}=1 \text{ ml/min}$, $V_{max}=25 \text{ nmol/(s.cm}^3)$, $K_m=5.6 \text{ mm Hg}$, $\epsilon_{cc}=0.42$, $\epsilon_m=0.7$.

Urea concentration profile inversely follows similar trends as DOC, since the former is being produced and latter is consumed in the spheroids. Urea concentration in the ECS increases in x and y directions by ~470%

- **Both bundles removing the culture medium:**

Contrary to all-supplying model, here the culture medium is supplied through the housing connection, and removed by both bundles. However, the amount of total perfusion rate of the bioreactor and the radial permeation flux rate through the hollow fibers is equal to the previous case. Lower DOC values are observed in the spheroids (Figure 7. 17) and the ECS (Figure 7. 18), while they decrease in x and y directions in the ECS and lumina (Figure 7. 19).

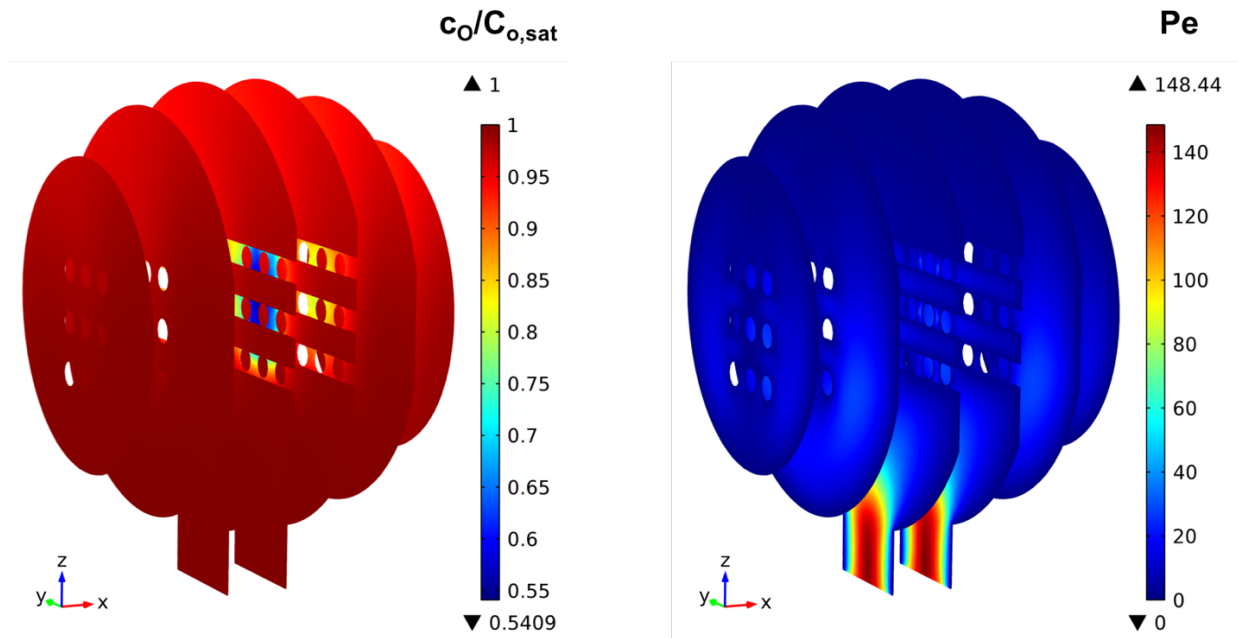


Figure 7. 18 Oxygen concentration in the extra-capillary space, both bundles removing the culture medium. $D_{sph}=400 \mu\text{m}$, $C_{o,sat}=185 \mu\text{mol/L}$, $QBR=1 \text{ ml/min}$, $V_{max}=25 \text{ nmol/(s.cm}^3\text{)}$, $K_m=5.6 \text{ mm Hg}$, $\epsilon_{cc}=0.42$, $\epsilon_m=0.7$.

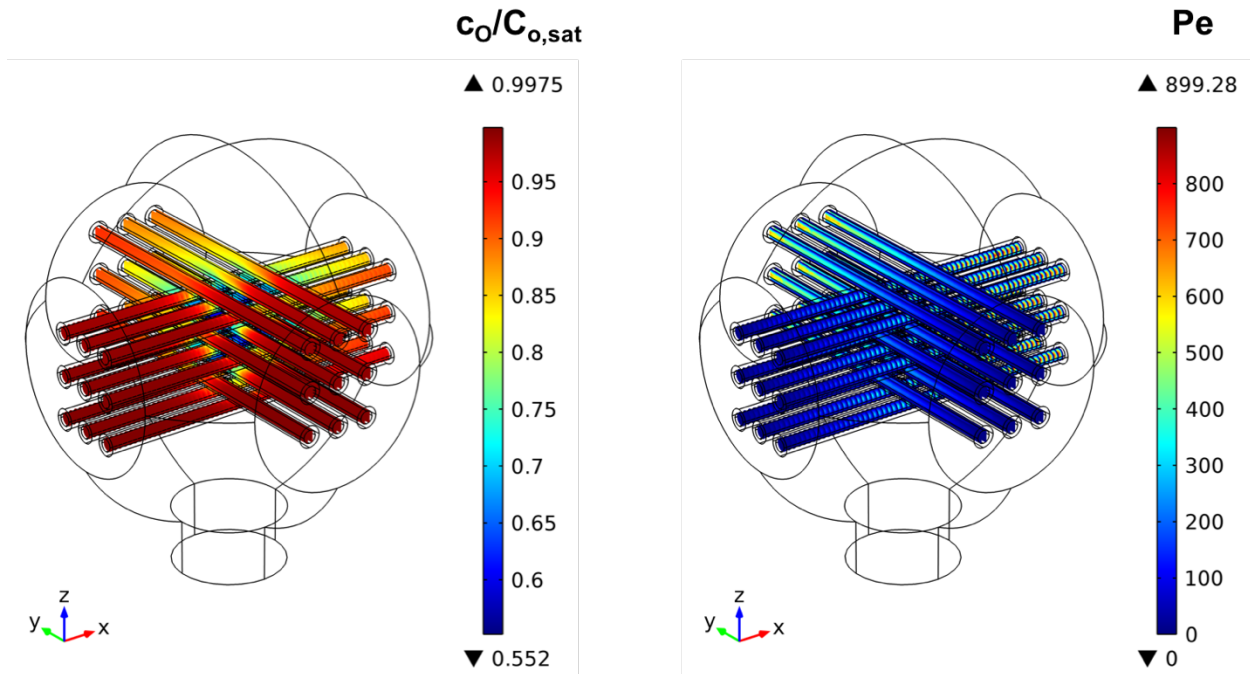


Figure 7. 19 Oxygen concentration in the lumina, both bundles removing the culture medium. $D_{sph}=400 \mu\text{m}$, $C_{o,sat}=185 \mu\text{mol/L}$, $Q_{BR}=1 \text{ ml/min}$, $V_{max}=25 \text{ nmol/(s.cm}^3\text{)}$, $K_m=5.6 \text{ mm Hg}$, $\epsilon_{cc}=0.42$, $\epsilon_m=0.7$.

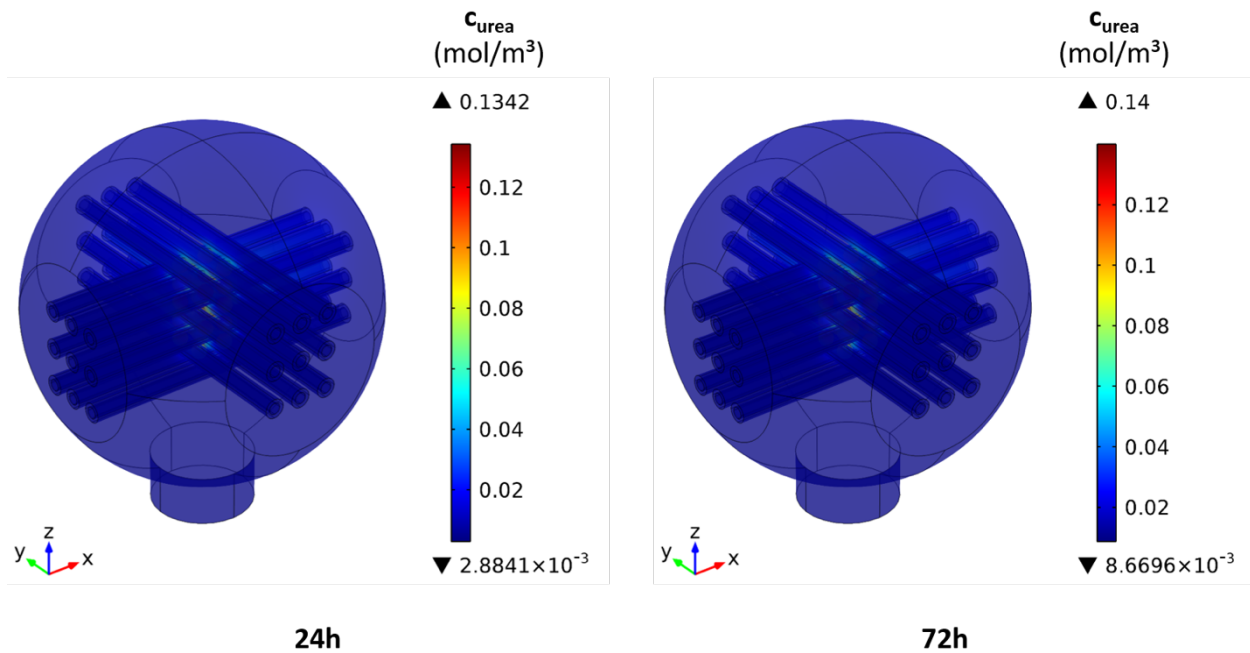


Figure 7. 20 Urea concentration in the bioreactor, both bundles removing the culture medium. $D_{sph}=400 \mu\text{m}$, $Q_{BR}=1 \text{ ml/min}$, $\epsilon_{cc}=0.42$, $\epsilon_m=0.7$.

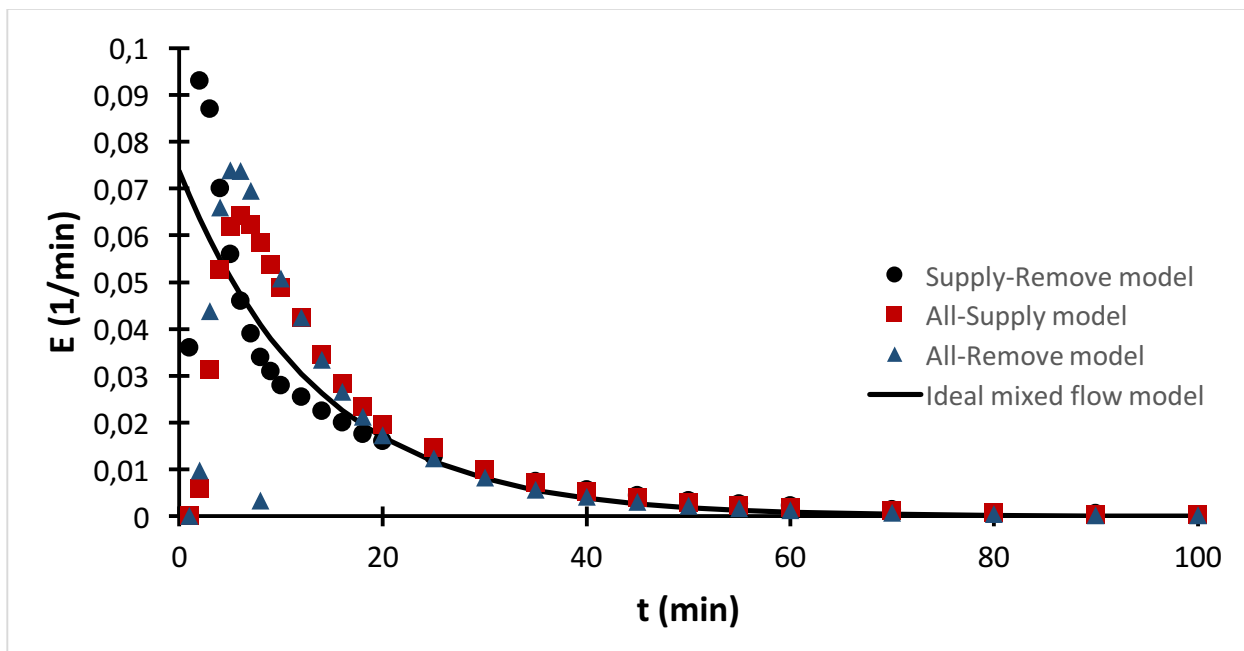
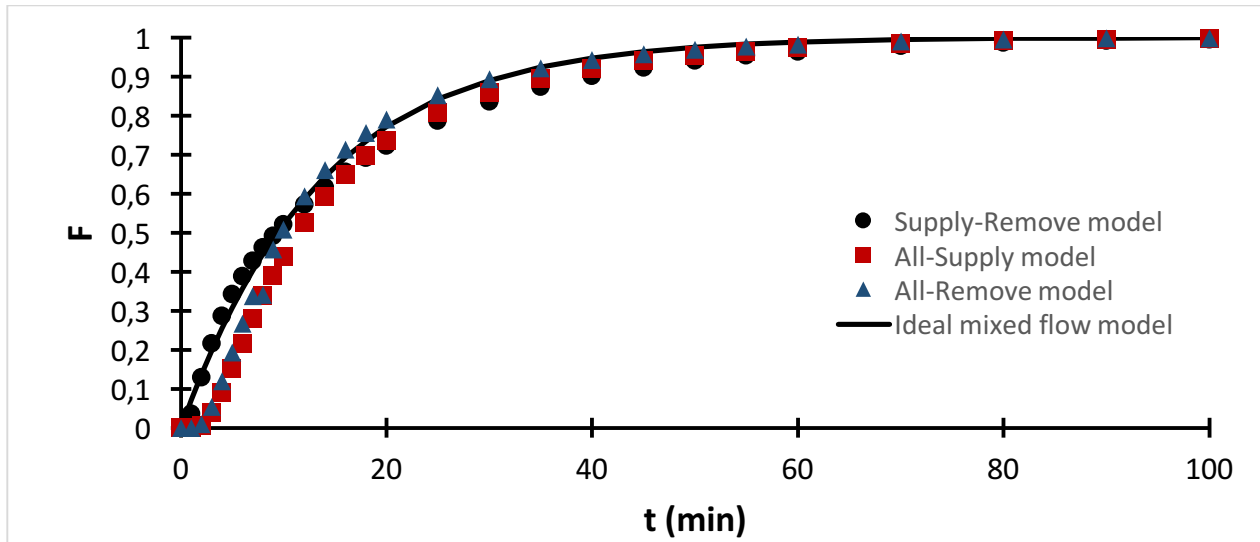


Figure 7. 21 F (top) and E (bottom) curves used in residence time distribution analysis, obtained through modelling for three different flow patterns.

Tracer experiment for residence time distribution analysis is generally carried out experimentally. However, it can also be modelled in the miniaturized bioreactor as an insightful predictive/analytic tool. Figure 7. 21 shows the F and E curves (previously explained in Chapter 2), obtained for the aforementioned flow patterns and compared to the ideal mixed flow model [6]. The tracer solution (with the same concentration of 2.2 g/L) was fed into the bioreactor at $t=0$ at a flow rate of 1 ml/min, and its average concentration at the bioreactor outlet was obtained through a time-

dependent study. Steady-state conditions is reached in all the systems after around 80 min, while slight differences are observed among the F curves. Supply-remove model follows the ideal mixed flow at first and then diverges slightly, while the other two conditions show the opposite behaviour. Early curve (narrow distribution with a rather steep slope) is observed in all three E curves, the sharpest belonging to supply-remove model.

7.3.4 Model based on experimental data

Experimental values for the operational conditions and other properties were applied to the miniaturized bioreactor model, as explained in section 6.3.3 for single-spheroid model: $C_{o,sat}=224$ $\mu\text{mol/L}$, $Q_{BR}=0.6$ ml/min, $V_{max}=17$ nmol/(s.cm³), $K_m=5.6$ mm Hg, $\epsilon_{cc}=0.41$, $\epsilon_m=0.8$, $\delta_{HF}=250\mu\text{m}$. The procedure for miniaturization of the geometry was already explained. “Scaling down” the number of cells for the miniaturized bioreactor also needs to be established. Two different methods were used:

- (i) According to the experimental procedures carried out, average number of spheroids in each inter-HF “void” within the crossed section is 5-6. First, 6 spheroids were considered in each of the 20 available inter-HF voids. Next, the possibility of having a larger spheroid resulting from merging [7] of the six spheroids (equivalent diameter of 363 μm) was considered.
- (ii) Total number of cells seeded during the experiment was directly scaled down using the ratio of the total mass transfer area (outer surface of the hollow fibers) in the miniaturized model to that of the actual bioreactor. The equivalent diameter of the resulting spheroid was calculated as 359 μm .

Figure 7. 22 shows the DOC values in ECS and the cellular compartment in the 6-spheroid model, suggesting that the cells are exposed to oxygen concentrations higher than the physiological range. Merging process resulted in lower DOC values in the equivalent spheroid (Figure 7. 23). As a matter of fact, the minimum observed DOC dropped 25%, from 150 $\mu\text{mol/L}$ to 112 $\mu\text{mol/L}$.

The 6-spheroid model contains slightly higher total number of cells compared to the experimental conditions. However, the difference between the equivalent spheroid diameters calculated based on 6-spheroid model and the scaled-down model (Figure 7. 24) is rather small, thus the DOC values do not significantly differ.

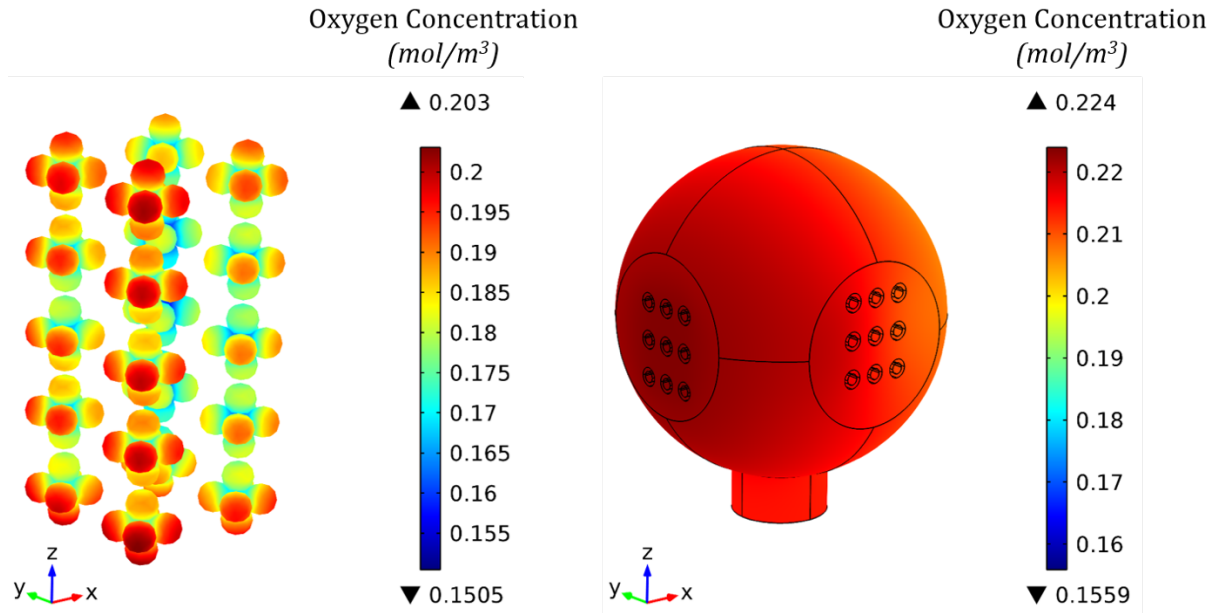


Figure 7. 22 (Left) Oxygen concentration in the spheroids, supplying-removing pattern, 6 spheroids per ECS unit, (Right) oxygen concentration in the ECS. $D_{sph}=200 \mu\text{m}$, $C_{o,sat}=224 \mu\text{mol/L}$, $Q_{BR}=0.6 \text{ ml/min}$, $V_{max}=17 \text{ nmol/(s.cm}^3\text{)}$, $K_m=5.6 \text{ mm Hg}$, $\epsilon_{cc}=0.41$, $\epsilon_m=0.8$.

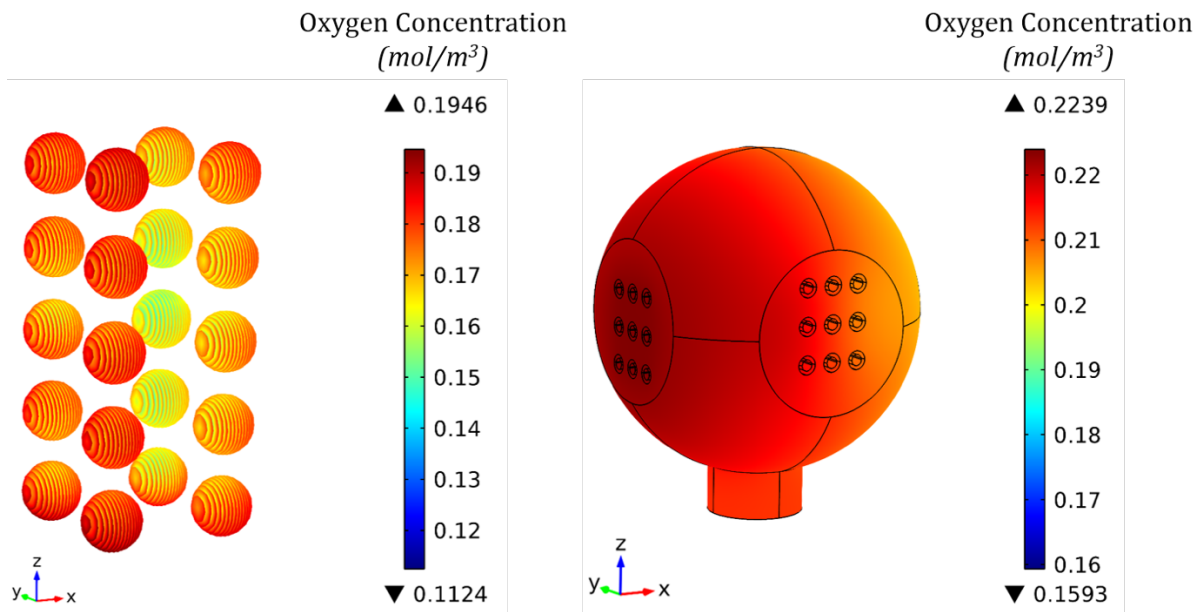


Figure 7. 23 (Left) Oxygen concentration in the merged 6 spheroids, supplying-removing pattern. (Right) Oxygen concentration in the ECS. Equivalent $D_{sph}=363 \mu\text{m}$, $C_{o,sat}=224 \mu\text{mol/L}$, $Q_{BR}=0.6 \text{ ml/min}$, $V_{max}=17 \text{ nmol/(s.cm}^3\text{)}$, $K_m=5.6 \text{ mm Hg}$, $\epsilon_{cc}=0.41$, $\epsilon_m=0.8$.

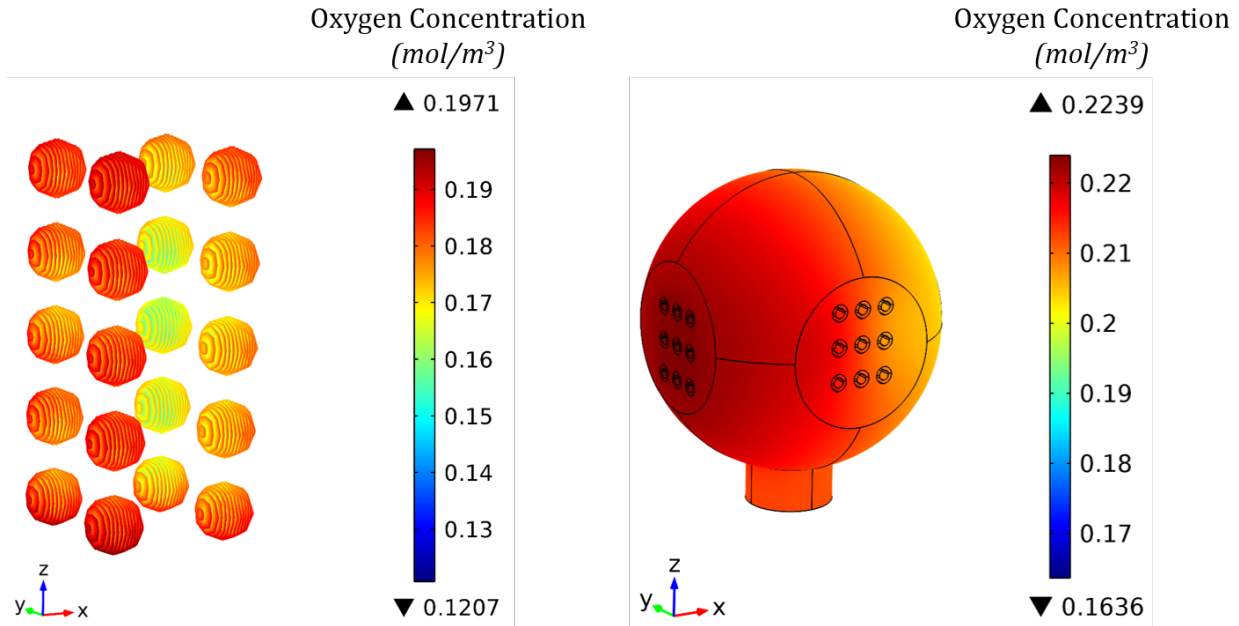


Figure 7. 24 (Left) Oxygen concentration in the spheroids based on scaling down seeded cell number, supplying-removing pattern. (Right) Oxygen concentration in the ECS. Equivalent $D_{sph}=359 \mu\text{m}$, $C_{o,sat}=224 \mu\text{mol/L}$, $QBR=0.6 \text{ ml/min}$, $V_{max}=17 \text{ nmol/(s.cm}^3\text{)}$, $K_m=5.6 \text{ mm Hg}$, $\epsilon_{cc}=0.41$, $\epsilon_m=0.8$.

7.4 Discussion

In the supplying-removing model, a drop of 15% in oxygen concentration is observed along the lumina of the supplying bundle and in the ECS in the x-direction (i.e. along the supplying bundle). Needless to say, the oxygen concentration within the crossed section in the vicinity of spheroids is much lower, down to 0.084 mol/m^3 . The oxygen concentration within the spheroids lies between 0.022 to 0.143 mol/m^3 ($\beta_{Bm}=0.43$, $\beta_{Hpx}=0.02$).

All-supplying model further exacerbates the problem. In this case, the concentration difference between the two ends of the lumina is around 22%. Lower DOC values observed in comparison to the previous case results in higher hypoxia ($\beta_{Hpx}=0.08$). On the other hand, less cells are exposed to oxygen concentrations higher than the in vivo periportal and perivenous range ($\beta_{Bm}=0.52$). For proper comparison between different conditions, the permeation flux in all cases are the same. Therefore, since in here the number of supplying bundles is doubled, the inlet flowrate in each bundle is half of the previous case. This results in reduced Pe numbers and increased influence of

the radial diffusion of oxygen. In the ECS, high concentrations are observed at the region around and in between the bundles' inlets, reducing towards the opposite side.

Another possible pattern is to use both bundles to remove the medium fed from the bottom connection of the bioreactor. An oxygen gradient is also observed here, with the lower concentrations at the region between the bundles' outlets. In terms of hypoxia inside the spheroids, the difference between all-supplying and all-removing models is negligible ($\beta_{Bm}=0.52$, $\beta_{Hpx}=0.09$).

The opposite trends are observed in the urea concentrations of different patterns: increasing concentrations along the supplying bundle in supplying-removing pattern, minimum values in the region between the inlets and increasing to the opposite site in both-supplying pattern.

In the cubic bioreactor with minimized stagnant region, the oxygen concentrations drop significantly along the supplying bundle (by 41-65%). Elimination of the stagnant region results in a smaller geometry and therefore lower lumina flow rates, thus the low Pe numbers in this case. Under the conditions used, such cubic geometry of the bioreactor significantly reduces oxygen transfer into the spheroids, resulting in more cells exposed to hypoxia ($\beta_{Bm}=0.34$, $\beta_{Hpx}=0.62$).

Increasing the luminal flow rate by adding a retentate to the supplying bundle improves the oxygen transfer to the spheroids. The concentration drop along the supplying bundle is reduced to only 4%, and the minimum spheroid concentration is increased by 10% compared to having zero retentate flow. Adding retentate yielded in lower DOC drop in ECS, and most importantly, elimination of hypoxic conditions ($\beta_{Bm}=0.32$, $\beta_{Hpx}\sim 0$).

In the experimentally-adjusted model, all the cells are exposed to DOC values higher than the physiological range ($\beta_{Bm}=\beta_{Hpx}=0$). The average DOC values in the outlet of the removal bundle in each model are as follows: 207 $\mu\text{mol/L}$ in the 6-spheroid model, 205 $\mu\text{mol/L}$ in the equivalent 6 merged spheroid model, and 205 $\mu\text{mol/L}$ in the equivalent scaled spheroids. The last model is the closest to the experimental value at the outlet of the bioreactor (198 $\mu\text{mol/L}$). It is noteworthy to mention that the mesh grid for miniaturized bioreactor was selected based on the memory requirements to carry out the simulation while single-spheroid model benefitted from proper mesh grid. The results herewith presented are subject to slight changes using when using finer meshes.

7.5 Conclusions

Three possible flow patterns were studied in this chapter, as well as the effect of retentate in the supplying lumina and elimination of the stagnant region. The flow pattern does not drastically change the oxygen concentration profiles. However, it seems slightly more uniform when both bundles are removing the medium, while it is somewhat higher inside the spheroids in the supplying-removing pattern. Presence of concentration gradients could strongly influence monitoring/evaluator procedures in larger systems, e.g. in terms of positioning oxygen sensors inside the bioreactor or the sampling location.

Using higher flow rates in the supplying lumina by adding the retentate at the outlet was proved very effective, reducing the concentration drop along the lumen and providing better oxygen supply to the spheroids. Elimination of the stagnant region while using the same permeation flux adversely affects the oxygen transfer due to the same reason of lower flow rate in the lumina.

References

- [1] A. Krogh, "The number and distribution of capillaries in muscles with calculations of the oxygen pressure head necessary for supplying the tissue," *The Journal of physiology*, vol. 52, pp. 409-415, 1919.
- [2] R. J. Shipley and S. L. Waters, "Fluid and mass transport modelling to drive the design of cell-packed hollow fibre bioreactors for tissue engineering applications," *Math Med Biol*, vol. 29, pp. 329-59, Dec 2012.
- [3] L. De Bartolo, S. Salerno, E. Curcio, A. Piscioneri, M. Rende, S. Morelli, *et al.*, "Human hepatocyte functions in a crossed hollow fiber membrane bioreactor," *Biomaterials*, vol. 30, pp. 2531-43, May 2009.
- [4] P. Hay, A. Veitch, M. Smith, R. Cousins, and J. Gaylor, "Oxygen Transfer in a Diffusion-Limited Hollow Fiber Bioartificial Liver," *Artificial organs*, vol. 24, pp. 278-288, 2000.
- [5] K. Jungermann and T. Kietzmann, "Oxygen: modulator of metabolic zonation and disease of the liver," *Hepatology*, vol. 31, pp. 255-60, Feb 2000.
- [6] O. Levenspiel, "Chemical reaction engineering," *Industrial & engineering chemistry research*, vol. 38, pp. 4140-4143, 1999.
- [7] A. Messina, S. Morelli, G. Forgacs, G. Barbieri, E. Drioli, and L. De Bartolo, "Self-assembly of tissue spheroids on polymeric membranes," *J Tissue Eng Regen Med*, Nov 09 2015.

Chapter 8

Conclusions and future directions

8.1 Summary of contributions

Perfused bioreactors are increasingly used as 3D cell culture systems – especially in development of liver support systems – aimed to enhance and prolong the viability and functionality of the cultured cells. However, their design and operation are challenged by numerous factors, including biological aspects (cell types in mono-cultures or co-cultures, cell density, seeding procedure, culture protocols, etc.), and transport phenomena (sufficient oxygen and nutrient supply to the cell population, efficient removal of catabolites produced, limitations in mass transfer, mixing inside the bioreactor, shear stress exerted on cells, etc.). The latter topic has been extensively investigated in this study.

First, a diffusion-reaction model was developed and applied to simulate mass transport in static spheroid culture in a multi-well plate. This simple model enabled the evaluation of oxygen and urea concentrations at the cellular periphery and elucidated the necessity of having well-designed perfused systems. Moreover, this system facilitates evaluation of some of the properties, as well as comparison with the experimental data.

A general model was developed for mass and momentum transfer in a convection-enhanced, crossed-configuration, hollow fiber membrane bioreactor. The feasibility of exploiting this bioreactor to culture spheroids as 3D cellular constructs in terms of sufficient oxygen supply was investigated. Important transport properties such as diffusion coefficients and permeabilities of the porous media were parametrized and expressed as a function of porosity as a microstructural characteristic. The model can be adapted and applied to any membrane-based bioreactor. Oxygen transfer into the spheroids was thoroughly investigated, and establishment of *in vivo*-like oxygen concentrations was found achievable in large, high-porosity spheroids.

The geometry of the bioreactor studied here is rather complex, due to which the conventional Krogh cylinder approach considering each hollow fiber individually does not apply. To decrease the computational complexity of the model, a periodic unit element representative of the system was employed.

Many parameters are involved to mathematically define the system, evident from the presented model. Operational and design parameters can be altered to obtain optimum results, while the kinetics and microstructure of the cellular mass are intrinsic to the system and are not modifiable in a controlled manner. The sensitivity of the system towards different conditions and properties, as well as their effect on oxygen transfer was investigated through a parametric study. One important finding of this study – as expected from the developed model – was the significant importance of the porosities. Theoretically speaking, the governing role of microstructural properties in transport phenomena in porous media is well-known. However, they are sometimes overlooked (especially in the cellular mass) in modelling studies since their evaluation and monitoring is very challenging and limited data is available in this regard. Knowing the spheroid diameter and average number of cells per spheroid, its porosity was estimated. Monitoring the cell density and temporal changes in spheroid size during culture time in a systematic manner provides a means to estimate the porosity. In extra-capillary space, convection and diffusion rate were in the same order ($Pe_{ecs} \sim 1$), while inside the spheroids diffusion is the dominant transport mechanism. Consequently, extra-spheroid diffusive properties still play an important role and cannot be underestimated. Moreover, the study confirms saturated oxygen concentration in culture medium as the influential operational condition, more so than the perfusion rate.

The size and density of the “cellular mass” can be controlled before seeding. However, during the culture period, they are subject to change. Formation of larger cellular masses due to merging of spheroids (or due to proliferation in other systems) increases the diffusion length, potentially causing necrosis at the core due to hypoxia. The feasibility of achieving physiological oxygen concentrations in large spheroids was investigated for two different intra-spheroid porosities. Regulation of oxygen concentration gradient was more manageable in spheroids with higher porosity which lead to feasibility of achieving an in vivo-like microenvironment in terms of oxygen concentration. At low porosities, the spheroid core suffers from hypoxia while the outer shell is exposed to hyperoxia.

Another important temporal microstructural change is the shrinkage of spheroids during the culture period, due to which the number of cells per spheroid remains intact but the diameter and consequently the porosity changes. A %10 decrease in the diameter of the spheroid was mathematically investigated. The results showed drastic changes in DOC profile with nearly anoxic conditions at the center, despite keeping the number of cells per spheroid intact.

Periodic unit element approach is commonly used in modelling studies and as already explained, provides insightful information regarding the cellular microenvironment. However, investigation of the fluid dynamics and other aspects arising from the bioreactor design as a whole – such as mixing – may not be thoroughly performed. In this study, a miniaturized bioreactor model was also developed to address such shortcomings. Employment of the miniaturized bioreactor model enabled us to study fluid dynamics inside the bioreactor, namely the effect of different flow patterns, mixing properties and concentration gradients across the extra-capillary space. It was also used to simulate the residence time distribution analysis for different conditions. According to this model, significant oxygen concentration drop is observed in the lumina of the hollow fibers. Accordingly, concentration gradients in ECS follow the same pattern, resulting in non-uniform concentration profiles across the bioreactor. This phenomenon can be exacerbated in large-scale systems which in turn adversely affects the bioreactor performance and monitoring measures such as the accuracy of oxygen readings or liability of samplings.

8.2 Recommendations for future work

The bioreactor introduced and investigated in this study was a prototype assembled in-house and used for small-scale experiments. However, both the geometry and the assembly procedure need to be improved. As apparent from the figures and established by the RTD analysis, the stagnant region in current bioreactor is significant. Using another type of housing, e.g. cubic instead of spherical, can allow a packed hollow fiber bundles covering most of the volume. Additionally, through consultation with commercial companies in the field, the assembling process can be immensely simplified by using personalized polymeric housings in which the upper part of the bioreactor can be detached during assembly and attached upon completion, with a mesh readily positioned at the connections for hollow fibers.

The model can be applied for any molecule of interest, granted that the kinetics is provided. Even though several oxygen uptake rates are available in the literature for different hepatocyte systems, it should be precisely established through experiments for primary hepatocyte spheroids. This will minimize the differences between the model and the experimental setup, resulting in more robust and reliable results. Additionally, the kinetics for glucose consumption, urea secretion and albumin synthesis need to be obtained. Using the model for these molecules assists us to gain more

information on species transport and to extract more practical data such as the optimum time for changing the culture medium.

Temporal changes in the porous media should be systematically monitored and possibly correlated. Micro-structural changes of the spheroids due to shrinkage, merging, disintegration, necrosis or proliferation of cells (the latter for cell types other than hepatocytes) should be observed and analyzed through imaging through the course of culture time. Realistic estimation or even formulation of the transport properties will then be possible through (advanced) image analysis and incorporated into the system.

In this study, absorption of species on the membranes was not studied. Evaluation of the rate and extent of absorption of different molecules, especially common proteins, during culture time and their effect on the transport properties of the membrane is highly essential for accurate analysis of the cellular functionality and the performance of the bioreactor. If formulated, it can be incorporated into the model – e.g. as a reaction term on or within the membranes – to further advance the mass transport model.

In this study, only hepatocyte mono-culture was investigated. Due to the significant importance of co-cultures, the model should be made applicable cellular masses consisting of different cell types. The optimum composition is generally determined experimentally. In this case, one should notice that other cell types proliferate and increase in number over time. Therefore, the size and cell density of the cellular mass is a function of time. Additionally, the intrinsic metabolic kinetics are different for each cell type, with hepatocytes having the highest oxygen consumption rate. Moreover, the cellular products are not the same, for example albumin is only produced by hepatocytes and not by endothelial or stellate cells. Experimental estimation of the rate of proliferation and necrosis of cells, along with the reaction rates can be remarkable additions to the model.

The miniaturized bioreactor model enabled us to detect (or predict) the oxygen concentration gradient along the lumina of the hollow fibers and consequently within the extra-capillary space of the bioreactor. This is a very important finding which needs to be considered, especially in large-scale systems. Adding retentate flow in the supplying bundle results in higher luminal throughput, and the model showed lower luminal oxygen concentration drop, more uniform concentration profile in ECS and improved oxygen supply to the spheroids. However, actuating

and maintain a known, modifiable perfusion and retentate flow rates requires a precise control system and additional instrumentation. Given the small scale of the system, realization of such control system could be very challenging.

Upon establishment of the aforementioned issues, the next step will be control and automation of the bioreactor. Aside from controlling the retentate flow, it is also necessary to have oxygen control in larger systems. The findings from this study, e.g. the sensitivity analysis or the significance of the retentate flow can be very useful in development of the control systems.

Appendix

Appendix 1: Fluidized-bed bioreactor

A secondment was organized with University of Technology of Compiègne to provide trainings on mass transfer inside the bioreactor and the concept of fluidized bed bioreactor using alginate beads, through experimental investigation of influential operational parameters, fluidization aspects and beads properties.

Main training points during the first section:

- Preparation of monodisperse alginate beads
- Recognition of parameters influencing beads' properties
- Operation of fluidized bed bioreactor using alginate beads
- Theoretical and experimental familiarization with the concept of fluidization
- Evaluation of the terminal velocity of falling alginate beads
- Experimental mass transfer analysis into the alginate beads under static and dynamic conditions.

The secondment was considered as an introductory step for getting acquainted with the fluidized bed bioreactor and gathering preliminary data. Only the performed experiments and the learning points are herewith reported. No cells have been used in this part of the secondment. Only the inert beads and their fluidization have been studied from a merely engineering point of view. The performed experiments are briefly explained in the following sections.

1. Introduction

Fluidization of particles as a multiphase system has been employed for various applications in chemical engineering and biotechnology [1]. In fluidized bed systems, the bed of particles is in fact an expanded, homogenous suspension. A carefully controlled expansion of particles yields in limited pressure drop and advantageous mass transfer properties due to the convection outside the beads and high surface area to volume ratio of the spherical particles. Numerous advantages of fluidization has encouraged researchers to investigate this concept in bioreactors for cell culture or as bioartificial organs. Legallais et al. have proposed a fluidized bed bioreactor using alginate

beads as a potential BAL device [2-4]. In this system, hepatocytes are trapped inside the alginate beads (as mono-culture or co-culture, isolated or 3-D aggregates), providing: (i) a platform for anchorage-based hepatocytes, (ii) protection from shear stress, (iii) immunoprotection of cells, (iv) optimal oxygen and nutrient supply to the cells and transport of catabolites to the medium. The concept and basic process steps for this system are illustrated in Figure 8. 1.

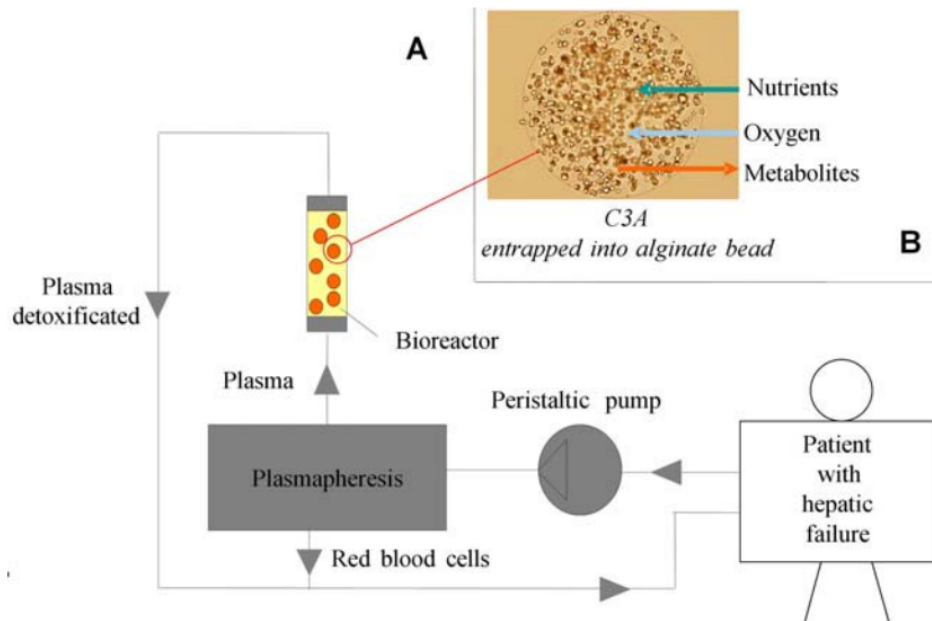


Figure 8. 1 The concept of fluidized bed bioreactor as bioartificial liver [5]

This appendix reports on evaluation of some of the basic yet crucial aspects of the fluidized bed bioreactor. The studies were carried out in University of Technology of Compiègne (Compiègne, France) as training activities.

2. Methods

2.1 Alginate beads preparation

The alginate beads were prepared by alginate drops polymerization in calcium chloride. 1.5% alginate(w/v) in extrusion solution (NaCl, HEPES) was pumped by a syringe pump under controlled flow rate and extruded to monodisperse droplets by a pressure-controlled air jet.

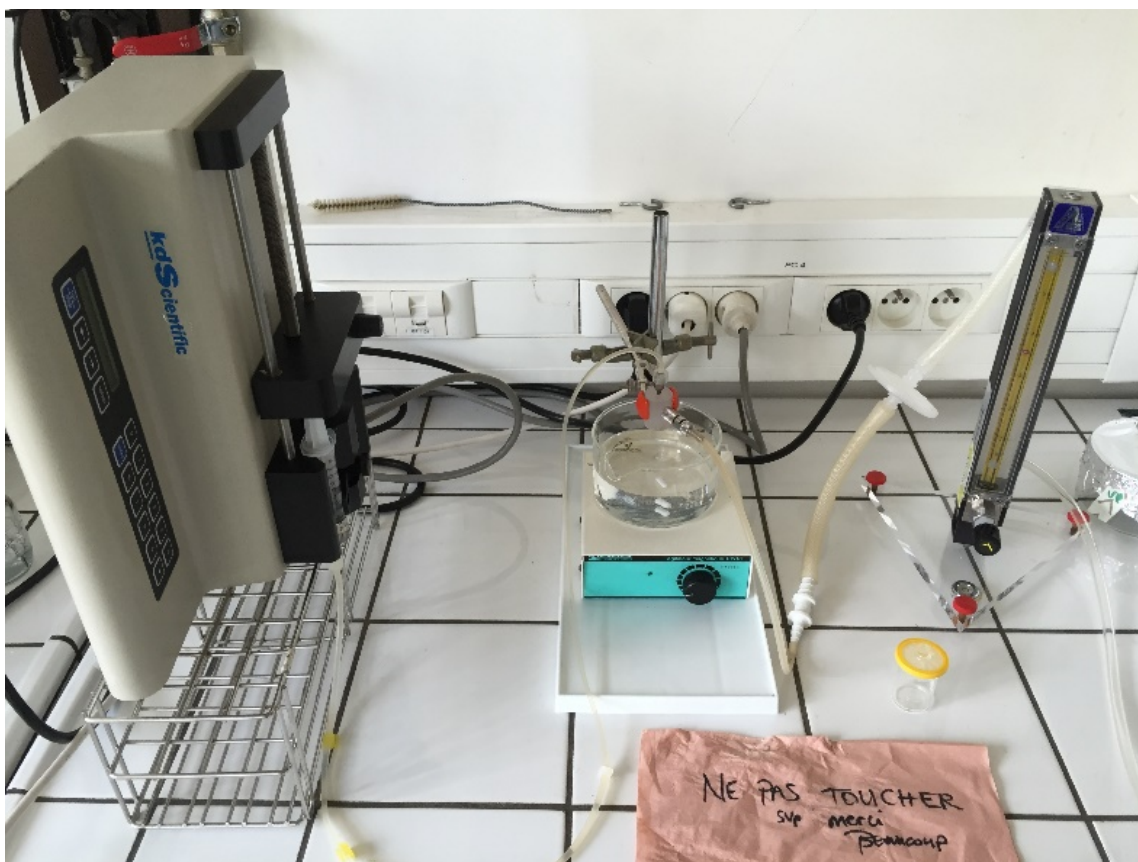


Figure 8. 2 Setup used for preparation of alginate beads

The droplets were then polymerized in gelation solution bath (NaCl , HEPES and CaCl_2) placed under the extrusion needle at the optimum distance. Once polymerized, the beads were subsequently rinsed with and stored in Ringer solution.

In order to make the colorless beads more visible for other experiments in this report, two methods were employed to dye the beads: (i) methylene blue solution added to the already-prepared alginate beads, (ii) blue dextran added to alginate solution before extrusion. The former was used mixed with uncolored beads for visualization of the fluidization and the latter was employed for falling velocity measurement.

2.2 Fluidization

A small lab-scale bioreactor was employed for fluidization experiments. The volume of the seeded beads and the flow rate of the medium fed from the bottom of the bioreactor were adjusted so that the expansion ratio of the bed (final height of the fluidized beads (h_f)/(h_i) initial height of the beads

in the tube at static state) is maintained at 2. Additionally, a bead-free space was carefully remained at the upper part of the bioreactor.

2.3 Beads' swelling over time

The changes in size of the freshly made beads was studied in static and fluidized conditions. After preparation, the beads were divided into two groups: 11ml was used in the bioreactor for fluidization, and some were kept in a petri dish, both using Ringer solution. Over time, samples taken from the fluidized bed and the petri dish were analysed under an inverted light microscope equipped with phase contrast (Leica DMI 6000B, Wetzlar, Germany). In order to determine the diameter, images from 6 spheroids were sized (4 times each) over time.



Figure 8. 3 Fluidized bed bioreactor using (cell-free) alginate beads, expansion ratio 2 ($h_i=5\text{cm}$), flow rate 1.4 ml/min

2.4 Beads' falling velocity

Beads' terminal (or settling) velocity is one of the decisive parameters in the study of the fluidized bed bioreactors. While there are theories to calculate the terminal velocity, experimental evaluation of this parameter can potentially be very suggestive in validating bead's properties and the mathematical models.

The beads were carefully placed on the liquid surface in the cylinder to minimize the initial velocity as much as possible. A uniform light screen was placed behind the cylinder while the camera on the other side of the cylinder recorded the movement of the beads. Colored beads (using blue dextran) were employed for better detection. The camera recordings were then processed using a specialized software. The dimension of the camera screen was calculated separately and thus known, while the software gave the time interval for each image frame, from which the settling velocity was calculated.

2.5 Mass transport into the beads

Mass transfer dynamics into the inert beads was studied using vitamin B12. The beads were exposed to 0.2 g/L vitamin B12 in Ringer solution in both static and dynamic setups and the changes in the concentrations were monitored using spectrophotometry (at wavelength 550nm). This experiment can also be very valuable in validating numerical analysis of the mathematical models as well as bead's properties.

- **Static system**

Alginate beads were carefully placed at the bottom of a cuvette so that the optical beam is not obstructed. 2ml of vitamin B12 (0.2 g/L) solution was added on top and the cuvette was placed in the spectrophotometer. The decrease in absorbance due to diffusion of the molecules into the beads was recorded until it reached steady-state.

- **Dynamic system**

5.5 ml of inert, fresh beads was seeded into the bioreactor and upon starting the pump, were exposed to vitamin B12 solution (25ml total volume, 0.2 g/L). 100 μ L samples were taken over time for absorbance measurement as before.

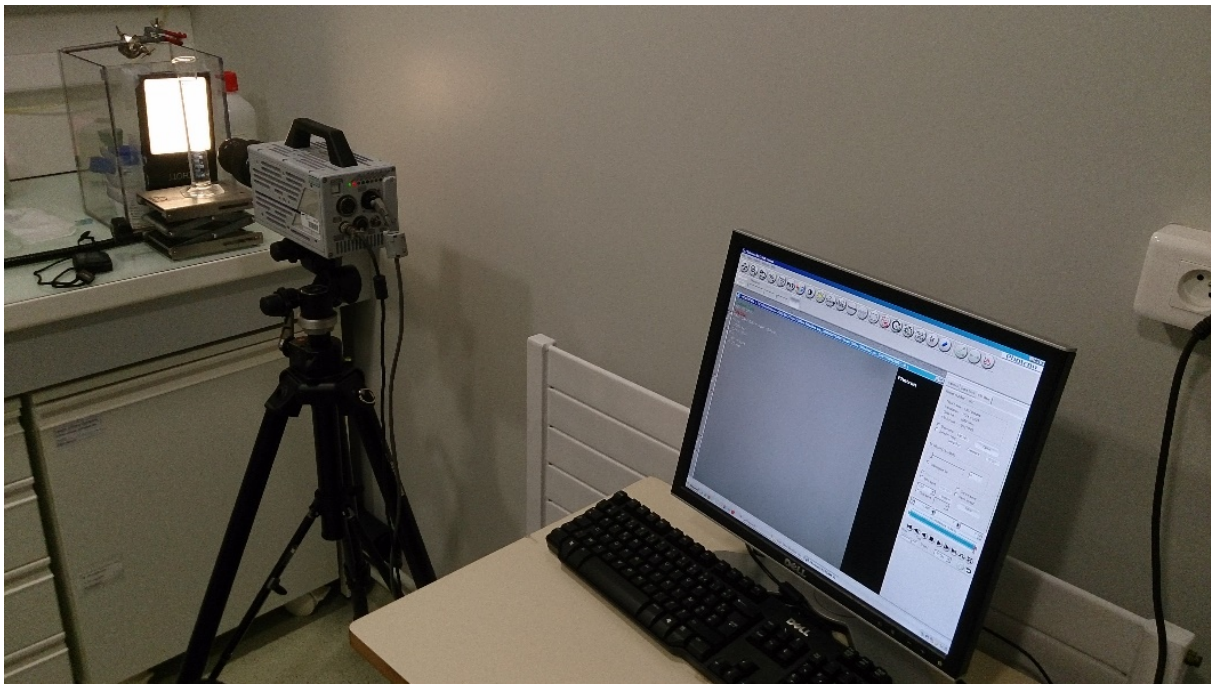


Figure 8. 4 Setup for recording the falling beads inside the cylinder for evaluation of the terminal velocity



Figure 8. 5 Fluidized bed bioreactor used to study the transport of vitamin B12 into the beads (dynamic system)

3. Results

Figure 8. 6 and Figure 8. 7 show the image of a sample bead under microscope, and the colored beads using methylene blue, respectively. The size of the bead depends on various factors, such as the extrusion needle-s diameter, the distance of the needle from the gelation solution bath, the flow rate at which the alginate is pumped into the extrusion, etc. However, controlling the size of the beads was not part of this study.

Swelling of the freshly made beads was evaluated during 2.5 hours after their preparation, both in static and fluidized conditions. According to the acquired data, a slight increase in beads' diameters was observed, around 5% under static conditions (Figure 8. 8).

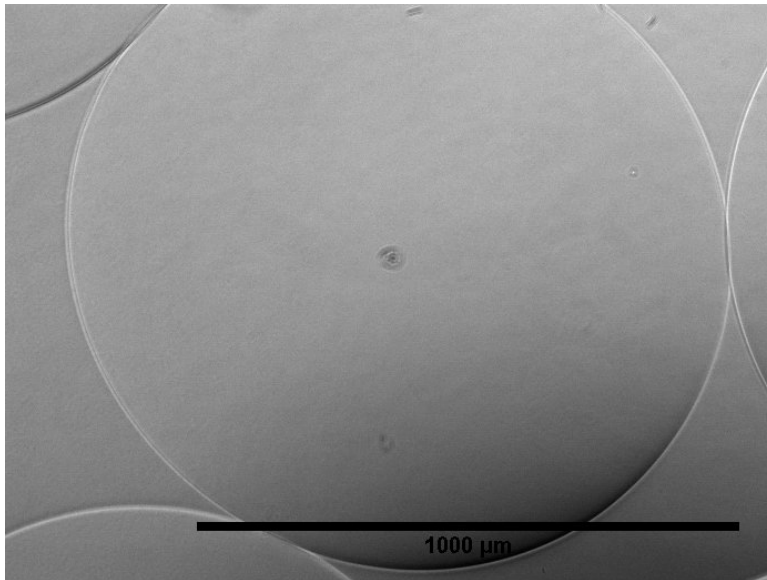


Figure 8. 6 A sample image of an alginate bead under the microscope.

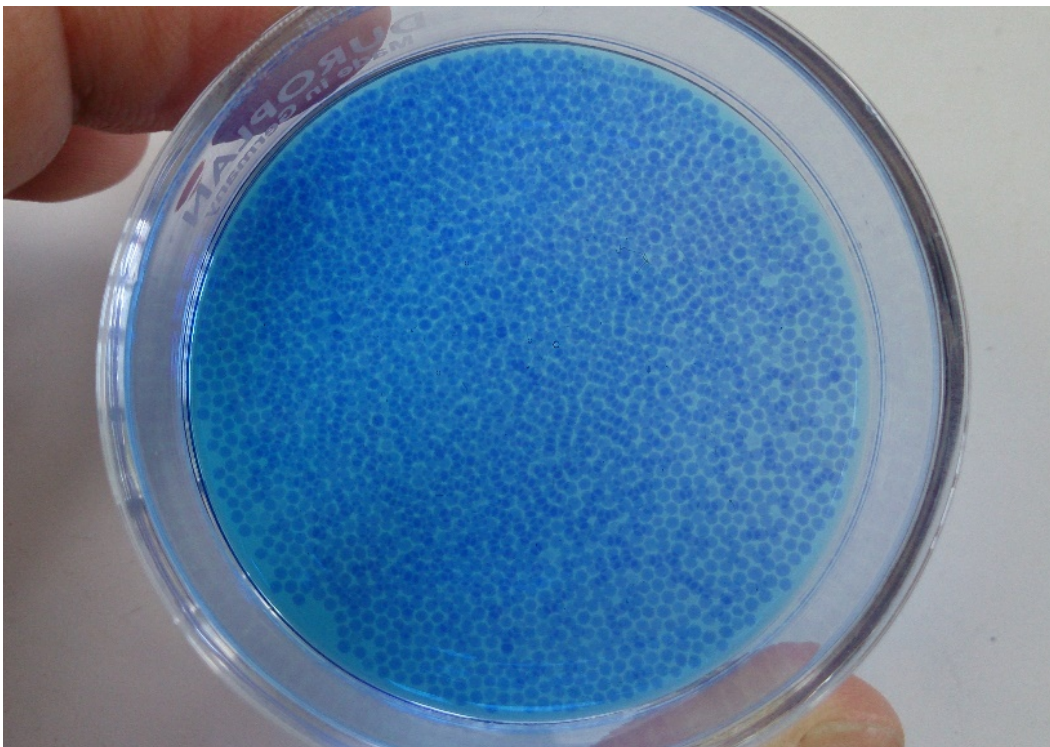


Figure 8. 7 Prepared beads colored with methylene blue.

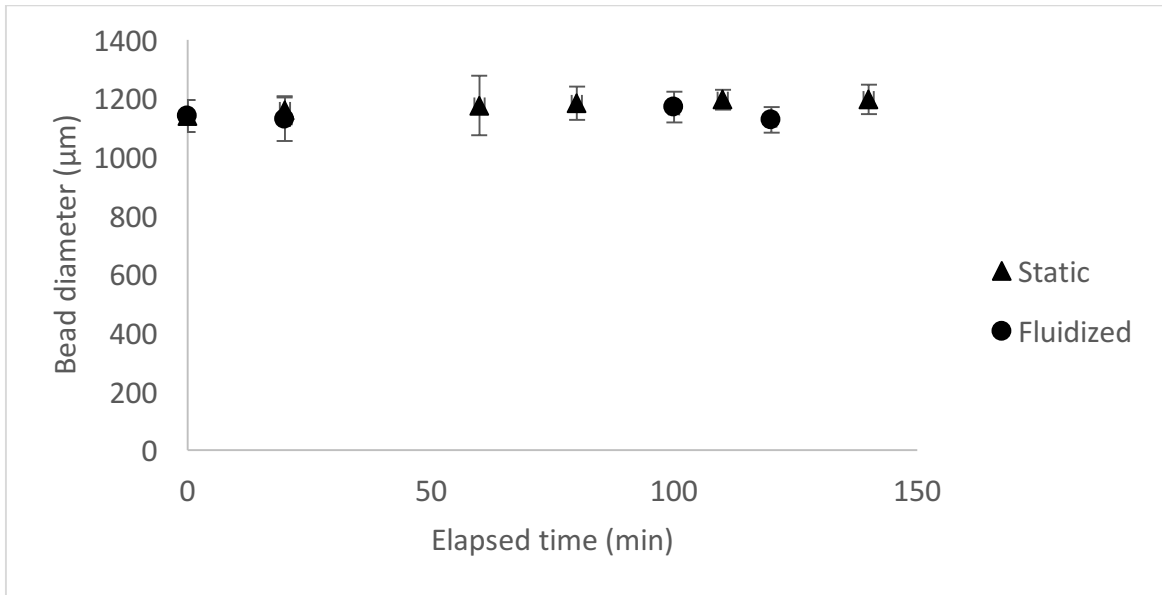


Figure 8. 8 Swelling of the freshly prepared beads over time in static and fluidized conditions.

Figure 8. 9 shows the processing of the images for calculation of the terminal velocity. The velocity was calculated for 8 beads, resulting in an average of 1.92 mm/s. Diffusion of B12 molecules in the beads was also studied in static and fluidized conditions in terms of reduced B12 concentration in the medium over time (Figure 8. 10 and Figure 8. 11). Concentration drop in static system is quite smooth, while the results from dynamic (fluidized) system are rather uneven.

4. Discussion

Fluidization of the beads were studied at an introductory level. When the medium flow starts, the bed of settled-down beads is initially lifted up as a whole, the rate and amount of which depends on the medium flowrate. The beads subsequently start to fall down from the lifted packed bed, causing disintegration of the bed and circulation of the beads.

Considering that a laminar flow is applied to the cylindrical bioreactor, a parabolic velocity profile exists in the bioreactor, with highest velocity prevailing in the middle. Accordingly, the beads show a circular motion in the bioreactor as they move upwards through the middle section of the bioreactor to the top of the expanded bed and fall down at the sides close to the wall. At the center, the drag force exerted on the beads is larger than the gravitational force, which is the opposite of what happens near the wall.



Figure 8.9 Sample of the captured images, showing three alginate beads and their position through time: 9.72 (top), 13.08 (middle), 15.48 (bottom) seconds after starting to record. The beads are marked by circles for better visualization.

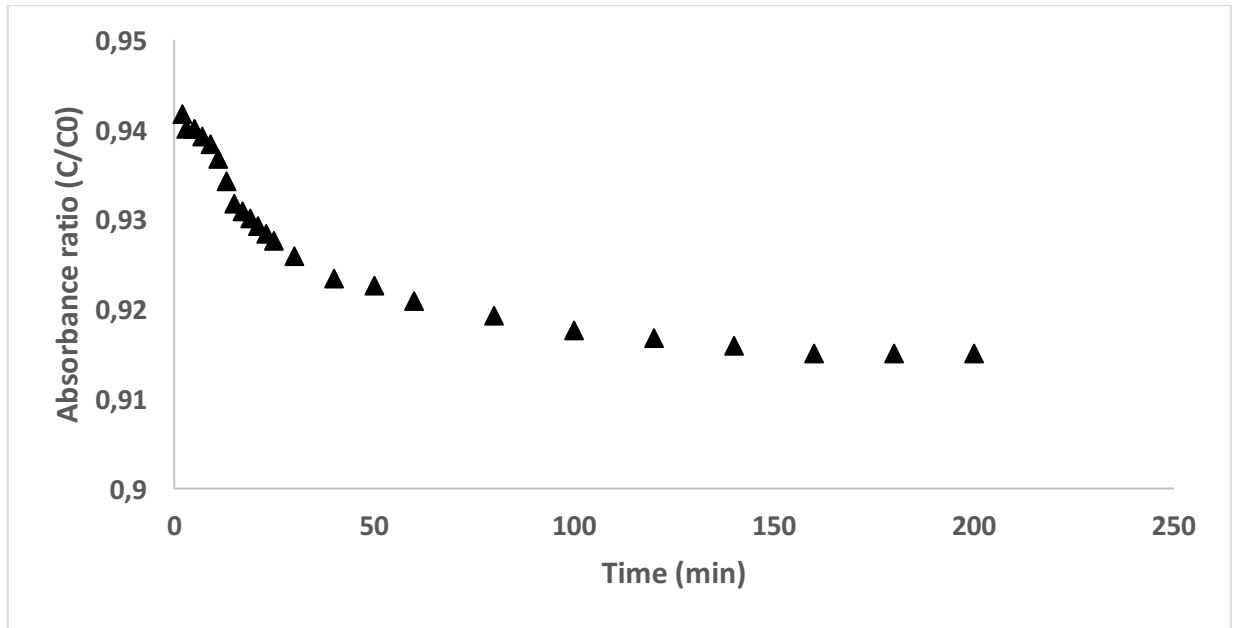


Figure 8. 10 Decrease in the concentration of vitamin B12 in the free medium due to its diffusion into the beads (static condition)

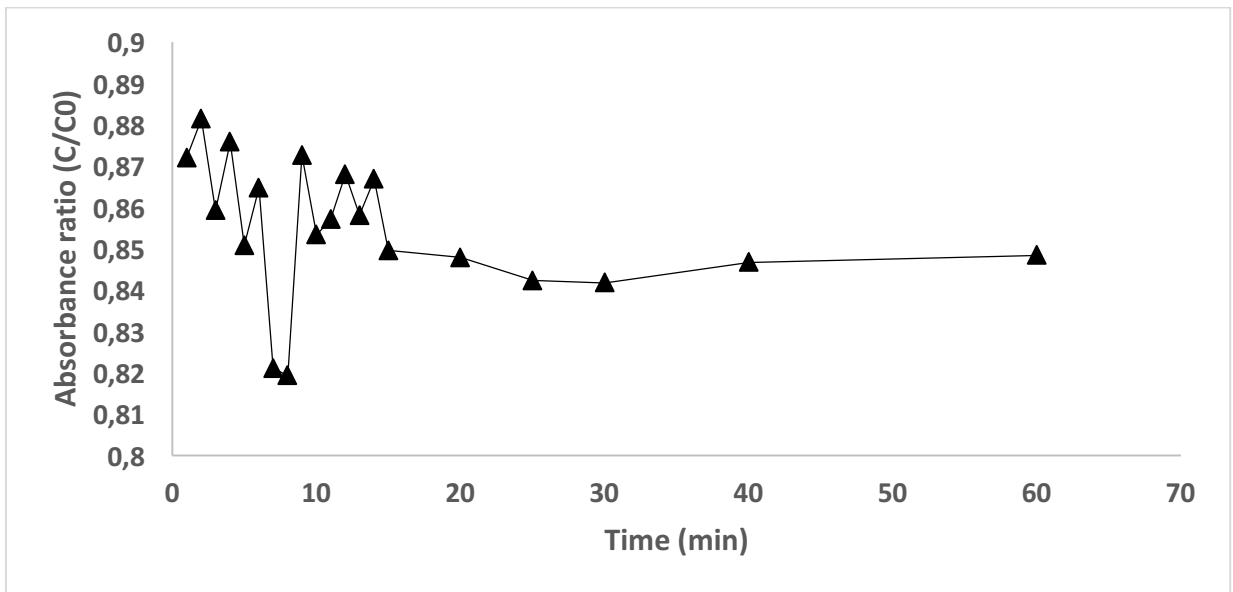


Figure 8. 11 Decrease in the concentration of vitamin B12 in the free medium due to its transport into the beads (dynamic condition)

Observation of the beads in motion was very challenging due to the high transparency of the beads and the small difference between the refractive indices of the solution and alginate. In an attempt to increase the contrast, the beads were colored using methylene blue solution (added to the

already-prepared alginate beads) and blue dextran (added to alginate solution before extrusion). However, neither of the methods gave satisfactory results. A significant amount of blue dextran was lost during the preparation steps, especially alginate filtration. Adding methylene blue to the beads initially seemed satisfactory. However, during both experiments of fluidization and falling beads, the color was eventually washed away from the beads. Since decreasing the beads' transparency turned out to be unsuccessful, imaging of the falling beads through the column was employed, which allowed us to calculate the terminal velocity.

Although the swelling test showed a general increasing trend in size of the beads, drawing any conclusions is not statistically credible due to small number of samples, particularly in the fluidized system. Additionally, here the swelling was tested within 140 minutes after preparation of the beads which is a short period of time.

As vitamin B12 solution was added to the beads, its concentration was observed to decrease due to diffusion of the molecules into the beads. Figure 8. 10 shows the concentration of vitamin B12 in the solution above the beads inside the cuvette. It is indeed very challenging to completely remove the Ringer solution from the voids between the beads and add vitamin B12 solution without causing any turbulence, both of which adversely affects the results. The former is especially noticeable since the curve in Figure 8. 10 does not begin from 1 at $t=0$. The concentration of vitamin B12 in the fluidized bed is rather sporadic. This could be attributed to having inadequately mixed solution in the reservoir or improper sampling, although this experiment is also not suitable to make valid conclusions.

5. Conclusions

This Appendix presented some of the major aspects in a fluidized bed bioreactor such as fluidization, terminal velocity, swelling and diffusion into the alginate beads studied as a training activity. Even though drawing conclusions and making comparisons with a hollow fiber bioreactor is unfortunately not credible based on obtained results, this was a great opportunity to familiarize with another type of bioreactor potentially used as a BAL device nonetheless.

References

1. Di Felice, R., *Hydrodynamics of liquid fluidisation*. Chemical Engineering Science, 1995. **50**(8): p. 1213-1245.
2. Dore, E. and C. Legallais, *A new concept of bioartificial liver based on a fluidized bed bioreactor*. Ther Apher, 1999. **3**(3): p. 264-7.
3. Legallais, C., E. Dore, and P. Paullier, *Design of a fluidized bed bioartificial liver*. Artif Organs, 2000. **24**(7): p. 519-25.
4. Figaro, S., et al., *Development and validation of a bioartificial liver device with fluidized bed bioreactors hosting alginate-encapsulated hepatocyte spheroids*. Conf Proc IEEE Eng Med Biol Soc, 2015. **2015**: p. 1335-8.
5. Gautier, A., et al., *Impact of alginate type and bead diameter on mass transfers and the metabolic activities of encapsulated C3A cells in bioartificial liver applications*. Eur Cell Mater, 2011. **21**: p. 94-106.

